frontiers | Research Topics

Single-molecule image analysis

Edited by
Christian Franke, Thomas Pengo and Siân Culley

Published in
Frontiers in Bioinformatics

ISSN 1664-8714
ISBN 978-2-88976-034-3
DOI 10.3389/978-2-88976-034-3

About Frontiers

Frontiers is more than just an open access publisher of scholarly articles: it is a pioneering approach to the world of academia, radically improving the way scholarly research is managed. The grand vision of Frontiers is a world where all people have an equal opportunity to seek, share and generate knowledge. Frontiers provides immediate and permanent online open access to all its publications, but this alone is not enough to realize our grand goals.

Frontiers journal series

The Frontiers journal series is a multi-tier and interdisciplinary set of open-access, online journals, promising a paradigm shift from the current review, selection and dissemination processes in academic publishing. All Frontiers journals are driven by researchers for researchers; therefore, they constitute a service to the scholarly community. At the same time, the *Frontiers journal series* operates on a revolutionary invention, the tiered publishing system, initially addressing specific communities of scholars, and gradually climbing up to broader public understanding, thus serving the interests of the lay society, too.

Dedication to quality

Each Frontiers article is a landmark of the highest quality, thanks to genuinely collaborative interactions between authors and review editors, who include some of the world's best academicians. Research must be certified by peers before entering a stream of knowledge that may eventually reach the public - and shape society; therefore, Frontiers only applies the most rigorous and unbiased reviews. Frontiers revolutionizes research publishing by freely delivering the most outstanding research, evaluated with no bias from both the academic and social point of view. By applying the most advanced information technologies, Frontiers is catapulting scholarly publishing into a new generation.

What are Frontiers Research Topics?

Frontiers Research Topics are very popular trademarks of the *Frontiers journals series*: they are collections of at least ten articles, all centered on a particular subject. With their unique mix of varied contributions from Original Research to Review Articles, Frontiers Research Topics unify the most influential researchers, the latest key findings and historical advances in a hot research area.

Find out more on how to host your own Frontiers Research Topic or contribute to one as an author by contacting the Frontiers editorial office: frontiersin.org/about/contact

Single-molecule image analysis

Topic editors
Christian Franke — Friedrich Schiller University Jena, Germany
Thomas Pengo — University of Minnesota Twin Cities, United States
Siân Culley — Randall Centre for Cell & Molecular Biophysics, School of Basic & Medical Biosciences, Faculty of Life Sciences & Medicine, King’s College London, United Kingdom

Citation
Franke, C., Pengo, T., Culley, S., eds. (2022). *Single-molecule image analysis*. Lausanne: Frontiers Media SA. doi: 10.3389/978-2-88976-034-3

Table of contents

frontiers | Frontiers in Bioinformatics

EDITORIAL
published: 06 April 2022
doi: 10.3389/fbinf.2022.897938

Editorial: Single-Molecule Image Analysis

Thomas Pengo[1]*, *Siân Culley*[2]* and *Christian Franke*[3,4,5]*

[1]Informatics Institute, University of Minnesota, Minneapolis, MN, United States, [2]Randall Centre for Cell and Molecular Biophysics, School of Basic and Medical Biosciences, Faculty of Life Sciences and Medicine, King's College London, London, United Kingdom, [3]Institute of Applied Optics and Biophysics, Faculty of Physics and Astronomy, Friedrich Schiller University Jena, Jena, Germany, [4]Abbe Center of Photonics, Friedrich Schiller University Jena, Jena, Germany, [5]Jena Center for Soft Matter, Friedrich Schiller University Jena, Jena, Germany

Keywords: single-molecule localisation microscopy, SMLM, super-resolution microscopy, image analysis, clustering, tracking, software

Editorial on the Research Topic

Single-Molecule Image Analysis

Seeing is believing. This little sentence illustrates the prime reason why microscopy is such a widespread and powerful tool for the study of biological systems. To observe something with one's own eyes, even with the help of a microscope, is a potent experience. The super-resolved approach single-molecule localization microscopy (SMLM), however, goes beyond the qualitative aspects of biological imaging at an unprecedented level of detail: it offers the unique ability to capture spatio-temporal coordinates for detected fluorescence emission events from individual molecules. Today, SMLM is applied increasingly as a quantitative tool for, e.g., molecular clustering, tracking and stoichiometry, benefitting from the multitude of extractable parameters within the set of localized coordinates.

In this research topic we have gathered contributions from scientists working on a broad range of aspects in SMLM, all unified in their focus on extracting information from multi-dimensional localization data. In total, 12 articles have been included, with a mixture of 10 original research articles (2 technology and code, 5 original research, 3 methods), 1 review and 1 opinion article.

Since we started working on the research topic, we all have witnessed a very difficult year. The pandemic is claiming and changing the lives of countless people around the world, hitting the already disadvantaged worst and exacerbating the painful reality of disparity between those who have access to wealth and those who don't. Meanwhile, other diseases still persist, and sadly last year saw the loss of one of the SMLM community's most respected leaders, Kat Gaus, to cancer. In his special contribution to the research topic Cebecauer offers a heartfelt tribute to her life and a glimpse into the rich legacy she left behind.

Since its first description in the literature a decade and a half ago, SMLM has flourished into a well-established method, albeit one that is difficult to master due to its reliance on specialized fluorophores, stringent illumination requirements, and intensive data processing.

Here, Martens et al. have demystified the computational aspect of SMLM by producing a wonderful summary of the processing required to bring a dataset from raw data to analysis and visualization. In their work, the authors provide not only a general introduction to the methods, divided in eight modules, but also ready-to-use educational code and tutorials in both MATLAB and Python.

One of the key computational challenges in SMLM is extracting biologically meaningful information from molecular coordinates. A number of articles in this research topic are thus dedicated to tackling the analysis of multi-dimensional spatial localization distributions.

Edited and reviewed by:
Kevin Eliceiri,
University of Wisconsin-Madison,
United States

****Correspondence:***
Thomas Pengo
tpengo@umn.edu
Siân Culley
sian.culley@kcl.ac.uk
Christian Franke
christian.franke@uni-jena.de

Specialty section:
This article was submitted to
Computational BioImaging,
a section of the journal
Frontiers in Bioinformatics

Received: *16 March 2022*
Accepted: *17 March 2022*
Published: *06 April 2022*

Citation:
Pengo T, Culley S and Franke C (2022)
Editorial: Single-Molecule
Image Analysis.
Front. Bioinform. 2:897938.
doi: 10.3389/fbinf.2022.897938

In an ideal SMLM experiment, a single fluorophore blinking event would be detected within one camera frame. However, in reality, one individual emission event can span multiple camera frames; without appropriate analytical treatment this can result in over-counting the number of emitting molecules. Here, Schodt and Lidke present a molecularly-informed grouping algorithm, formulated as a linear assignment problem, that accounts for photophysical kinetics, e.g., multiple blinking steps and bleaching, and local emitter density variations. This helps assign detected emission events to the correct fluorophore.

Structural resolution is one of the key parameters in SMLM experiments and is a multivariate problem, since not only the localization precision of single fluorophores, but also the final localization density is significant. Especially in experimental settings, where resolution is mainly limited by the resulting localization density, e.g., in expansion microscopy, backfilling the image by deep-learning approaches has become a promising approach. In their manuscript, Berberich et al. describe a clever approach of utilizing Fourier Ring Correlation as a trainable quality metric that can be based on sparse SMLM data sets. This new loss function can complement a multiscale structural similarity index, leading to an overall improved reconstruction and can be easily integrated in existing deep-learning and analysis workflows.

SMLM data is not limited to just two dimensions, and several articles here describe analytical methods relating to extension of SMLM in the axial, temporal, and spectral dimensions.

In an interesting overlap with computer vision, Blundell et al. show how it is possible to use Deep Learning to perform what is otherwise a hard problem: finding 3D structure from individual 2D projections. HOLLy, their software, uses a Convolutional Neural Network, coupled to a differentiable renderer, to explore the space of 3D structures and find candidates that match the input data.

The single molecule nature of SMLM dovetails into the field of single particle tracking (SPT), whereby the temporal dynamics of labelled protein species can be measured. In order to increase the throughput of SMLM for tracking approaches, Butler et al. designed a microscope capable of spectrally resolving 3D localizations in dynamic samples, allowing for identification of different fluorophores without imaging in multiple channels. Alongside this hardware development, they showcase an analytical framework for disentangling the multi-dimensional data acquired and leveraging spectral information to inform multi-emitter fitting analysis.

SPT data from living samples presents a complex analysis problem for dissecting contributions from biological environments with an unknown number of diffusive states. Chen et al. combine Deep Learning with non-parametric Bayesian inference to tackle complicated live-SPT data for which: “the number of diffusive states is unknown, mixtures of different diffusive populations may exist within single trajectories, symmetry cannot be assumed between the x and y directions, and anomalous diffusion is possible.”

Many signalling pathways in cell biology are mediated by protein clustering at the cell membrane. As SMLM provides the coordinates of individual molecules, it is an ideal technique for quantifying the spatial distributions of such clusters. This quantification is enabled by Kutz et al., who provide access to advanced Bayesian cluster analysis algorithms through a Graphical User Interface, BaClAva. This software not only supports the analysis of SMLM data, but also simulation, through which the user can explore the effect of algorithm and parameter choice on clustering performance.

Cluster analysis is a challenging problem not just within the context of a single image, but also when aggregating results across different datasets. Feher et al. have developed a novel algorithm called KNA (K-neighborhood analysis), based on principal component analysis of vectors between nearest-neighbor molecule coordinates. The authors demonstrate the application of this approach in enhancing the performance of existing clustering algorithms, visualising SMLM data in terms of molecule neighborhood, and joint analysis across distinct datasets. Beyond these technical advances, this manuscript is particularly remarkable as it was finalized in a spirited manner by Kat Gaus‘ group after her death in March 2021.

In addition to uncovering whether molecules of the same species form clusters, extending SMLM into multiple colors can provide information on interactions between different molecular species. Mancebo et al. describe a novel method for efficiently isolating clusters which co-localize with a second channel, based on using k-dimensional trees. This method, implemented in MATLAB, offers a dramatic reduction in memory and computational power requirements over other methods.

One of the topics the scientific community is particularly concerned about at the moment is reproducibility. In this research topic, we had contributions that tackled the issue of how far we can trust the results, either by quantifying the uncertainty or, complementarily, how to integrate quality metrics to improve the final resolution.

Thiele et al. present a theoretical discourse of the estimation of the fluorescence lifetime in FLIM and SML-FLIM. By using a maximum likelihood estimator, they derive the Cramer-Rao lower bound of the lifetime variance with noise and demonstrate its usage with simulated and experimental data. The described approach is part of their open-domain software “Fluorescence-Lifetime TrackNTrace” and thus readily available for users.

Schneider and Schütz discuss and demonstrate the so far underused application of significance testing in single-molecule experiments. They deliver on their manuscript title, by showcasing the appropriate usage of p-value testing for localization cluster analysis and the proper combination of results obtained from multiple cells and/or experiments. Since cluster analysis has become its own sub-field within SMLM and the pointillistic nature of localization microscopy coupled with the iterative detection of the same molecules poses an ongoing bottleneck, their approach of attaining an overall p-value, testing against a random distribution of molecules has the potential to become an important standard for future SMLM cluster studies. Furthermore they present a block permutation test for single-molecule tracking data, circumventing their inherent correlation which can obscure conventional statistical significance testing.

TABLE 1 | Comprehensive list of the software packages mentioned in the manuscripts in this research topic, along with their code availability destination at the time of publishing and public licensing specifications.

Authors	Software	Code	Licensing
Martens et al.	SMLMComputational	GitHub | Google Drive	GPL-3.0
Schodt and Lidke	SMLMFrameConnection	GitHub	MIT
Berberich et al.	FRCnet	GitHub	MIT
Blundell et al.	HOLLy	GitHub	GPL-3.0
Butler et al.	PALMTracer	GitHub	Custom
Chen et al.	NOBIAS	GitHub	GPL-3.0
Kutz et al.	BaClAva	GitHub	MIT
Feher et al.	KAN	Supplementary Material #2	GPL-3.0
Mancebo et al.	cross-correlation-filtering	GitHub	MIT
Thiele et al.	TrackNTrace	GitHub	GPL-3.0
Schütz and Schneider	Block-permutation method	GitHub	GPL-3.0

Taken together, these articles present an overview of the broad application range of SMLM and its current trends. In light of the emerging reproducibility crisis, which includes algorithm driven high-end microscopy, it is of utmost importance to make the relevant source code or analysis software accessible to the widest possible audience. We are therefore especially pleased with the contributions to this special research topic, as virtually all presented approaches are accompanied with open-domain software and/or well documented source code (see **Table 1**). Thus, the work collected in this special research topic functions both as a useful, accessible resource for interested SMLM newcomers and users, as well as hopefully an inspiration for future endeavors.

AUTHOR CONTRIBUTIONS

TP, CF and SC conceived the research topic. TP, CF and SC wrote the manuscript.

ACKNOWLEDGMENTS

We wanted to thank all the contributors to this research topic for their insightful and interesting manuscripts.

Conflict of Interest: The authors declare that the research was conducted in the absence of any commercial or financial relationships that could be construed as a potential conflict of interest.

frontiers in Bioinformatics

ORIGINAL RESEARCH
published: 10 September 2021
doi: 10.3389/fbinf.2021.742073

NOBIAS: Analyzing Anomalous Diffusion in Single-Molecule Tracks With Nonparametric Bayesian Inference

Ziyuan Chen[1], *Laurent Geffroy*[2] *and Julie S. Biteen*[1,2]*

[1]*Department of Biophysics, University of Michigan, Ann Arbor, MI, United States,* [2]*Department of Chemistry, University of Michigan, Ann Arbor, MI, United States*

Single particle tracking (SPT) enables the investigation of biomolecular dynamics at a high temporal and spatial resolution in living cells, and the analysis of these SPT datasets can reveal biochemical interactions and mechanisms. Still, how to make the best use of these tracking data for a broad set of experimental conditions remains an analysis challenge in the field. Here, we develop a new SPT analysis framework: NOBIAS (NOnparametric Bayesian Inference for Anomalous Diffusion in Single-Molecule Tracking), which applies nonparametric Bayesian statistics and deep learning approaches to thoroughly analyze SPT datasets. In particular, NOBIAS handles complicated live-cell SPT data for which: the number of diffusive states is unknown, mixtures of different diffusive populations may exist within single trajectories, symmetry cannot be assumed between the *x* and *y* directions, and anomalous diffusion is possible. NOBIAS provides the number of diffusive states without manual supervision, it quantifies the dynamics and relative populations of each diffusive state, it provides the transition probabilities between states, and it assesses the anomalous diffusion behavior for each state. We validate the performance of NOBIAS with simulated datasets and apply it to the diffusion of single outer-membrane proteins in *Bacteroides thetaiotaomicron*. Furthermore, we compare NOBIAS with other SPT analysis methods and find that, in addition to these advantages, NOBIAS is robust and has high computational efficiency and is particularly advantageous due to its ability to treat experimental trajectories with asymmetry and anomalous diffusion.

Keywords: single-molecule tracking (SPT), nonparametric Bayesian statistics, hierarchical Dirichlet process (HDP), hidden Markov model (HMM), recurrent neural network (RNN), anomalous diffusion

Edited by:
Thomas Pengo,
University of Minnesota Twin Cities,
United States

Reviewed by:
Colin Kinz-Thompson,
Rutgers University, Newark,
United States
Carl-Magnus Svensson,
Leibniz Institute for Natural Product
Research and Infection Biology,
Germany

***Correspondence:**
Julie S. Biteen
jsbiteen@umich.edu

Specialty section:
This article was submitted to
Computational BioImaging,
a section of the journal
Frontiers in Bioinformatics

Received: *15 July 2021*
Accepted: *25 August 2021*
Published: *10 September 2021*

Citation:
Chen Z, Geffroy L and Biteen JS (2021)
NOBIAS: Analyzing Anomalous
Diffusion in Single-Molecule Tracks
With Nonparametric
Bayesian Inference.
Front. Bioinform. 1:742073.
doi: 10.3389/fbinf.2021.742073

INTRODUCTION

The biophysical dynamics of biomolecules reflect the biochemical interactions in the system, and these dynamics can be quantified within a dataset of single-particle trajectories obtained by tracking individual molecules. The invention of the super-resolution microscope (Moerner and Kador, 1989; Hell and Wichmann, 1994; Betzig et al., 2006; Hess et al., 2006; Rust et al., 2006) and single-particle tracking (SPT) methods (Yildiz et al., 2003; Deich et al., 2004; Elmore et al., 2005; Manley et al., 2008) have made possible investigations of biomolecular dynamics at a high temporal and spatial resolution both *in vitro* and *in vivo*. Moreover, quantitative SPT algorithms can connect the real-time dynamics from biophysical trajectories to biochemical roles to uncover whether a molecule interacts with other cellular components (Izeddin et al., 2014), freely diffuses (Badrinarayanan et al., 2012), is actively transported (Park et al., 2014), or is constrained to a certain region (Bayas et al., 2018).

Conventionally, SPT trajectory datasets have been assumed to be Brownian, such that the mean squared displacement, MSD, of each track is linearly proportional to the time lag, τ, and the diffusion coefficient, D, can be calculated from a linear fit to this curve (Qian et al., 1991; Saxton, 1997). This Brownian motion assumption works accurately for freely diffusing molecules in solution. Despite the accessibility of this method, it has a simplified assumption that the molecule is freely diffusing with a single diffusive state (a single D value) for each trajectory. In the complicated cellular environment, however, multiple diffusive states, each characterized by an average D, can exist—for instance due to binding and unbinding events—and molecules can transition between different states to produce heterogeneity even within single trajectories. To reveal these heterogeneous dynamics, probability distribution-based methods such as cumulative probability distribution (Schütz et al., 1997; Mazza et al., 2012), have been applied. Probability distribution-based models use kinetic modeling with a predetermined number of diffusive states and are fit to histograms of displacements calculated at different time lags. These probability-based kinetic models pool displacements from the SPT dataset to estimate the D and weight fraction for each diffusive state in the model. Probability distribution-based analytical tools (Rowland and Biteen, 2017; Hansen et al., 2018) have been widely applied to SPT datasets with extra corrections that consider the experimental microscopy data collection process. These corrections include localization error (Michalet and Berglund, 2012), confinement (Kusumi et al., 1993), motion blur (Berglund, 2010; Deschout et al., 2012), and out-of-focus effects (Lindén et al., 2017) in the probability model.

For some well-studied biological systems in which the biochemical states of molecules have been determined through other methods, a fixed-state number analytical tool can be suitable for quantifying the dynamics and weight for each state (Elf et al., 2007; Hansen et al., 2017). However, SPT can also be used as the beginning step to investigate biomolecule dynamics without prior knowledge of how many diffusive states there supposed to be (Monnier et al., 2015; Sungkaworn et al., 2017; Biswas et al., 2021). In these cases, how to objectively determine the number of diffusive states is a great challenge. Moreover, these models provide a D value for each subpopulation, but they do not assign the diffusive state to each individual single-molecule step, nor do they quantify the transition probability between distinct diffusive states within one trajectory. However, these transition probabilities can reveal important biological meaning such as the presence of critical biochemical intermediates (Biswas et al., 2021).

Bayesian statistics and Hidden Markov Models (HMMs) have been applied to analyze SPT datasets without assuming a predetermined number of diffusive states and to access the probabilities of transitioning between distinct states (Persson et al., 2013; Monnier et al., 2015; Karslake et al., 2020; Heckert et al., 2021). vbSPT, which was one of the first applications of HMM for SPT analysis (Persson et al., 2013), uses a maximum-evidence criterion to select between models with different numbers of diffusive states; within each model, a fixed-order HMM is used to infer the diffusion coefficient, weight fraction, and transition probabilities for each state. More recently, nonparametric Bayesian models based on Dirichlet processes were combined with HMM to recover the number of diffusive states from SPT trajectory datasets, such as in SMAUG (Karslake et al., 2020) and DSMM (Heckert et al., 2021). In these models, the motion of the molecule is approximated to be symmetric and Brownian, which is an oversimplification considering the crowded environment and various interaction partners for biomolecules in cells.

To move beyond Brownian motion, here we consider a more general random walk family: anomalous diffusion. In anomalous diffusion, MSD and τ are related by a power law distribution, $MSD \sim \tau^{\alpha}$, where α is the anomalous diffusion exponent (Metzler et al., 2014). Brownian motion is a special case of anomalous diffusion ($\alpha = 1$), and other cases can be further divided into subdiffusion ($\alpha > 1$) and superdiffusion ($\alpha < 1$). Biomolecules have been reported to diffuse anomalously in many situations, such as constrained membrane protein motion (Jeon et al., 2016), the facilitated diffusion of DNA binding protein (Bauer and Metzler, 2012), and active transportation of cargoes (Caspi et al., 2002). Different designs of neural networks effectively classify the diffusion type of trajectories (Bo et al., 2019; Granik et al., 2019; Argun et al., 2021; Gentili and Volpe, 2021), however these analyses typically assume that each track is dynamically homogeneous and is characterized by a single type of diffusion and a single D value. It remains a challenge to classify the diffusion type within a trajectory when considering the possibility of changes in dynamics or diffusion types within a single track.

Here we introduce the NOnparametric Bayesian Inference for Anomalous diffusion in Single-molecule tracking (NOBIAS) framework to address the assumptions and simplifications discussed above and provide a more physiologically relevant analysis algorithm to quantify the dynamics encoded in SPT datasets (**Figure 1**). In particular, NOBIAS recovers the number of diffusive states and predict the diffusion type for each diffusive state, even in heterogeneous trajectories. The NOBIAS framework consists of two modules. The first module uses a Hierarchical Dirichlet Process Hidden Markov Model (HDP-HMM) with multivariate Gaussian emission to recover the number of diffusive states and infer their corresponding diffusion coefficients and weight fractions. This module also assigns each single-molecule step a diffusive state label to provide the state label sequence and the matrix of transition probabilities. In the second module, the original trajectories are segmented by diffusive state label and a pre-trained Recurrent Neural Network (RNN) is used to classify these segments and assign the diffusion type (Brownian motion, Fractional Brownian motion, Continuous Time Random Walk, or Lévy Walk) for each diffusive state. We simulated trajectory datasets with mixtures of heterogeneous dynamics and diffusion types to validate the NOBIAS framework, and we analyzed the

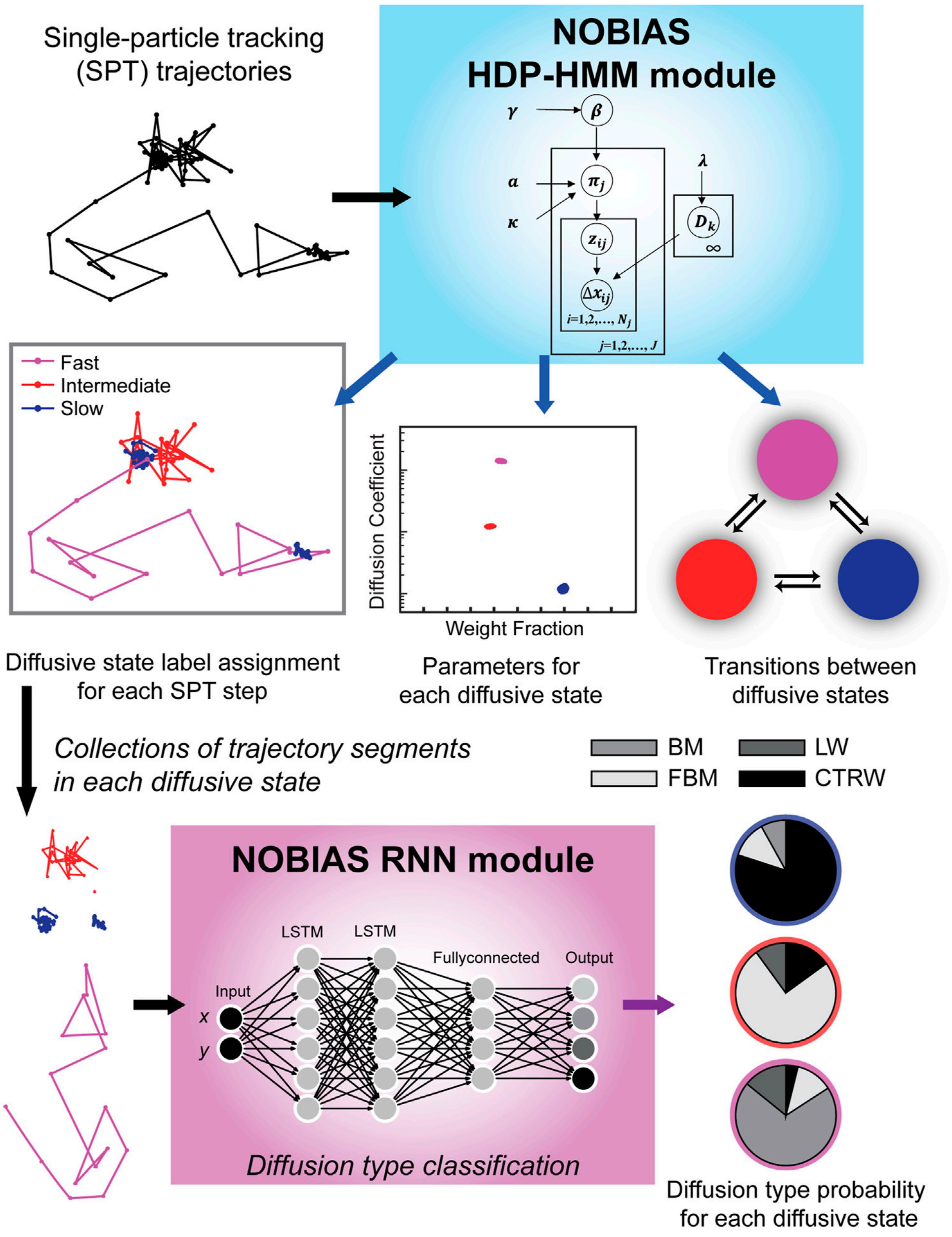

FIGURE 1 | NOBIAS workflow. (1) Single-particle tracking (SPT) trajectory datasets are processed in the NOBIAS HDP-HMM module: the observed data (the displacements, $\Delta \boldsymbol{x}$) are analyzed in the context of the emission parameters (the diffusion coefficients, $\boldsymbol{D}$). The state sequence, z, indicates the diffusive state corresponding to each step, and the transition matrix, π, is estimated with a Hierarchical Dirichlet process prior using concentration hyperparameters a and γ and the sticky parameter, κ. The HDP-HMM module provides D and the weight fraction for each diffusive state, the π for transition probabilities between these states, and a state label assignment for each SPT step. (2) In the NOBIAS RNN module, trajectory segments of the same diffusive state are collected and put in a pre-trained Recurrent Neural Network (RNN) with two long short-term memory (LSTM) layers to classify the diffusion type for each diffusive state.

SPT dataset from experimental measurements of the SusG outer-membrane protein in living *Bacteroides thetaiotaomicron* to access its dynamics and anomalous diffusion behaviors, which are consistent with its role in starch catabolism in gut microbiome. This framework uses nonparametric Bayesian statistics and Deep learning to thoroughly analyze a single-molecule tracking dataset. It provides an objective method to determine the number of diffusive states in an SPT dataset and accesses the multidirectional dynamics of each state. A further diffusion type classification for each diffusive state is also included in the framework. The NOBIAS framework overcomes some oversimplified assumptions in SPT analysis and provides a powerful tool to fully make use of single-molecule tracking data.

METHODS

Hidden Markov Model

A HMM infers a system with a discrete-valued sequence of unobservable states that can be modeled as a Markovian process (Rabiner, 1989). The HMM assumes that the observed data have a hidden discrete-valued state sequence, and at each observed time, the observed data only depends on its hidden state. In our NOBIAS application of the HMM model, the observed data is the single-molecule displacements and the hidden state is the molecule's distinct biophysical diffusive state.

Suppose z_t is the hidden state of the Markovian chain at time t and y_t is the observed data at time t, the HMM follows the following generative process:

$$z_1 \sim \pi^{(0)},\ z_{t+1}\big|z_t \sim \pi^{(z_t)},\ y_t\big|z_t \sim f\left(\theta^{(z_t)}\right) \tag{1}$$

Here, π refers to the transition matrix of a HMM and $\pi^{(z_t)}$ is the z_t row of the transition matrix and is the transition distribution for state z_t. Given z_t and the corresponding emission parameter $\theta^{(z_t)}$, y_t is independently generated from the emission function $f(\theta^{(z_t)})$. In NOBIAS, the observed data, y_t, is the vector of single-step displacements, $\Delta\boldsymbol{x}_t$, and the emission function is a zero-mean multivariate Gaussian distribution, and the emission parameter is the set of diffusion coefficients, $\boldsymbol{D}^{(z_t)}$:

$$\Delta\boldsymbol{x}_t\big|z_t \sim Norm\left(0,\ 4\boldsymbol{D}^{(z_t)}\tau\right)$$

Dirichlet Process for Nonparametric Bayesian

In NOBIAS, the Dirichlet Process (DP) is used in the prior for the parameters of a mixture model with an unknown number of components. A random probability measure, G_0, on a measurable space, Θ, is distributed according to a DP when (Ferguson, 1973):

$$(G_0(B_1),\ldots,G_0(B_n))|\gamma,\ H \sim Dir\left(\left(\gamma H(B_1),\ldots,\gamma H(B_k)\right)\right. \tag{2}$$

Here, Dir is a Dirichlet distribution, H is a base measurement, γ is a positive concentration parameter, and $\{B_i\}_{i=1}^{n}$ is a finite partition of Θ. In this case, we write $G_0 \sim DP(\gamma, H)$.

From this definition follow two properties of Dirichlet processes. First, if $G_0 \sim DP(\gamma, H)$, then G_0 is atomic and can be written as:

$$G_0 = \sum_{i=1}^{\infty}\beta_i\delta_{\theta_i} \tag{3}$$

Here, β_i is a weight and δ_{θ_i} is a unit-mass measure at observation $\theta_i|H \sim H$.

Second, based on the conjugacy of the finite Dirichlet distribution, given a set of observations $\theta_1, \ldots, \theta_N$ where $\theta_i \sim G_0$, the posterior distribution for a Dirichlet process G_0 is:

$$G_0|\theta_1,\ldots,\ \theta_N,\ H,\gamma \sim DP\left(\gamma+N, \frac{\gamma}{\gamma+N}H+\frac{1}{\gamma+N}\sum_{i=1}^{N}\delta_{\theta_i}\right) \tag{4}$$

A stick-breaking process is used to construct the weight parameter β_i as follows:

$$\beta_i = \nu_i\prod_{l=1}^{i}(1-\nu_l),\ \nu_l\big|\gamma \sim \mathrm{Beta}(1,\gamma),\qquad i = 1,2,\ldots$$

In this process, the weight β_i comes from a unit stick according to a weight that is beta-distributed based on the remaining stick length after the last breaking. This stick-breaking process is also called a Griffiths-Engen-McCloskey (GEM) distribution (Ishwaran and James, 2001; Pitman, 2006) and the weights from this construction, which is denoted $\beta \sim \mathrm{GEM}(\gamma)$, have been proven (Sethuraman, 1994) to be the weights β_i of a Dirichlet process as in **Eq. 3**.

For each value of θ_i, a random indicator variable z_i is used to denote that $\theta_i = \theta_{z_i}{'}$, and then a predictive distribution of z can be written as:

$$p(z_{N+1} = z|z_1,\ldots,z_N,\gamma) = \frac{\gamma}{\gamma+N}\delta(z, K+1)+\frac{1}{\gamma+N}\sum_{k=1}^{K}N_k\delta(z,k) \tag{5}$$

Where K is the current unique number of values of z and N_k is the number of z_i that take value k. This predictive distribution implies that a new observation takes the value of a seen observation θ_{z_k} with probability proportional to N_k or takes a unseen value θ_{K+1} with probability proportional to concentration parameter γ. When a seen observation θ_{z_k} is chosen for the new observation, the indicator $z_{N+1} = k$, or if unseen value θ_{K+1} is taken, the indicator $z_{N+1} = K + 1$. This "the rich get richer" property is essential for inferring a finite generated mixture model. Because the DP posterior nonparametrically converges to parameters of a mixture model for a finite mixture dataset (Ishwaran and Zarepour, 2002), the DP is an appropriate prior for the parameters of a mixture model with an unknown number of components.

Hierarchical Dirichlet Process and Sticky Extension

In NOBIAS, the different single-molecule trajectories of multiple molecules under different biological condition and from different cells, so the groups of data are related but generated independently. Therefore, the DP is extended to a Hierarchical Dirichlet Process (HDP) (Teh et al., 2006). In the HDP, a first Dirichlet process, G_0, is the base measure of a new Dirichlet process, G_j:

$$G_j \sim DP(a, G_0),\ G_0 \sim DP(\gamma, H)$$

To apply a HDP as prior for a HMM model, a HDP-HMM model is generated according to:

$$\beta \sim \mathrm{GEM}(\gamma),\ \pi_j \sim \mathrm{DP}(a,\beta),\ \theta^{(j)}\big|\lambda \sim H(\lambda)\qquad j = 1,2,\ldots$$

$$z_t\ \big|\{\pi\},\ z_{t-1} \sim \pi_{z_{t-1}},\ y_t\big|\{\theta\},\ z_t \sim F\left(\theta^{(z_t)}\right)\quad t = 1,2,\ldots,T$$

In the NOBIAS parameter setting, the observed data y_t would be the single-step displacement $\Delta\boldsymbol{x}_t$, the emission parameter θ

would be the diffusion coefficient D, and the hyperparameter λ for θ would be the Normal-inverse-Wishart distribution (NIW) with four prior hyperparameters $\{\kappa,\ \vartheta,\ \nu, \Delta\}$ as stated below in the Multivariate Normal Model section.

A common issue for the HDP-HMM model is that if the algorithm artificially divides a set of observations into an alternating pattern of rapid switching between several different states, then this alternating pattern will be reinforced by the DP (Fox et al., 2008). This assignment would result in an artificial over-splitting of one state into multiple substates characterized by a high probability of transitions between the substates. Because we would not expect such rapid transitions back and forth between two distinct but similar dynamical states in the single-molecule trajectory data studied here, a sticky parameter κ, is introduced which enforces self-transitions and avoids this over-splitting of states. With this new hyperparameter, the π_j can be sampled as:

$$\pi_j \sim DP\left(a+\kappa, \frac{a\beta+\kappa\delta_j}{a+\kappa}\right),\ j=1,2,\ldots \tag{6}$$

Which add a self-transition bias to the jth components of the DP. The effects of κ on the results are shown in **Supplementary Figure S1D**: if κ is too small, the over-splitting of states still occurs and if κ is too large, the model will underestimate the number of states.

Different Markov Chain Monte Carlo (MCMC) sampling methods such as Direct Assignment Sampling, Beam Sampling, and Blocked Sampling have been developed for the HDP-HMM model (Teh et al., 2006; Fox et al., 2007; Van Gael et al., 2008). In NOBIAS, we apply the most computationally efficient Blocked Sampling method (Fox et al., 2007), which uses a fixed-order truncation with weak-limit approximation HDP-HMM. In this approach, the DP is L-degree approximated as:

$$\beta \sim \mathrm{GEM}_L(\gamma) \sim Dir(\gamma/L,\ldots,\gamma/L) \tag{7}$$

$$\pi_j \sim \mathrm{DP}_L\left(a+\kappa, \frac{\alpha\beta+\kappa\delta_j}{\alpha+\kappa}\right) \sim Dir\left(a\beta_1,\ldots,a\beta_j+\kappa,\ldots,a\beta_L\right) \tag{8}$$

with a truncation level, L, that is larger than the expected total number of mixture components. Increasing L does not affect the posterior results, but L does affect the running time (**Supplementary Figure S1C**). The Blocked Sampling method algorithm is detailed in the Supplementary Note, which describes how the state sequence is generated and how the parameters for each state are sampled.

Multivariate Normal Model

Bayes' rule states that the posterior distribution is proportional to the product of the prior probability and the likelihood, i.e., $P(\theta|y) \sim P(\theta)\,P(y|\theta)$. It is crucial to build conjugacy in order to elegantly and concisely express the posterior distribution. If we choose an appropriate prior distribution class for $P(\theta)$ given a known sampling distribution $P(y|\theta)$, then the posterior distribution $P(\theta|y)$ will have the same distribution class as the prior distribution. This choice of a prior distribution is called a conjugate prior, and this property that the posterior and prior distributions are in the same class is called conjugacy.

In NOBIAS HDP-HMM module, we assume 2D Brownian motion trajectories. In this case, the displacements follow a zero-mean 2D Gaussian and the diffusion coefficients $\boldsymbol{D}$ determine the variance, Σ, of the 2D Gaussian. Without loss of generality, the mean, μ, is also included in the model, $\theta = \{\mu,\ \Sigma\}$, and the data distribution is written as:

$$p(y|\theta) = \frac{1}{(2\pi)|\Sigma|^{\frac{1}{2}}}\exp\left\{-\frac{1}{2}(\Delta\boldsymbol{x}-\mu)^T|\Sigma|^{-1}(\Delta\boldsymbol{x}-\mu)\right\} \tag{9}$$

In the 2D case, the observed data, $\Delta\boldsymbol{x}$, is a 1×2 vector of the 2D displacements, μ is a 1×2 vector and Σ is the 2×2 covariance matrix.

As derived in reference Gelman (2004), the general conjugate prior model for this multivariate normal model is the prior for the mean and the variance of the step displacement follow a Normal-inverse-Wishart distribution (NIW):

$$p(\mu,\Sigma) \sim NIW(\kappa,\ \vartheta,\ \nu, \Delta) \tag{10}$$

Specifically, the variance, Σ, follows an inverse-Wishart prior distribution $IW(\nu, \Delta)$, and the mean, μ, has a conditional Normal distribution: $p(\mu|\Sigma) \sim N(\vartheta,\ \Sigma/\kappa)$.

The posterior updates for this normal model with NIW prior follows (Gelman, 2004):

$$p\left(\mu^{(z_t)},\Sigma^{(z_t)}|\Delta\boldsymbol{x}^{(z_t)}\right) \sim NIW\left(\overline{\kappa},\ \overline{\vartheta},\ \overline{\nu}, \overline{\Delta}\right) \tag{11}$$

Where $\Delta\boldsymbol{x}^{(z_t)}$ is the entire displacement dataset in state z_t, and for each state z_t, we update these parameters as:

$$\overline{\kappa} = \kappa + N,\ \overline{\kappa}\overline{\vartheta} = \kappa\vartheta + \sum_{n=1}^{N}\Delta\boldsymbol{x}_n,\ \overline{\nu} = \nu + N,$$
$$\overline{\nu}\overline{\Delta} = \nu\Delta + \sum_{n=1}^{N}\Delta\boldsymbol{x}_n\Delta\boldsymbol{x}_n^T + \kappa\vartheta\vartheta^T - \overline{\kappa}\overline{\vartheta}\overline{\vartheta}^T.$$

To decrease the running time, we apply the conjugate prior for the Multivariate Normal Distribution, though a non-conjugate prior is permissible. For further discussion of choice of prior see (Gelman, 2004).

Trajectory Simulation

A state label sequence was firstly simulated with a given transition matrix through a Markov chain process. Then according the state label and the D of corresponding diffusive state, the 2D displacement step is generated, and cumulatively summed to get a single trajectory. Standard trajectory datasets are simulated by generate 2D Gaussian random variable where mean is 0 and variance is determined by the set diffusion coefficients with symmetry and no correlation in two directions.

Motion blur trajectory datasets are generated by simulating a state label sequence that is T_{exp} times of the desired length with a transition matrix that self-transit enhanced T_{exp} times. Also according to the label of this T_{exp} times longer label sequence a true trajectories with T_{exp} times more steps can be generated as in the standard dataset case. 2D localization error is added to the average position of every T_{exp} steps in the true trajectory and saved to create a motion-blur trajectory with desired length. In the motion blur trajectory datasets used in this study, T_{exp} was set to 10.

Anomalous Diffusion

In the NOBIAS RNN module, trajectory segments of the same diffusive state (identified by the HDP-HMM module) are evaluated to classify the diffusion type for each diffusive state. In Brownian Motion, the mean squared displacement (*MSD*) is linearly proportional to the time lag, τ. In anomalous diffusion, *MSD* is related to τ according to a power law (Metzler et al., 2014):

$$MSD \propto \tau^{\alpha} \tag{12}$$

Here, α is the anomalous exponent. When $\alpha = 1$, this relation describes Brownian motion; when $\alpha > 1$, **Eq. 12** describes superdiffusion; and when $\alpha < 1$, **Eq. 12** describes subdiffusion. The NOBIAS framework includes the three specific types of anomalous diffusion types that are most common in biology: Fractional Brownian motion (FBM) (Mandelbrot and Van Ness, 1968), Continuous Time Random Walk (CTRW) (Scher and Montroll, 1975), and Lévy Walk (LW) (Klafter and Zumofen, 1994).

FBM is a Gaussian process with correlated increments such that *MSD* is related to τ according to: $MSD = 2D_H\tau^{2H}$ (Mandelbrot and Van Ness, 1968; Jeon and Metzler, 2010). Here, the Hurst exponent, H, is related to α in **Eq. 12** by $\alpha = 2H$. The D_H is the generalized coefficients with physical dimension m^2s^{-2H}. The correlation between two time points for FBM is $x(t_1)x(t_2) = D_H(t_1^{2H} + t_2^{2H} - |t_1 - t_2|^{2H})$. When this correlation is positive, $H > 0.5$ and the motion is superdiffusive; when the correlation is negative, $H < 0.5$ and the motion is subdiffusive.

CTRW defines a random walk family in which the particle displacement, Δx, follows a wait at its current position for a random waiting time t that is a stochastic variable (Scher and Montroll, 1975). NOBIAS considers the case where t follows a power-law distribution, $\psi(t) \propto t^{-\sigma}$, and the following displacement is sampled from a zero-mean Gaussian with fixed variance. In this case, the σ in CTRW is related to α in **Eq. 12**, by $\alpha = \sigma - 1$. This CTRW can only be subdiffusion, i.e., $0 < \alpha \leq 1$.

LW is a special case of CTRW in which the waiting time, t, still follows power law, but the displacement is not Gaussian, and is instead determined by the waiting time (Klafter and Zumofen, 1994). The displacement will have a constant speed, $v = |\Delta x|/t$, and this process can only be superdiffusive with exponent $1 \leq \alpha \leq 2$.

We simulated these three types of anomalous diffusion with the open-source Python package from the recent AnDi challenge (Muñoz-Gil et al., 2020).

Recurrent Neural Network for NOBIAS

All segments 40 steps or greater identified in the HDP-HMM module were further analyzed by the NOBIAS Recurrent Neural Network (RNN) consisting of two long short-term memory (LSTM) layers (Hochreiter and Schmidhuber, 1997). We trained this RNN to classify trajectory segments identified to have the same diffusive state from the HDP-HMM module. We implemented this architecture, which is based on the design of the RANDI package classification task (Bo et al., 2019; Argun et al., 2021) with the MATLAB Deep Learning Toolbox™. The two LSTM layers have 100 and 50 units, respectively, and these two LSTM layers are followed by a fullyconnected layer, and the output classification layer order is given in **Figure 1**.

The input to the network is the set of 2D coordinates from the track segments; these coordinates are normalized to have zero mean and unit variance. Despite a much higher classification performance when using tracks > 50 steps long to train and validate (Argun et al., 2021; Gentili and Volpe, 2021; Muñoz-Gil et al., 2021), we trained two networks with 20-step tracks and with 40-step tracks, respectively, after considering the typical segment lengths from real biological trajectories. The training data of 750,000 trajectories were simulated with the open-source Python package from the AnDi challenge (Muñoz-Gil et al., 2020). Regression networks with similar two LSTM layers architecture were also trained for FBM and CTRW to estimate the anomalous exponent α for the experimental data. The performance of the classification network with 40-step data is shown in the confusion matrix which was made with 10,000 test trajectories (**Supplementary Figure S2**). However, although the RNN module can classify CTRW and LW motion (**Supplementary Figure S2**), because our HDP-HMM module assumes Brownian motion, this first module cannot predict the correct state label for these two diffusion types. We therefore test a mixture of FBM and BM motion in **Figure 3**.

Single-Molecule Tracking in Living *Bacteroides thetaiotaomicron* Cells

B. thetaiotaomicron cells expressing SusG-HaloTag fusions at the native SusG promoter were grown as previously described (Karunatilaka et al., 2014). Briefly, cells were cultured overnight in 0.5% tryptone-yeast-extract-glucose medium and incubated at 37°C under anaerobic conditions (85% N_2, 10% H_2, 5% CO_2) in a Coy chamber. Approximately 24 h before imaging, cells were diluted into *B. theta* minimal medium (MM) (Martens et al., 2008) containing 0.25% (wt/vol) amylopectin. On the day of the experiment, cells were diluted into fresh MM and carbohydrate and grown until reaching $OD_{600\ nm}$ 0.55–0.60 (Tuson et al., 2018).

Before labeling, 900 μL of cells were washed twice by pelleting (6,000 G, 2 min) followed by resuspension in MM. Cells were then incubated in MM supplemented with 100 nM $PAJF_{549}$ dye (Grimm et al., 2016) for 15 min in the dark. Cells were then washed five times in MM, transferring to a new tube on every step, to remove excess dye (Lepore et al., 2019). Finally, 100 μL cells were resuspended in MM containing 0.25% (wt/vol) amylopectin for 30 min in the dark. 1.5 μL labeled cells were pipetted onto a pad of 2% agarose in MM and placed between a large and a small coverslip. The two coverslips were sealed

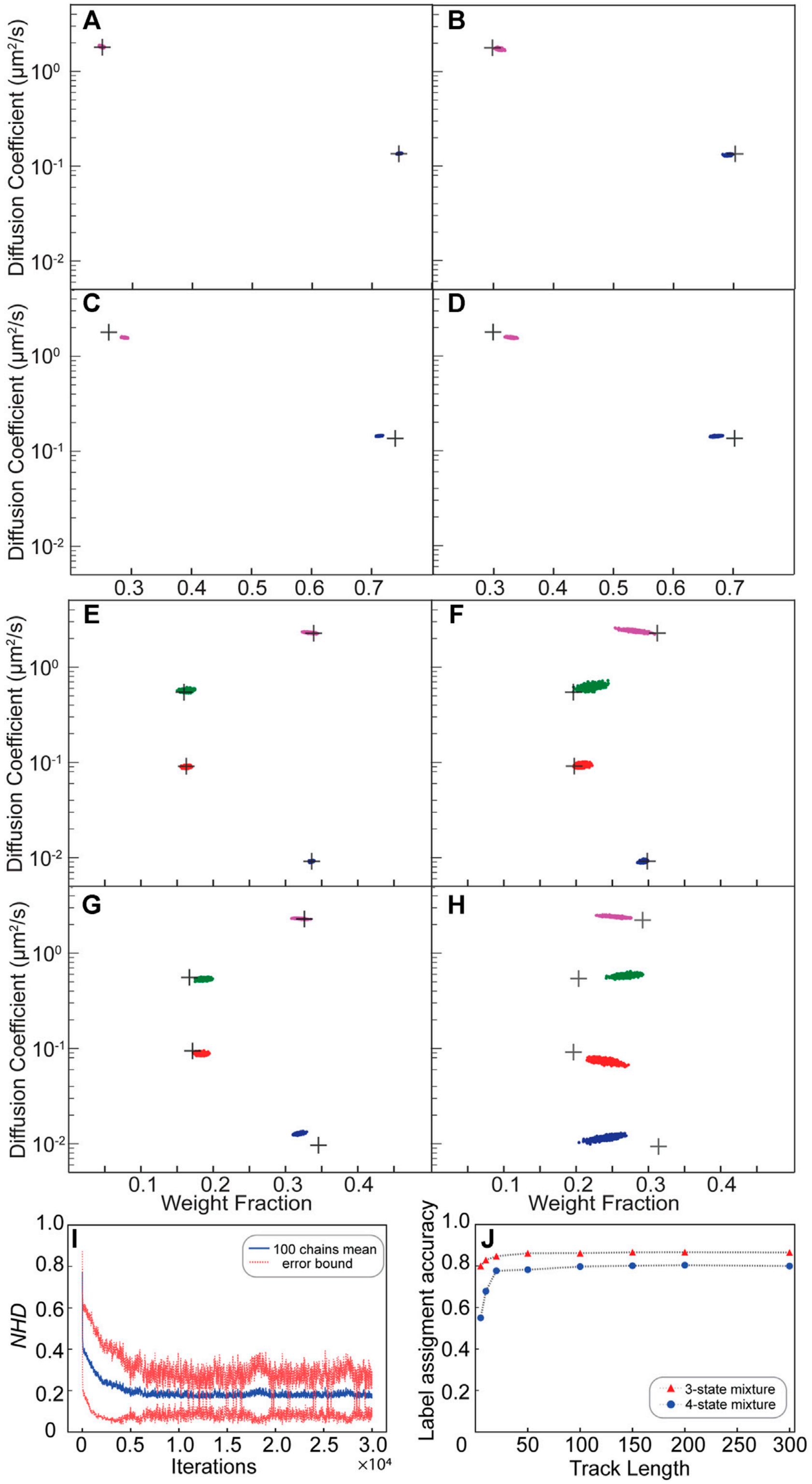

FIGURE 2 | Validation of the NOBIAS HDP-HMM module with simulated trajectories. **(A–H)** The HDP-HMM module identifies distinct mobility states (colored clusters). All scatter plots include at least 500 uncorrelated samples. Each point represents the average apparent single-molecule diffusion coefficient vs. weight fraction in each distinct mobility state at each iteration of the Bayesian algorithm saved after convergence. The black crosses indicate the ground truth input for these simulated trajectories. **(A–D)** Results for two-state mixture simulated trajectories results: **(A)** Standard (no motion blur) and abundant (500 100-step trajectories) simulations, **(B)** Standard and sparse (2,000 10-step trajectories) simulations, **(C)** Motion blur and abundant simulations, and **(D)** Motion blur and sparse simulations. **(E,H)** Results

(*Continued*)

FIGURE 2 | for four-state mixture simulated trajectories results: **(E)** Standard (no motion blur) and abundant (500 100-step trajectories) simulations, **(F)** Standard and sparse (2,000 10-step trajectories) simulations, **(G)** Motion blur and abundant simulations, and **(H)** Motion blur and sparse simulations. **(I)** The normalized Hamming distance (*NHD*) decreases and converges with the number of iterations. All 100 chains use the same dataset under the settings in panel **(E)**. **(J)** The final label assignment accuracy increases with the track length for three- and four-state mixture datasets. The number of trajectories decreases as the track lengths increase such that the total amount of steps is 30,000 for all track lengths.

together with epoxy (Devcon 31345 2 Ton Clear Epoxy, 25 ml) to keep the media anaerobic (Karunatilaka et al., 2014).

Cells were imaged on an Olympus IX71 inverted epifluorescence microscope with a 1.45 numerical aperture, 100× oil immersion phase-contrast objective (Olympus UPLXAPO100XOPH) and a 3.3× beam expander. Frames were collected continuously on a 512 × 512 pixel electron-multiplying charge-coupled device camera (Photometrics Evolve 512) at 50 frames/s. In this microscopy geometry, one camera pixel corresponds to 48.5 nm PAJF_{549} dyes were photoactivated one at a time with a 200–400 ms exposure by a 406-nm laser (Coherent Cube 405-100; 0.1 $\mu W/\mu m^2$) and imaged with a 561-nm laser (Coherent-Sapphire 561-50; 1 $\mu W/\mu m^2$) using appropriate filters as previously described (Tuson et al., 2018).

In each movie, each cell was analyzed separately by using an appropriate mask. The collected frames were processed with SMALL-LABS (Isaacoff et al., 2019) to detect single molecules frame-by-frame and localize their position with typically ~30 nm uncertainty. Single molecules were identified as non-overlapping punctuate spots of diameter larger than seven pixels and with pixel intensities larger than the 92nd percentile intensity of the fame. The punctate spots were fit to a 2D Gaussian and true single-molecule localizations satisfied the following conditions: 1) standard deviation > 1 pixel and 2) fit error ≤ 0.06 pixel. Localizations in each cell over time were connected into trajectories using a merit value: trajectories were selected for further analysis based on their highest merit ranking.

RESULTS

The NOBIAS HDP-HMM Module Recovers the Number of Diffusive States and the Associated Diffusion Parameters

We first validated the NOBIAS HDP-HMM module with simulated single-molecule tracks, beginning from the most basic case: a mixture of Brownian motion trajectories. **Figures 2A–D** depicts the results for a mixture of two distinct diffusive states with $D_1 = 0.135\ \mu m^2/s$ and $D_2 = 1.8\ \mu m^2/s$ (**Supplementary Table S1**). A sequence of state labels (1 or 2) was first simulated with a given transition matrix (probability of transitioning from state 1 to 2 or from state 2 to 1) through a Markov chain process (Methods). Then, according the state label and the apparent diffusion coefficient, *D*, of the corresponding diffusive state, each 2D displacement step was generated, and cumulatively summed to get a single trajectory. Similar state label sequences were simulated to generate other trajectory datasets with four diffusive states (**Figures 2E–G**; **Supplementary Table S2**).

The posterior results of the HDP-HMM module are shown in scatter plots of the inferred *D* and weight fraction from each iteration after the inferred number of states converges. **Figure 2A** shows the result for a dataset of 500 trajectories each with 100 steps. Here, the black crosses indicate the ground truth diffusion coefficient and weight fraction for each diffusive state; the posterior samples of the HDP-HMM model for the two states after convergence are distributed around the true values. Based on the posterior sample autocorrelation function (ACF) analysis (**Supplementary Figure S3**), the posterior samples are thinned by saving every 10 iterations; this setting is the same for all results in this paper and was chosen by considering the effective sample sizes and the ACF analysis for all the diffusive states. The number could be updated accordingly depending on the correlation of posterior samples from output. The mean values and standard deviations for the estimation of *D* and weight fractions for the two states are listed in **Supplementary Table S1**. The estimated number of unique states for this simulated dataset converges quickly over the course of iterations to the true number of states and remains mostly stable at that number (**Supplementary Figure S4**). Next, we considered the less ideal case that often occurs experimentally: much shorter trajectory lengths (10 steps) and many fewer total steps (2,000 10-step trajectories). We refer to the 2,000 10-step trajectories as a sparse dataset and the 500 100-step trajectories are an abundant dataset. **Figure 2B** shows that the HDP-HMM model still successfully converges to the true number of states (two) for this dataset, and the posterior samples of the diffusive parameters are still distributed near the true inputs (black crosses).

We further considered the true form of collected microscope experimental data by including the localization error due to finite photon counts and noise and motion blur due to the finite image acquisition time (Methods). We refer these datasets "Motion blur dataset" in contrast with the more ideal "Standard" dataset. In the case of motion blur, the sticky parameter is increased to avoid oversampling a single diffusive state into multiple state with similar dynamics. The hyperparameter settings for this sticky HDP-HMM model are listed in **Supplementary Table S3**. For both the abundant dataset (**Figure 2C**: 500 100-step trajectories) and the sparse dataset (**Figure 2D**: 2,000 10-step trajectories), the true number of states (two) is recovered with our sticky HDP-HMM model, and despite these added errors, the estimated parameters deviate only slightly from the true inputs (black crosses).

We extended our simulations of standard and motion blur Brownian motion track mixtures to a more complicated 4-state scenarios for abundant (500 100-step trajectories) and sparse (2,000 10-step trajectories) datasets (**Figures 2E–H**). Even with four diffusive states, the performance of the HDP-HMM module is still excellent for the standard mixture (**Figures 2E,F**). For the 4-state mixture simulation that includes localization error and motion blur, the HDP-HMM still successfully recovers the true number of

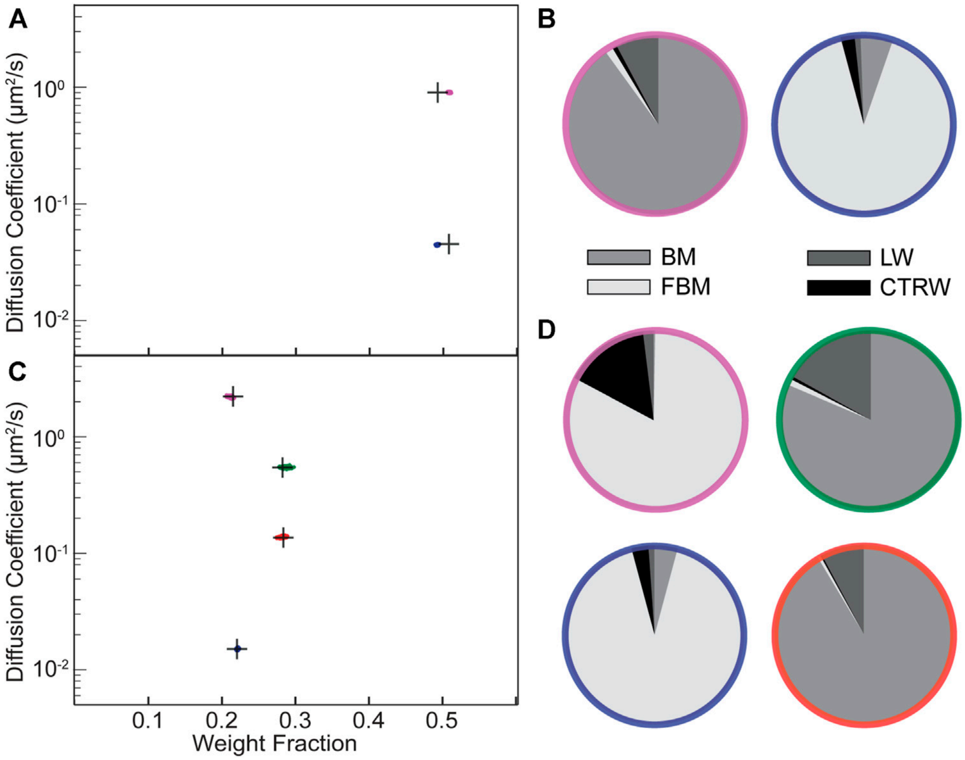

FIGURE 3 | Validation of the NOBIAS-RNN module with simulated trajectories containing mixtures of different diffusion types. **(A,C)** The HDP-HMM module identifies distinct mobility states (colored clusters). Each point represents the average apparent single-molecule diffusion coefficient, *D*, vs. weight fraction in each distinct mobility state at each iteration of the Bayesian algorithm saved after convergence. The black crosses indicate the ground truth input for these simulated trajectories. **(A)** Two-state mixture comprising a subdiffusive Fractional Brownian Motion (FBM) state with lower *D* and a Brownian Motion (BM) state with higher *D*. **(B)** The NOBIAS-RNN determines the probability that the diffusion type for each diffusive state in **(A)** is classified as BM, FBM, Continuous Time Random Walk (CTRW), or Lévy Walk (LW). The final probability for each diffusive state is the average of the classification probability of its track segments weighted by the segment length. The color of each pie chart indicates the diffusive state corresponding to the color in **(A)**. **(C)** Four-state mixture comprising a subdiffusive FBM state, two BM states, and a superdiffusive FBM state with *D* in ascending order. **(D)** Diffusion type classification probability pie chart for each diffusive state in **(C)**. The final probability for each diffusive state is the average of the classification probability of its track segments weighted by the segment length and the color of each pie chart indicates the diffusive state corresponding to the corresponding color in **(C)**.

states, and the parameters for the four distinct states are still estimated well, though the posterior samples have increased variance and deviation from the true value (**Figures 2G,H**). The statistics of the posterior samples for estimated parameters of the 4-state simulation result are listed in **Supplementary Table S2**, and the transition matrices for all the simulations in **Figure 2** are shown in **Supplementary Tables S1, S2**.

The NOBIAS HDP-HMM module also assigns diffusive state labels to each single-molecule step within the trajectories dataset; we call this the state sequence for each track. We quantified the performance of the state sequence assignment relative to the ground truth simulated state sequence with the Hamming distance: the Hamming distance between two 1D sequences with equal length is the number of points where the components are different (Hamming, 1950). The resulting distances were normalized to the total length to demonstrate the Normalized Hamming Distance (*NHD*) convergence over iterations (**Figure 2I**). The *NHD* decreases with increasing iteration number and converges to approximately 0.18. This final converged *NHD* depends on the dataset size, the true transition matrix, and how separable the diffusive state are from one another.

The true number of diffusive states can be recovered for datasets of both abundant and sparse tracks, but the HDP-HMM module performance depends strongly on the length of the individual tracks. Using the overall state sequence assignment accuracy (1 – *NHD*) as a performance evaluator for datasets with the same total amount of steps (30,000), we found that the assignment accuracy is considerably worse for tracks shorter than 20 steps and almost linearly increases with the track length till asymptotes for longer tracks (>20 steps; **Figure 2J**). This trend is shared for a 3-state and 4-state dataset, but the overall accuracy for 3-state dataset is higher than 4-state one for all the track length.

The NOBIAS RNN Module Predicts the Diffusion Type for Each Diffusive State

To analyze anomalous diffusion in an SPT dataset, NOBIAS includes a second module: we built an RNN to classify the type of

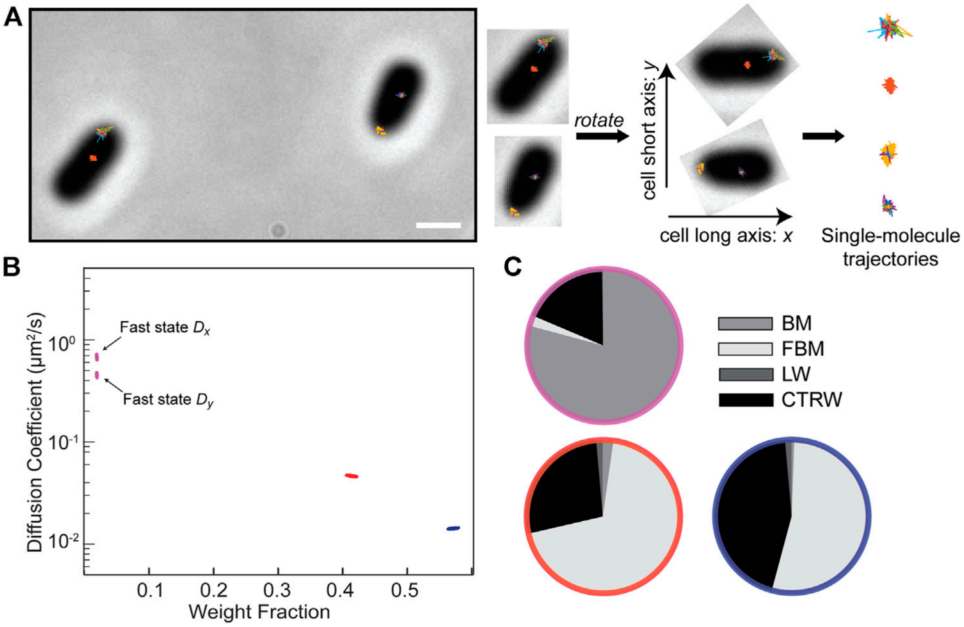

FIGURE 4 | Application of NOBIAS to single-molecule trajectories of the SusG protein in living *Bacteroides thetaiotaomicron* cells. **(A)** Single-molecule trajectories of SusG-HaloTag overlaid on the phase-contrast image of the corresponding *B. thetaiotaomicron* cells, scale bar: 1 μm. The long axis of the phase mask for each cell was detected and a rotation transform was applied to all the trajectories in each cell such that the *x*-axis is the cell long axis for all cells. **(B)** The NOBIAS HDP-HMM module identifies three diffusive states for SusG (colored clusters). Each point represents the average apparent singlemolecule diffusion coefficient vs. weight fraction in each distinct mobility state at each iteration of the Bayesian algorithm saved after convergence. The blue and red points clusters average the *x*- and *y*-diffusion coefficients as they are symmetric (Supplementary Table S4); the asymmetric fast state (purple) shows a different D_x and D_y. **(C)** The NOBIAS-RNN determines the probability that the diffusion type for each diffusive state in **(B)** is classified as Brownian Motion (BM), Fractional Brownian Motion (FBM), Continuous Time Random Walk (CTRW), or Lévy Walk (LW). The color of each pie chart indicates the diffusive state corresponding to the color in **(B)**. The fast state (purple) is predicted with high probability to be BM; the two slower states (red and blue) are predicted to be FBM or CTRW.

motion [Brownian motion (BM), Fractional Brownian motion (FBM), Continuous Time Random Walk (CTRW), or Lévy Walk (LW)] corresponding to the track segments within each diffusive state identified by HDP-HMM module. The RNN consists of two LSTM layers, a fullyconnected layer, and data input/output layer (Methods). Although the HDP-HMM module is based on BM, for some anomalous diffusion types, for example FBM, if the dynamics level for each state is distinct, the HDP-HMM module still performs well.

We simulated a mixture of BM and FBM with distinct apparent diffusion coefficients for the two states ($D_1 = 0.045\ \mu m^2/s$ and $D_2 = 0.90\ \mu m^2/s$) to validate the performance of NOBIAS on mixtures of different diffusion types. **Figure 3A** shows the HDP-HMM posterior results for this 2-state BM-FBM mixture (500 100-step trajectories) where the FBM state is anomalous subdiffusion with $\alpha = 0.5$ (**Eq. 12**) and with lower diffusion coefficient. Then, based on the state sequence labels from the HDP-HMM module, we generated track segments for the two diffusive states and put them into the trained NOBIAS RNN network to predict the diffusion types. NOBIAS RNN successfully predicts the diffusion types for both states (**Figure 3B**; **Supplementary Table S4**).

We further simulated a 4-state mixture (500 100-step trajectories) corresponding to subdiffusive FBM, BM, BM, and superdiffusive FBM (in order of increasing *D*). The HDP-HMM module still successfully recovers the four states and make excellent estimations for *D* and weight fraction for each state (**Figure 3C**). The NOBIAS RNN module also predicts the true diffusion type for the segments from each of the four states (**Figure 3D**; **Supplementary Table S4**). Note that all track segments are normalized before being put into the RNN to avoid dynamics information bias in the diffusion type prediction (Methods). One limitation for this RNN classification analysis methodology is that only track segments with at least certain length (20 or 40 in our analysis depending on the trained network) could be classified with high accuracy; it is very challenging to use very short track segments to identify these modes of diffusion. Therefore, when the overall trajectory length is short (~10 steps), the network classification module might not be usable. Another limitation of the HDP-HMM module is that the current implementation is based on BM displacement distributions, thus it would fail for anomalous diffusion types like LW, which does not have a similar Gaussian distribution of displacements.

Performance of NOBIAS on Experimental Data for the Diffusion of SusG-HaloTag in *Bacteroides thetaiotaomicron* Cells

After validating the performance of the two NOBIAS modules on simulated data, we applied this framework to experimental single-molecule trajectories. The SusG amylase recognizes and binds starch on the surface of *B. thetaiotaomicron* cells to enable starch catabolism (Koropatkin and Smith, 2010). We measured the motion of 7,897 trajectories (minimum length of 6 and average length of 64) of single SusG molecules in 226 movies of 149 *B. thetaiotaomicron* cells based on imaging photoactivatable fluorescently labeled SusG-HaloTag fusions (Methods).

We analyzed this data with NOBIAS to infer the number of diffusive states and to estimate the diffusion coefficient, weight fraction, and type of motion for each state as was done for the simulated data (**Figures 2**, **3**). Additionally, NOBIAS analyzes 2D trajectories with a 2D Gaussian function and can therefore infer the diffusion coefficients for the x and y directions separately and estimate the potential correlation between the two directions. Though the simulations used symmetric tracks in an unbound domain, the experiments measure motion on the surface of cells with a long axis and a short axis, which may create an asymmetry in the diffusion. We rotated the cell orientations to orient the long axis in the x direction without rescaling (**Figure 4A**). We analyzed this rotated dataset with NOBIAS and found that it converged to a 3-state model, with a very small (1.8%) fast state fraction (**Figure 4B**). Interestingly, we found that the D_x and D_y values were similar for each of the two slower states (**Supplementary Table S5**), while they were significantly different for the fastest state ($D_x = 0.68\ \mu m^2/s$ vs. $D_y = 0.45\ \mu m^2/s$). This asymmetry for the fast state indicates that it corresponds to free diffusion that is constrained by the cell shape (and therefore is more constrained in the short-axis y direction), while the symmetry for the two slower states implies molecules that only diffuse regionally and are not affected by the cell shape. Compared with previous SPT analysis methods, NOBIAS provides a two-dimensional analysis of the dynamics of experimental single-molecule trajectories.

We separated the track segments by the state sequence label from the HDP-HMM module and placed each group into the RNN classification module. The fastest state was predicted with high probability (80%) to be Brownian motion (**Figure 4C**; **Supplementary Table S4**), consistent with the asymmetry between D_x and D_y that was attributed to free diffusion (**Figure 4B**). The two slower states were predicted to be either FBM or CTRW. We used a RNN regression network (Methods) to estimate the anomalous exponent α for the track segments of the two slower states and both were found to be subdiffusion ($\alpha_1 = 0.38, \alpha_2 = 0.46$), consistent with the symmetry between D_x and D_y found (**Supplementary Table S5**). This finding of subdiffusion is also consistent with the role of SusG in starch catabolism: we have previously found that SusG motion slows in the presence of its amylopectin substrate, as well as when it transiently associates other outer-membrane proteins, indicating starch-mediated Sus complex formation (Karunatilaka et al., 2014).

DISCUSSION

Single-molecule tracking measures dynamics in biological systems at high spatial and temporal resolution, but how to make the best use of these tracking data for a broad set of experimental conditions remains an analysis challenge in the field (Shen et al., 2017; Elf and Barkefors, 2019). Here, we have introduced NOBIAS to quantify single-molecule dynamics and to associate these biophysical measurements with the underlying biochemical function and biological processes. NOBIAS handles complicated live-cell SPT datasets for which: 1) the number of diffusive states is unknown, 2) mixtures of different diffusive populations may exist, even within single trajectories, 3) symmetry cannot be assumed between the x and y directions, and 4) anomalous diffusion is possible. These features are enabled based on applying Nonparametric Bayesian statistics (Teh et al., 2006; Fox et al., 2008; Johnson and Willsky, 2013) to SPT datasets that have the same means but different variance with a HDP-HMM module that has a 2D Gaussian as the emission function and then by further investigating the anomalous diffusion types in the RNN module of NOBIAS.

Compared with previous applications of nonparametric Bayesian statistics in this field (Persson et al., 2013; Karslake et al., 2020; Heckert et al., 2021), the NOBIAS HDP-HMM module is more robust and has high computational efficiency (**Supplementary Table S6**). NOBIAS and SMAUG both consider motion blur effects and their estimation of D for each state is closer to the ground truth then other methods. As Bayesian method with similar principle NOBIAS is almost 10 times faster than SMAUG. This HDP-HMM module also provides a multivariate output to quantify and correlate dynamics in multiple directions instead of assuming symmetry (**Supplementary Table S7**). We observed that for asymmetric simulated trajectories, vbSPT overestimates the true number of states, and SMAUG can only provide the average D of for each diffusive state while NOBIAS provides the respective diffusion coefficients in two directions. The high accuracy of step state sequence prediction also enables the classification of anomalous diffusion type in the NOBIAS RNN module. We also applied SMAUG and vbSPT on the experimental dataset (**Supplementary Table S8**): SMAUG ran slow on large datasets and suggested four diffusive state, while vbSPT suggested the best model to be 10 diffusive state which is hard to explain their corresponding biological meanings.

A further advantage of NOBIAS lies in its ability to treat sets of relatively short trajectories (10-step trajectories in the simulated data of **Figures 2**, **3** and minimal 6-step trajectories in the experimental data of **Figure 4**). The recent AnDi (Anomalous Diffusion) Challenge (Muñoz-Gil et al., 2021) demonstrated that Deep Learning and Neural Network methods are currently the most powerful tools to study anomalous diffusion (Argun et al., 2021; Gentili and Volpe, 2021). However, in this challenge, the target dataset was an ideal collection of simulated anomalous diffusion trajectories with 100–1,000 steps, and only the simple case of one state transition in the middle part of a track was considered. There are also probability-based models that consider confinement and anomalous diffusion (Robson et al., 2013) and Bayesian methods that directly predict the diffusion type (Thapa et al., 2018; Cherstvy et al., 2019), but these analyses, like the neural network-based methods, are used for very long trajectories or assume a single diffusive state in each track. To apply a deep learning-based diffusion type classifier to realistic simulated trajectories and real experimental trajectories, NOBIAS segments the raw trajectories into collections of track segments that belong to the same diffusive state (as identified by the HDP-HMM module) and then predicts the diffusion type of the long segments in the RNN module. Since different biophysical diffusive states correspond to different biochemical functions which will exhibit different diffusion types due to interactions like confinement, binding, directional motion, NOBIAS enables a thorough investigation of these biochemical roles by revealing the diffusion coefficients, the transition probabilities between states, and the anomalous diffusion behaviors. Ultimately, NOBIAS will enable investigators to extract a complete information set from SPT data and to understand the role of each tracked molecule, even in the living cell.

Despite these strengths, NOBIAS has several limitations. Firstly, as an HMM-based method, NOBIAS is limited by the length of each track. Under the extreme case where only very short trajectories (~2–5 steps) are available, the HDP-HMM module may suggest a number of states and posterior results with extremely high uncertainty; probability-based models (Rowland and Biteen, 2017; Hansen et al., 2018) or the histogram-based Bayesian method DPMM (Heckert et al., 2021) should be applied for these short trajectories. The track length also limits the RNN module, as the trained network need tracks with at least 20 steps for good classification performance because some anomalous diffusion types are characterized by memory of previous steps (Metzler et al., 2014). Therefore the application of the RNN module is limited for short experimental tracks. Secondly, NOBIAS performs the diffusive state estimation based on apparent diffusion coefficient in the HDP-HMM module and then carries out the anomalous diffusion classification in the RNN module. NOBIAS therefore assumes that each biochemical state has a unique average apparent diffusion coefficient. Although the RNN module can classify the diffusion types of two different diffusive states with the same diffusion coefficient, the HDP-HMM module would fail to separate these processes. Furthermore, for some diffusion types like LW, the trajectory displacements may exhibit different types of dynamics even though the trajectories are generated from one process. Finally, even for Brownian trajectories, a single biochemical state might not be represented by a single diffusion coefficient value. Thus, the actual number of biochemical states may not be equal to the number of diffusive states. Future development of NOBIAS could use spatial filtering to distinguish between these similar biochemical states.

NOBIAS provides a pioneering and compatible framework for the analysis of dynamical mixtures that also classifies the anomalous diffusion types. Future development of NOBIAS could include more types of diffusion and could integrate the anomalous distributions directly into the Bayesian framework for more accurate prediction of the stepwise state labels and the diffusion types. Furthermore, extra experimental corrections corresponding to the specific microscope setting (Berglund, 2010; Lindén et al., 2017; Hansen et al., 2018) could also help adapt NOBIAS more broadly to different types of SPT datasets. Overall, NOBIAS has provided a powerful framework to analyze of SPT dataset with unknown number of diffusive states and potential asymmetric diffusion, and to access the anomalous diffusion type for each diffusive state. The combination of nonparametric Bayesian statistics and Deep learning enables NOBIAS to fully extract the rich dynamics information from the SPT dataset.

DATA AVAILABILITY STATEMENT

The original contributions presented in the study as well as simulated and experimental raw data, are included in the article/**Supplementary Material**. The Open-source Matlab code for implementing NOBIAS (GNU General Public License) and sometest datasets are provided at https://github.com/BiteenMatlab/NOBIAS; further development and expansion of the code post-publication will be hosted at that website as well. Further inquiries can be directed to the corresponding author.

AUTHOR CONTRIBUTIONS

ZC and JB conceived of the idea. ZC developed the theory, implemented the algorithm, performed simulations, and analyzed simulated and experimental data. LG carried out the experiments. ZC and JB wrote the manuscript with input from all authors.

FUNDING

This work was supported by National Institutes of Health grant R21-GM128022 and National Science Foundation grant EF-1921677 to JB.

ACKNOWLEDGMENTS

Thanks to Christopher Azaldegui and Guoming Gao for helpful discussions.

SUPPLEMENTARY MATERIAL

The Supplementary Material for this article can be found online at: https://www.frontiersin.org/articles/10.3389/fbinf.2021.742073/full#supplementary-material

REFERENCES

A. Gelman (2004). *Bayesian data analysis*. 2nd ed. (Boca Raton, Fla: Chapman & Hall/CRC).

Argun, A., Volpe, G., and Bo, S. (2021). Classification, inference and segmentation of anomalous diffusion with recurrent neural networksfication, inference and segmentation of anomalous diffusion with recurrent neural networks. *J. Phys. A: Math. Theor.* 54, 294003. doi:10.1088/1751-8121/ac070a

Badrinarayanan, A., Reyes-Lamothe, R., Uphoff, S., Leake, M. C., and Sherratt, D. J. (2012). *In Vivo* Architecture and Action of Bacterial Structural Maintenance of Chromosome Proteins. *Science* 338, 528–531. doi:10.1126/science.1227126

Bauer, M., and Metzler, R. (2012). Generalized Facilitated Diffusion Model for DNA-Binding Proteins with Search and Recognition States. *Biophys. J.* 102, 2321–2330. doi:10.1016/j.bpj.2012.04.008

Bayas, C. A., Wang, J., Lee, M. K., Schrader, J. M., Shapiro, L., and Moerner, W. E. (2018). Spatial organization and dynamics of RNase E and ribosomes in *Caulobacter crescentus*. *Proc. Natl. Acad. Sci. U S A.* 115, E3712–E3721. doi:10.1073/pnas.1721648115

Berglund, A. J. (2010). Statistics of camera-based single-particle tracking. *Phys. Rev. E Stat. Nonlin Soft Matter Phys.* 82, 011917. doi:10.1103/PhysRevE.82.011917

Betzig, E., Patterson, G. H., Sougrat, R., Lindwasser, O. W., Olenych, S., Bonifacino, J. S., et al. (2006). Imaging Intracellular Fluorescent Proteins at Nanometer Resolution. *Science* 313, 1642–1645. doi:10.1126/science.1127344

Biswas, S., Karslake, J. D., Chen, Z., Farhat, A., Freddolino, P. L., Biteen, J. S., et al. (2021). HP1 oligomerization compensates for low-affinity H3K9me recognition and provides a tunable mechanism for heterochromatin-specific localization. *bioRxiv* 01 (26), 428151. doi:10.1101/2021.01.26.428151

Bo, S., Schmidt, F., Eichhorn, R., and Volpe, G. (2019). Measurement of anomalous diffusion using recurrent neural networks. *Phys. Rev. E* 100, 010102. doi:10.1103/PhysRevE.100.010102

Caspi, A., Granek, R., and Elbaum, M. (2002). Diffusion and directed motion in cellular transport. *Phys. Rev. E Stat. Nonlin Soft Matter Phys.* 66, 011916. doi:10.1103/PhysRevE.66.011916

Cherstvy, A. G., Thapa, S., Wagner, C. E., and Metzler, R. (2019). Non-Gaussian, non-ergodic, and non-fickian diffusion of tracers in mucin hydrogels. *Soft Matter* 15, 2526–2551. doi:10.1039/C8SM02096E

Deich, J., Judd, E. M., McAdams, H. H., and Moerner, W. E. (2004). Visualization of the movement of single histidine kinase molecules in live Caulobacter cells. *Proc. Natl. Acad. Sci. U S A.* 101, 15921–15926. doi:10.1073/pnas.0404200101

Deschout, H., Neyts, K., and Braeckmans, K. (2012). The influence of movement on the localization precision of sub-resolution particles in fluorescence microscopy. *J. Biophotonics* 5, 97–109. doi:10.1002/jbio.201100078

Elf, J., and Barkefors, I. (2019). Single-Molecule Kinetics in Living Cells. *Annu. Rev. Biochem.* 88, 635–659. doi:10.1146/annurev-biochem-013118-110801

Elf, J., Li, G. W., and Xie, X. S. (2007). Probing Transcription Factor Dynamics at the Single-Molecule Level in a Living Cell. *Science* 316, 1191–1194. doi:10.1126/science.1141967

Elmore, S., Müller, M., Vischer, N., Odijk, T., and Woldringh, C. L. (2005). Single-particle tracking of oriC-GFP fluorescent spots during chromosome segregation in Escherichia coli. *J. Struct. Biol.* 151, 275–287. doi:10.1016/j.jsb.2005.06.004

Ferguson, T. S. (1973). A Bayesian Analysis of Some Nonparametric Problems. *Ann. Stat.* 1, 209–230. doi:10.1214/aos/1176342360

Fox, E. B., Sudderth, E. B., Jordan, M. I., and Willsky, A. S. (2008). "An HDP-HMM for systems with state persistence," in *Proceedings of the 25th international conference on Machine learning - ICML '08* (Helsinki, Finland: ACM Press), 312–319. doi:10.1145/1390156.1390196

Fox, E. B., Sudderth, E. B., and Willsky, A. S. (2007). "Hierarchical Dirichlet processes for tracking maneuvering targets," in *2007 10th International Conference on Information Fusion* (Quebec City, QC: Canada: IEEE). 1–8. doi:10.1109/ICIF.2007.4408155

Gentili, A., and Volpe, G. (2021). Characterization of anomalous diffusion classical statistics powered by deep learning (CONDOR). *J. Phys. A: Math. Theor.* 54, 314003. doi:10.1088/1751-8121/ac0c5d

Granik, N., Weiss, L. E., Nehme, E., Levin, M., Chein, M., Perlson, E., et al. (2019). Single-Particle Diffusion Characterization by Deep Learning. *Biophys. J.* 117, 185–192. doi:10.1016/j.bpj.2019.06.015

Grimm, J. B., English, B. P., Choi, H., Muthusamy, A. K., Mehl, B. P., Dong, P., et al. (2016). Bright photoactivatable fluorophores for single-molecule imaging. *Nat. Methods* 13, 985–988. doi:10.1038/nmeth.4034

Hamming, R. W. (1950). Error Detecting and Error Correcting Codes. *Bell Syst. Tech. J.* 29, 147–160. doi:10.1002/j.1538-7305.1950.tb00463.x

Hansen, A. S., Pustova, I., Cattoglio, C., Tjian, R., and Darzacq, X. (2017). CTCF and cohesin regulate chromatin loop stability with distinct dynamics. *eLife* 6, e25776. doi:10.7554/eLife.25776

Hansen, A. S., Woringer, M., Grimm, J. B., Lavis, L. D., Tjian, R., and Darzacq, X. (2018). Robust model-based analysis of single-particle tracking experiments with Spot-On. *eLife* 7, e33125. doi:10.7554/eLife.33125

Heckert, A., Dahal, L., Tjian, R., and Darzacq, X. (2021). Recovering mixtures of fast diffusing states from short single particle trajectories. *bioRxiv.* 05.03.442482. doi:10.1101/2021.05.03.4424822021

Hell, S. W., and Wichmann, J. (1994). Breaking the diffraction resolution limit by stimulated emission: stimulated-emission-depletion fluorescence microscopy. *Opt. Lett.* 19, 780–782. doi:10.1364/OL.19.000780

Hess, S. T., Girirajan, T. P., and Mason, M. D. (2006). Ultra-High Resolution Imaging by Fluorescence Photoactivation Localization Microscopy. *Biophys. J.* 91, 4258–4272. doi:10.1529/biophysj.106.091116

Hochreiter, S., and Schmidhuber, J. (1997). Long Short-Term Memory. *Neural Comput.* 9, 1735–1780. doi:10.1162/neco.1997.9.8.1735

Isaacoff, B. P., Li, Y., Lee, S. A., and Biteen, J. S. (2019). SMALL-LABS: Measuring Single-Molecule Intensity and Position in Obscuring Backgrounds. *Biophys. J.* 116, 975–982. doi:10.1016/j.bpj.2019.02.006

Ishwaran, H., and James, L. F. (2001). Gibbs Sampling Methods for Stick-Breaking Priors. *J. Am. Stat. Assoc.* 96, 161–173. doi:10.1198/016214501750332758

Ishwaran, H., and Zarepour, M. (2002). Dirichlet Prior Sieves in Finite Normal Mixtures. *Stat. Sinica* 12, 941–963.

Izeddin, I., Récamier, V., Bosanac, L., Cissé, I. I., Boudarene, L., Dugast-Darzacq, C., et al. (2014). Single-molecule tracking in live cells reveals distinct target-search strategies of transcription factors in the nucleus. *eLife* 3, e02230. doi:10.7554/eLife.02230

Jeon, J.-H., Javanainen, M., Martinez-Seara, H., Metzler, R., and Vattulainen, I. (2016). Protein Crowding in Lipid Bilayers Gives Rise to Non-gaussian Anomalous Lateral Diffusion of Phospholipids and Proteins. *Phys. Rev. X* 6, 021006. doi:10.1103/PhysRevX.6.021006

Jeon, J. H., and Metzler, R. (2010). Fractional Brownian motion and motion governed by the fractional Langevin equation in confined geometries. *Phys. Rev. E Stat. Nonlin Soft Matter Phys.* 81, 021103. doi:10.1103/PhysRevE.81.021103

Johnson, M. J., and Willsky, A. S. (2013). Bayesian Nonparametric Hidden Semi-markov Models. *J. Machine Learn. Res.* 14, 673–701.

Karslake, J. D., Donarski, E. D., Shelby, S. A., Demey, L. M., DiRita, V. J., Veatch, S. L., et al. (2021). SMAUG: Analyzing single-molecule tracks with nonparametric Bayesian statistics. *Methods* 193, 16–26. doi:10.1016/j.ymeth.2020.03.008

Karunatilaka, K. S., Cameron, E. A., Martens, E. C., Koropatkin, N. M., and Biteen, J. S. (2014). Superresolution Imaging Captures Carbohydrate Utilization Dynamics in Human Gut Symbionts. *mBio* 5, e02172. doi:10.1128/mBio.02172-14

Klafter, J., and Zumofen, G. (1994). Lévy statistics in a Hamiltonian system. *Phys. Rev. E Stat. Phys. Plasmas Fluids Relat. Interdiscip. Top.* 49, 4873–4877. doi:10.1103/PhysRevE.49.4873

Koropatkin, N. M., and Smith, T. J. (2010). SusG: a unique cell-membrane-associated alpha-amylase from a prominent human gut symbiont targets complex starch molecules. *Structure* 18, 200–215. doi:10.1016/j.str.2009.12.010

Kusumi, A., Sako, Y., and Yamamoto, M. (1993). Confined lateral diffusion of membrane receptors as studied by single particle tracking (nanovid microscopy). Effects of calcium-induced differentiation in cultured epithelial cells. *Biophys. J.* 65, 2021–2040. doi:10.1016/S0006-3495(93)81253-0

Lepore, A., Taylor, H., Landgraf, D., Okumus, B., Jaramillo-Riveri, S., McLaren, L., et al. (2019). Quantification of very low-abundant proteins in bacteria using the HaloTag and epi-fluorescence microscopy. *Sci. Rep.* 9, 7902. doi:10.1038/s41598-019-44278-0

Lindén, M., Ćurić, V., Amselem, E., and Elf, J. (2017). Pointwise error estimates in localization microscopy. *Nat. Commun.* 8, 15115. doi:10.1038/ncomms15115

Mandelbrot, B. B., and Van Ness, J. W. (1968). Fractional Brownian Motions, Fractional Noises and Applications. *SIAM Rev.* 10, 422–437. doi:10.1137/1010093

Manley, S., Gillette, J. M., Patterson, G. H., Shroff, H., Hess, H. F., Betzig, E., et al. (2008). High-density mapping of single-molecule trajectories with photoactivated localization microscopy. *Nat. Methods* 5, 155–157. doi:10.1038/nmeth.1176

Martens, E. C., Chiang, H. C., and Gordon, J. I. (2008). Mucosal Glycan Foraging Enhances Fitness and Transmission of a Saccharolytic Human Gut Bacterial Symbiont. *Cell Host Microbe* 4, 447–457. doi:10.1016/j.chom.2008.09.007

Mazza, D., Abernathy, A., Golob, N., Morisaki, T., and McNally, J. G. (2012). A benchmark for chromatin binding measurements in live cells. *Nucleic Acids Res.* 40, e119. doi:10.1093/nar/gks701

Metzler, R., Jeon, J. H., Cherstvy, A. G., and Barkai, E. (2014). Anomalous diffusion models and their properties: non-stationarity, non-ergodicity, and ageing at the centenary of single particle tracking. *Phys. Chem. Chem. Phys.* 16, 24128–24164. doi:10.1039/C4CP03465A

Michalet, X., and Berglund, A. J. (2012). Optimal diffusion coefficient estimation in single-particle tracking. *Phys. Rev. E Stat. Nonlin Soft Matter Phys.* 85, 061916. doi:10.1103/PhysRevE.85.061916

Moerner, W. E., and Kador, L. (1989). Optical detection and spectroscopy of single molecules in a solid. *Phys. Rev. Lett.* 62, 2535–2538. doi:10.1103/PhysRevLett.62.2535

Monnier, N., Barry, Z., Park, H. Y., Su, K. C., Katz, Z., English, B. P., et al. (2015). Inferring transient particle transport dynamics in live cells. *Nat. Methods* 12, 838–840. doi:10.1038/nmeth.3483

Muñoz-Gil, G., Volpe, G., Garcia-March, M. A., Aghion, E., Argun, A., Hong, C. B., et al. (2021). Objective comparison of methods to decode anomalous diffusion. arXiv:2105.06766 [cond-mat, physics:physics, q-bio]. Available at: http://arxiv.org/abs/2105.06766 (Accessed July 12, 2021).

Muñoz-Gil, G., Volpe, G., García-March, M. A., Metzler, R., Lewenstein, M., and Manzo, C. (2020). The anomalous diffusion challenge: single trajectory characterisation as a competition. *Emerging Top. Artif. Intelligence* 2020, 44. doi:10.1117/12.2567914

Park, H. Y., Lim, H., Yoon, Y. J., Follenzi, A., Nwokafor, C., Lopez-Jones, M., et al. (2014). Visualization of Dynamics of Single Endogenous mRNA Labeled in Live Mouse. *Science* 343, 422–424. doi:10.1126/science.1239200

Persson, F., Lindén, M., Unoson, C., and Elf, J. (2013). Extracting intracellular diffusive states and transition rates from single-molecule tracking data. *Nat. Methods* 10, 265–269. doi:10.1038/nmeth.2367

Pitman, J. (2006). "Sequential constructions of random partitions," in *Combinatorial Stochastic Processes: Ecole d'Eté de Probabilités de Saint-Flour XXXII – 2002*. Editors J. Pitman and J. Picard (Berlin, Heidelberg: Springer Berlin Heidelberg), 55–75. doi:10.1007/3-540-34266-4_4

Qian, H., Sheetz, M. P., and Elson, E. L. (1991). Single particle tracking. Analysis of diffusion and flow in two-dimensional systems. *Biophys. J.* 60, 910–921. doi:10.1016/S0006-3495(91)82125-7

Rabiner, L. R. (1989). A tutorial on hidden Markov models and selected applications in speech recognition. *Proc. IEEE* 77, 257–286. doi:10.1109/5.18626

Robson, A., Burrage, K., and Leake, M. C. (2013). Inferring diffusion in single live cells at the single-molecule level. *Philos. Trans. R. Soc. Lond. B Biol. Sci.* 368, 20120029. doi:10.1098/rstb.2012.0029

Rowland, D. J., and Biteen, J. S. (2017). Measuring molecular motions inside single cells with improved analysis of single-particle trajectories. *Chem. Phys. Lett.* 674, 173–178. doi:10.1016/j.cplett.2017.02.052

Rust, M. J., Bates, M., and Zhuang, X. (2006). Sub-diffraction-limit imaging by stochastic optical reconstruction microscopy (STORM). *Nat. Methods* 3, 793–795. doi:10.1038/nmeth929

Saxton, M. J. (1997). Single-particle tracking: the distribution of diffusion coefficients. *Biophys. J.* 72, 1744–1753. doi:10.1016/S0006-3495(97)78820-9

Scher, H., and Montroll, E. W. (1975). Anomalous transit-time dispersion in amorphous solids. *Phys. Rev. B* 12, 2455–2477. doi:10.1103/PhysRevB.12.2455

Schütz, G. J., Schindler, H., and Schmidt, T. (1997). Single-molecule microscopy on model membranes reveals anomalous diffusion. *Biophys. J.* 73, 1073–1080. doi:10.1016/S0006-3495(97)78139-6

Sethuraman, J. (1994). A Constructive Definition of Dirichlet Priors. *Stat. Sinica* 4, 639–650.

Shen, H., Tauzin, L. J., Baiyasi, R., Wang, W., Moringo, N., Shuang, B., et al. (2017). Single Particle Tracking: From Theory to Biophysical Applications. *Chem. Rev.* 117, 7331–7376. doi:10.1021/acs.chemrev.6b00815

Sungkaworn, T., Jobin, M. L., Burnecki, K., Weron, A., Lohse, M. J., and Calebiro, D. (2017). Single-molecule imaging reveals receptor-G protein interactions at cell surface hot spots. *Nature* 550, 543–547. doi:10.1038/nature24264

Teh, Y. W., Jordan, M. I., Beal, M. J., and Blei, D. M. (2006). Hierarchical Dirichlet Processes. *J. Am. Stat. Assoc.* 101, 1566–1581. doi:10.1198/016214506000000302

Thapa, S., Lomholt, M. A., Krog, J., Cherstvy, A. G., and Metzler, R. (2018). Bayesian analysis of single-particle tracking data using the nested-sampling algorithm: maximum-likelihood model selection applied to stochastic-diffusivity data. *Phys. Chem. Chem. Phys.* 20, 29018–29037. doi:10.1039/C8CP04043E

Tuson, H. H., Foley, M. H., Koropatkin, N. M., and Biteen, J. S. (2018). The Starch Utilization System Assembles around Stationary Starch-Binding Proteins. *Biophys. J.* 115, 242–250. doi:10.1016/j.bpj.2017.12.015

Van Gael, J., Saatci, Y., Teh, Y. W., and Ghahramani, Z. (2008). "Beam sampling for the infinite hidden Markov model," in *Proceedings of the 25th international conference on Machine learning - ICML '08* (Helsinki, Finland: ACM Press), 1088–1095. doi:10.1145/1390156.1390293

Yildiz, A., Forkey, J. N., McKinney, S. A., Ha, T., Goldman, Y. E., and Selvin, P. R. (2003). Myosin V Walks Hand-Over-Hand: Single Fluorophore Imaging with 1.5-nm Localization. *Science* 300, 2061–2065. doi:10.1126/science.1084398

Conflict of Interest: The authors declare that the research was conducted in the absence of any commercial or financial relationships that could be construed as a potential conflict of interest.

frontiers
in Bioinformatics

TECHNOLOGY AND CODE
published: 11 October 2021
doi: 10.3389/fbinf.2021.723915

An Efficient GUI-Based Clustering Software for Simulation and Bayesian Cluster Analysis of Single-Molecule Localization Microscopy Data

*Saskia Kutz[1], Ando C. Zehrer[1], Roman Svetlitckii[1], Gülce S. Gülcüler Balta[2], Lucrezia Galli[2†], Susanne Kleber[2], Jakob Rentsch[1], Ana Martin-Villalba[2] and Helge Ewers[1]**

[1]Institut für Biochemie, Freie Universität Berlin, Berlin, Germany, [2]Department of Molecular Neurobiology, German Cancer Research Center (DKFZ), Heidelberg, Germany

Ligand binding of membrane proteins triggers many important cellular signaling events by the lateral aggregation of ligand-bound and other membrane proteins in the plane of the plasma membrane. This local clustering can lead to the co-enrichment of molecules that create an intracellular signal or bring sufficient amounts of activity together to shift an existing equilibrium towards the execution of a signaling event. In this way, clustering can serve as a cellular switch. The underlying uneven distribution and local enrichment of the signaling cluster's constituting membrane proteins can be used as a functional readout. This information is obtained by combining single-molecule fluorescence microscopy with cluster algorithms that can reliably and reproducibly distinguish clusters from fluctuations in the background noise to generate quantitative data on this complex process. Cluster analysis of single-molecule fluorescence microscopy data has emerged as a proliferative field, and several algorithms and software solutions have been put forward. However, in most cases, such cluster algorithms require multiple analysis parameters to be defined by the user, which may lead to biased results. Furthermore, most cluster algorithms neglect the individual localization precision connected to every localized molecule, leading to imprecise results. Bayesian cluster analysis has been put forward to overcome these problems, but so far, it has entailed high computational cost, increasing runtime drastically. Finally, most software is challenging to use as they require advanced technical knowledge to operate. Here we combined three advanced cluster algorithms with the Bayesian approach and parallelization in a user-friendly GUI and achieved up to an order of magnitude faster processing than for previous approaches. Our work will simplify access to a well-controlled analysis of clustering data generated by SMLM and significantly accelerate data processing. The inclusion of a simulation mode aids in the design of well-controlled experimental assays.

Keywords: cluster analyis, SMLM, cell membrane proteins, software, GUI

Edited by:
Thomas Pengo,
University of Minnesota Twin Cities,
United States

Reviewed by:
Jean-Baptiste Masson,
Institut Pasteur, France
Juliette Griffie,
École Polytechnique Fédérale de
Lausanne, Switzerland

***Correspondence:**
Helge Ewers
helge.ewers@fu-berlin.de

[†]Present Address:
Lucrezia Galli,
Research Institute of Molecular
Pathology (IMP), Vienna BioCenter
(VBC), Campus-Vienna-Biocenter 1,
1030 Vienna, Austria

Specialty section:
This article was submitted to
Computational BioImaging,
a section of the journal
Frontiers in Bioinformatics

Received: *11 June 2021*
Accepted: *17 September 2021*
Published: *11 October 2021*

Citation:
Kutz S, Zehrer AC, Svetlitckii R, Gülcüler Balta GS, Galli L, Kleber S, Rentsch J, Martin-Villalba A and Ewers H (2021) An Efficient GUI-Based Clustering Software for Simulation and Bayesian Cluster Analysis of Single-Molecule Localization Microscopy Data.
Front. Bioinform. 1:723915.
doi: 10.3389/fbinf.2021.723915

1 INTRODUCTION

Cells rely on transmembrane signaling to interact with the outside world. It is essential that cells can specifically and decisively be put into action in response to signals in a noisy and complex environment (Pierce et al., 2002). To do so, mechanisms have evolved that allow the triggering of an all-or-none, lasting response if required. This often involves a threshold number of ligand-activated membrane molecules that recruit auxiliary molecules to form a larger assembly that, upon reaching threshold size, will switch the cell into a different state. These signaling assemblies appear as clusters of membrane proteins in the plasma membrane of cells. However, the clusters may represent only a small subfraction of the membrane protein in question in an otherwise randomly distributed larger population (Janeway et al., 2001; Schultz and Schaefer, 2008). Cluster algorithms can detect such active signaling clusters in a randomly distributed background if the exact spatial distribution of membrane proteins is known (Williamson et al., 2011; Khater et al., 2020). Cartography of membrane protein distribution at the nanoscale has been made possible by super-resolution microscopy approaches based on the sequential localization of single fluorescence-labeled proteins [Single-Molecule Localisation Microscopy (SMLM), Betzig et al., 2006; Rust et al., 2006; Heilemann et al., 2008]. Clustering has since developed into an essential readout for membrane protein function in many cellular processes. Over the last years, several cluster algorithms have been adapted specifically for the analysis of single-molecule fluorescence data of membrane proteins (Owen et al., 2010; Annibale et al., 2011a,b; Nicovich et al., 2017; Baumgart et al., 2019; Arnold et al., 2020; Pike et al., 2020). SMLM of membrane proteins and their cluster analysis still requires a high level of experimental and analytical expertise. To make cluster analysis more accessible, we here combined a selection of the latest clustering approaches with several useful computational features to speed up and streamline cluster analysis in a single, user-friendly software. Specifically, we implemented Bayesian Cluster Analysis, Ripley's-K-based clustering, DBSCAN (Rubin-Delanchy et al., 2015; Griffié et al., 2016), and ToMATo (Pike et al., 2020) for cluster analysis. We then compared the performance of these approaches on simulated and newly generated experimental data from different cellular systems. Furthermore, we implemented a pipeline for parallelized computing of cluster analysis and, as a result, could analyze even large datasets at a fraction of the time required before. Our software will simplify and accelerate cluster analysis as a readout of membrane protein function.

2 RESULTS

2.1 Structure of the GUI

To facilitate the use of parallelized Bayesian cluster analysis for the community, we developed an easy-to-use software called BaClAva (Bayesian Cluster Analysis and visualization application) with a graphical user interface (GUI, **Figure 1**). This software consists of a pipeline of three modules for simulations, clustering, and analysis that can be used independently via the GUI. Thought experiments are an essential tool in developing reliable experimental strategies and are especially important for data processing-intensive assays because they might offer crucial insights into the experimental setup and data processing strategies. To allow for the freehand design of ground-truth data while simulating realistic experimental output, we included a simulation module similar to FluoSim (Lagardère et al., 2020). This module allows the generation of user-defined clusters of molecules combined with a selected level of randomly placed background molecules. The results of this ground truth are then modeled as images resulting from an SMLM-experiment emulated based on experimental statistics of dye blinking, camera noise, and localization accuracy. The resulting image stack is localized using standard algorithms and can be used as an alternative to or alongside actual SMLM localization data in downstream clustering analysis. If desired, the generation of emulated microscopy images from the constructed localizations can be omitted, as exemplified in **Figure 3**. This option is based on Griffié et al. (2016).

The second module is the clustering module, which analyzes single-molecule localization datasets in the format [X (nm), Y (nm), STDEV (nm)]. STDEV is the localization precision as calculated by the localization software. Once the data are loaded into the software, the user can choose between ToMATo, Ripley's-K-based, or DBSCAN cluster analysis, define the desired parameter space for Bayesian analysis and select, whether the computation is done sequentially or in parallel. The third and final module allows the visualization and export of the results in a graphic or tabular form, including essential analytical parameters such as the number of clusters, cluster area, and cluster density.

To decrease the number of files stored on the computer disk, we decided to store all information in a Hierarchical Data Format (hdf5) (**Figure 1**). The hdf5 format enables us to store the localization table (simulation or experimental), the Bayesian engine scores and labels, and further information in a single data file.

2.2 Benchmarking

First, we aimed to benchmark our cluster software on simulated clustering data. To do so, we generated 100 simulated images of clustered molecules, each containing ten clusters of 100 localizations. For example, see **Figure 2A**. These simulations were generated in the following way: Clusters were generated from single points ≥100 nm apart for each of which 100 localizations were generated by drawing from a normal distribution with a standard deviation of 50 nm. The random background was generated at a density of 111 localizations per μm^2. Thus, the proportion of unclustered localization was designed to be 50% of all localizations (**Section 4.6**).

These data were then analyzed with the Bayesian model and the three different cluster detection algorithms. **Figure 2** shows the simulated data and the corresponding clustering outputs. Since the cluster centers were set to be at least two standard

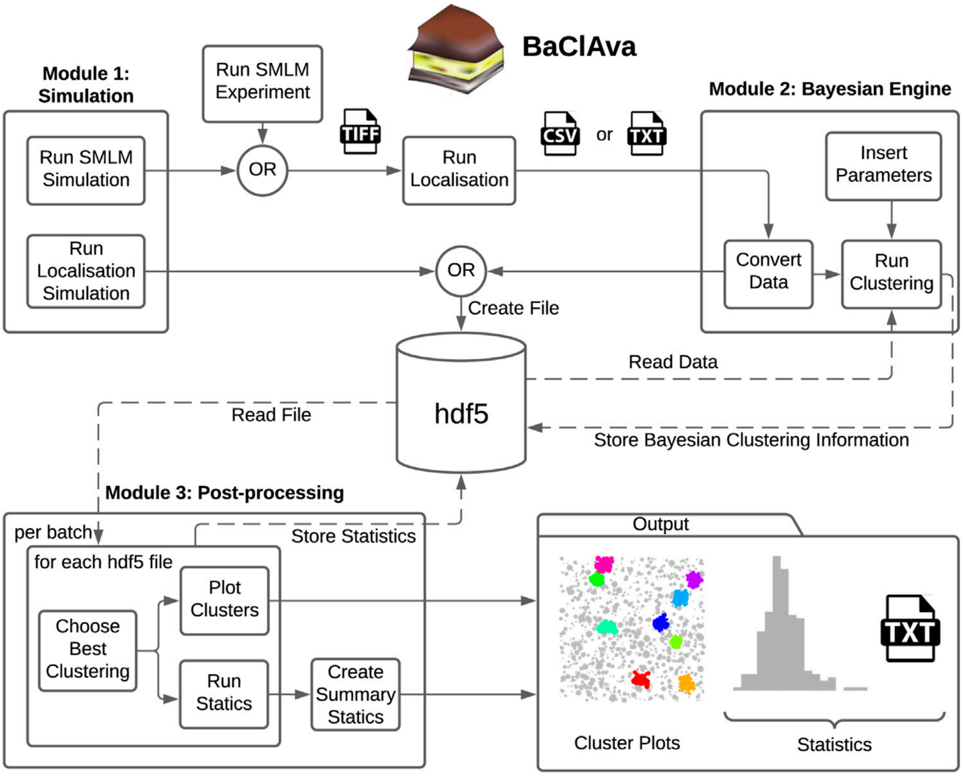

FIGURE 1 | Overview of the software GUI. Schematic of the three independently usable software modes and organization of the software. Simulations can be prepared individually or as batches, and the localization results get exported as tiff or hdf5 files, depending on the simulation option. For the second module, the simulated data is imported from the hdf5 file, or experimental datasets can be imported in the form of a text or csv file. The user can set various parameters, most notably the cluster method, the type of computation, and additional Bayesian clustering parameters. This module's output, namely the scores and the labels for all proposals, is stored in the hdf5 file. In the final processing step, the original localization table and the Bayesian clustering module's output are used to produce the best cluster plots and the corresponding (batch) statistics. The statistics are exported as text files as well as plots.

deviations apart from each other, the individual clusters can be correctly identified by eye (**Figure 2A**) and as well with DBSCAN (**Figure 2C**) and ToMATo (**Figure 2D**). In contrast and as shown before (Pike et al., 2020), the approach based on Ripley's K-function (**Figure 2B**) fails to separate nearby clusters and thus commonly misidentifies cluster number and area (**Figures 2E,F**). As previously shown, this behavior is due to the incapability of this approach to correctly take into account the local density of the data points (Rubin-Delanchy et al., 2015; Griffié et al., 2017). In contrast, both DBSCAN and ToMATo could quantify both cluster number and overall cluster area quite accurately in the majority of simulations (**Figures 2E,F**).

These methods in the Bayesian cluster approach rely not on a single set of parameters but instead on a continuum of so-called proposals, defined sets of values computed to cover an ample parameter space to find an overall optimum of cluster identification (Rubin-Delanchy et al., 2015; Griffié et al., 2016). While this approach has proven to lead to superior results, it is necessarily computationally costly. We aimed to overcome this problem to increase processing speed and thus experimental throughput.

In the original work (Rubin-Delanchy et al., 2015; Griffié et al., 2016), the cluster proposals' calculation in Bayesian analysis is done in nested for-loops on a single CPU core. Since the individual cluster proposals are independent of each other, the processing could also be implemented in parallel. This means that the program uses multiple CPU cores instead of a single core and therefore calculates multiple proposals at the same time. In our software, we implemented the parallelized computing of Bayesian cluster analysis and compared the results with the sequential computational approach.

We first used ten simulations to benchmark the clustering methods described above in Bayesian analysis. We found that typical runtimes for Ripley's K-based and DBSCAN clustering were 25.78 ± 0.86 and 28.45 ± 0.78 min, respectively (mean ± standard deviation). The ToMATo implementation from the RSMLM package (Pike et al., 2020) had a runtime of 23.87 ± 0.80 min (mean ± standard deviation, **Figure 3**). By parallelizing the clustering and scoring process to multiple cores, we found the computation time to decrease by 60% for Ripley's K-based, 10.41 ± 0.23 min, and DBSCAN, 11.90 ± 0.27 min (**Figure 3**). For the ToMATo implementation, the computational time decreased by one order of magnitude to 3.062 ± 0.072 min. In summary, the parallelization significantly reduced processing time for Bayesian cluster analysis.

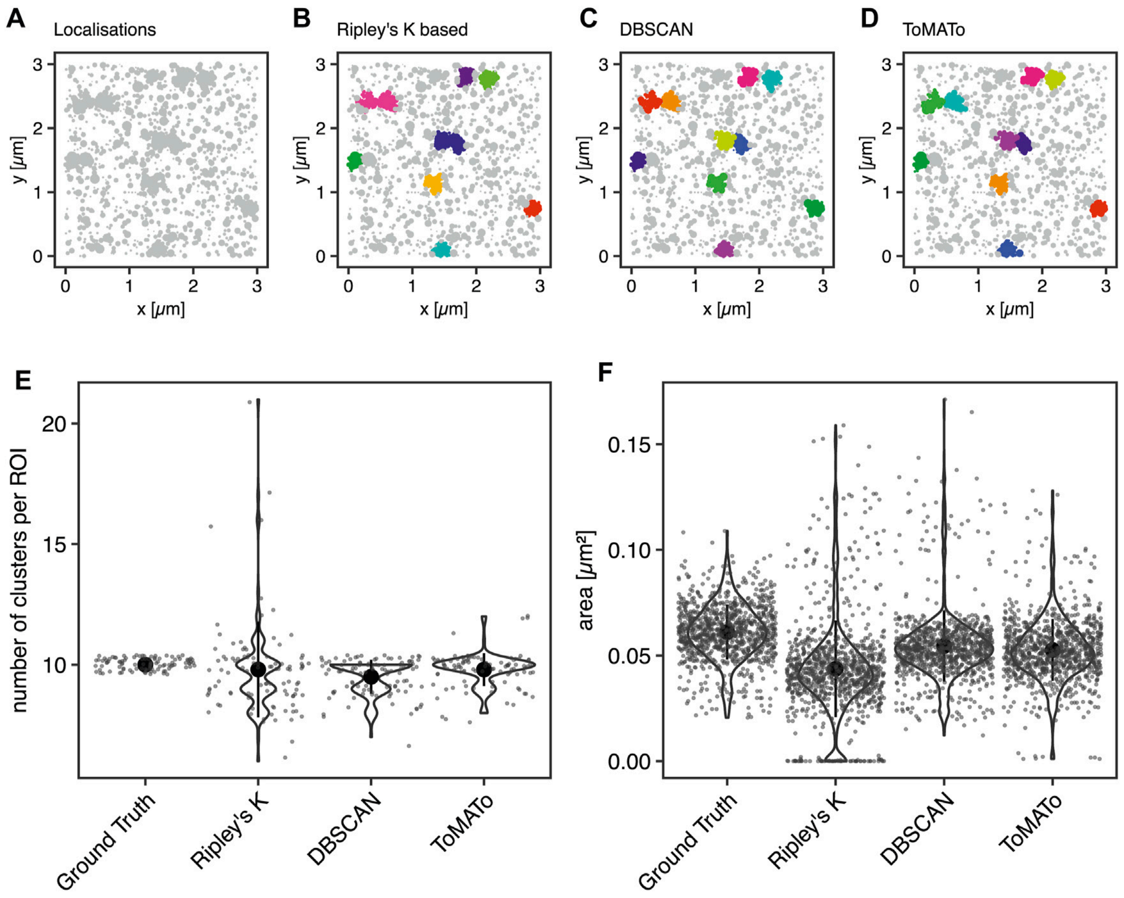

FIGURE 2 | Comparison of cluster algorithms. **(A)** Example of one of 100 simulated ground truth datasets. **(B,C)** Cluster detection (colored) by **(B)** Ripley's-K-function-based implementation, **(C)** DBSCAN, and **(D)** ToMATo for this dataset demonstrating the respectively detected clusters. **(E)** Violin plots of the number of detected clusters in 100 simulations containing 10 ground-truth clusters for each of the algorithms implemented. The mean is emphasized as a black circle. Ten clusters were simulated, and the mean for Ripley's-K-based clustering was 9.8 ± 2.0, for DBSCAN 9.5 ± 0.7, and 9.8 ± 0.7 for ToMATo. Note that the spread is significantly larger for Ripley's-K-based, DBSCAN never overcounted, and ToMATo was the most accurate overall. **(F)** Plot of all ground truth and recognized cluster areas. The ground truth data's cluster area has an average size of 0.061 ± 0.013 μm^2, the Ripley's-K-based clustering results in 0.044 ± 0.023 μm^2, DBSCAN in 0.055 ± 0.017 μm^2, and ToMATo clustering averages the area to 0.053 ± 0.015 μm^2 (mean ± standard deviation).

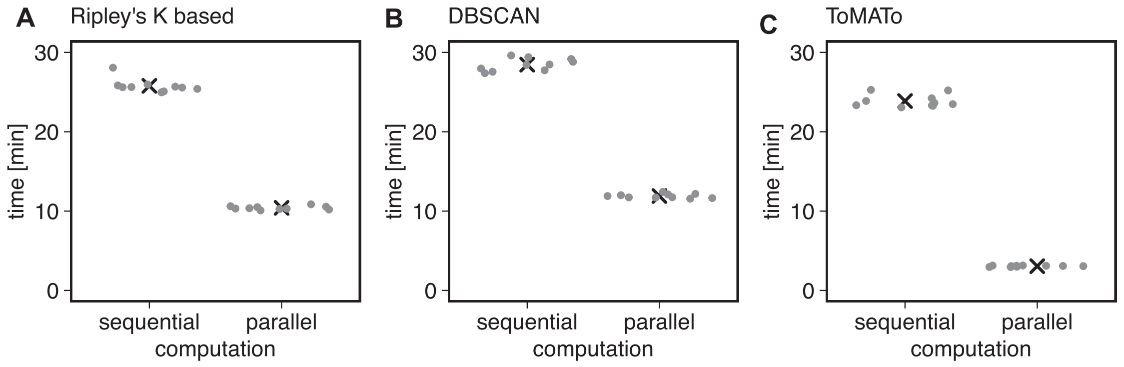

FIGURE 3 | Computational costs for sequential and parallel implementations. Shown is the computational time of the Bayesian engine (in min) in sequential and parallel mode for **(A)** Ripley's-K-based clustering, **(B)** DBSCAN, and **(C)** ToMATo.

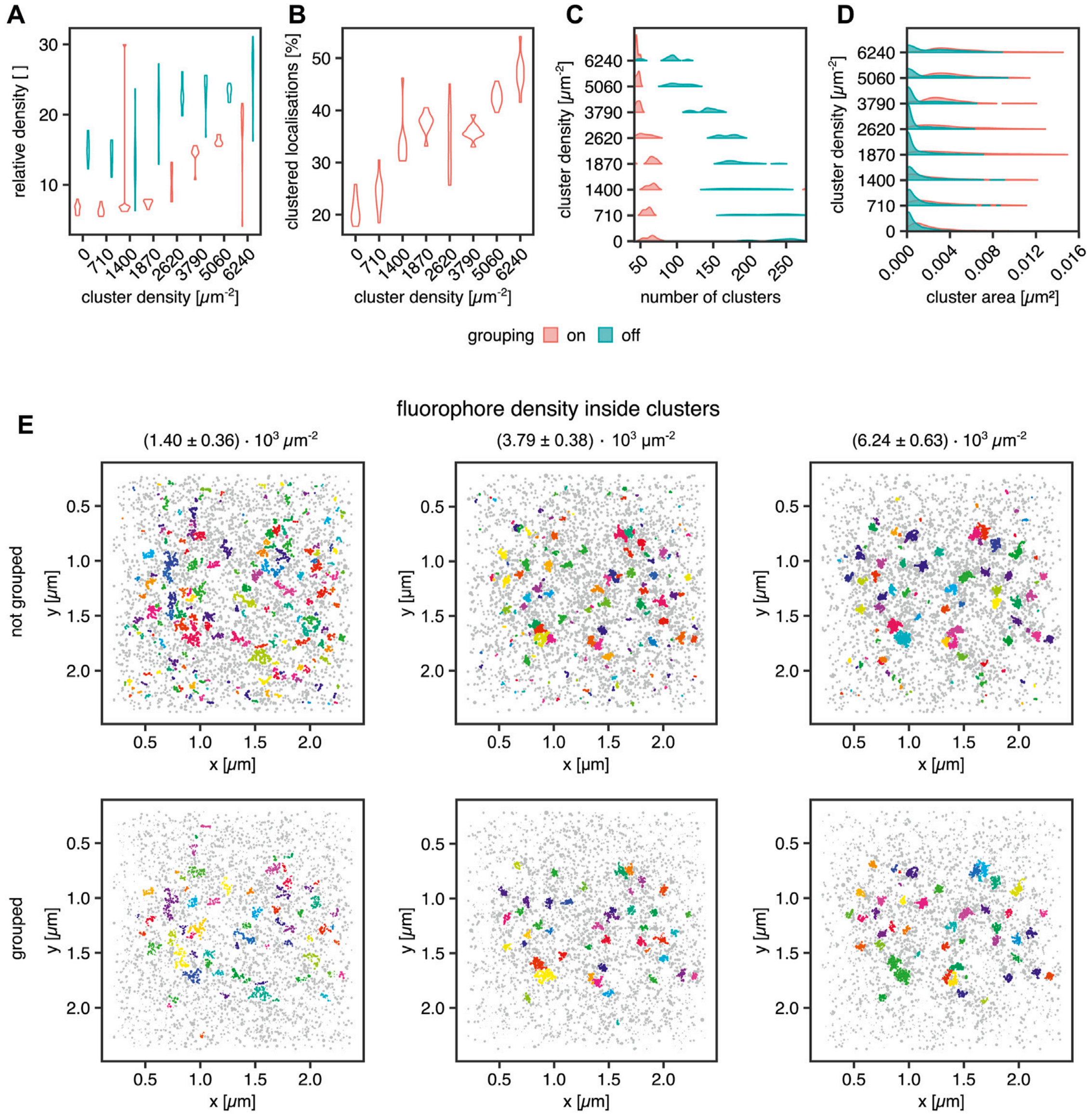

FIGURE 4 | Influence of fluorophore blinking on clustering. **(A)** Violin plot for the relative density of the clusters vs. the background with and without grouping applied, **(B)** Violin plot of the percentage of the clustered localization with grouping, **(C)** Violin plot of the number of clusters per ROI with and without grouping applied, **(D)** Violin plot of the areas of the clusters with and without grouping, **(E)** Examples for clustering of a random distribution of fluorophores and 40 clusters at a density of 1.40 ± 0.36 × 10^3 μm^{-2} **(left column)**, 3.79 ± 0.38 × 10^3 μm^{-2} **(middle column)** and 6.24 ± 0.63 × 10^3 μm^{-2} **(right column)**. Each dataset was analyzed in SMAP with and without grouping. The cluster analysis was performed by the Bayesian engine plus ToMATo.

Next, we aimed to investigate several known sources of error in clustering single-molecule localization microscopy data. An important source of error in the cluster analysis of SMLM data is caused by multiple localizations of the same fluorescent molecule generated by most SMLM approaches that necessarily generate a cluster of localizations from every single fluorophore. Consequently, this fact must be considered for declaring any statement on fundamental information such as cluster size in terms of area and number of molecules in the cluster. In the case of PALM, algorithms have been published which aim at correcting this artifact (Annibale et al., 2011b,a; Jensen et al., 2021b,a). By simulating blinking SMLM data with realistic blinking statistics for Alexa Fluor 647, we determined how dense the underlying molecules must be for proper cluster detection. The simulations of (*d*)STORM experiments were generated in the following way: Cluster areas were generated by randomly distributing 40 non-overlapping clusters with an area of 0.0078 μm^2 (diameter = 50 nm). Their molecular density was increased from 0.71 ± 0.25 × 10^3 to 6.24 ± 0.63 × 10^3 μm^{-2}, translating to molecules per cluster ranging from 5.6 ± 1.9 up to 49.0 ± 4.9. The random background was generated at a density of 639 ± 49 molecules per μm^2 for sparse clusters up to a density of

346 ± 51 molecules per μm^2 for dense clusters. For sparse clusters, almost 94 and 51% of all molecules are assigned to the background for dense clusters. The blinking parameters were $k_{on} = 0.01\ s^{-1}$ and $k_{off} = 10\ s^{-1}$. The FWHM of the PSF was set to 200 nm with an intensity of 2007. The pixel size of the camera was set to 0.096 μm, which is identical to the pixel size of the Evolve Delta 512 Photometrics camera on our microscope. The exposure time was set to 10 ms, which is the exposure time we use in experiments with Alexa Fluor 647 dyes, and as in a (*d*)STORM experiment, 50,000 frames were acquired. The localization procedure and grouping were done in SMAP (Ries, 2020). The obtained localization table was used for the Bayesian Analysis. The results are visualized in **Figure 4**.

In **Figure 4A**, the cluster to background density for grouped and non-grouped data is shown. For both cases, the relative density increases with increasing cluster density and a smaller spread of the distributions for grouped data, whereas the non-grouped data distributions show a broader spread, indicating the efficiency of the grouping function in SMAP. Additionally, the number of clusters per region of interest (ROI) is reduced by the grouping, which removes clusters caused by single blinking fluorophores (**Figures 4C,E**). The higher relative density of fluorophores in clusters compared with background localizations indicates that a local density threshold must be surpassed to render the interpretation of cluster data independent of fluorophore blinking properties. As shown in **Figure 4C**, the number of clusters is constant for grouped data up to a concentration of $2.62 \pm 0.39 \times 10^3\ \mu m^{-2}$ localizations. For higher concentrations, the number of clusters approaches the ground truth of 40 clusters. Without grouping, the number of identified clusters decreases with increasing fluorophore concentration, reflecting a higher relative enrichment of fluorophores inside the clusters than outside them. The improved situation for grouped data is also visible in **Figure 4B**, showing that the percentage of clustered localizations increases with increasing fluorophore density. For the best cluster result in these simulations, more than 30% of the localizations must occur in clusters, and a relative density (localization density inside vs. outside of cluster) threshold of 10 must be overcome for the localizations inside clusters versus outside.

Moreover, the cluster size (**Figure 4D**), meaning the area covered by localizations in a cluster, shows the influence of background localizations on the data distribution. Cluster area increases in size for grouped data starting from a concentration of $1.87 \pm 0.39 \times 10^3\ \mu m^{-2}$. For the non-grouped data, there is a significant proportion of very small clusters at all concentrations. This cluster population is not present for the grouped data, indicating that these clusters emerge from multiple detections of a single fluorophore, i.e., blinking. For a density of $2.62 \pm 0.39 \times 10^3\ \mu m^{-2}$ molecules and higher, a second population emerges in the non-grouped data distributions, which corresponds to the main population in the grouped distributions. Therefore, they can be considered correctly identified clusters. Similarly, from $2.62 \pm 0.39 \times 10^3\ \mu m^{-2}$ molecules onwards, the number of clusters per ROI decreases. As demonstrated in **Figure 4E**, small background clusters are removed with the grouping functionality (top row vs. bottom row) and with increasing fluorophore density within the clusters (from left to right). As expected, the ground truth clusters become more apparent when the number of clustered molecules is increased even in the non-grouped data, indicating that single fluorophore blinking has a significantly reduced impact on density-based cluster identification for denser clusters. We concluded that grouping is essential in the detection of smaller clusters.

Finally, we aimed to apply our algorithm to experimental data from single-molecule localization experiments of intact cells. We used standard controls in the field for non-clustered and clustered molecules respectively at the plasma membrane. The lipid-anchored glycosylphosphatidylinositol-coupled green fluorescent protein GPI-GFP should be more or less homogeneously distributed and functioned as the negative control. The clathrin-light chain (CLC), of which dozens of copies are incorporated into every ~150 nm diameter clathrin-coated pit and thus appears strongly clustered, served as the positive control. In order to keep our results comparable, all molecules of interest were tagged with a GFP protein, and the (*d*) STORM dye Alexa Fluor 647 was bound to the GFP via anti-GFP nanobodies in all experiments (Ries et al., 2012). From the simulation work, we know that the cluster results for GPI-GFP should show a wide range of cluster areas, whereas, for the CLC, we expect to yield well-defined cluster areas. Finally, we asked whether we could detect clustering for the transmembrane receptor CD95, as the receptor activation via its ligand may trigger apoptosis or tumorigenesis of cancer cells and has been suggested to result in the formation of high order molecular clustering (Martin-Villalba et al., 2013). CD95 was likewise labeled via GFP and AF647 nanobodies.

The reconstructed images in **Figure 5** of these three proteins show differences in the spatial distribution of the localizations. For GPI-GFP imaged in CV-1 cells in **Figure 5A**, the localizations are evenly distributed, and the cluster maps for the zoom-ins show small clusters, which are probably due to the blinking of the Alexa Fluor 647 dye. In contrast, in **Figure 5B**, the CLC imaged in HeLa cells show well-defined clusters in agreement with clathrin-coated pit size (**Supplementary Figure S1**) with little background localizations, as seen in the cluster maps of the zoom-ins. The CD95 receptor in T98G glioblastoma cells presents a localization distribution with smaller clusters and more background localizations than CLC. The cumulative distribution of the cluster areas of several cells for each condition in **Figure 5D** reveals that GPI and CLC exhibit distinct distributions of their respective cluster areas in agreement with expectations. The cumulative distribution of cluster areas for the CD95 receptor is positioned between the two controls, demonstrating that CD95 forms small clusters likely consisting of around 0.54 molecules/nm^2 in the plane of the membrane.

3 DISCUSSION

Here we present a user-friendly software solution for cluster analysis of SMLM data. Our software significantly reduces processing time and allows the user to select different algorithms to identify and quantify cluster formation.

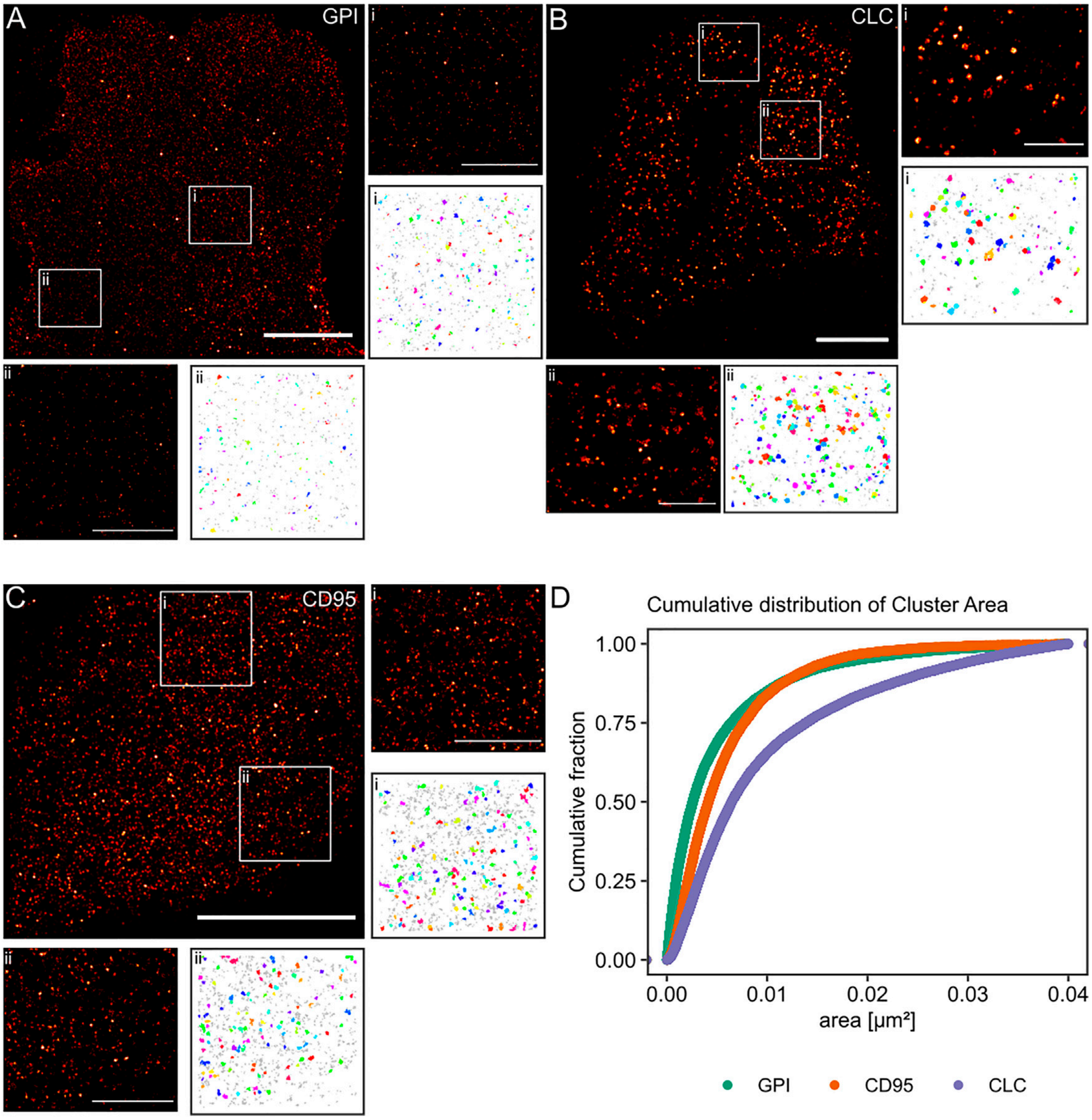

FIGURE 5 | Practical application of the Bayesian engine on three different target molecules. Three different molecules were coupled to GFP and stained with nanobodies labeled with Alexa Fluor 647. **(A)** GPI-GFP in CV-1 cells, **(B)** CLC-GFP in HeLa cells, and **(C)** CD95-GFP in T98G cells. Scale bars are 10 µm for the large reconstructed images and 3 µm for the zoom-ins (i, ii). **(D)** Plot of the cumulative distribution of cluster areas for the three target molecules. A Kruskal-Wallist-test showd that the three distributions are significantly different ($p < 2e^{-16}$).

The simplest cluster algorithms, such as nearest-neighbor algorithms, can answer whether areas of above-average concentration, clusters, exist in a field of view (Endesfelder et al., 2014). For a more detailed analysis of clusters found in cellular membranes, Ripley's K-function can provide answers to the length scale of interparticle distances and the proportion of entities found in clusters in a given dataset (Owen et al., 2010). However, these methods are prone to artifacts intrinsic to single-molecule fluorescence-based microscopy approaches, which lead to small local clusters due to the blinking behavior of individual fluorophores. To overcome errors due to blinking, approaches have been developed to determine the degree of clustering in challenging experimental circumstances, such as for dense membrane molecules by varying the dye density (Baumgart et al., 2019; Arnold et al., 2020).

To understand the functional underpinnings of cluster formation in cell biology, a qualitative view of clustering is not sufficient, but reproducible, robust quantitative assays are required. One of the first ideas put forward was to use Ripley's function not on the entire sample but on individual localizations convoluted with a search radius and a clustering threshold for cluster identification in dense backgrounds. To facilitate the differentiation of Ripley's K function on the entire sample or individual localizations, we termed the second case Ripley's-K-based clustering.

Ripley's K-based clustering cannot adequately determine clusters in samples with variations in cluster density and final cluster size. Therefore, density-based clustering methods, like DBSCAN (density-based spatial clustering of applications with noise), have been adapted for SMLM cluster analysis, and they are less error-prone, as shown before (Pike et al., 2020). In DBSCAN, the search parameters are the search radius and the minimal number of data points within this search radius. Points for which these parameters are valid are counted towards this cluster. After identifying all clusters, the remaining data points are assigned to the background, and other parameters such as the individual cluster area and density can be extracted from the data.

Even though density-based methods, like DBSCAN, can handle datasets with density variations, they still often fail to separate individual clusters that are very close to one another but are easily distinguishable by eye. Additionally, it has been shown that the detection of clusters by DBSCAN and Ripley's-K-based clustering (Pike et al., 2020) can be sensitive to even small changes in the analytical parameters, possibly leading to artifactual results. One of the latest introductions to SMLM cluster analysis is persistence-based clustering which is based on density estimation (Griffié et al., 2015). The introduced scheme is called Topological Model Analysis Tool (ToMATo, Pike et al., 2020; Chazal et al., 2012, 2013). In contrast to the above-mentioned density-based methods, in this algorithm, local maxima in molecular density are identified and termed clusters by introducing a density gradient generated by creating a path emanating from a molecule to its neighbors and using the intermolecular distance as a measure of density. If this intermolecular distance increases, the border of a cluster may be reached. Such a local maximum in distance or minimum in density may be a saddle point between clusters or define the outer perimeter of a cluster. A threshold value defines the persistence of a cluster from its center into space. Clusters with persistence smaller than the threshold are assigned to neighboring clusters, or they are deemed background. As a result, ToMATo allows for a separation of even partially overlapping clusters, and additionally, the output clustering results are less sensitive to analytical input parameters as compared to Ripley's K-based clustering and DBSCAN. Further clustering methods for SMLM data are based on Voronoï tessellation (Levet et al., 2015), which detects clusters based on polygonal regions. Voronoï tessellation intrinsically generates contours of regions of density that may also be used for boundary detection of cells. Recently, machine-learning has been employed to improve cluster detection (Williamson et al., 2020), but the number of input neurons limits the correct processing of the underlying information. The Bayesian engine's main drawback is that due to the calculation and scoring of thousands of cluster proposals for optimal results, the process is significantly slowed down compared to traditional methods with a single cluster proposal, hampering the routine use of this method. On the other hand, ToMATo clustering parameters are determined based on a persistence diagram which can cause user bias.

To overcome these limitations and provide accessible GUI-based software for state-of-the-art cluster analysis, we implemented Ripleys-K-based clustering, DBSCAN, and ToMaTo in a common software that allowed for parallel computing. In this software, we first improved the Bayesian engine's speed by implementing parallel computation and introduced ToMATo clustering to the Bayesian engine, thereby dramatically decreasing computational time. In combination with the software GUI, the Bayesian engine has an improved user experience and processing speed, which we hope will make state-of-the-art SMLM cluster analysis available in many laboratories.

During an SMLM measurement of several thousands of frames, a fluorescent molecule may cycle several times between a bright and a dark state, and thus, one molecule may be detected multiple times within a radius determined by its localization precision. As a result, it is impossible to differentiate between a single molecule detected several times in different frames and different molecules in close proximity detected in different frames. This is, of course, especially problematic in cluster analysis, where localizations are processed first without bias. To overcome this problem, it is important to develop an understanding of the degree of influence of blinking in the dataset at hand. As we showed in **Figure 4**, the number of the small clusters resulting from dye blinking decreases with increasing molecular density within the clusters while keeping the actual cluster size constant. Thus, there is an intrinsic threshold for relative localization densities inside and outside clusters that render blinking irrelevant. This holds true under the assumption that all localizations are caused by dyes bound to molecules of interest, and no false localizations are present in the sample. Below this threshold, the number of detected clusters is highly overestimated, and the cluster radii are dramatically underestimated. From simulations, we know that such single-molecule clusters can be detected as sub-peaks within clusters at low-density ratios. Increasing the density ratio now increases the chance that clusters are quantified at their true size. It is common in SMLM data analysis that multiple temporally and spatially closely correlated localizations are grouped together in a final reconstruction and are thus counted as a single molecule. In clustering, this procedure reduces the number of small background clusters dramatically, and we analyze this effect in depth in **Figure 4**. Our grouping is based on the blinking behavior of the most used (*d*)STORM dye Alexa Fluor 647, which we also used in our experiments. Likewise, we also based our simulations on the blinking behavior of this dye (Heilemann et al., 2008; Dempsey et al., 2011). In order to detect clusters of smaller density ratios and smaller sizes either or both, the cluster detection may be improved by changing the dye or even the SMLM method from (*d*)STORM to DNA-PAINT as shown in Jayasinghe et al. (2018).

Microscopy experiments in cells are much more complex than the corresponding *in-silico* experiments because many different known and unknown cellular processes are involved in the temporal and spatial organization of the cell molecules and may interfere in the process studied. Therefore, we chose highly abundant molecules as cellular controls for clustering experiments. A simple positive control is clathrin-coated pits expressed at a well-defined radius of around 80 nm ($A \approx 0.02\ \mu m^2$) (Sochacki et al., 2017). Negative controls for clustering in a cellular environment are far more challenging to identify because natural cellular signaling processes result in a spatial and temporal reorganization of the involved molecules, and many membrane molecules exhibit clustering of some extent (Gowrishankar et al., 2012; Saka et al., 2014; Baumgart et al., 2016; Kalappurakkal et al., 2020). Therefore, the influence for altering the negative control's organization by cell processes should be kept at a minimum, and an artificially introduced protein that is only anchored to the outer membrane of the plasma membrane and has no natural interaction partners, such as GPI, is the ideal option (Li et al., 2020). These extreme cases of clustering and non-clustering probes can be well differentiated in their reconstructed images as well as their cumulative distribution functions. Proteins with so far unknown spatial distribution on the plasma membrane, such as the transmembrane receptor CD95, should present a behavior between these two extremes. If they are less clustered, they should tend towards a behavior similar to GPI, and with increasing cluster areas, they should tend towards a distribution similar to clathrin-coated pits. Since CD95 can be found at the plasma membrane as monomers or homodimers and homotrimers (Micheau et al., 2020), it should be detected as small clusters, as observed in **Figure 5**. We conclude that our software can correctly distinguish between unclustered molecules and clusters of even small size and a few molecules in number.

Taken together, our work allows the implementation of single-molecule clustering analysis at a high rate of data throughput for beginning users. We expect our work to accelerate research in this area significantly and to contribute to the acceptance of reproducible standards in clustering data analysis. In future work, other analytical methods such as Voronoï tessellation (Andronov et al., 2018; Levet et al., 2015) and extensions to 3D (Griffié et al., 2017) and dual-color co-clustering (Jayasinghe et al., 2018) may be implemented, and the processing speed may be further improved, i.e., by the implementation of GPU-processing.

4 MATERIALS AND METHODS

4.1 Cell Culture and Preparation

CV-1 cells were cultured in a standard DMEM medium (1X, Gibco) supplemented with 10% FBS (ThermoFisher) and 1% GlutaMax (100X, Gibco by Life Technologies). Stable HeLa CLC-GFP cells were cultured in the same medium with an additional 1% Penicillin-Streptomycin (Sigma), and for the T98G CD95-GFP cells, 1% sodium pyruvate (stock: 100 mM, Gibco) was added to the medium. The vector CD95-GFP was infected into the cells with a lentiviral construct. The cells were then FACS sorted for the stably transfected clones. All cell lines were regularly tested for mycoplasmas and only used when tested negative. For the seeding of the cells, 18 mm diameter #1.5 glass slides (VWR) were cleaned in an ultrasound bath for 20 min using 2% Hellmanex III (Hellma) and 70% ethanol, respectively. Afterward, the glasses were dried and plasma cleaned for another 30 min.

4.2 Cell Staining

CV-1 GPI-GFP Cells

Transfection of GPI-GFP into CV-1 cells was done with lipofectamine 3000 following the standard protocol (lipofectamine protocol by Invitrogen/ThermoFischer). Cells were treated with trypsin-EDTA and seeded on the glass slides for incubation of 24 h (densities: 6×10^6 cells/ml for CV-1, 7×10^4 cells/ml for HeLa CLC-GFP and T98G CD95-GFP). The transfected CV-1 cells were fixed with prewarmed 4% PFA with 0.2% GA in PBS for 20 min at 37°C. Then, cells were quenched with freshly prepared 0.1% $NaBH_4$ in PBS for 7 min at room temperature and extensively washed. Cells were blocked in two steps: for 30 min with ImageIT, followed by 4% goat serum in 1% BSA in PBS for 1 h. CV-1 GPI-GFP cells were stained with anti-GFP nanobodies (FluoTag-Q anti-GFP) labeled 1:1 with Alexa Fluor 647 from NanoTag Biotechnologies GmbH at a concentration of 50 nM for 1 h. Afterward, cells were postfixed with 4% PFA and 0.2% GA in PBS for 20 min and quenched with 0.1% $NaBH_4$ in PBS for 5 min at room temperature.

HeLa CLC-GFP Cells

HeLa CLC-GFP cells were fixed with prewarmed 4% PFA in PEM for 20 min at 37°C and quenched with NH_4Cl in PBS for 5 min at room temperature. After quenching for 5 min with 0.2% saponin in PEM, the cells were blocked with 4% goat serum in 1% BSA in PEM for 1 h. HeLa CLC-GFP cells were stained with the NanoTag Biotechnologies GmbH nanobody for 30 min at a concentration of 50 nM and afterward post-fixated with 4% PFA in PEM for 20 min at room temperature. The cells were quenched with NH_4Cl in PBS for 5 min. In between all steps, the HeLa cells were extensively washed with PEM.

T98G CD95-GFP Cells

The T98G CD95-GFP cells were fixed for 20 min at 37°C with prewarmed 4% PFA plus 0.2% GA in PEM and quenched with freshly prepared 0.1% $NaBH_4$ in PEM for 7 min T98G cells were permeabilized with 0.2% saponin in PEM for 5 min and blocked with 4% goat serum in 1% BSA/PEM for 1 h. The cells were stained with the NanoTag Biotechnologies GmbH nanobody at a concentration of 50 nM for 30 min and post-fixated with 4% PFA with 0.2% GA in PEM for 20 min at room temperature. For the post-quenching, the cells were incubated in 0.1% $NaBH_4$ in PEM for 7 min. In between all steps, the cells were extensively washed with PEM.

4.3 (*d*)STORM Imaging

The fixed and stained samples were mounted and imaged in beta-mercaptoethanol and GLOX (2.5 mg/ml glucose oxidase, 0.2 mg/ml catalase, 200 mM Tris-HCl pH 8.0, 50% glycerol) as imaging buffer (10:1). The (*d*)STORM images were acquired on a home build TIRF microscope as described in (Albrecht et al., 2016). For the imaging, an Olympus 60x, 1.49 NA back focal plane TIRF objective was used to reach a pixel size of 96 nm. The samples were illuminated with a 639 nm laser (Changchun New Industries Optoelectronics Tech. Co., Ltd.) at powers of 0.008–0.015 mW/ μm^2. For the acquisition of the (*d*)STORM images, a water-cooled and back-illuminated Photometrics EMCCD camera with 512 × 512 pixels at a pixel size of 16 × 16 μm was used for the acquisition of 30,000 frames at an exposure time of 10 ms. The EMCCD camera was calibrated before the data acquisition, and the image acquisition was controlled with MicroManager.

4.4 (*d*)STROM Reconstruction

The acquired and simulated (*d*)STORM datasets were localized using SMAP (Ries, 2020). Important camera and acquisition parameters were extracted from the metadata file, which had been saved with the data. Furthermore, the electron multiplier (EM) gain was set to 300, and the conversion factor to 6.7 (analog to digital units to photons). The minimum distance between two candidate peaks in order to be fitted separately was set to 7 pixels. For the point-spread function (PSF) fitting, the following parameters were set to a differential of Gauss with sigma = 1.2, dynamic factor = 1.7, and free PSF, using the workflow “set Cam parameters.”

4.5 Grouping in SMAP

The grouping procedure is a part of SMAP, which we used for the reconstruction. The number of frames, dT, for which a single molecule can be non-fluorescent but still be grouped with the first localization of that molecule was set to dT = 1. The distance, dX, the centroid of a single molecule can be shifted in the image plane between two consecutive frames, but still, be grouped with the first localization of the molecule, was set to dX = 1. These are the standard values in SMAP, and they were identified as the optimal parameter values for out (*d*)STORM experiments.

4.6 Simulations

Simulations Used for Cluster Algorithm Comparison

The simulations were done with an adapted simulation code published by Rubin-Delanchy et al. (2015). The number of clusters, the number of molecules inside each cluster, the corresponding standard distribution for the cluster size, and the background percentage were set depending on the analysis. Unlike the original publication, the cluster centers are set to be at least two standard distributions apart from each other. In total, 100 simulations were done for each case.

Simulations Used for Computational Time Evaluations

Ten simulations with a standard deviation of 50 nm, 10 clusters with 100 molecules each, and 50% of the total number of localizations in the background were used to determine the computational cost for the three cluster algorithms combined with the Bayesian engine. The field of view had a size of 3,000 × 3,000 nm^2, and the background is uniformly distributed. The localization precisions are generated from a gamma function with shape = 5 and rate = 0.166667 (default parameters, Griffié et al., 2016).

Simulations With Blinking Molecules

Simulations were prepared in Fluosim (Lagardère et al., 2020). For the simulation of the sample staining, a geometry file was created with a python script. The field of view had a size of 25 × 25 μm^2 and was composed of 40 randomly distributed, non-overlapping clusters with a diameter of 50 nm. The clusters were positioned with a minimum distance of 500 nm from any border of the sample. The background image was an image of the Evolve 512 EMCCD camera (Photometrics) with a size of 26 × 26 μm^2. The pixel size matched the pixel size of our experimental setup. Each pixel’s noise values were not considered because only the pixel shape was used in the further course. The number of molecules was set to 4,000 to match the density of optimal CV-1 GPI-GFP samples stained with anti-GFP nanobodies labeled with Alexa Fluor 647. For a fixed period (5–50 s), the molecules were diffusing within the field of view with a coefficient of 0,01 μm^2/s. A binding rate of 0,997–1,007 s^{-1} was set to allow cluster formation inside the clusters. Outside the designated cluster areas, the binding rate was set to 0 s^{-1}. After the binding period, the molecules were freely diffusing for 50 s. During this time, the binding and unbinding rates within the clusters were set to zero and set to 0,997–1,007 s^{-1} outside of the cluster areas, thereby causing a homogeneous distribution of background molecules.

For simulating an actual SMLM experiment, the fluorophores’ blinking parameters and the optical properties of the fluorescence emission were set accordingly. The on-rate was 0.01 s^{-1}, and the off-rate 10 s^{-1}, based on an estimated 1:1,000 ratio in an SMLM experiment. For fitting the point-spread function, full-width at half maximum was fixed at 200 nm with a fluorescence emission intensity of 2007. As in a microscopy experiment, 5,000 frames were acquired of the simulated sample, and the exposure time was set to 10 ms/frame. The output tiff-file was localized in SMAP with the standard parameters used for SMLM imaging. The camera parameters were the default values of the Delta 512 as given by its metadata file.

4.7 Computational Runtime Measurements

To evaluate the implemented cluster algorithms’ speed, we used a standard 64-bit laptop computer running Linux (Ubuntu 18.04.5 LTS), equipped with GNOME 3.28.2, 7.7 GiB of memory, and 4 Intel® Core™ i5-6200U CPU @ 2.30 GHz processors. The R library “tictoc” (Izrailev, 2014) was used to measure the time needed for each dataset to be processed.

4.8 Bayesian Analysis

Cluster Algorithms

The Ripley’s-K-based and DBSCAN cluster algorithms used were written by (Rubin-Delanchy et al., 2015; Griffié et al., 2016). The code was adapted for improvement by using functions from several R packages and the ToMATo cluster algorithm for SMLM data adapted from the R package RSMLM (Pike et al., 2020). The library “doParallel” was used for parallel implementation (Analytics and Weston, 2014).

Bayesian Parameters

All Bayesian cluster scorings were done with the same set of parameters. The percentage of background localizations was set to 50%, and the Dirichlet process’s concentration coefficient was

20. The optimal cluster parameters (radius and threshold) were searched in the sequences 5 to 300 for the first parameter and 5 to 500 for the second parameter in steps of 5.

Statistical Analysis

The statistical comparison was performed with a self-developed R script.

DATA AVAILABILITY STATEMENT

The raw data supporting the conclusions of this article will be made available by the authors, without undue reservation.

AUTHOR CONTRIBUTIONS

Funding acquisition: AM-V, HE; Software: SaK, RS; Sample preparation & acquisition: SaK, AZ; Simulations: AZ, RS, and SaK; Writing – original draft: SaK, HE; Resources: GG, LG, SuK, AM-V, and JR; Writing – review & editing: SaK, AZ, and HE.

FUNDING

This work was funded by the Deutsche Forschungsgemeinschaft (DFG, German Research Foundation) – Project-ID 278001972 – TRR 186 to AM-V and HE.

ACKNOWLEDGMENTS

We would like to acknowledge the assistance of the Core Facility BioSupraMol supported by the DFG. The authors would like to thank the HPC Service of ZEDAT, Freie Universität Berlin, for computing time. We acknowledge support by the Open Access Publication Initiative of Freie Universität Berlin.

SUPPLEMENTARY MATERIAL

The Supplementary Material for this article can be found online at: https://www.frontiersin.org/articles/10.3389/fbinf.2021.723915/full#supplementary-material

REFERENCES

Albrecht, D., Winterflood, C. M., Sadeghi, M., Tschager, T., Noé, F., and Ewers, H. (2016). Nanoscopic Compartmentalization of Membrane Protein Motion at the Axon Initial Segment. *J. Cel Biol.* 215, 37–46. doi:10.1083/jcb.201603108

Analytics, R., and Weston, S. (2014). Doparallel: Foreach Parallel Adaptor for the Parallel Package. *R. Package Version 1.016.* https://CRAN.R-project.org/packge=doParallel.

Andronov, L., Michalon, J., Ouararhni, K., Orlov, I., Hamiche, A., Vonesch, J. L., et al. (2018). 3dclustervisu: 3d Clustering Analysis of Super-resolution Microscopy Data by 3d Voronoi Tessellations. *Bioinformatics* 34, 3004–3012. doi:10.1093/bioinformatics/bty200

Annibale, P., Vanni, S., Scarselli, M., Rothlisberger, U., and Radenovic, A. (2011b). Quantitative Photo Activated Localization Microscopy: Unraveling the Effects of Photoblinking. *PLoS ONE* 6, e22678. doi:10.1371/journal.pone.0022678

Annibale, P., Vanni, S., Scarselli, M., Rothlisberger, U., and Radenovic, A. (2011a). Identification of Clustering Artifacts in Photoactivated Localization Microscopy. *Nat. Methods* 8, 527–528. doi:10.1038/nmEth.1627

Arnold, A. M., Schneider, M. C., Hüsson, C., Sablatnig, R., Brameshuber, M., Baumgart, F., et al. (2020). Verifying Molecular Clusters by 2-color Localization Microscopy and Significance Testing. *Sci. Rep.* 10, 4230–4312. doi:10.1038/s41598-020-60976-6

Baumgart, F., Arnold, A. M., Leskovar, K., Staszek, K., Fölser, M., Weghuber, J., et al. (2016). Varying Label Density Allows Artifact-free Analysis of Membrane-Protein Nanoclusters. *Nat. Methods* 13, 661–664. doi:10.1038/nmeth.3897

Baumgart, F., Arnold, A. M., Rossboth, B. K., Brameshuber, M., and Schütz, G. J. (2019). What We Talk about when We Talk about Nanoclusters. *Methods Appl. Fluoresc* 7, 013001. doi:10.1088/2050-6120/aaed0f

Betzig, E., Patterson, G. H., Sougrat, R., Lindwasser, O. W., Olenych, S., Bonifacino, J. S., et al. (2006). Imaging Intracellular Fluorescent Proteins at Nanometer Resolution. *Science* 313, 1642–1645. doi:10.1126/science.1127344

Chazal, F., de Silva, V., Glisse, M., and Oudot, S. (2012). *The Structure and Stability of Persistence Modules*. Springer.

Chazal, F., Guibas, L. J., Oudot, S. Y., and Skraba, P. (2013). Persistence-based Clustering in Riemannian Manifolds. *J. Acm* 60, 1–38. doi:10.1145/2535927

Dempsey, G. T., Vaughan, J. C., Chen, K. H., Bates, M., and Zhuang, X. (2011). Evaluation of Fluorophores for Optimal Performance in Localization-Based Super-resolution Imaging. *Nat. Methods* 8, 1027–1036. doi:10.1038/nmeth.1768

Endesfelder, U., Malkusch, S., Fricke, F., and Heilemann, M. (2014). A Simple Method to Estimate the Average Localization Precision of a Single-Molecule Localization Microscopy experiment. *Histochem. Cel Biol.* 141, 629–638. doi:10.1007/s00418-014-1192-3

Gowrishankar, K., Ghosh, S., Saha, S., C, R., Mayor, S., and Rao, M. (2012). Active Remodeling of Cortical Actin Regulates Spatiotemporal Organization of Cell Surface Molecules. *Cell* 149, 1353–1367. doi:10.1016/j.cell.2012.05.008

Griffié, J., Boelen, L., Burn, G., Cope, A. P., and Owen, D. M. (2015). Topographic Prominence as a Method for Cluster Identification in Single-Molecule Localisation Data. *J. Biophotonics* 8, 925–934. doi:10.1002/jbio.201400127

Griffié, J., Shannon, M., Bromley, C. L., Boelen, L., Burn, G. L., Williamson, D. J., et al. (2016). A Bayesian Cluster Analysis Method for Single-Molecule Localization Microscopy Data. *Nat. Protoc.* 11, 2499–2514. doi:10.1038/nprot.2016.149

Griffié, J., Shlomovich, L., Williamson, D. J., Shannon, M., Aaron, J., Khuon, S., et al. (2017). 3d Bayesian Cluster Analysis of Super-resolution Data Reveals Lat Recruitment to the T Cell Synapse. *Sci. Rep.* 7, 4077–4079. doi:10.1038/s41598-017-04450-w

Heilemann, M., van de Linde, S., Schüttpelz, M., Kasper, R., Seefeldt, B., Mukherjee, A., et al. (2008). Subdiffraction-resolution Fluorescence Imaging with Conventional Fluorescent Probes. *Angew. Chem. Int. Ed. Engl.* 47, 6172–6176. doi:10.1002/anie.200802376

Izrailev, S. (2014). *Tictoc: Functions for Timing R Scripts, as Well as Implementations of Stack and List Structures*. R package version 1.

Janeway, C. A., Jr, Travers, P., Walport, M., and Shlomchik, M. J. (2001). "General Principles of Transmembrane Signaling," in *Immunobiology: The Immune System in Health and Disease*. 5th edition (Garland Science).

Jayasinghe, I., Clowsley, A. H., Lin, R., Lutz, T., Harrison, C., Green, E., et al. (2018). True Molecular Scale Visualization of Variable Clustering Properties of Ryanodine Receptors. *Cell Rep.* 22, 557–567. doi:10.1016/j.celrep.2017.12.045

Jensen, L. G., Hoh, T. Y., Williamson, D. J., Griffié, J., Sage, D., Rubin-Delanchy, P., et al. (2021a). *Correction of Multiple-Blinking Artefacts in Photoactivated Localisation Microscopy*. bioRxiv.

Jensen, L. G., Williamson, D. J., and Hahn, U. (2021b). *Semiparametric point Process Modelling of Blinking Artifacts in palm*. arXiv preprint arXiv:2101.12285.

Kalappurakkal, J. M., Sil, P., and Mayor, S. (2020). Toward a New Picture of the Living Plasma Membrane. *Protein Sci.* 29, 1355–1365. doi:10.1002/pro.3874

Khater, I. M., Nabi, I. R., and Hamarneh, G. (2020). A Review of Super-resolution Single-Molecule Localization Microscopy Cluster Analysis and Quantification Methods. *Patterns* 1, 100038. doi:10.1016/j.patter.2020.100038

Lagardère, M., Chamma, I., Bouilhol, E., Nikolski, M., and Thoumine, O. (2020). Fluosim: Simulator of Single Molecule Dynamics for Fluorescence Live-Cell and Super-resolution Imaging of Membrane Proteins. *Sci. Rep.* 10, 19954–20014. doi:10.1038/s41598-020-75814-y

Levet, F., Hosy, E., Kechkar, A., Butler, C., Beghin, A., Choquet, D., et al. (2015). Sr-tesseler: A Method to Segment and Quantify Localization-Based Super-resolution Microscopy Data. *Nat. Methods* 12, 1065–1071. doi:10.1038/nmeth.3579

Levoin, N., Jean, M., Legembre, P., Martin-Villalba, A., Levoin, N., Legembre, P., et al. (2020). Cd95 Structure, Aggregation and Cell Signaling. *Front. Cel Dev. Biol.* 8, 314. doi:10.3389/fcell.2020.00314

Li, J. H., Santos-Otte, P., Au, B., Rentsch, J., Block, S., and Ewers, H. (2020). Directed Manipulation of Membrane Proteins by Fluorescent Magnetic Nanoparticles. *Nat. Commun.* 11, 4259–4267. doi:10.1038/s41467-020-18087-3

Martin-Villalba, A., Llorens-Bobadilla, E., and Wollny, D. (2013). Cd95 in Cancer: Tool or Target? *Trends Mol. Med.* 19, 329–335. doi:10.1016/j.molmed.2013.03.002

Nicovich, P. R., Owen, D. M., and Gaus, K. (2017). Turning Single-Molecule Localization Microscopy into a Quantitative Bioanalytical Tool. *Nat. Protoc.* 12, 453–460. doi:10.1038/nprot.2016.166

Owen, D. M., Rentero, C., Rossy, J., Magenau, A., Williamson, D., Rodriguez, M., et al. (2010). Palm Imaging and Cluster Analysis of Protein Heterogeneity at the Cell Surface. *J. Biophotonics* 3, 446–454. doi:10.1002/jbio.200900089

Pierce, K. L., Premont, R. T., and Lefkowitz, R. J. (2002). Seven-transmembrane Receptors. *Nat. Rev. Mol. Cel Biol.* 3, 639–650. doi:10.1038/nrm908

Pike, J. A., Khan, A. O., Pallini, C., Thomas, S. G., Mund, M., Ries, J., et al. (2020). Topological Data Analysis Quantifies Biological Nano-Structure from Single Molecule Localization Microscopy. *Bioinformatics* 36, 1614–1621. doi:10.1093/bioinformatics/btz788

Ries, J. (2020). Smap: a Modular Super-resolution Microscopy Analysis Platform for Smlm Data. *Nat. Methods* 17, 870–872. doi:10.1038/s41592-020-0938-1

Ries, J., Kaplan, C., Platonova, E., Eghlidi, H., and Ewers, H. (2012). A Simple, Versatile Method for Gfp-Based Super-resolution Microscopy via Nanobodies. *Nat. Methods* 9, 582–584. doi:10.1038/nmeth.1991

Rubin-Delanchy, P., Burn, G. L., Griffié, J., Williamson, D. J., Heard, N. A., Cope, A. P., et al. (2015). Bayesian Cluster Identification in Single-Molecule Localization Microscopy Data. *Nat. Methods* 12, 1072–1076. doi:10.1038/nmeth.3612

Rust, M. J., Bates, M., and Zhuang, X. (2006). Sub-diffraction-limit Imaging by Stochastic Optical Reconstruction Microscopy (STORM). *Nat. Methods* 3, 793–796. doi:10.1038/NMETH929

Saka, S. K., Honigmann, A., Eggeling, C., Hell, S. W., Lang, T., and Rizzoli, S. O. (2014). Multi-protein Assemblies Underlie the Mesoscale Organization of the Plasma Membrane. *Nat. Commun.* 5, 4509–4514. doi:10.1038/ncomms5509

Schultz, G., and Schaefer, M. (2008). *Transmembrane Signaling*. Berlin, Heidelberg: Springer Berlin Heidelberg, 1236–1242. doi:10.1007/978-3-540-38918-7_143

Sochacki, K. A., Dickey, A. M., Strub, M. P., and Taraska, J. W. (2017). Endocytic Proteins Are Partitioned at the Edge of the Clathrin Lattice in Mammalian Cells. *Nat. Cel Biol.* 19, 352–361. doi:10.1038/ncb3498

Williamson, D. J., Burn, G. L., Simoncelli, S., Griffié, J., Peters, R., Davis, D. M., et al. (2020). Machine Learning for Cluster Analysis of Localization Microscopy Data. *Nat. Commun.* 11, 1493–1510. doi:10.1038/s41467-020-15293-x

Williamson, D. J., Owen, D. M., Rossy, J., Magenau, A., Wehrmann, M., Gooding, J. J., et al. (2011). Pre-existing Clusters of the Adaptor Lat Do Not Participate in Early T Cell Signaling Events. *Nat. Immunol.* 12, 655–662. doi:10.1038/ni.2049

Conflict of Interest: The authors declare that the research was conducted in the absence of any commercial or financial relationships that could be construed as a potential conflict of interest.

frontiers
in Bioinformatics

ORIGINAL RESEARCH
published: 15 October 2021
doi: 10.3389/fbinf.2021.752788

Fourier Ring Correlation and Anisotropic Kernel Density Estimation Improve Deep Learning Based SMLM Reconstruction of Microtubules

*Andreas Berberich[1], Andreas Kurz[2], Sebastian Reinhard[2], Torsten Johann Paul[1], Paul Ray Burd[3], Markus Sauer[2] and Philip Kollmannsberger[1]**

[1]Center for Computational and Theoretical Biology, University of Wuerzburg, Wuerzburg, Germany, [2]Department of Biotechnology and Biophysics, University of Wuerzburg, Wuerzburg, Germany, [3]Institute for Theoretical Physics and Astrophysics, University of Wuerzburg, Wuerzburg, Germany

Single-molecule super-resolution microscopy (SMLM) techniques like *d*STORM can reveal biological structures down to the nanometer scale. The achievable resolution is not only defined by the localization precision of individual fluorescent molecules, but also by their density, which becomes a limiting factor e.g., in expansion microscopy. Artificial deep neural networks can learn to reconstruct dense super-resolved structures such as microtubules from a sparse, noisy set of data points. This approach requires a robust method to assess the quality of a predicted density image and to quantitatively compare it to a ground truth image. Such a quality measure needs to be differentiable to be applied as loss function in deep learning. We developed a new trainable quality measure based on Fourier Ring Correlation (FRC) and used it to train deep neural networks to map a small number of sampling points to an underlying density. Smooth ground truth images of microtubules were generated from localization coordinates using an anisotropic Gaussian kernel density estimator. We show that the FRC criterion ideally complements the existing state-of-the-art multiscale structural similarity index, since both are interpretable and there is no trade-off between them during optimization. The TensorFlow implementation of our FRC metric can easily be integrated into existing deep learning workflows.

Keywords: *d*STORM, deep learning–artificial neural network (DL-ANN), single molecule localization microscopy, microtubule cytoskeleton, super-resolution

Edited by:
Christian Franke,
Friedrich Schiller University Jena,
Germany

Reviewed by:
Guilherme De Alencar Barreto,
Federal University of Ceara, Brazil
Zoltan Cseresnyes,
Leibniz Institute for Natural Product
Research and Infection Biology,
Germany

****Correspondence:***
Philip Kollmannsberger
Philip.Kollmannsberger@uni-wuerzburg.de

Specialty section:
This article was submitted to Computational BioImaging, a section of the journal Frontiers in Bioinformatics

Received: *03 August 2021*
Accepted: *04 October 2021*
Published: *15 October 2021*

Citation:
Berberich A, Kurz A, Reinhard S, Paul TJ, Burd PR, Sauer M and Kollmannsberger P (2021) Fourier Ring Correlation and Anisotropic Kernel Density Estimation Improve Deep Learning Based SMLM Reconstruction of Microtubules.
Front. Bioinform. 1:752788.
doi: 10.3389/fbinf.2021.752788

INTRODUCTION

Single-molecule localization microscopy (SMLM) can overcome the diffraction barrier in fluorescence microscopy by stretching the activation of fluorophores over time. To achieve this, individual non-overlapping active emitters are localized with a precision of a few nanometers, limited only by the number of photons acquired and the noise (van de Linde et al., 2011). The trade-off in SMLM is the acquisition time required to obtain enough localizations to reconstruct a dense super-resolved image. New deep learning-based fitting algorithms can reconstruct localizations from raw frames at higher densities (Nehme et al., 2018; Speiser et al., 2021). This allows for shorter acquisition times by increasing the number of blinking fluorophores in each frame. In some cases, however, the density of localizations is inherently limited, for example due to unstable photodyes or low emitter density in expanded samples. The density of localizations limits the resolution of SMLM independent of localization precision, since no structures at a length scale smaller than two emitter distances can be resolved according to the Nyquist limit.

Applications of deep convolutional neural networks to SMLM have so far mainly been for fitting: using raw diffraction-limited frames as input, trained deep networks predict localization coordinates (Zelger et al., 2018), super-resolved images (Nehme et al., 2018), or images with localization coordinates encoded in the pixel values (Speiser et al., 2021). By learning non-linear mappings from intensity distributions to point coordinates, the sparsity requirements needed for accurate Gaussian fitting can be relaxed and much higher localization densities can be imaged, thus reducing the necessary measuring time. In fluorescence microscopy in general, deep learning has many other applications, including denoising and image restoration (Weigert et al., 2018), classification, and segmentation. Most of these applications are image-to-image tasks, i.e., the network takes images as input and generates denoised images or segmentation labels as output.

For image-to-image tasks like denoising and segmentation, the *U-Net* architecture introduced by (Ronnebergeret al., 2015) is considered state-of-the-art. It consists of an autoencoder-like convolutional network with additional skip connections between the down- and upsampling part. This way, a high-level feature-based representation is efficiently combined with spatial information. To train a U-Net, the generated image or label map is compared to a ground truth image using various image-based metrics (Zhao et al., 2017). The classical metric in image-to-image tasks is the L_2 loss, corresponding to the pixel-wise mean squared error between output and target image. L_2 is common standard but causes artifacts as it does not penalize small errors. The structural similarity index measure (SSIM) is a good alternative as it takes the properties of the human perceptive system into account. It shows best results when combined with the absolute pixel-wise error or L_1 loss to prevent an intensity offset (Zhao et al., 2017). Alternatively, the loss function can be learned by optimizing the image generator against a second network (discriminator) that tries to discriminate ground truth images from those generated by the U-Net in an approach called “conditional generative adversarial network” or *cGAN* (Isola et al., 2017). While this architecture can learn to generate surprisingly realistic-looking images, the authors note that it is not suitable for segmentation due to its tendency to generate plausible-looking but non-existing structures in images.

To reconstruct dense SMLM images from sparse subsets of localization, ANNA-PALM by (Ouyang et al., 2018) elegantly combines the *pix2pix* cGAN architecture from (Isola et al., 2017) with a consistency check against low-resolution images to overcome the limitations of generative networks. In addition, multiscale SSIM and L_1 loss as described in (Zhao et al., 2017) are used for training the U-Net generator. The generator-discriminator loss by itself cannot be interpreted as measure of prediction accuracy, as the two networks depend on each other. During supervised training, there are ground truth images that can serve as target to compare the prediction to the ground truth and to determine the error, but when applying the trained network to new images, this information is not available. To solve this problem, a comparison with low-resolution wide-field images is performed in (Ouyang et al., 2018) in cases where such images are available.

Due to the stochastic blinking during the measurement, the SMLM imaging process can be interpreted as sampling from an underlying fluorophore-labeled density. This sampling contains errors due to mislabeling, photobleaching, and post-processing. Hence, one goal for each SMLM method is to estimate the real underlying fluorophore distribution from a measured error-prone sample. In some cases, the precise coordinates of individual emitters are relevant, for example when looking at the relative arrangements of discrete, isolated labeled molecules. In most cases, however, the individual locations are of secondary interest, and the reconstruction of the underlying density is the central goal. This is the case for example when imaging continuous structures in the cell, for example, cytoskeletal filaments.

Localization coordinates can be visualized in different ways to give an impression of the underlying density. When represented as 2D histogram where each pixel contains the number of localizations detected within the area of the pixel, blurring each localization with a Gaussian kernel with a variance sigma corresponding to the localization uncertainty can give a more accurate impression of density. A single value for sigma based on the average localization uncertainty of the entire image is an efficient approximation (R. P. J. Nieuwenhuizen et al., 2014). This Gaussian filter is an example of a kernel density estimate (KDE) with a constant (non-adaptive) kernel width sigma. More elaborate versions of KDE use adaptive kernels, for example with a sigma proportional to the density of localizations in the region of the image. Some interesting aspects of density estimation from discrete localizations are described in (Rees et al., 2012). Going one step further, the kernel for density estimation could be made anisotropic. In different context, adaptive anisotropic kernel density estimates have been used by (Hensen et al., 2009) for improving configurational entropies of macromolecules, or by (Ronneberger et al., 2015) for human motion capture. The use of adaptive anisotropic KDE for density estimation in SMLM localization data was demonstrated by (Chen et al., 2014). They used anisotropic Gaussian kernels where the covariance is a function of the surrounding density of points and show that thresholding the estimated density results in a better segmentation of subcellular structures compared to conventional Gaussian rendering.

Estimating the resolution in a single image is not easily possible, but when two images of the same structure are available, their resolution can be estimated using Fourier Ring Correlation (FRC). The 2D cross correlation of the two images is calculated, and the intensity in the Fourier transformed correlation image is summed up and binned by frequency. The resulting curve shows how much the signal in the two images is correlated as a function of frequency, or correspondingly, length scale. If the images are dominated by uncorrelated random noise beyond a certain frequency or below a certain length scale, then these length scales cannot be resolved. FRC was originally developed for electron cryomicroscopy, where two independent images each using one half of the information are compared. It can easily be applied to SMLM, since it is possible to reconstruct two subimages using one half of the localizations each (Robert P. J. Nieuwenhuizen et al., 2013). FRC is also used for image volume reconstruction, where adjacent slices in a volume can be compared against each other using the integral of the FRC (Preusser et al., 2021). FRC has recently been shown to be useful to improve and monitor image restoration and deconvolution, and can also be applied to single images by constructing different subsamplings (Koho et al., 2019). It was noted in (Legant et al., 2016) that the result cannot always be interpreted as a measure for image resolution, and that care must be taken when two different types of images are compared. FRC can vary within images depending on the content, and local FRC maps can be used to compare super-resolved images to wide-field images (Culley et al., 2018). A suitable quantification of SMLM resolution remains challenging and is an active field of research (Cohen et al., 2019; Descloux et al., 2019). A robust quality measure of reconstructed images is a key requirement to assess image reconstruction methods, and there is a general interest to develop robust quality measures for SMLM images and to integrate them into trainable image reconstruction workflows. FRC as an established measure in the SMLM field is a promising candidate for such a measure but using it for deep learning would require it to be available as differentiable loss function.

Here, we present a deep learning approach to reconstruct density estimates for microtubules from small subsets of localizations. We show how the preprocessing of ground truth images can be improved by using an anisotropic kernel density estimate. We then introduce a new loss function based on a modified FRC criterion and implement it as differentiable function that can be used for training deep neural networks. In combination, this can help to make deep learning based SMLM density reconstruction easier to interpret. The FRC loss is compared to the multiscale structural similarity index (MSSIM) by training a U-Net with different combinations of loss functions to reconstruct microtubules. As ground truth, we use conventional Gaussian rendered histograms and density estimates based on anisotropic adaptive kernels. Finally, we discuss the differences of our approach to the existing state of the art (ANNA-PALM) regarding ease of use and interpretability. Our implementation is openly available on our github repository, enabling its application for trainable image reconstruction also beyond SMLM.

MATERIALS AND METHODS

Cell Culture, Fixation, and Staining

African green monkey kidney fibroblast-like cells (COS7, Cell Lines Service GmbH, Eppelheim, #605470) were cultured in DMEM (Sigma, #D8062) containing 10% FCS (Sigma-Aldrich, #F7524), 100 U/ml penicillin and 0.1 mg/ml streptomycin (Sigma-Aldrich, #P4333) at 37°C and 5% CO_2. Cells were grown in standard T25-culture flasks (Greiner Bio-One). Staining of tubulin filaments was performed as described earlier (van de Linde et al., 2011). COS-7 cells were permeabilized for 1–2 min and simultaneously pre-fixed with a prewarmed buffer (37°C) containing 0.3% glutaraldehyde and 0.25% Triton X-100 in Cytoskeletal Buffer. The buffer is then exchanged for preheated (37°C) 2% glutaraldehyde (in CB) and incubated for 10 min. Fixation is stopped by 100 mM glycine (in PBS) step for 5 min, and cells were washed at least 3 times 5 min with PBS. Blocking of epitopes inducing unspecific labeling was carried out by 30 min incubation with 5% BSA. Primary antibody (rabbit α-tubulin, PA5-19489, Thermo Fisher) was added at concentrations of 10 μg/ml (in 5% BSA) for 60 min at room temperature, and unspecifically bound primary antibody was removed by rinsing the sample several times with 0.05% Tween20 (in PBS) solution followed by washing with normal PBS for 3 times 5 min. Secondary antibody [F (ab') 2 goat-anti-rabbit IgG (H + L) Alexa-647] was added at concentrations of 10 μg/ml in 5% BSA for at least 60 min at room temperature. Washing steps with tween solution and PBS were applied as described above. To maintain the labeling of both antibodies a post fixation step with 4% formaldehyde (in PBS) for 10 min was performed.

*d*STORM Imaging

Imaging was performed on a Nikon Eclipse Ti inverted wide-field microscope using a 640 nm laser at 200 mW excitation output power, a Nikon APO TIRF 100x/1.49 oil immersion objective, adapted HILO illumination and ×22 binning resulting in a pixel size of 108 nm. In total 12 spots with microtubules were imaged, and 50.000 frames were acquired per position. Each image covers a square of about 21 × 21 μm^2. Exposure time was set to 20 ms. Raw frames were processed with the MLE fitter in Picasso (Schnitzbauer et al., 2017) using a net gradient setting of 4,500 and drift correction.

Anisotropic Kernel Density Estimate

Localization files generated by Picasso were spatially binned into 2D histograms with a pixel size of 5 nm. These super-resolved images were then filtered by convolution of the image I with a discrete filter kernel K such that the estimated density $f(\vec{x}_i)$ of the i-th pixel p_i is

$$f\left(\vec{x}_i\right) = \frac{1}{n}\sum_{j=1}^{k} I\left(\vec{x}_j\right) K\left(\vec{x}_i, \vec{x}_j\right),$$

where $\vec{x}_i$ is the pixel's position in the image. The summation is performed over all k pixels within the kernel window placed on top of x_i. The classical isotropic Gaussian filter corresponds to the kernel

$$K\left(\vec{x}_i, \vec{x}_j\right) = \frac{1}{2\pi b} exp\left(-\frac{\left(\vec{x}_i - \vec{x}_j\right)^2}{2b^2}\right),$$

where b denotes the constant variance of the Gaussian filter. This density estimator is commonly used to render super-resolved images from localization tables (R. P. J. Nieuwenhuizen et al., 2014). It accounts for the localization uncertainty but does not consider the heterogeneity and anisotropy of the localization

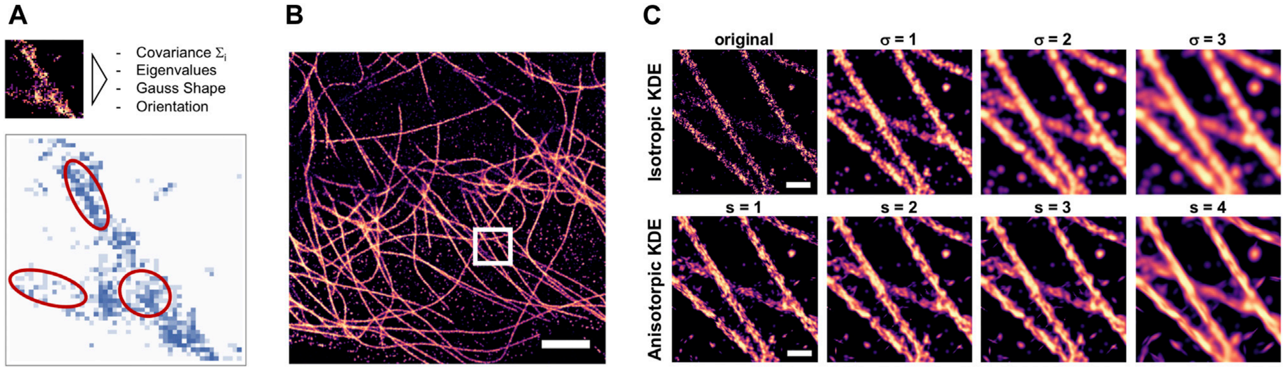

FIGURE 1 | Anisotropic KDE as density estimate for filaments. **(A)** Illustration of the method as proposed by (Chen et al., 2014) but here implemented in image space; red ellipses indicate the different shapes and orientations of the 2D anisotropic Gaussian filter kernels. **(B)** Histogram rendering of a complete field of view of a reconstructed dSTORM image of microtubules in a COS7 cell, scale bar = 2 µm. **(C)** zoomed-in detail indicated by the box in b) (scale bar = 0.2 µm), top: unfiltered histogram (left) and density estimation by classical Gaussian filtering with fixed sigma of 1–3 pixels, corresponding to 5–15 nm; bottom: same region, but with anisotropic KDE applied using an adaptive multivariate Gaussian kernel scaled by a factor of 1–4 (from left to right).

density. Adaptive KDE as an alternative (Rees et al., 2012) scales *b* with the density of localizations but is still isotropic. The main limitation of a Gaussian KDE, adaptive or not, is that it is not sensitive to anisotropic spatial distributions of fluorophores. For anisotropic structures like microtubule filaments, the density within the filaments becomes increasingly continuous when increasing *b*, approximating the actual filament. The edges however become more and more blurred as higher frequencies in the image are increasingly suppressed by the Gaussian kernel, since it acts as a low-pass filter.

The anisotropic adaptive KDE proposed by (Chen et al., 2014) uses a kernel that adapts not only its scale, but also its shape and orientation to the local distribution of localizations for each pixel. We implemented anisotropic adaptive KDE using the 2D multivariate Gaussian convolution kernel

$$K\left(\vec{x}_i, \vec{x}_j\right) = \frac{1}{\sqrt[2]{(2\pi)^2|\Sigma_i|}} \exp\left(-\frac{1}{2}\left(\vec{x}_i - \vec{x}_j\right)^T \sum\nolimits_i^{-1} \left(\vec{x}_i - \vec{x}_j\right)\right),$$

where Σi is the positive definite covariance matrix that defines the properties of the kernel at position x_i, and $|\Sigma_i|$ is its determinant. To adapt to the local distribution of localizations, the covariance is estimated as

$$\Sigma_i = \frac{1}{\tilde{I}} \sum_{j=1}^{k} \left(\vec{x}_j - \vec{\mu}_i\right)\left(\vec{x}_j - \vec{\mu}_i\right)^T \quad \text{with} \quad \tilde{I} = \sum_{j=1}^{k} I\left(\vec{x}_j\right),$$

with $\vec{\mu}_i$ the mean intensity within the kernel window at pixel p_i. Again, the summation is performed over all *k* pixels within the kernel window placed around p_i. At each pixel p_i, the corresponding covariance Σ_i shaped by the spatial intensity distribution within the filter window is calculated. The eigenvectors of Σ_i are perpendicular and define the orientation of the kernel, whereas its eigenvalues λ_1 and λ_2 define its shape. The covariance is diagonal along the main axis of the kernel, i.e., when rotated towards the direction of highest localization density. The resulting kernel is scaled by a constant factor and applied to the corresponding region of the original image. We used a constant odd window size of 11 × 11 pixel and varied the scale between 1 and 4 (**Figure 1**). The same approach can be used for higher dimensions, as multivariate Gaussian functions can easily be generalized to 3D, as demonstrated e.g. for spatial directional statistics simulations–see (Paul and Kollmannsberger, 2020) for an implementation in python.

Fourier Ring Correlation Loss

Fourier Ring Correlation (FRC) measures the correlation of a pair of images as a function of spatial frequency. When applied to a pair of super-resolved images generated by dividing the list of localization coordinates in two subsamples, it can be interpreted as a measure of resolution of the full SMLM image (Robert P. J. Nieuwenhuizen et al., 2013). The two images are correlated by multiplying their Fourier transforms F_x and F_y, and the FRC_{xy} is obtained by summing over concentric rings r_i in Fourier space:

$$\mathrm{FRC}_{xy}(r_i) = \frac{\sum_{r\epsilon r_i} F_x(r) F_y(r)^*}{\sqrt{\sum_{r\epsilon r_i} F_x^2(r) \sum_{r\epsilon r_i} F_y^2(r)^*}},$$

normalized by the total intensities in each ring. The signal at a distance r_i from the center of the Fourier transformed images corresponds to the spatial frequency.

$$f_i = \frac{r_i}{N},$$

with *N* the number of frequency bins, or pixels in the image. The spatial frequency where the FRC falls below a value of 1/7 is defined as cut-off frequency and interpreted as resolution of the full image (Robert P. J. Nieuwenhuizen et al., 2013).

The value of the cut-off frequency by itself does not contain any information about the magnitude of correlation at lower frequencies. Maximizing it is thus not an ideal target for optimization (**Figure 2**). Instead of maximizing the cut-off frequency during optimization, we calculate the area of the

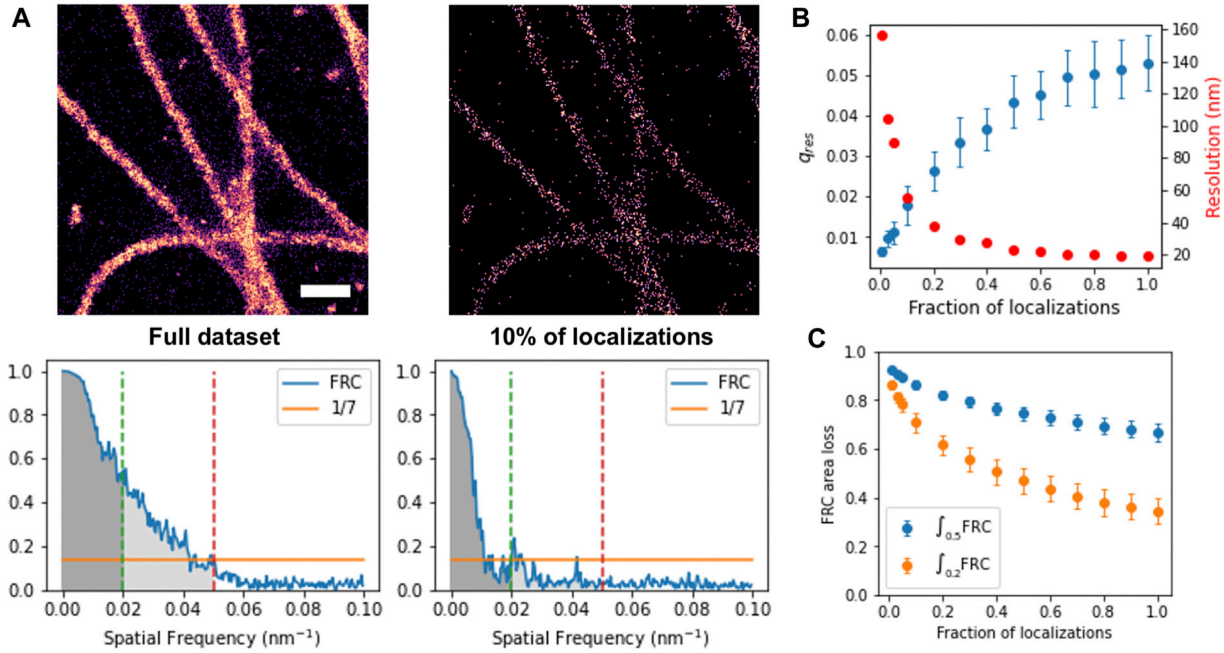

FIGURE 2 | Fourier Ring Correlation to estimate image improvement with increasing density of localizations. **(A)** Histogram rendering (top) and corresponding FRC (bottom) of full and sparse set of localizations, with threshold 1/7 and area threshold 0.2 (green) and 0.5 (red) indicated. Scale bar: 300 nm, **(B)** FRC cutoff frequency (blue) and corresponding resolution (red) as function of the fraction of total localizations, **(C)** FRC area loss for a threshold of 0.2 (yellow) and 0.5 (blue) as function of the fraction of total localizations.

FRC similar to (Preusser et al., 2021) but only up to a fixed frequency f' and use it as target:

$$\mathcal{L}_{xy}\left(f'\right) = 1 - \overline{\mathrm{FRC}_{xy,f'}} \quad \text{with} \quad \overline{\mathrm{FRC}_{xy,f'}} = \sum_{j=0}^{f'} \mathrm{FRC}_{xy,f'}\left(j\right),$$

where the summation is performed over all FRC values corresponding to the spatial frequency j.

We implemented the differentiable area-FRC as described above using the built-in complex multiplication, 2D-FFT and reduce_sum functions of Tensorflow2. The frequency rings are precomputed and held in GPU memory as constant masks.

Deep Neural Network for Image Restoration

We used a 2D *U-Net*-like (Ronneberger et al., 2015) deep convolutional neural network. The details of the architecture are identical to the generator part used in the *pix2pix* cGAN (Isola et al., 2017) and in ANNA-PALM (Ouyang et al., 2018): the input image is downsampled with eight consecutive 2D convolution layers with stride = 2 and size = 4, *Leaky ReLU* activation, and increasing filter number (64-128-256-512-. . .-512), followed by a mirrored upsampling part with the corresponding transposed convolutions using identical stride and filter number, *ReLU* activation, and skip connections concatenating the output of the corresponding downsampling layer to the upsampling layer of the same size. The last layer is a transposed convolution with *tanh* activation and generates the final output image. The network was implemented in Tensorflow2 based on the *pix2pix* implementation in the official documentation (https://www.tensorflow.org/tutorials/generative/pix2pix) but without the discriminator part.

Network Training

Training data were generated from localization tables produced by Picasso as follows: first, each full localization table was rendered into a 2D histogram with a pixel size of 5 nm. Isolated localizations were removed, and density was estimated either by filtering with a Gaussian blur filter of sigma = 5 nm (isotropic KDE) or by applying anisotropic KDE with window size 11 × 11 and scale factor between 1 and 4. The resulting density estimates were used as training targets. The corresponding input images were generated by rendering 2D histograms of a subset of frames using randomly selected time windows containing between 5 and 30% of the total number of localizations. Input-target image pairs were created by randomly cropping pairs of corresponding patches with a size of 750 × 750 pixels from the sparse subset images, and from the density estimates of the full dataset. From the 11 fields of view, 2 were held back for validation. During training, patches were augmented by applying continuous on-GPU rotation to prevent overfitting, and a 512 × 512 patch was cropped from the center of the rotated images. ADAM optimization with a learning rate of 2×10^{-4} and $\beta_1 = 0.5$ was used to train the network for 1,000 epochs (iterations over the training set). The loss function was either area-FRC, multiscale structural similarity index, or the sum of both, as indicated. Additionally, we added a small L_1 loss (absolute pixel-wise difference) to stabilize training, since neither MS-SIM nor FRC punish deviations in background or total intensity, which can lead to offset or inverted output images.

RESULTS

Anisotropic Kernel Density Estimate

Density estimation can help to improve trainable image reconstruction algorithms that are designed to reconstruct the density from a given subset of localizations. The problem with such attempts is that the training data are available as point clouds, so the training optimizes reconstruction of discrete localization patterns rather than continuous densities. Rendered histograms of localization data contain the discrete count of localizations in each pixel, which can be non-continuous. KDE-smoothed histograms are better suited as target for trainable image reconstruction, as they do not encourage the training process to optimize for reconstructing discontinuous localization patterns, but instead for the continuous underlying density. Isotropic Gaussian KDE provides such a density estimate, but at the expense of lowering the effective resolution due to low-pass effect of Gaussian blur. We implemented an anisotropic kernel density estimation as proposed in (Chen et al., 2014) as window-based filter operation in Python (**Figure 1A**), and applied it to rendered histograms of localization datasets of tubulin (**Figure 1B**). The scale of the anisotropic KDE was systematically varied and compared to the results of conventional KDE by Gaussian filtering (**Figure 1C**).

The purpose of applying KDE is to obtain an estimate of the underlying true density of the labeled epitope that would be observed in the limit of perfect labeling efficiency and infinite measuring time, from the experimentally measured sample of localizations. We found that for high-density *d*STORM datasets of microtubules, the anisotropic KDE provides a better estimate of density as it does not blur the edges of the filaments (**Figure 1C**). We hypothesize that preprocessing of real training data with anisotropic KDE as shown in **Figure 1** is an alternative approach for anisotropic structures and will result in improved reconstruction quality.

Fourier Ring Correlation and Localization Density

Fourier Ring Correlation (FRC) can be used to measure image resolution of SMLM images by splitting the localization data in two subsets and calculating the FRC of the reconstructed histograms (Robert P. J. Nieuwenhuizen et al., 2013). Recently, FRC has been proposed to monitor the progress of image reconstruction and deconvolution methods (Koho et al., 2019). Here, we explore the potential of using FRC as target function to train deep neural networks to reconstruct the underlying density from sparse localization images. We implemented FRC in Tensorflow2 as differentiable function, as described in materials and methods. To determine how FRC depends on the localization density, we generated sparse localization datasets using a subset of frames with a defined fraction of localizations of the entire dataset. Each resulting subset of localizations was then split in two, and the FRC cut-off frequency of the corresponding rendered histograms was calculated (**Figures 2A,B**). When correlating sparse and dense images, the cut-off frequency cannot be directly used as resolution measure, because the already reconstructed images cannot be split in two subsets. The FRC vs. frequency plot nevertheless gives a measure for similarity between the sparse and dense images: two identical images would have FRC = 1 for all frequencies, whereas for unrelated images, FRC would be = 0 everywhere. We thus propose the integral of the FRC as new measure for reconstruction quality. To avoid the influence of spurious correlations at high frequencies, we calculate the FRC integral up to a cut-off frequency of 0.2 or 0.5 of the maximum frequency.

The dependency of our area-FRC measure is shown in **Figure 2C**. Here, the FRC between the reconstructed histogram of the subset and that of the full dataset was calculated and summed up to a cut-off frequency of 0.2 or 0.5. The area FRC scales similarly to the original FRC, and shows a stronger dependency on fraction of localizations when only using lower frequencies up to 0.2. For comparison, we also calculated the area FRC in the classical way, i.e., by splitting the localization data in two and summing up the FRC between the two sub-histograms (**Figure 2B**). As can be seen, the dependency is qualitatively similar. In summary, we conclude that the area of the FRC between the sparse and the full density SMLM image can be interpreted as a measure for the similarity between the two images. Consequently, by comparing a reconstructed density image to the true density image, one could monitor the quality of the reconstruction and thus the progress of a trainable reconstruction algorithm.

Training Neural Networks With FRC Loss

We implemented our area FRC measure as differentiable function in Tensorflow2 to be able to use it as loss function for deep neural network training. We generated a set of training and validation images from a *d*STORM experiment on labelled tubulin in cells, as described in the methods section, and trained a 2D U-Net-like image-to-image fully convolutional network (**Figures 3A–C**) using different loss functions and targets. The final trained network was then used to predict test images not used during training to assess network performance. The evaluation criteria were peak signal-to-noise ratio (PSNR), mean squared error (MSE) or L_2 loss, multiscale structural similarity index (MSSIM), and area FRC, independent of the loss function used during training.

We first investigated if using the anisotropic kernel density estimate as training target improves the training process. We trained the same network using MSSIM loss using either Gaussian KDE or anisotropic KDE target images and monitored the improvement of the loss during training (**Figure 3D**). The anisotropic density estimation target results in faster convergence of the training process. This shows that the smoothing effect of the anisotropic kernel provides a better optimization target compared to regular isotropic Gaussian density estimation for anisotropic structures like filaments.

Next, we compared our FRC area loss to MSSIM, which is the state-of-the-art loss function for image-to-image tasks and was shown to work well for SMLM sparse-to-dense reconstruction (Ouyang et al., 2018). We trained the network on the same data using either MSSIM only, FRC only, or both together, and monitored both losses during training (**Figures 3E,F**). We observed that the FRC loss decreases at the same rate when optimizing for FRC area only or for MSSIM + FRC, but at a slower rate when optimizing for MSSIM only. Correspondingly, MSSIM goes down at the same rate when optimizing for FRC + MSSIM as when optimizing for MSSIM only,

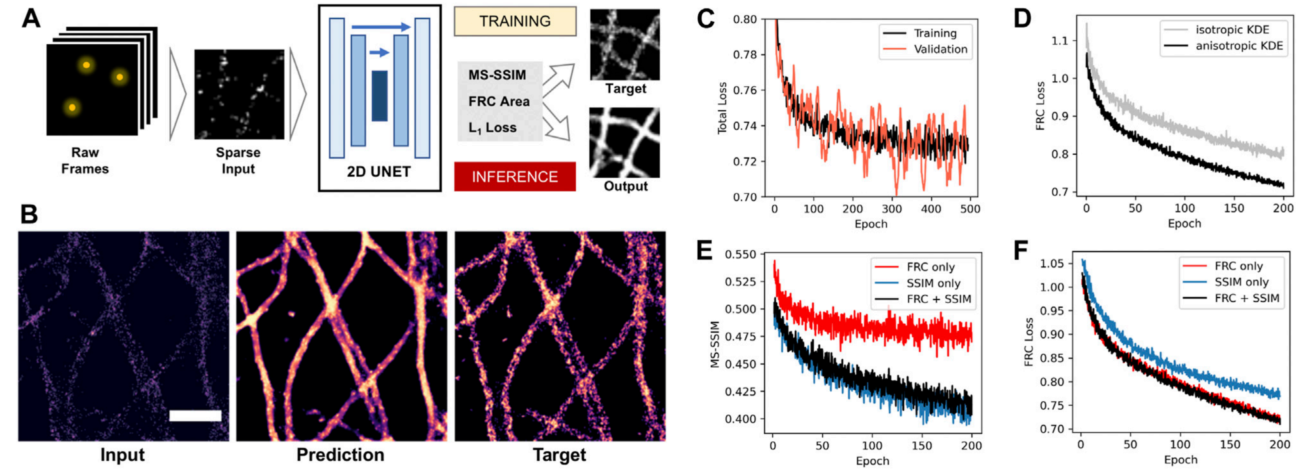

FIGURE 3 | Deep learning-based density reconstruction with FRC area loss. **(A)** Deep learning workflow using a 2D U-Net architecture to predict density images from sparse input. **(B)** Example of sparse input with 10% of localizations (left), network prediction after training (middle), and target image using the full dataset (right). Scale bar = 0.5 µm **(C)** Total loss monitored during network training for training (black) and unseen validation images (orange). **(D)** FRC loss during training for target density images generated by classical isotropic Gaussian (grey) and anisotropic kernel density estimation (black). **(E)** Structural similarity index (MS-SSIM) during training for a network trained on FRC loss only (red), SSIM (blue) and both together (black). **(F)** FRC area loss during training for a network trained on FRC loss only (red), SSIM (blue), and both together (black).

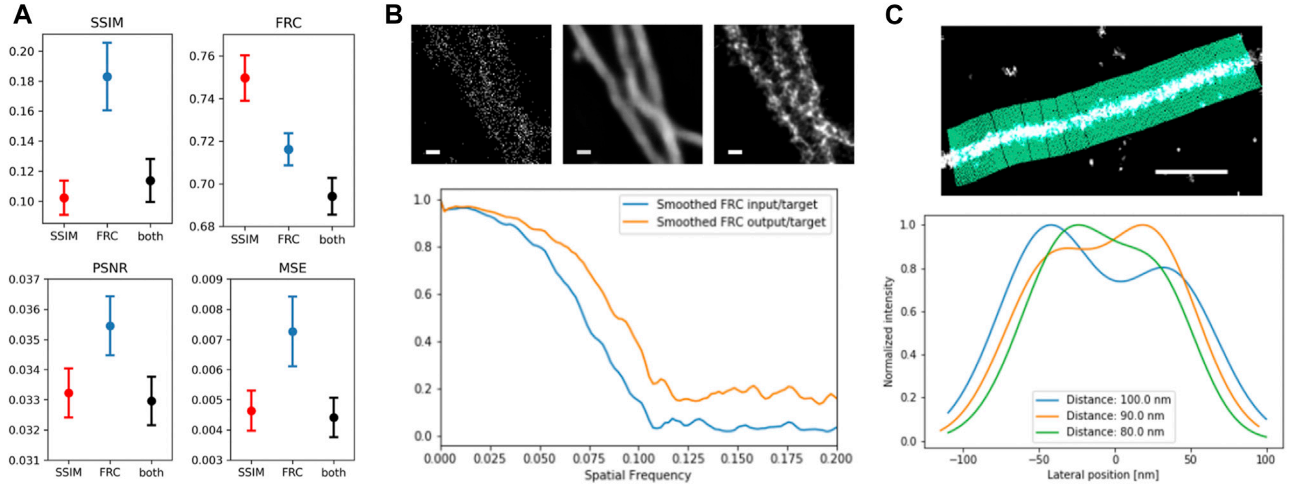

FIGURE 4 | Evaluation of trained networks. **(A)** averaged MS-SIM and FRC (top), as well as peak signal-to-noise ratio (PSNR) and mean squared error (MSE) for 20 network output and target images from the validation dataset; error bars denote SEM. **(B)** FRC improvement as function of spatial frequency of input (left) vs. target (right) and output (center) vs. target. Scale bar = 100 nm. **(C)** Line Profiler evaluation illustrated at the top and applied to two adjacent simulated filaments with distance of 80 nm (green), 90 nm (yellow) and 100 nm (blue), showing the emergence of two separate peaks.

but at a slower rate when optimizing for FRC only. This shows that there is no trade-off between both losses: using MSSIM and FRC together gives an improvement over using only one of the two. This shows that our new area FRC loss provides an improvement over using only MSSIM when both are combined.

Quantification of Reconstruction Quality

The final trained networks were used to predict images not used during training to assess network performance. The evaluation criteria were peak signal-to-noise ratio (PSNR), mean squared error (MSE) or L_2 loss, multiscale structural similarity index (MSSIM), and area FRC, independent of the loss function used during training (**Figure 4A**). In all cases, the network trained on the combination of both loss functions shows comparable or improved performance. The change of the FRC as function of frequency gives information on how different length scales or frequencies contribute to the improvement (**Figure 4B**). The FRC of predicted and ground truth image shows a shift to higher frequencies as well as a constant offset in the frequencies above the cut-off frequency in comparison to the FRC between input and target image. The quality of reconstructed filaments and image resolution is often measured by single line profiles perpendicular to filament direction, but this criterion is not objective. The tool LineProfiler was developed to provide an unbiased measure for filament image quality (Zwettler et al., 2020). We applied LineProfiler to reconstructions of simulated sparse microtubule filament images with predefined distances (**Figure 4C**). By defining the ability for resolving two filaments via the existence of two peaks and a minimum, and evaluation of 20 independent simulations, we obtained a resolution capability of 89.15 ± 2.61 nm.

DISCUSSION

We introduced a new loss function based on the area of the FRC for deep learning-based reconstruction of SMLM density estimates for microtubules from small subsets of localizations. Preprocessing of ground truth images by a novel anisotropic kernel density estimate improved the training process. The FRC loss ideally complements the multiscale structural similarity index (MSSIM) and leads to an improved reconstruction outcome. We implemented the adaptive anisotropic KDE proposed in (Chen et al., 2014) in pixel space using a defined support window and scale to calculate the covariance matrix. While being more efficient, the disadvantage of such an image-based implementation is the fixed window size, whereas in a localization-based algorithm also far away localizations would contribute to sparse regions, limiting the influence of isolated localizations. The principle behind anisotropic KDE calculated in image space is similar to anisotropic diffusion filtering, a widely used concept in image processing (Weickert 1996).

We used the area of the FRC, as described in (Preusser et al., 2021), up to a limit of 0.2 of the maximum frequency. Using the entire FRC area, the network learned to achieve correlation at high frequencies by blurring the image, but this did not improve image quality. Fixed FRC cut-off values like 1/7 (Robert P. J. Nieuwenhuizen et al., 2013) are problematic, as discussed in (Heel et al., 2005). When used as optimization target, the resulting FRC values are sometimes just above the threshold, leading to poor image quality and high background intensity. In general, FRC as image resolution metric must be used carefully since it can give biased results (Johnson et al., 2021).

As with many deep learning-based methods, the question is how much the generated images can be trusted, or if the network makes up information that is not in the original data. In principle, the information that is lost by removing a large fraction of the localizations cannot be regained, neither by applying deep learning nor by other reconstruction methods. In other words, there is no way to infer the precise location of emitters that were either never detected, or removed from the dataset. Instead, the idea behind density reconstruction from sparse localization data is to estimate the underlying density from a small sample of emitter positions. SMLM imaging in fact always involves such an estimate rather than measuring the true emitter density, since the latter would require perfect labeling efficiency and infinite measuring time. The benefit of density reconstruction by deep learning or other means is that it can use inherent redundancy in the localization data, thus reducing the number of required localizations while only minimally compromising the reconstruction quality. One could also argue that density estimation from localization point cloud data can be seen more as a segmentation task rather than denoising or deconvolution.

Although we demonstrate our approach only on microtubule filaments, the area-FRC loss is generally applicable, since FRC works also for other structures than filaments. The feasibility of NN-based SMLM reconstruction for a variety of structures was already demonstrated in (Ouyang et al., 2018). The absolute values of the FRC are however highly dependent on the frequency content of an image and thus on the imaged structures (Heel et al., 2005; Legant et al., 2016). Images with filaments (e.g., microtubules) yield a different FRC area or “resolution” compared to more continuous structures such as mitochondria, even when imaged with the same optical resolution. Nevertheless, using FRC area at low spatial frequencies as optimization target for improving the same image is possible, since only the change of the loss measure but not its absolute value is used as criterion.

For density reconstruction from sparse localization data, ANNA-PALM presented by Ouyang et al., (2018) presents the current state-of-the-art based on conditional generative adversarial networks, or cGANs. The original authors of the cGAN architecture (Isola et al., 2017) argue that cGANs are not suitable for image segmentation as they tend to hallucinate realistic-looking details to fool the discriminator. Ouyang et al. elegantly solve this problem by using a plausibility criterion where the consistency of the restored image with respect to a widefield low-resolution image is determined. Here, we did not use a cGAN, but a simpler architecture using only a generator U-Net, and focus on comparing the performance of different loss functions and preprocessing methods. We thus see this work as complementary to ANNA-PALM, and as basis for future extensions using new architectures. For example, the standard convolutional architecture could be modified to incorporate prior knowledge about the physical constraints of the measurement process. Introducing loss functions in Fourier space has recently been shown to make deep learning-based image reconstruction and perceptual superrsolution more efficient (Fuoli et al., 2021), and might have other interesting applications in the future. We make the python code of our training workflow and our implementation of the area FRC loss and the anisotropic kernel density estimation freely available to the community so that it can easily be integrated into other deep learning workflows.

DATA AVAILABILITY STATEMENT

The datasets presented in this study can be found in online repositories. The names of the repository/repositories and accession number(s) can be found below: https://github.com/CIA-CCTB/FRCnet.

AUTHOR CONTRIBUTIONS

PK, MS, PB, and AB designed the project, AB and PK developed the computational methods and analyzed data, AK acquired experimental data, SR and TP helped analyze data and develop computational methods, MS, PB, and PK supervised the project, AB, TP, and PK wrote the manuscript.

FUNDING

This project was funded by the German Research Foundation under the projects SFB/TR166 A04, KO 3715/5-1 and SA 829/19-1. Computational work was carried out using the High-Performance Computing Cloud “Julia” at Würzburg University (DFG project 327497565). This publication was supported by the Open Access Publication Fund of the University of Wuerzburg.

REFERENCES

Chen, K.-C. J., Yang, G., and Kovacevic, J. (Oct 2014). Spatial Density Estimation Based Segmentation of Super-resolution Localization Microscopy Images, 2014 IEEE International Conference on Image Processing. Paris, France, (ICIP), 867–871. doi:10.1109/ICIP.2014.7025174

Cohen, E. A. K., Abraham, A. V., Ramakrishnan, S., and Ober, R. J. (2019). Resolution Limit of Image Analysis Algorithms. *Nat. Commun.* 10 (1), 793. doi:10.1038/s41467-019-08689-x

Culley, S., Albrecht, D., Jacobs, C., Pereira, P. M., Leterrier, C., Mercer, J., et al. (2018). Quantitative Mapping and Minimization of Super-resolution Optical Imaging Artifacts. *Nat. Methods* 15 (4), 263–266. doi:10.1038/nmeth.4605

Descloux, A., Grußmayer, K. S., and Radenovic, A. (2019). Parameter-Free Image Resolution Estimation Based on Decorrelation Analysis. *Nat. Methods* 16 (9), 918–924. doi:10.1038/s41592-019-0515-7

Fuoli, Dario., Van Gool, Luc., and Radu, Timofte. (2021). *Fourier Space Losses for Efficient Perceptual Image Super-resolution*. Ithaca, NY: ArXiv:2106.00783 [Cs, Eess], June, Available at: http://arxiv.org/abs/2106.00783.

Hensen, U., Grubmüller, H., and Lange, O. F. (2009). Adaptive Anisotropic Kernels for Nonparametric Estimation of Absolute Configurational Entropies in High-Dimensional Configuration Spaces. *Physical Review. E, Statistical, Nonlinear, and Soft Matter Physics*. 80 (1), 011913. doi:10.1103/PhysRevE.80.011913

Isola, P., Zhu, J. Y., Zhou, T., and Efros, A. A., (July 2017). Image-to-Image Translation with Conditional Adversarial Networks, 2017 IEEE Conference on Computer Vision and Pattern Recognition. HI, USA, CVPR, 5967. 76. doi:10.1109/CVPR.2017.632

Johnson, E. K., Becker, S., Cogswell, C., Xing, J., and Chen, S. (2021). Limitations of Fourier Ring Correlation as an Image Resolution Metric. *Three-Dimensional Multidimensional Microsc. Image Acquisition Process*. XXVIII (11649), 1164909. doi:10.1117/12.2585852

Koho, S., Tortarolo, G., Castello, M., Deguchi, T., Diaspro, A., and Vicidomini, G. (2019). Fourier Ring Correlation Simplifies Image Restoration in Fluorescence Microscopy. *Nat. Commun.* 10 (1), 3103. doi:10.1038/s41467-019-11024-z

Legant, W. R., Shao, L., Grimm, J. B., Brown, T. A., Milkie, D. E., Avants, B. B., et al. (2016). High-Density Three-Dimensional Localization Microscopy across Large Volumes. *Nat. Methods* 13 (4), 359–365. doi:10.1038/nmeth.3797

Nehme, E., Weiss, L. E., Michaeli, T., and Shechtman, Y. (2018). Deep-STORM: Super-resolution Single-Molecule Microscopy by Deep Learning. *Optica* 5 (4), 458–464. doi:10.1364/OPTICA.5.000458

Nieuwenhuizen, R. P., Lidke, K. A., Bates, M., Daniela, L. P., Puig, D. L., Grünwald, D., et al. (2013). Measuring Image Resolution in Optical Nanoscopy. *Nat. Methods* 10 (6), 557–562. doi:10.1038/nmeth.2448

Nieuwenhuizen, R. P. J., Stallinga, S., and Rieger, B. (2014). Visualization and Resolution in Localization Microscopy. *Cell Membr. Nanodomains: Biochem. Nanoscopy*, 409–426. doi:10.1201/b17634-23

Ouyang, W., Aristov, A., Lelek, M., Hao, X., and Zimmer, C. (2018). Deep Learning Massively Accelerates Super-resolution Localization Microscopy. *Nat. Biotechnol.* 36 (5), 460–468. doi:10.1038/nbt.4106

Paul, T. J., and Kollmannsberger, P. (2020). Biological Network Growth in Complex Environments: A Computational Framework. *PLOS Computational Biology* 16 (11), e1008003. doi:10.1371/journal.pcbi.1008003

Preusser, F., dos Santos, N., Contzen, J., Stachelscheid, H., Costa, É. T., Mergenthaler, P., et al. (2021). FRC-QE: a Robust and Comparable 3D Microscopy Image Quality Metric for Cleared Organoids. *Bioinformatics* 37, 3088–3090. doi:10.1093/bioinformatics/btab160

Rees, E. J., Erdelyi, M., Pinotsi, D., Knight, A., Metcalf, D., and Kaminski, C. F. (2012). Blind Assessment of Localisation Microscope Image Resolution. *Opt. Nanoscopy* 1 (1), 12. doi:10.1186/2192-2853-1-12

Ronneberger, O., Fischer, P., and Brox, T. 2015. “U-net: Convolutional Networks for Biomedical Image Segmentation.” In *Medical Image Computing and Computer-Assisted Intervention – MICCAI 2015, Lecture Notes in Computer Science*, edited by N. Navab, J. Hornegger, W. M. Wells, and A. F. Frangi, 234–241. Springer International Publishing, New York,USA, .

Schnitzbauer, J., Strauss, M. T., Schlichthaerle, T., Schueder, F., and Jungmann, R. (2017). Super-Resolution Microscopy with DNA-PAINT. *Nat. Protoc.* 12 (6), 1198–1228. doi:10.1038/nprot.2017.024

Speiser, A., Lucas, R. M., Müller, L. R., Hoess, P., Matti, U., Obara, C. J., et al. (2021). Deep Learning Enables Fast and Dense Single-Molecule Localization with High Accuracy. *Nat. Methods* 18 (9), 1082–1090. doi:10.1038/s41592-021-01236-x

van de Linde, S., Löschberger, A., Klein, T., Heidbreder, M., Wolter, S., Heilemann, M., et al. (2011). Direct Stochastic Optical Reconstruction Microscopy with Standard Fluorescent Probes. *Nat. Protoc.* 6 (7), 991–1009. doi:10.1038/nprot.2011.336

van Heel, M., Schatz, M., and Schatz, Michael. (2005). Fourier Shell Correlation Threshold Criteria. *J. Struct. Biol.* 151 (3), 250–262. doi:10.1016/j.jsb.2005.05.009

Weickert, J. 1996. “Theoretical Foundations of Anisotropic Diffusion in Image Processing, 221, 236.” In *Theoretical Foundations of Computer Vision, Computing Supplement*, edited by W. Kropatsch, R. Klette, F. Solina, and R. Albrecht, 221–236. Vienna, Austria: Springer. doi:10.1007/978-3-7091-6586-7_13

Weigert, M., Schmidt, U., Boothe, T., Müller, A., Dibrov, A., Jain, A., et al. (2018). Content-Aware Image Restoration: Pushing the Limits of Fluorescence Microscopy. *Nat. Methods* 15 (12), 1090–1097. doi:10.1038/s41592-018-0216-7

Zelger, P., Kaser, K., Rossboth, B., Velas, L., Schütz, G. J., and Jesacher, A. (2018). Three-Dimensional Localization Microscopy Using Deep Learning. *Opt. Express* 26 (25), 33166–33179. doi:10.1364/OE.26.033166

Zhao, H., Gallo, O., Frosio, I., and Kautz, J. (2017). Loss Functions for Image Restoration with Neural Networks. *IEEE Trans. Comput. Imaging* 3 (1), 47–57. doi:10.1109/TCI.2016.2644865

Zwettler, F. U., Spindler, M.-C., Reinhard, S., Klein, T., Kurz, A., Benavente, R., et al. (2020). Marie-Christin Spindler, Sebastian Reinhard, Teresa Klein, Andreas Kurz, Ricardo Benavente, and Markus Sauer.Tracking Down the Molecular Architecture of the Synaptonemal Complex by Expansion Microscopy. *Nat. Commun.* 11 (1), 3222. doi:10.1038/s41467-020-17017-7

Conflict of Interest: The authors declare that the research was conducted in the absence of any commercial or financial relationships that could be construed as a potential conflict of interest.

frontiers in Bioinformatics

ORIGINAL RESEARCH
published: 18 October 2021
doi: 10.3389/fbinf.2021.724127

K-Neighbourhood Analysis: A Method for Understanding SMLM Images as Compositions of Local Neighbourhoods

Kristen Feher[1,2]*, Matthew S. Graus[1,2], Simao Coelho[1,2,3], Megan V. Farrell[1,2], Jesse Goyette[1,2]* and Katharina Gaus[1,2†]

[1]School of Medical Sciences, EMBL Australia Node in Single Molecule Science, University of New South Wales, Kensington, NSW, Australia, [2]ARC Centre of Excellence in Advanced Molecular Imaging, University of New South Wales, Sydney, NSW, Australia, [3]Structural Biology Program, Memorial Sloan Kettering Cancer Center, New York, NY, United States

OPEN ACCESS

Edited by:
Christian Franke,
Friedrich Schiller University Jena,
Germany

Reviewed by:
Philip Kollmannsberger,
University of Würzburg, Germany
Thanh-an Pham,
École Polytechnique Fédérale de
Lausanne, Switzerland

***Correspondence:**
Kristen Feher
k.feher@unsw.edu.au
Jesse Goyette
j.goyette@unsw.edu.au

†Deceased

Specialty section:
This article was submitted to
Computational BioImaging,
a section of the journal
Frontiers in Bioinformatics

Received: 12 June 2021
Accepted: 04 October 2021
Published: 18 October 2021

Citation:
Feher K, Graus MS, Coelho S,
Farrell MV, Goyette J and Gaus K
(2021) K-Neighbourhood Analysis: A
Method for Understanding SMLM
Images as Compositions of
Local Neighbourhoods.
Front. Bioinform. 1:724127.
doi: 10.3389/fbinf.2021.724127

Single molecule localisation microscopy (SMLM) is a powerful tool that has revealed the spatial arrangement of cell surface signalling proteins, producing data of enormous complexity. The complexity is partly driven by the convolution of technical and biological signal components, and partly by the challenge of pooling information across many distinct cells. To address these two particular challenges, we have devised a novel algorithm called K-neighbourhood analysis (KNA), which emphasises the fact that each image can also be viewed as a composition of local neighbourhoods. KNA is based on a novel transformation, spatial neighbourhood principal component analysis (SNPCA), which is defined by the PCA of the normalised *K*-nearest neighbour vectors of a spatially random point pattern. Here, we use KNA to define a novel visualisation of individual images, to compare within and between groups of images and to investigate the preferential patterns of phosphorylation. This methodology is also highly flexible and can be used to augment existing clustering methods by providing clustering diagnostics as well as revealing substructure within microclusters. In summary, we have presented a highly flexible analysis tool that presents new conceptual possibilities in the analysis of SMLM images.

Keywords: TCR clustering, single molecule localisation microscopy, image analysis, point pattern analysis, clustering, local density estimation, local indicators of spatial association

INTRODUCTION

SMLM has given insight into the spatial arrangement of signalling proteins with unprecedented resolution (Huang et al., 2009; Patterson et al., 2010; Nicovich et al., 2017; Schnitzbauer et al., 2017). The complex spatial arrangement of these proteins is an emergent property of interactions between many types of proteins, and reflect the external environment that is being sensed, as well as being dependent on prior states of the cell (Ditlev et al., 2018; Yoo et al., 2019; Espinosa et al., 2020). Being a snapshot of a dynamic process, it can be expected that the image will contain a mixture of spatially localised subprocesses that coexist side by side. Similar processes that are spatially separated may not be exactly temporally synchronised. For example, protein clustering, i.e., transition away from well mixed homogenous states towards droplets/condensates and beyond, is dynamic and may be at different stages of progress in different parts of the cell, or even within larger condensates. While genetically identical cells grown under the same conditions will result in unique and random instantiations, it could be expected that they are linked by universal properties, e.g., distribution of cluster sizes or distribution of distances between clusters.

Within the field of T cell activation, SMLM imaging has made a large impact on our understanding of the underlying processes. It is now well established that spatial organisation of T cell receptor (TCR) in the plasma membrane determines the probability of phosphorylation and downstream signalling processes (Grakoui et al., 1999; Pageon et al., 2016a; Sherman et al., 2016). As proteins that reside in the same regions in the plasma membrane are more likely to interact, it is important to map and better understand the organizing principles of membrane proteins (Saka et al., 2014). For example, chimeric antigen receptors (CARs) need to integrate into the T cell signalling network (Lim and June 2017) and therefore ought to adopt a spatial organisation similar to that of the TCR. However, quantifying the diversity in spatial organisations that a single protein can adopt within and across individual cells has remained challenging. The TCR, for example, has been described as randomly distributed (Rossboth et al., 2018), monomeric (James et al., 2007) or as a functional dimer (Kuhns et al., 2010), to form pre-existing (Sherman et al., 2011) (Schamel et al., 2005; Kumar et al., 2011) and antigen-induced clusters (Kumar et al., 2011; Pageon et al., 2016a; Boniface et al., 1998), which can reside in large, immobile protein islands (Lillemeier et al., 2010; Drbal et al., 2007; Purbhoo et al., 2010).

The mode of imaging adds a further layer of complexity, as the molecules are not directly observed. When individual molecules are not spatially resolvable due to the diffraction limit, sparsity is induced in both space and time by stochastic photoactivation or binding of fluorescent probes that generate localisations. Localisations are points in $\mathbb{R}^2$ (for 2D imaging, or $\mathbb{R}^3$ for 3D imaging), and a set of localisations over a small area is evidence for the existence of a molecule. In real images, it is virtually impossible to attribute localisations to specific molecular numbers and positions with high confidence (Feher et al., 2019). Molecules may be tightly packed and thus sets of localisations arising from multiple molecules may be spatially overlapping, dependent on instrument precision. Labelling efficiency and stochastic blinking effects induce a fundamental limitation in molecular counting at individual protein sites. It is possible to estimate the underlying molecular positions by collapsing repeated localisations in a procedure called "grouping" but this can introduce new artefacts due to the afore-mentioned reasons.

Overall, it can be expected that SMLM images of cells have a complex multiscale structure, generated by convoluting biological with technical effects and overlaid with spurious noise localisations. For any given localisation, the spatial arrangement of the immediately neighbouring localisations is dominated by the photophysics and the distance of the nearest neighbouring molecule. The spatial arrangement of more distant localisations is influenced by the emergent properties of many interacting proteins. To date, SMLM images of one or two protein types are possible, but technical advances in simultaneously imaging multiple protein types are underway. The broad goal of SMLM data analysis is to extract instances or types of protein arrangements and link it to biological function. Examples include droplet size and composition, indicating previous recruitment of proteins to the site; or proximity of proteins types to each other, indicating the possibility or otherwise of biochemical reactions taking place.

General approaches to analysing point pattern data often involve clustering or density estimation. Examples within SMLM data analysis include Ripley's K-function (Owen et al., 2010), pair correlation (Sengupta et al., 2013; Shivanandan et al., 2016), density-based clustering (Pageon et al., 2016a; Jiang et al., 2017; Rubin-Delanchy et al., 2015) or tessellation based analysis (Levet et al., 2015). Clustering is most straightforward when spacing between clusters (inter-cluster) dominates the spacing between points within the cluster (intra-cluster) in all instances, and there are no noise points between the clusters. In this case, a single unambiguous clustering can generally be found. As intra-cluster spacing grows with respect to inter-cluster spacing and background noise increases, multiple cluster organisations could be obtained depending on the chosen optimisation criteria (Liu et al., 2015; Maurus and Plant, 2016). On the other hand, density estimates are highly dependent on the chosen bandwidth (Davies and Baddeley, 2018), and thus multiple bandwidths may be needed to fully describe multiscale structure. As density is an average quantity within a window, it can be problematic to describe discontinuous events, e.g., a small cluster surrounded by a relatively large empty space.

Bridging the gap between clustering and density estimation are local indicators of spatial association (LISA) methods (Anselin, 1995). They represent the contribution of each point to a global spatial statistic, reflecting local spatial arrangements. For example, Ripley's K-function can be decomposed into local K-functions for each localisation. Other methods aim to deconvolute the superposition of two independent point patterns (Byers and Raftery, 1998; Cressie and Collins, 2001; Redenbach et al., 2015). In this work, we describe a novel LISA-like method of characterising SMLM images that is based on a vector of nearest neighbour distances corresponding to each localisation in the image. In more detail, our work extends ideas in Byers & Raftery (Byers and Raftery, 1998), by considering the joint distribution of *K*th nearest neighbour (NN) distances (NND) for $K = 1 \ldots 100$. This leads us to consider SMLM localisations as points in a multivariate coordinate system defined by the NNDs for each *K*, so that we can aggregate localisations with similar properties, in a manner analogous to that of Cressie and Collins (2001). However, instead of using local K-functions which requires the scale to be fixed, the NND vectors can probe the local topology of each localisation, regardless of that localisation's local density (*K*-neighbourhood analysis).

While clustering will remain central to SMLM data analysis, we aim to expand the conceptual possibilities in a manner that does not require explicit spatial segmentation *via* clustering. Instead, we wish to view each image as a collection of local neighbourhoods and use this concept to dissect individual images and compare between entire images with minimal assumptions. This will facilitate novel visualisations of SMLM images, comparisons amongst sets of SMLM images and provide a rational framework to find associations between the spatial structures of different types of proteins. This novel method can be performed on the entire set of localisations, thereby avoiding any artefacts introduced by grouping.

The major contribution of this paper is the Spatial Neighbourhood PCA (SNPCA). This is a transformation that is derived from the normalised nearest neighbour distance vectors of each point in a spatially random point pattern, using the first K neighbours. This basis can be used to compress the K-nearest neighbour vectors of an arbitrary point pattern and compare the neighbourhood compositions between sets of arbitrary point patterns. The properties of SNPCA are investigated using simulated point patterns to show it can capture structural nuances that are not apparent with univariate measures such as local density. The SNPCA is then used to develop a novel visualisation technique for individual SMLM images. Next, a set of SMLM images of activated T cells are analysed to demonstrate the global differences of the CD3 spatial patterns that occur between different types of cells. Finally, these results are used for a downstream analysis of CD3 phosphorylation patterns.

MATERIALS AND METHODS

Cell Culture

Jurkat-ILA1 T cells and Jurkat 76T cells were cultured in RPMI 1640 (Life Technologies, 21870076) supplemented with 10% FBS, 2 mMl-glutamine, 1 mM penicillin and streptomycin (all from Life Technologies). Characterization of the ILA1 TCR is described in the methods section of Pageon et al. (Pageon et al., 2016b). Jurkat 76 cells were transduced to express either LaG17-CD3ζ or LaG17-CD28-CD3ζ CAR construct.

Constructs

Lentiviral anti-GFP CAR constructs were produced and transduced into Jurkat 76 cells as described in Denham et al (Denham et al., 2019). We used Jurkat 76 cells since these cells lack surface expression of the TCR complex and thus anti-CD3ζ staining was specific for CAR constructs. For bacterial expression of CAR ligand, a construct of an N-terminally Avitag-labelled monovalent (A206K mutant), dark (Y66S mutant) EGFP (Avi-dGFP) was cloned into pTRC-HisA between the NheI and HindIII restriction sites. For the PI3K PAINT probe, amino acids 322–724 (constituting the tandem Src homology two domains) of the regulatory subunit, p85, with M479S, I493S, Y504S, Y508S hydrophobic to hydrophilic mutations of residues in the interface with the catalytic domain were fused with mNeon Green on C-terminus and cloned into pET21 between the NdeI and NotI restriction sites (p85 tSH2-mNG).

CAR Ligand and PI3K PAINT Probe Production

Chemically competent BL21 (DE3) *E. coli* cells (Agilent Technologies) were transformed with Avi-dGFP or p85 tSH2-mNG and grown on ampicillin (50 µg/ml) LB agar plates overnight at 37°C. The following day an individual colony was inoculated into LB media with 50 µg/ml ampicillin and grown in a shaker incubator overnight at 37°C. Ten ml of this starter culture was then inoculated into 1 L of LB media and the cells were grown in a shaker incubator at 37°C until the optical density at 600 nm was 0.6. The temperature in then decreased to 18°C and IPTG to 0.5 mM was added. For Avi-GFP biotin to 20 µM (to drive biotinylation of the Avitag) was added to the culture media. The protein was left to induce overnight, after which the cells were pelleted by centrifugation and stored at −80°C until protein extraction and purification was performed. Protein was extracted by thawing cells, resuspending in 50 mM NaH_2PO_4, 300 mM NaCl pH 7.5 (2×PBS), sonicating, and pelleting debris by centrifugation at 15,000 rcf for 15 min. The clarified lysate was passed through 2 ml Nickel-NTA agarose resin in a gravity-fed column, which was then washed with 10 column volumes of 2×PBS, then with 10 ml of 2×PBS with 10 mm imidazole. Proteins were eluted with 150 mM imidazole pH 7.5. Eluate was concentrated to 0.5 ml with a 30 kDa spin concentrator (Amicon) and a final polishing step of size exclusion chromatography on a HiPrep 16/60 Sephacryl S-200 HR (GE Healthcare) equilibrated in PBS with 1 mM DTT was performed. Purified protein was mixed with glycerol to a final concentration of 10% (v/v) and aliquots were frozen at −80°C until used.

Bilayer Preparation

Glass coverslips were cleaned with 1M KOH, rinsed in MilliQ water, and then placed in 100% ethanol prior to plasma cleaning. Eight-well silicone chambers (Ibidi, 80841) were then attached to the plasma cleaned coverslip. A 1 mg/ml liposome solution with a lipid ratio of 96.5% DOPC (1,2-dioleoyl-*sn*-glycero-3-phosphocholine), 2% DGS-NTA(Ni) (1,2-dioleoyl-*sn*-glycero-3-{[N-(5-amino-1-carboxypentyl)iminodiacetic acid]succinyl} (nickel salt)), 1% Biotinyl-Cap-PE [1,2-dioleoyl-*sn*-glycero-3-phosphoethanolamine-N-(cap biotinyl) (sodium salt)], and 0.5% PEG5000-PE {1,2-distearoyl-*sn*-glycero-3-phosphoethanolamine-N-[methoxy (polyethylene glycol)-5000]} (ammonium salt) (mol%; all available from Avanti Polar Lipids (DOPC, 850375C) [DGS-NTA(Ni), 790404C] (Biotinyl-Cap-PE, 870273C), (PEG5000-PE, 880220C) was created by vesicle extrusion, as described previously (Beemiller et al., 2012). The lipid solution was added to each well at a 1:5 ratio with MilliQ water along with 10 mM of $CaCl_2$ for 15 min and then washed three times with phosphate-buffered saline (PBS). 0.5 mM EDTA in MilliQ water was added to remove the excess $CaCl_2$ followed by washing with PBS. 1 mM of $NiCl_2$ in PBS was added for 15 min to recharge the NTA groups, then surfaces washed three times with PBS. Disruption of the lipid bilayer was avoided by maintaining 100–150 µl of PBS in the wells at all times.

To decorate the bilayer with proteins, 100 µg/ml of streptavidin (Life Technologies, SNN1001) and 200 ng/ml of His-tagged ICAM-1 (Thermo Fisher Scientific, 10346H08H50) were combined in PBS and added to the well for 15 min at room temperature and then washed with PBS. Biotinylated proteins were then combined with 5% BSA/PBS and added to each well for 30 min at room temperature; for Jurkat-ILA cells 1:500 dilution of pMHC 3G (from a 1 mg/ml stock) was used and for CAR-expressing Jurkat 76 cells 10 nM of dark GFP and 90 nM of dark mCherry were combined prior to being added to the bilayer. The wells are then washed with PBS to remove any unbound proteins.

Antibody Conjugation

CF568-succinimidyl-ester (Biotium, 92131) was conjugated to soluble pCD3ζ (pY142) antibody (BD Pharmingen, 558402). CF568-succinimidyl-ester and the antibody were mixed at a 6: 1 molecular at pH 8.0 for 1 h at room temperature in the dark. The antibody was purified by using Zeba desalting columns (Thermo Fisher Scientific, 89883). Absorption spectroscopy determined that the degree of labelling was 1.5:1 dye: antibody ratio.

T Cell Activation on Bilayer and Immunostaining

The wells containing bilayers were washed with RPMI culture media and warmed to 37°C for 30 min prior to adding the cells. Cells were added to the bilayer at a density of 250,000 cells/well for 4–5 min at 37°C and fixed using 4% PFA in PBS warmed to 37°C. Fixation of cells was done for 15 min at 37°C. Prior to immunostaining, cells were permeabilized with Triton X-100 (Sigma-Aldrich, T8787) at 0.1% for 5 min at room temperature and washed with PBS. The cells were blocked with 5% BSA in PBS for 1 h at room temperature.

Staining of the cells was performed sequentially with primary labelled antibodies against l CD3ζ conjugated to Alexa Flour 647 (Abcam, 197037) and pCD3ζ (pY142) conjugated to CF568. Staining was done in 5% BSA in PBS at a concentration of 10 μg/ml for both antibodies for 30 min at room temperature in the dark, then washed with PBS. Fiducials in the form of TetraSpeck Microspheres (Thermo Fisher Scientific, T7279) were added to each well for 15 min then washed with PBS.

dSTORM and PAINT Imaging

For dSTORM imaging, a buffer consisting of 50 mM Tris, 10% (wt/vol) glucose, 10 mM NaCl, 20 μg/ml catalase (Sigma-Aldrich, C100), 0.8 mg/ml glucose oxidase (Sigma-Aldrich, G2133), and 30 mM cysteamine (Sigma-Aldrich, 30070), pH 8.0 was used during data acquisition. Data was acquired on a Zeiss ELYRA microscope with TIRF illumination using a ×100 oil-immersion objective (NA = 1.46) coupled to a cooled, electron-multiplying charge-coupled device camera (Andor, iXon DU-897). Sample excitation was done with 637 nm laser and 561 nm laser. For single channel acquisitions 20,000 frames were collected at an exposure time of 33 ms. Sequential imaging of the fluorescent probes was performed to acquire two-channel data with the farther red channel acquired first. For each channel, 20,000 frames were collected with an exposure time of 33 ms. Drift correction and channel alignment algorithms were performed on the raw data to produce data tables containing x-y localization coordinates using Zen 2012 SP5 (Zeiss MicroImaging).

PBS buffer containing 1% (wt/vol) BSA, 0.1% (wt/vol) saponin, 1 mM DTT and 1 mM EDTA was used for the preparation and imaging of the PI3K probe. PAINT imaging was performed by adding 600 pM of the PI3K-mNeonGreen probe to the well and exciting with 488 nm laser in TIRF mode. For each cell, 10,000 frames were collected with an exposure time of 200 ms. Raw image stacks were fitted for molecular localisations and drift corrected using the "Picasso" software package (Schnitzbauer et al., 2017).

DNA origami rulers. A single well of an eight-well chamber (ibidi 80841) was attached to a clean coverslip and washed with 500 μl of PBS. The well was incubated with 200 μl of BSA-biotin solution (1 mg/ml in PBS) for 5 min. Excess BSA-biotin was removed by washing with 500 μl of PBS. The surface was incubated with 200 μl of neutravidin (1 mg/ml in PBS) for 5 min and washed with a PBS with 10 mM magnesium. Biotin-coated polystyrene beads (Spherotech, TP-305) (40 μg/ml) were incubated for 1 h and the excess beads were removed. The well was incubated with the DNA-origami ruler (GATTA-PAINT, HiRes 20R or 80R) diluted 40 times in PBS with 10 mM magnesium to get ~100 rulers per field-of-view. Excess DNA origamis were removed by washing with PBS with 10 mM magnesium. The imaging strand was a 9-bp complementary target strand with Atto 655, with a concentration of 5 nM. Acquisition was performed as previously described by Coelho et al., 2020 (Coelho et al., 2020).

Statistical Description of Localisations

Let there be N localisations in a region of interest (ROI), and each localisation is indexed by i with $1 \leq i \leq N$. In order to describe each localisation i *via* its local topology, i.e., the spatial arrangement of its neighbouring localisations, the distance D_{ij} from the ith localisation to its jth nearest neighbour (NN) is calculated for $1 \leq j \leq K$. Thus localisation i is described by a K-dimensional nearest neighbour vector $NNV_i = (D_{i1}, \ldots, D_{ij}, \ldots, D_{iK})$ (K-neighbourhood).

Choice of *K*

The parameter K is chosen to be larger than the number of localisations arising from a single molecule. However, the K-neighbourhood analysis is quite robust over a range of K values. Within large aggregates of molecules (e.g., microclusters), K-neighbourhoods may appear to be spatially random because the edge of the cluster has not been reached. To understand how the K-neighbourhoods are related to long-range structure, we examined the NNDs for $K = 200, 500$.

Comparison of Image Localisations to Spatially Random Localisations

The expected value of D_{ij} under complete spatial randomness is $\alpha\sqrt{j}$ where α is a constant that accounts for the rate of the Poisson process, i.e., the density of localisations (Thompson, 1956). To examine a localisation's topology independently of scale, we set $\alpha = 1/\sqrt{K}$ and normalised NNV_i to yield $nNNV_i = NNV_i/D_{iK}$ such that $nNNV_i$ falls on the interval (0, 1). Additionally, the $nNNV_i$s of a ROI collectively forms the rows of a table of dimension $N \times K$, which we named NN feature table (NNFT). The NNFT is an abstract description of a ROI.

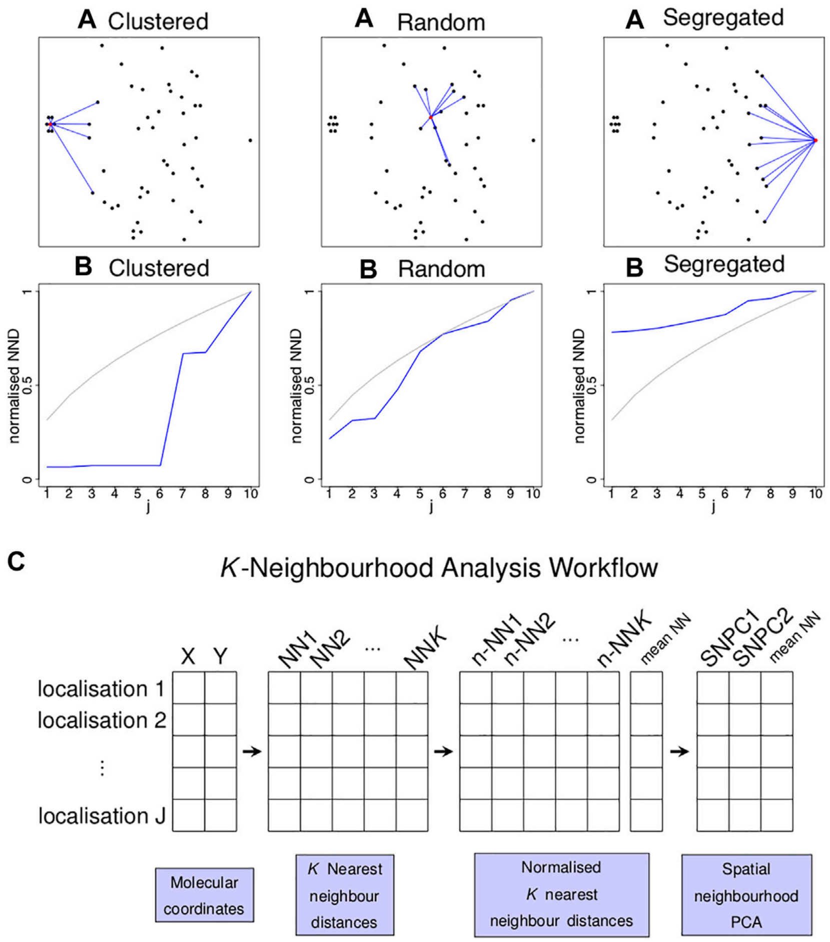

FIGURE 1 | Concept of k nearest neighbour distances to identify localised spatial organisations for each point in an image. **(A)** Three examples of a single point (highlighted in red) residing in a cluster of six points **(left)**, random point distribution **(middle)** and segregated from other points **(left)** and its $K = 10$ nearest neighbours (blue lines). **(B)** Plots of the normalised distance from the red localisation to the jth nearest neighbour (y-axis) against j (x-axis) for the examples above (blue lines) and for completely spatially random (CSR) data (grey lines). Each of the three scenarios shown in **(A)** gives rise to a characteristic curve in **(B)**. **(C)** Schematic diagram illustrating the workflow of the K-Neighbourhood Analysis.

Principal Component Analysis (PCA) of the Nearest Neighbour Feature Table (NNFT)

Localisation i can be viewed as a point in $\mathbb{R}^K$ *via* NNV_i. To summarise the major features of the NNFT (**Figure 1**), dimension reduction is needed. Principal component analysis (PCA) could performed on individual NNFTs to yield a new orthonormal basis corresponding to the directions of largest variance. However, each PCA will yield a different basis, reflecting the individual properties of each NNFT, rendering comparisons between images or cellular conditions impossible. To generate a universal basis for any NNFT, we simulated 100,000 completely spatial random (CSR) points with a two-dimensional Poisson process on the unit square with intensity $\lambda = 10^5$. For each simulated point, the $nNNV_i$ was calculated, the edge points discarded, the NNFT mean-centred and the PCA calculated. For a NNFT arising from an experimental ROI, each localisation can be represented by the orthogonal projection of its $nNNV_i$ on the first two principal components of the CSR PCA, yielding new coordinates ($PC1_i$, $PC2_i$).

Local Density

In each K-neighbourhood, localisation density is defined as $Den_i = (K/2)/(\pi \bar{D}_i^2)$, with $\bar{D}_i = (1/K)\sum_j D_{ij}$ (i.e., the mean NND). Den_i is plotted on a logarithmic scale.

Comparison of Images and Standardised Frequency Table

A group of localisations in a single image can be represented by an $N \times 3$ table with the ith row defined (Den_i, $PC1_i$, $PC2_i$). To make comparisons between images, we compared the joint density of these three parameters. To do this, we binned each parameter into equally sized intervals, with the intervals being fixed for all images. To construct the bins, for each parameter the combined range over all images was determined. The range was then split into 50 equal sized bins, and the 1-dimensional bins were merged to form a 3-dimensional grid composed of 3-dimensional bins. Finally, the localisations were counted in each 3-dimensional bin, and the bins are clustered using average linkage hierarchical clustering (Ward, 1963) to yield a small number of 3-dimensional bin subsets (termed "groups") that correspond to a colour key. When performed on an ensemble of images, a frequency table was obtained, with each row being one image and each column corresponding to the total frequency of localisations falling in a group of 3-dimensional bins. The frequency table is compositional, i.e., rows sum to one, so log ratio analysis is performed for dimension reduction (Aitchison and Greenacre, 2002). This entails log transformation followed by mean-centering, then principal component analysis (PCA) on the column centred matrix. To facilitate visualisation of the three categories, between component analysis is performed on the dimension reduced table, which is the PCA on the experimental means of the 3 cell types followed by the projection of the individuals onto the found space (Thioulouse, 2011). The table can also be visualised as a heatmap (Gu et al., 2016). To test for differences in variance between the experimental groups, the procedure in Anderson (Anderson, 2006) is used. To test for differences in multivariate means between the experimental groups, the procedure in Ellis et al. (Burchett et al., 2017) is used.

Simulations

Point patterns were simulated to investigate the performance of *K*-neighbourhood analysis. Spatially random cluster centres were simulated using a Poisson process. They were populated with localisations by randomly selecting the localisation count C on an interval, and drawing C points from a bivariate normal distribution with a fixed variance and zero correlation. Finally, the simulated image is overlaid with spatially random noise localisations that are simulated with a Poisson process.

Phosphorylation Enrichment Score

To calculate a spatially dependent phosphorylation enrichment score, each CD3ζ localisation in an image is scored TRUE or FALSE according to whether it is within 10 nm of a pCD3ζ localisation (co-localised CD3ζ localisation). For each localisation group indexed by k (here $1 \leq k \leq 9$), the frequency of localisations in k that also score TRUE is compared to the frequency of all localisations in k such that $Enrichment = \log[Freq(k \text{ AND TRUE})/Freq(k)]$. When $Enrichment > 0$, phosphorylation is overrepresented among localisations in k and when $Enrichment < 0$, phosphorylation in underrepresented among localisations in k. Differences of multivariate enrichment scores between experimental groups are tested as described above in "Comparison between images." The enrichment score is additionally plotted for thresholds of 10, 20, 30, 500 nm. To understand whether enrichment scores are significantly different from zero, random scores are simulated as follows: For each image, if there are n_p co-localised CD3ζ localisations, then a random vector is drawn from a multinomial distribution characterised by the CD3ζ frequency vector of that image and n_p, the random vector is normalised to sum to one, and an enrichment score is calculated. This is repeated 10,000 times, and the 5 and 95th percentiles of the simulated random scores are obtained. After repeating for each image, the minimum and maximum (respectively) scores over all images are reported and plotted.

RESULTS

In order to characterise the neighbourhood of any point in a point pattern (a point pattern here is defined as a set of points in $\mathbb{R}^2$), the vector of the first K nearest neighbour (NN) distances is considered. The normalised NN (n-NN) distances can be plotted as a curve vs the index j (for $1 \leq j \leq K$) (**Figure 1**). Independently of the magnitude of the NN distances, the shape of this n-NN curve is related to the spatial organisation of neighbouring points. The n-NN curve can be compressed using a principal component analysis (PCA) that is defined using n-NN curves arising from spatially random data (SNPCA), meaning that different point patterns can be expressed using a set of common basis vectors and compared directly. The algorithm takes a point pattern and K as input, calculates a n-NN curve for each point and transforms it using the SNPCA. Two components have been shown to be sufficient for SNPCA (**Supplementary Figures 1–3**). For completeness, the mean NN value can also be stored along with the two components, so that information about the NN magnitude is available. For ease of interpretation, the mean NN value can be converted to a density. The algorithm is referred to as *K*-neighbourhood analysis (KNA).

The properties of the KNA are investigated using simulated point patterns that mimic an SMLM image of spatially random binding sites (**Figure 2A**). First, the region of interest (ROI) is populated with molecules using a Poisson process of a given intensity. Next, each molecule is replaced with clusters of localisations generated from a bivariate normal distribution (fixed variance in x and y, and correlation coefficient of zero), with the number N of localisations being uniformly distributed between 10 and 90. Finally, spurious background localisations are generated using a Poisson process of a given intensity. For each localisation associated with a "parent" molecule (signal localisations), its local neighbourhood is strongly influenced by the total number N_{clus} of localisations associated with the parent molecule, the distance D_B to the parent molecule, and the distance D_{BNN} from its parent molecule to the neighbouring molecule. For noise localisations, its local neighbourhood is strongly influenced by the distance D_B to the nearest molecule. Further properties such as distance to the second neighbouring molecule also influence local neighbourhoods but they are not considered here.

These three quantities are plotted against kernel density estimates (adaptive smoothing using a Gaussian kernel) calculated at each point, for two different bandwidths (**Figures 2B,C**). For signal localisations, there are negative and positive trends (resp.) with D_{BNN} and N_{clus}. However, there are two separate trends with D_N, with density estimates occuring in the same range for signal and some noise localisations. While this differentiation can be improved by lowering the bandwidth, it

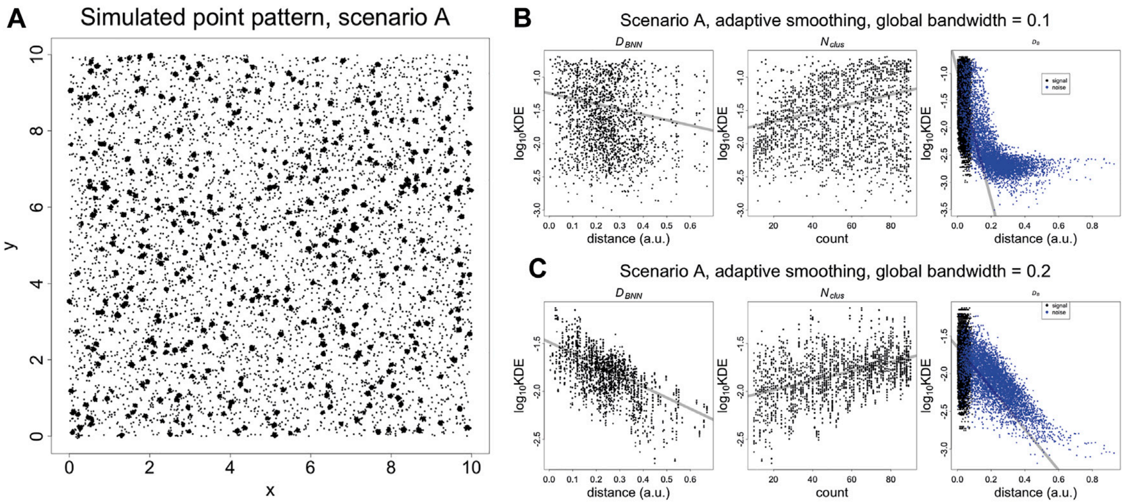

FIGURE 2 | (A) Simulated SMLM image of spatially random molecules. Molecules are generated using a Poisson process with intensity of five over a square window with sides of length 10 (arbitrary units). The molecules are replaced with clusters of localisations, generated with a bivariate normal distribution with variance of 0.000625 and covariance of zero. The number of localisations per cluster is an integer randomly sampled on the interval (10, 90). Finally, the noise localisations are generated using a Poisson process with intensity of 50. D_B, D_{BNN}, N_{clus} plotted vs Kernel Density Estimates (KDE). **(B)** KDE (adaptive smoothing) of **Figure 4** fitted with a global bandwidth of 0.1. **(C)** KDE (adaptive smoothing) of **Figure 4** fitted with a global bandwidth of 0.2. At low values of the bandwidth, it is possible to differentiate between signal and noise localisations but the trend with D_{BNN} and N_{clus} becomes less clear. At a higher value of the bandwidth, the trend D_{BNN} and N_{clus} becomes clear but it is no longer possible to differentiate between signal and noise localisations. This highlights that a KDE at using a single bandwidth is not adequate to capture the entire spatial structure. Trend lines are fitted with a linear model and are supplied for visualisation purposes.

indicates that a single univariate parameter such as density cannot capture the nuance of coexisting spatial arrangements. A similar phenomenon occurs when plotting nearest neighbour distances for individual values of K (**Supplementary Figure 4**).

The KNA of the same simulated dataset is carried out, and the first two components are converted to polar coordinates r and θ relative to the origin of the axes. There is a trend between D_{BNN} and r, showing that D_{BNN} has radial dependence, and the slope of this trend also depends on N_{clus} (**Figures 3A,B**). There is a trend between N_{clus} and θ, showing that N_{clus} has an angular dependence, and this effect is strongest for clusters that are further from other clusters (as clusters in close proximity to each other start to resemble larger aggregates) (**Figures 3C,D**). Noise localisations occupy a distinct angular region in relation to signal localisations (**Supplementary Figure 5**). For localisations belonging to the same cluster, those closer to the parent molecule have a lower value of SNPC1 than those farther from the parent molecule, i.e., there is a local trend between D_B and SNPC1. Noise localisations generally have higher values of SNPC1 than signal localisations (**Figure 3E**). While these trends have been evaluated separately, they are in fact linked and jointly contribute to each localisation's local neighbourhood. Other aspects of structure such as distance to the second nearest binding site have not been considered, but they will also potentially contribute to each local neighbourhood. Finally, as the density of noise localisations increases (**Supplementary Figures 6–7**), it will cause an apparent increase in the counts per cluster, and cause low count clusters to be indistinguishable from noise localisations. For this reason, meaningful comparisons can only be made between images acquired under the same imaging conditions, unless batch effects are being assessed.

Because the SNPCA is fixed, any point in the SNPC1-SNPC2 plane will always correspond to a fixed normalised NN curve, but interpretation of the process it arises from requires careful consideration of the context. For example, consider two different scenarios with different densities of noise. In scenario A (**Figure 3**), the density is low, and so the noise localisations in fact appear to be segregated. In other words, the definition of noise arises due to the fact they do not carry biological signal but they are not spatially random within their neighbourhoods due to positioning of surrounding clusters. In contrast, the noise points in scenario D (**Supplementary Figures 6–7**) are much denser and so their neighbourhoods have a larger tendency towards being spatially random. Correspondingly, their SNPC1 and SNPC2 values have decreased compared to scenario A.

Having tested KNA on simulated data we then applied it to a DNA PAINT image of DNA origami rulers. This image is composed of localisations corresponding to a single type of structure randomly scattered over the ROI (**Supplementary Figure 8A**). As this image has low complexity, the image components can easily be gated in a plot of mean NN distance and SNPC1 (**Supplementary Figure 8B**). The gated components correspond to specific structures in the image (**Supplementary Figures 8C,D**). The KNA of an image can also be used to assess parameter choice when clustering, e.g., with DBSCAN (**Supplementary Figure 9**). Here, this assessment demonstrates that it is hard to find a parameter choice that perfectly captures all localisations belonging to the rulers while

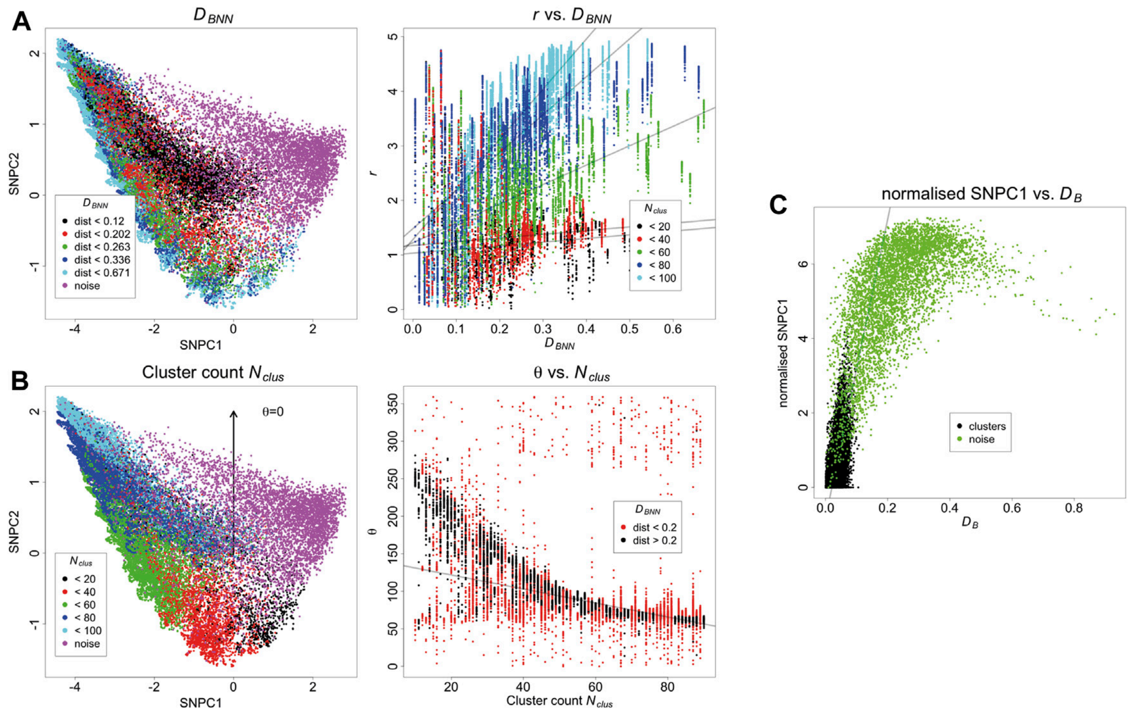

FIGURE 3 | (A) Relationship between SNPCA and D_{BNN}. D_{BNN} has a positive trend with r, and this effect is strongest for larger clusters. Trend lines are fitted with robust linear models and are supplied for visualisation purposes. **(B)** Relationship between SNPCA and cluster count N_{clus}. N_{clus} has an angular dependence within the SNPCA. The relationship is strongest for well separated binding sites otherwise individual clusters appear to be larger aggregates. Trend lines are fitted with robust linear models and are supplied for visualisation purposes. **(C)** Relationship of D_B with SNPCA. After normalising SNPC1 to the smallest value in each cluster, it has a positive trend with D_B. Trend lines are fitted with robust linear models and are supplied for visualisation purposes.

rejecting other localisations. Next, KNA is applied to a T cell image stained with a PAINT probe for phosphoinositide 3-kinase (PI3K) binding sites (**Figure 4**). The structure in the localisation pattern can be visualised by creating a colour key (hue) for each localisation that corresponds to θ which is performed at $K = 100$. The colour key is selected such that blue/violet lines up with the largest clusters, and yellow/green lines up with noise localisations, creating an obvious contrast. The visualisation could be further extended by introducing a saturation or value corresponding to r, but in practice it became visually confusing.

The power of this method is being able to express unique images in a fixed basis which facilitates direct comparison amongst a set of images. This opens up new concepts in SMLM image analysis such as being able to define variance in a set of images, or defining differences between different sets of images. To do this, KNA is performed on each image of the set, and SNPC1, SNPC2 and mean NN distance are retained. A fixed grid is defined in $\mathbb{R}^3$ (with sets of parallel planes) and the data is binned (**Figures 5A,B**). The number of points in each bin are counted and the grid is unfolded to yield a frequency vector. Thus each image is now represented by a frequency vector and multivariate statistics can be applied to the set of images. A set of 11T cells images are compared with 13 first generation chimeric antigen receptor (first gen CAR) images and 13 2nd gen CAR images by performing correspondence analysis (CA) on the frequency matrix (columns are first filtered such that all bins are occupied in all images) (**Figure 6**). While there is overlap between the different sets, they are significantly different from each other. Furthermore, the two CAR sets show a wider variance than the T cell set.

While a visualisation based on KNA was previously developed for individual cells, the frequency table can also be used to develop a joint visualisation for a set of cells (**Figures 5B–D**). For this, the filtered frequency matrix is first clustered using k-means clustering ($k_{kmeans} = 4$). The remaining bins, which are not occupied by all images, become another category. This category is split in two based on density. Finally, frequency clusters that have a large extent in SNPC1 are split into two, with the boundary being SNPC1 = 0 (**Figure 3E**). In this example, three out of six frequency clusters are split to yield nine frequency clusters, and they were chosen based on visual inspection. The frequency clustering is then converted into a localisation colour key that can be applied to an image. In the k-means step, higher values of k_{kmeans} were tested (not shown) but this led to a confusing visualisation. The process is summarised graphically in **Figure 5**. The major intent of this visualisation is to highlight the contrast in global structure between images. For this image set, black, green and cyan generally correspond to nanoclusters with decreasing separation (resp.) to other clusters. Magenta, coral and purple transition from low count nanoclusters to noise

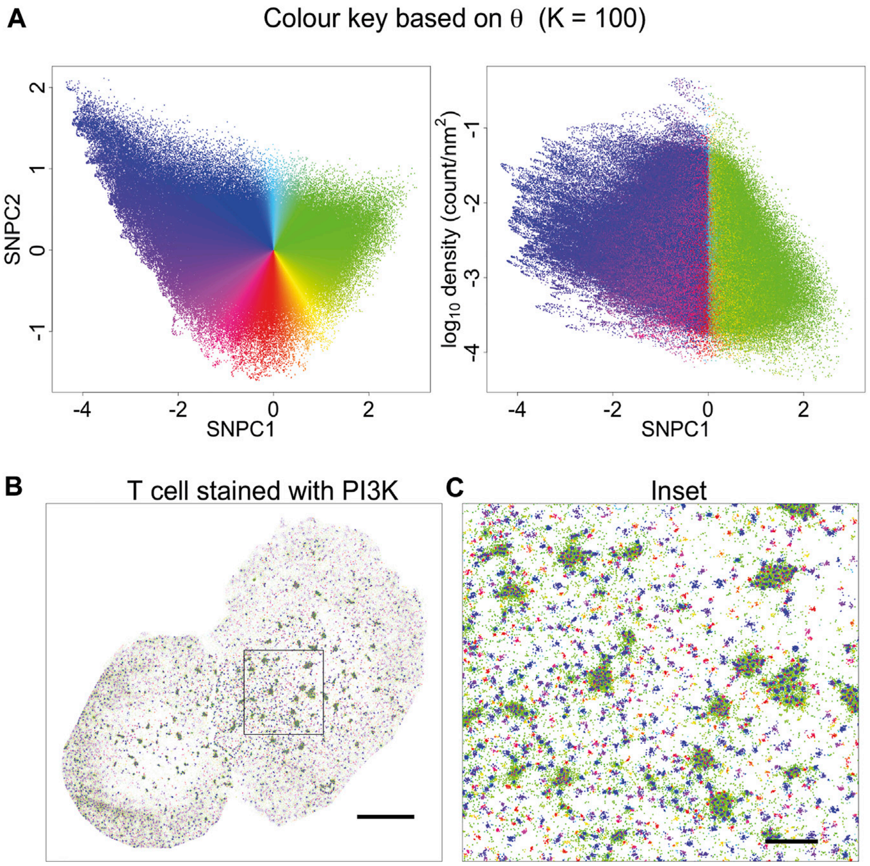

FIGURE 4 | Visualisation based on theta for K = 100. **(A)** A novel visualisation is constructed by converting θ to hue. **(B)** PAINT image of T cell stained with PI3K probe, and coloured according to **(A)**. This choice of visualisation highlights cluster size (or local aggregation within microclusters) and contrasts aggregation (blue, violet, magenta, red, orange) with segregation (green). **(C)** Inset of **(B)**. This visualisation is limited in that it is only based on a single parameter. Other information is suppressed, for example, segregated points (green) have a different density within or outside microclusters. This indicates that they arise from different processes: they occur in-between tightly packed molecules within microclusters, and as spurious noise outside the microclusters.

localisations, with decreasing separation (resp.) from other clusters. Microclusters are composed of red, blue, cyan and purple localisations, with red patches having the highest density. Finally, violet localisations have a relatively low frequency and often correspond to a very small number of unusually dense nanoclusters. These properties can be gleaned from the n-NND curves (**Figure 5E**). While the frequency clustering will often be aligned with discrete spatial structures, e.g., nanoclusters, sometimes discrete spatial structures will have memberships of more than one frequency cluster. Given that this method is not intended to be a new spatial clustering method, it is not a necessarily a fault but it does point to future refinements that can be made.

To a rough approximation, KNA will be most sensitive to the regions on the PC axes with the maximum freedom to vary (**Supplementary Figure 3**). For K = 100 this is roughly in the range of 10–70 nearest neighbours and in our T cell receptor dataset this corresponds to nanoclusters and structures within the large microclusters. However longer-range structure can be probed with larger K values. Although the local topology description is truncated at K = 100, the distribution of single NND values for K = 200, 500, partitioned by the nine groups (**Supplementary Figure 10**), mostly have well defined peaks which are highly reproducible amongst all the T cells. The colours dominating the microclusters consistently have the smallest NNDs. This indicates that the spatial organisations found with K = 100 have highly specific relationships to long-range structure. These properties are biologically important because neighbouring spatial organisations are likely to exchange proteins and facilitate protein interactions.

Finally, the frequency clusters are used to assess phosphorylation patterns. For each cell, the proportion of co-localised localisations in each frequency cluster is compared to the global proportions of each frequency cluster (**Supplementary Figure 11**). Here, co-localisation is defined as a CD3 localisation being within 10 nm of a pCD3 localisation. These frequency pairs are used to define a phosphorylation enrichment score, which is the log-ratio of the two frequencies. Scores greater than one indicate an enrichment for phosphorylation while scores less than one indicate a depletion. These results are displayed in **Figure 7**

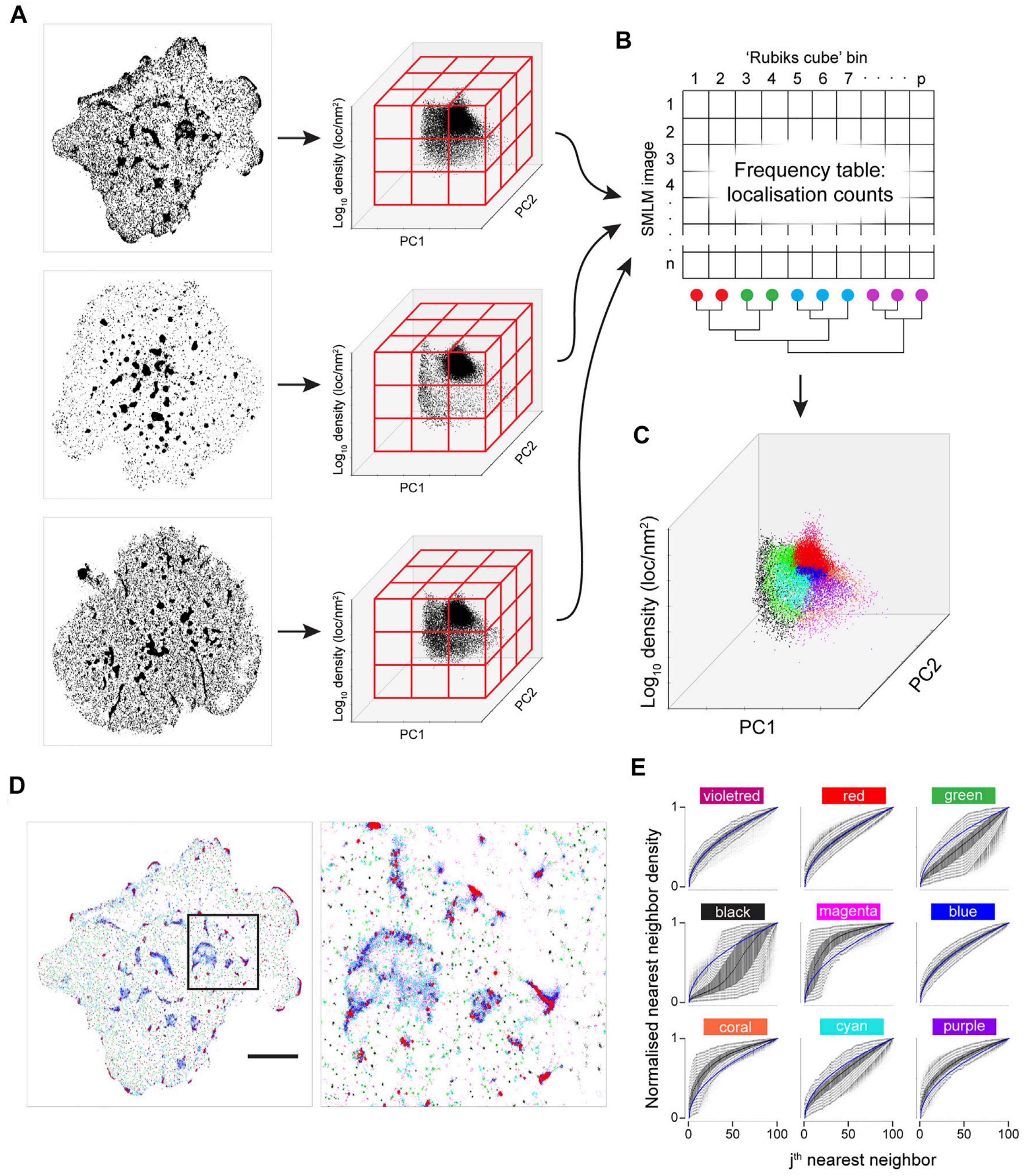

FIGURE 5 | Joint K-neighbourhood analysis over a set of diverse SMLM images. SMLM data are from ILA TCR, first gen CAR and second gen CAR in Jurkat cells activated on supported lipid bilayers containing ICAM-1 and pMHC or CAR ligands. **(A)** Each image is converted into topological coordinates, and the ensuing cloud of points is discretised using a 50 × 50 × 50 grid that is common to all images. Example images of TCR **(top panel)**, first gen CAR **(middle panel)** and second gen CAR **(bottom panel)** are shown. **(B)** The number of localisations in each bin is counted and the grid is unfolded to yield a count vector. The count vector forms a frequency table, where each image is now represented by a row of the frequency table. The bins (columns) are clustered to give localisation groups that have a similar frequency profiles across all images. **(C)** The colour key derived in **(B)** is transferred to the topological coordinate system. **(D)**. The colour key is transferred back to the SMLM image. Scale bar = 5 µm. **(E)** Density-normalized nearest neighbour distances (NND) from the entire dataset for the first $K = 100$ neighbouring localisations for each of the nine spatial organisations arranged in the pattern of the 2-D plot in a. identifies differences in local topology. Colour key as in **(C)**.

and while the three types of cells form markedly different patterns of CD3 clustering, this does not seem to alter the local thresholds for phosphorylation. Enrichment scores are simulated for a random assignment of phosphorylation to each frequency cluster, and the actual enrichment scores are almost always significantly different from random (**Supplementary Figure 12**). The enrichment scores are re-calculated at multiple co-localisation thresholds up to 500 nm

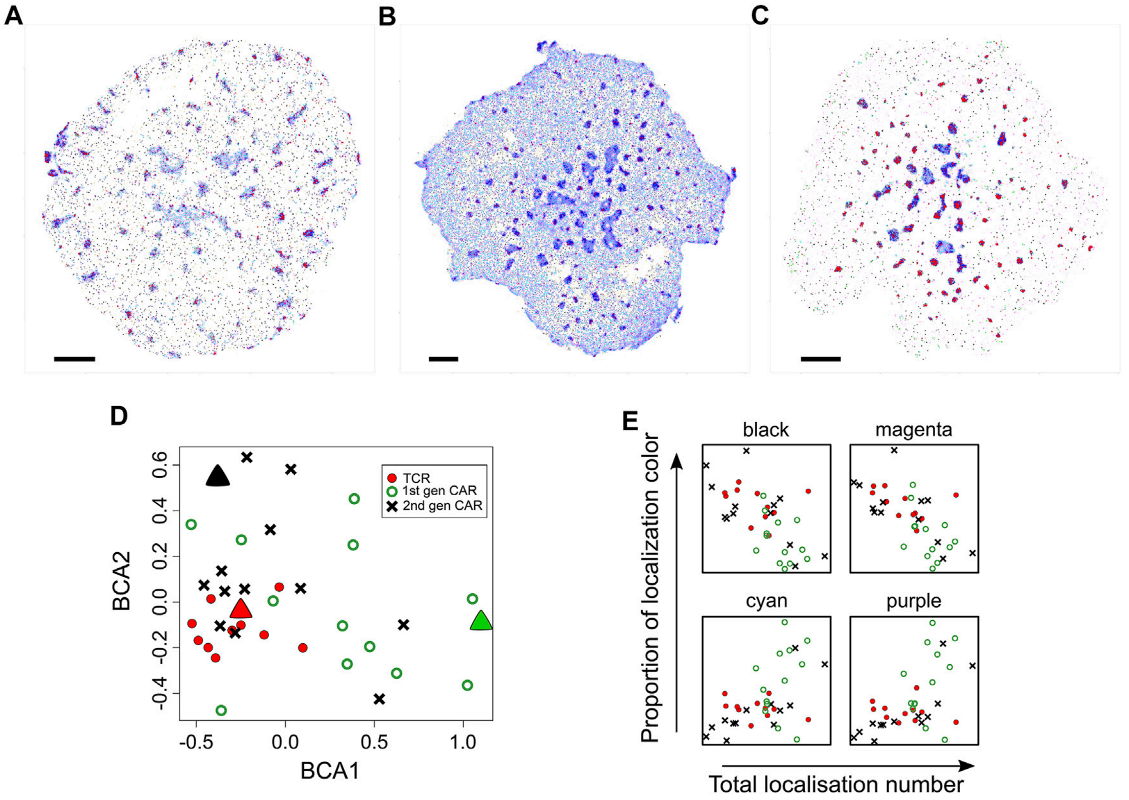

FIGURE 6 | Comparison of diversity in spatial organisation between cells expressing TCR, first generation CAR or second generation CAR. **(A–C)** Representative SMLM images of CD3ζ chain in the TCR-CD3 complex [**(A)**, *n* = 11 images], first generation CAR [**(B)**, *n* = 13 images)] second generation CAR [**(C)**, *n* = 13 images] in Jurkat cells activated on pMHC-containing bilayers. Spatial organisations are colour coded as in **Figure 1**. Scale bars = 2.5 μm **(D)** Between-component analysis (BCA) of the 9-dimensional frequency table that contains the occupancy of each spatial group as percentages of total localisations. Each symbol represents the total point pattern of TCR (red symbols), first generation CAR (green symbols) and second generation CAR (black symbols) obtained from one SMLM image. Large triangles represent the SMLM images shown in **(A–C)** Adjacent data points indicate that their images have a similar overall spatial composition even though each image is unique. The three data sets are significantly different from each other (Methods) with the TCR exhibiting the least cell-to-cell variability. **(E)** Occupancy of the black, magenta, cyan and purple spatial organisations as a function of expression levels (total localisations) for TCR (red circles), first generation CAR (green open circles) and second generation CAR (black crosses). Other spatial groups showed no correlation with expression levels.

(**Supplementary Figure 13**). As the co-localisation thresholds increase, the scores approach zero however at different rates for the different frequency clusters. Of particular note are the red and blue localisations, which are consistently the most enriched in phosphorylation across all cell types. The median enrichment score for the red group was 0.29, which means that phosphorylation of red CD3ζ localisations was nearly twice as frequent compared to a hypothetical random phosphorylation event, even though red localisations exhibited a wide variance in number. Although red localisations resided in microclusters, not all spatial groups in microclusters were enriched in phosphorylation suggesting that highly local organisations determined the likelihood of TCR triggering.

DISCUSSION

The promise of SMLM is to transition away from static biochemical networks, which can be likened to the ingredient list of a recipe, to dynamic spatial signalling networks, i.e., the instructions of a recipe. To do this in a reliable way, it is necessary to move away from the visual inspection of individual cells towards robust statistics over large cohorts of cells. This needs to happen at two levels: picking out the functionally relevant molecular interactions within cells, and quantifying the variance of occurrence across cells (both within and between cell types). To the best of our knowledge, we have presented the first framework which makes it possible to pick out multiscale molecular structures with minimal assumptions, and examine their prevalence across multiple cells with different types of receptors, giving a systematic overview. We have demonstrated that while the three receptor types TCR, first Gen CAR and second gen CAR have general similarities in how they self-arrange, they in fact are subtly distinct from each other which can be attributed to their different structure. The analysis has pooled the information across multiple biological replicates and characterised the variance within the three cell types, which is of key importance in performing reproducible research. We devised a method to characterise the interaction of two molecular species, namely CD3ζ and pCD3ζ, and concluded that the spatial

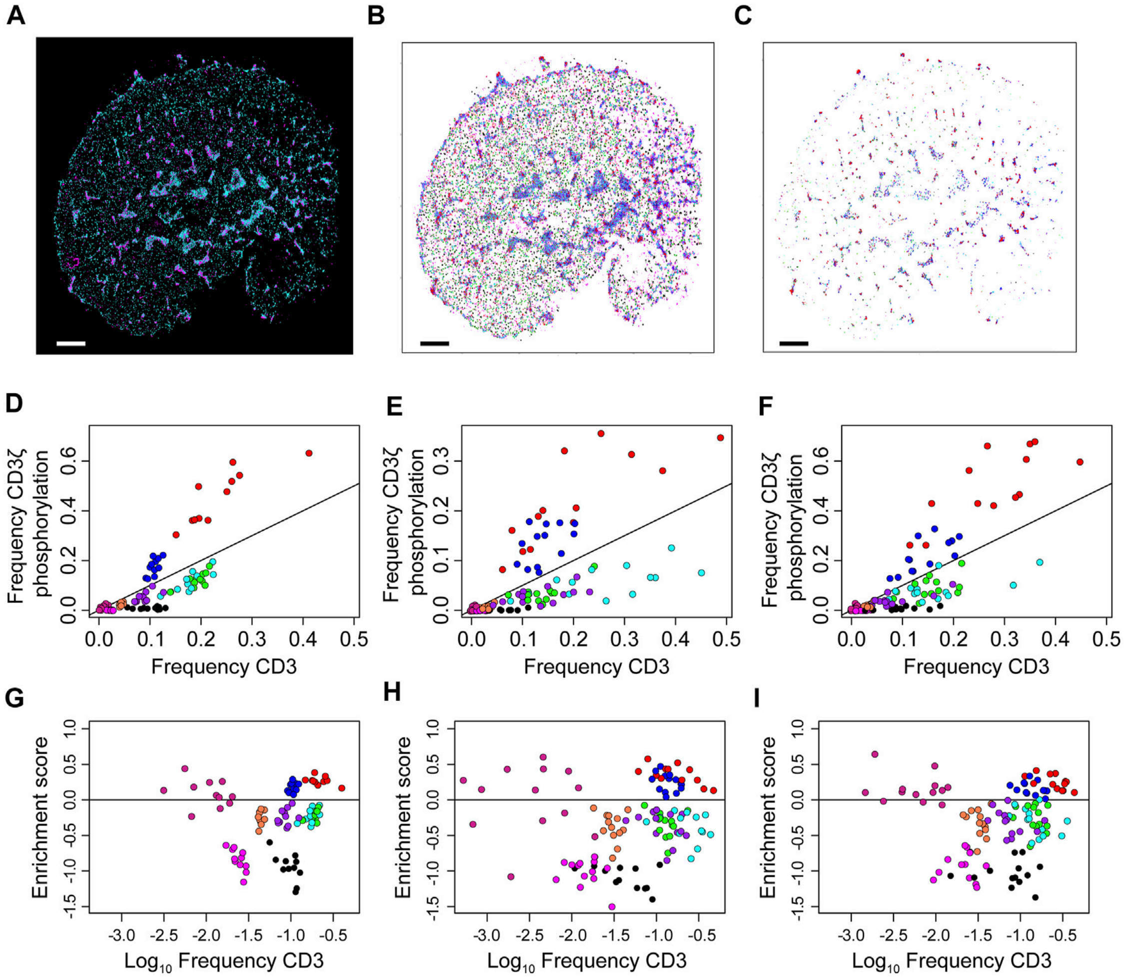

FIGURE 7 | Over- and under-representation of CD3ζ phosphorylation for each of nine co-existing spatial organisations in cells expressing TCR, first generation CAR or second generation CAR. **(A)** Two-colour SMLM images of CD3ζ (cyan) and phosphorylated CD3ζ (pCD3ζ, magenta) of the TCR-CD3 complex in a Jurkat ILA cell activated on a pMHC-decorated bilayer. **(B)** SMLM images of CD3ζ with localisation colour-coded according to the nine spatial groups. **(C)** SMLM images of CD3ζ that are within 10 nm of pCD3ζ localisations. The frequency of these CD3ζ localisations are plotted in **(D–F)**. Colour key as in **(B)**. In **(A–C)**, scales bar = 2.5 µm **(D–F)**. Frequency of CD3ζ phosphorylation as a function of the percentage of total CD3ζ localisations among the nine spatial organisations for TCR **(D)**, first generation CAR **(E)** and second generation CAR **(F)**. Each symbol represents one spatial group from one SMLM image. The black line indicates no preference in phosphorylation; groups above the line are preferably phosphorylated, groups below the line are under-represented in CD3ζ phosphorylation. Note the similarity between the three receptor types. **(G–I)** Phosphorylation enrichment score as a function of CD3ζ occupancy in the nine spatial organisations for TCR **(G)**, first generation CAR **(H)** and second generation CAR **(I)**. Each symbol represents one spatial group from one SMLM image. Symbols above the black horizontal line represent spatial groups that are over-represented in CD3ζ phosphorylation; symbols below the black line represent spatial groups that are under-represented in CD3ζ phosphorylation. The phosphorylation patterns are not significantly different over the three experimental groups (Methods).

preference of phosphorylation remained constant across the three cell types, despite the differences in receptor spatial composition. Moreover, this analysis can be extended to 1) further types of T cells to further characterise the spatial preference of phosphorylation, 2) other key pairs of molecular species and 3) images of >2 molecular species. Finally, as an outlook, this analysis can be used to build an "atlas"of known cell types (T cell or other interesting cells), to identify commonalities and differences in receptor clustering and also integrate spatial information with other forms of single cell "omics" data. Such an atlas can then be used to classify novel and unknown cell types using machine learning.

DATA AVAILABILITY STATEMENT

The original contributions presented in the study are included in the article/**Supplementary Material**, further inquiries can be directed to the corresponding authors.

AUTHOR CONTRIBUTIONS

KF designed analysis concept, carried out all analysis, interpreted analysis, wrote software, wrote manuscript. MG designed experiment, imaged T cells, interpreted analysis. SC designed experiment, imaged DNA origami, wrote manuscript. MF imaged T cells. JG designed experiment, interpreted analysis, wrote manuscript. KG designed analysis concept, designed experiment, interpreted analysis, wrote manuscript.

REFERENCES

Aitchison, J., and Greenacre, M. (2002). Biplots of compositional data. *J. R. Stat. Soc C* 51, 375–392. doi:10.1111/1467-9876.00275

Anderson, M. J. (2006). Distance-based tests for homogeneity of multivariate dispersions. *Biometrics* 62, 245–253. doi:10.1111/j.1541-0420.2005.00440.x

Anselin, L. (1995). Local Indicators of Spatial Association-LISA. *Geogr. Anal.* 27.

Beemiller, P., Beemiller, P., Jacobelli, J., and Krummel, M. (2012). Imaging and analysis of OT1 T cell activation on lipid bilayers. *Protoc. Exchange*. doi:10.1038/protex.2012.028

Boniface, J. J., Rabinowitz, J. D., Wülfing, C., Hampl, J., Reich, Z., Altman, J. D., et al. (1998). Initiation of signal transduction through the T cell receptor requires the multivalent engagement of peptide/MHC ligands [corrected]. *Immunity* 9, 459–466. doi:10.1046/j.1365-3180.1998.00074.x10.1016/s1074-7613(00)80629-9

Burchett, W. W., Ellis, A. R., Harrar, S. W., and Bathke, A. C. (2017). Nonparametric inference for multivariate data: The R package npmv. *J. Stat. Soft.* 76, 76. doi:10.18637/jss.v076.i04

Byers, S., and Raftery, A. E. (1998). Nearest-neighbor clutter removal for estimating features in spatial point processes. *J. Am. Stat. Assoc.* 93, 577–584. doi:10.1080/01621459.1998.10473711

Coelho, S., Baek, J., Graus, M. S., Halstead, J. M., Nicovich, P. R., Feher, K., et al. (2020). Ultraprecise single-molecule localization microscopy enables *in situ* distance measurements in intact cells. *Sci. Adv.* 6, eaay8271–10. doi:10.1126/sciadv.aay8271

Cressie, N., and Collins, L. B. (2001). Analysis of spatial point patterns using bundles of product density LISA functions. *Jabes* 6, 118–135. doi:10.1198/108571101300325292

Davies, T. M., and Baddeley, A. (2018). Fast computation of spatially adaptive kernel estimates. *Stat. Comput.* 28, 937–956. doi:10.1007/s11222-017-9772-4

Denham, E. M., Barton, M. I., Black, S. M., Bridge, M. J., de Wet, B., Paterson, R. L., et al. (2019). A generic cell surface ligand system for studying cell-cell recognition. *Plos Biol.* 17, e3000549–30. doi:10.1371/journal.pbio.3000549

Ditlev, J. A., Case, L. B., and Rosen, M. K. (2018). Who's in and Who's Out-Compositional Control of Biomolecular Condensates. *J. Mol. Biol.* 430, 4666–4684. doi:10.1016/j.jmb.2018.08.003

Drbal, K., Moertelmaier, M., Holzhauser, C., Muhammad, A., Fuertbauer, E., Howorka, S., et al. (2007). Single-molecule microscopy reveals heterogeneous dynamics of lipid raft components upon TCR engagement. *Int. Immunol.* 19, 675–684. doi:10.1093/intimm/dxm032

Espinosa, J. R., Joseph, J. A., Sanchez-burgos, I., Garaizar, A., Frenkel, D., and Collepardo-Guevara, R. (2020). Liquid network connectivity regulates the stability and composition of biomolecular condensates with many components. *Proc. Natl. Acad. Sci. U S A.* 117, 13238–13247. doi:10.1073/pnas.1917569117

Feher, K., Halstead, J. M., Goyette, J., and Gaus, K. (2019). Can single molecule localization microscopy detect nanoclusters in T cells? *Curr. Opin. Chem. Biol.* 51, 130–137. doi:10.1016/j.cbpa.2019.05.019

Grakoui, A., Bromley, S. K., Sumen, C., Davis, M. M., Shaw, A. S., Allen, P. M., et al. (1999). The Immunological Synapse: A Molecular Machine Controlling T Cell Activation. *Science* 80-285, 221–227. doi:10.1126/science.285.5425.221

Gu, Z., Eils, R., and Schlesner, M. (2016). Complex heatmaps reveal patterns and correlations in multidimensional genomic data. *Bioinformatics* 32, 2847–2849. doi:10.1093/bioinformatics/btw313

Huang, B., Bates, M., and Zhuang, X. (2009). Super-Resolution Fluorescence Microscopy. *Annu. Rev. Biochem.* 78, 993–1016. doi:10.1146/annurev.biochem.77.061906.092014

James, J. R., White, S. S., Clarke, R. W., Johansen, A. M., Dunne, P. D., Sleep, D. L., et al. (2007). Single-molecule level analysis of the subunit composition of the T cell receptor on live T cells. *Proc. Natl. Acad. Sci. U S A.* 104, 17662–17667. doi:10.1073/pnas.0700411104

Jiang, S., Park, S., Challapalli, S. D., Fei, J., and Wang, Y. (2017). Robust nonparametric quantification of clustering density of molecules in single-molecule localization microscopy. *PLoS One* 12, e0179975–15. doi:10.1371/journal.pone.0179975

Kuhns, M. S., Girvin, A. T., Klein, L. O., Chen, R., Jensen, K. D., Newell, E. W., et al. (2010). Evidence for a functional sidedness to the alphabetaTCR. *Proc. Natl. Acad. Sci. U S A.* 107, 5094–5099. doi:10.1073/pnas.1000925107

Kumar, R., Ferez, M., Swamy, M., Arechaga, I., Rejas, M. T., Valpuesta, J. M., et al. (2011). Increased Sensitivity of Antigen-Experienced T Cells through the Enrichment of Oligomeric T Cell Receptor Complexes. *Immunity* 35, 375–387. doi:10.1016/j.immuni.2011.08.010

Levet, F., Hosy, E., Kechkar, A., Butler, C., Beghin, A., Choquet, D., et al. (2015). SR-tesseler: a method to segment and quantify localization-based super-resolution microscopy data. *Nat. Methods* 12, 1065–1071. doi:10.1038/nmeth.3579

Lillemeier, B. F., Mörtelmaier, M. A., Forstner, M. B., Huppa, J. B., Groves, J. T., and Davis, M. M. (2010). TCR and Lat are expressed on separate protein islands on T cell membranes and concatenate during activation. *Nat. Immunol.* 11, 90–96. doi:10.1038/ni0610-543b10.1038/ni.1832

Lim, W. A., and June, C. H. (2017). The Principles of Engineering Immune Cells to Treat Cancer. *Cell* 168, 724–740. doi:10.1016/j.cell.2017.01.016

Liu, Q., Li, Z., Deng, M., Tang, J., and Mei, X. (2015). Modeling the effect of scale on clustering of spatial points. *Comput. Environ. Urban Syst.* 52, 81–92. doi:10.1016/j.compenvurbsys.2015.03.006

Maurus, S., and Plant, C. (2016). Skinny-dip. *Proc. ACM SIGKDD Int. Conf. Knowl Discov. Data Min* 13-17, 1055–1064. doi:10.1145/2939672.2939740

Nicovich, P. R., Owen, D. M., and Gaus, K. (2017). Turning single-molecule localization microscopy into a quantitative bioanalytical tool. *Nat. Protoc.* 12, 453–460. doi:10.1038/nprot.2016.166

Owen, D. M., Rentero, C., Rossy, J., Magenau, A., Williamson, D., Rodriguez, M., et al. (2010). PALM imaging and cluster analysis of protein heterogeneity at the cell surface. *J. Biophotonics* 3, 446–454. doi:10.1002/jbio.200900089

Pageon, S. V., Tabarin, T., Yamamoto, Y., Ma, Y., Nicovich, P. R., Bridgeman, J. S., et al. (2016). Functional role of T-cell receptor nanoclusters in signal initiation and antigen discrimination. *Proc. Natl. Acad. Sci. U S A.* 113, E5454–E5463. doi:10.1073/pnas.1607436113

Pageon, S. V., Tabarin, T., Yamamoto, Y., Ma, Y., Nicovich, P. R., Bridgeman, J. S., et al. (2016). Functional role of T-cell receptor nanoclusters in signal initiation and antigen discrimination. *Proc. Natl. Acad. Sci. U S A.* 113, E5454–E5463. doi:10.1073/pnas.161576311310.1073/pnas.1607436113

Patterson, G., Davidson, M., Manley, S., and Lippincott-schwartz, J. (2010). Superresolution Imaging using Single-Molecule Localization. *Annu. Rev. Phys. Chem.* 61, 345–367. doi:10.1146/annurev.physchem.012809.103444

Purbhoo, M. A., Liu, H., Oddos, S., Owen, D. M., Neil, M. A., Pageon, S. V., et al. (2010). Dynamics of Subsynaptic Vesicles and Surface Microclusters at the Immunological Synapse. *Sci. Signal.* 3, ra36. doi:10.1126/scisignal.2000645

Redenbach, C., Särkkä, A., and Sormani, M. (2015). Classification of points in superpositions of Strauss and Poisson processes. *Spat. Stat.* 12, 81–95. doi:10.1016/j.spasta.2015.03.003

Rossboth, B., Arnold, A. M., Ta, H., Platzer, R., Kellner, F., Huppa, J. B., et al. (2018). TCRs are randomly distributed on the plasma membrane of resting antigen-experienced T cells. *Nat. Immunol.* 19, 821–827. doi:10.1038/s41590-018-0162-7

Rubin-Delanchy, P., Burn, G. L., Griffié, J., Williamson, D. J., Heard, N. A., Cope, A. P., et al. (2015). Bayesian cluster identification in single-molecule localization microscopy data. *Nat. Methods* 12, 1072–1076. doi:10.1038/nmeth.3612

Saka, S. K., Honigmann, A., Eggeling, C., Hell, S. W., Lang, T., and Rizzoli, S. O. (2014). Multi-protein assemblies underlie the mesoscale organization of the plasma membrane. *Nat. Commun.* 5, 4509. doi:10.1038/ncomms5509

SUPPLEMENTARY MATERIAL

The Supplementary Material for this article can be found online at: https://www.frontiersin.org/articles/10.3389/fbinf.2021.724127/full#supplementary-material

Schamel, W. W., Arechaga, I., Risueño, R. M., van Santen, H. M., Cabezas, P., Risco, C., et al. (2005). Coexistence of multivalent and monovalent TCRs explains high sensitivity and wide range of response. *J. Exp. Med.* 202, 493–503. doi:10.1084/jem.20042155

Schnitzbauer, J., Strauss, M. T., Schlichthaerle, T., Schueder, F., and Jungmann, R. (2017). Super-resolution microscopy with DNA-PAINT. *Nat. Protoc.* 12, 1198–1228. doi:10.1038/nprot.2017.024

Sengupta, P., Jovanovic-Talisman, T., and Lippincott-Schwartz, J. (2013). Quantifying spatial organization in point-localization superresolution images using pair correlation analysis. *Nat. Protoc.* 8, 345–354. doi:10.1038/nprot.2013.005

Sherman, E., Barr, V., Manley, S., Patterson, G., Balagopalan, L., Akpan, I., et al. (2011). Functional nanoscale organization of signaling molecules downstream of the T cell antigen receptor. *Immunity* 35, 705–720. doi:10.1016/j.immuni.2011.10.004

Sherman, E., Barr, V. A., Merrill, R. K., Regan, C. K., Sommers, C. L., and Samelson, L. E. (2016). Hierarchical nanostructure and synergy of multimolecular signalling complexes. *Nat. Commun.* 7, 12161. doi:10.1038/ncomms12161

Shivanandan, A., Unnikrishnan, J., and Radenovic, A. (2016). On characterizing protein spatial clusters with correlation approaches. *Sci. Rep.* 6, 31164. doi:10.1038/srep31164

Thioulouse, J. (2011). Simultaneous analysis of a sequence of paired ecological tables: A comparison of several methods. *Ann. Appl. Stat.* 5, 2300–2325. doi:10.1214/10-AOAS372

Thompson, H. R. (1956). Distribution of Distance to Nth Neighbour in a Population of Randomly Distributed Individuals. *Ecology* 37, 391–394. doi:10.2307/1933159

Ward, J. H. (1963). Hierarchical Grouping to Optimize an Objective Function. *J. Am. Stat. Assoc.* 58, 236–244. doi:10.1080/01621459.1963.10500845

Yoo, H., Triandafillou, C., and Drummond, D. A. (2019). Cellular sensing by phase separation: Using the process, not just the products. *J. Biol. Chem.* 294, 7151–7159. doi:10.1074/jbc.TM118.001191

Conflict of Interest: The authors declare that the research was conducted in the absence of any commercial or financial relationships that could be construed as a potential conflict of interest.

frontiers
in Bioinformatics

ORIGINAL RESEARCH
published: 20 October 2021
doi: 10.3389/fbinf.2021.724325

Spatiotemporal Clustering of Repeated Super-Resolution Localizations via Linear Assignment Problem

David J. Schodt and Keith A. Lidke*

Department of Physics and Astronomy, University of New Mexico, Albuquerque, NM, United States

OPEN ACCESS

Edited by:
Christian Franke,
Friedrich Schiller University Jena,
Germany

Reviewed by:
Perrine Paul-Gilloteaux,
INSERM US16 Santé François Bonamy, France
Jean-Karim Hériché,
European Molecular Biology Laboratory Heidelberg, Germany
Alexander Raymond Small,
California State Polytechnic University, United States

Correspondence:
Keith A. Lidke
klidke@unm.edu

Specialty section:
This article was submitted to Computational BioImaging, a section of the journal Frontiers in Bioinformatics

Received: *12 June 2021*
Accepted: *04 October 2021*
Published: *20 October 2021*

Citation:
Schodt DJ and Lidke KA (2021) Spatiotemporal Clustering of Repeated Super-Resolution Localizations via Linear Assignment Problem. Front. Bioinform. 1:724325. doi: 10.3389/fbinf.2021.724325

Many fluorescence super-resolution techniques, such as (d)STORM, PALM, and DNA-PAINT, generate datasets wherein multiple localizations across many camera frames may arise from a single blinking event of an emitter. These repeated localizations not only hinder interpretation and analysis of such datasets, but also represent an incomplete use of the fluorescence photons. Such localizations are typically combined into a single localization either by clustering with hard distance and time thresholds, or by classical hypothesis testing assuming Gaussian localization errors. In this work, we describe a method for clustering that accounts for localization precision, local emitter density estimates, and a kinetic model for blinking which is used to optimize connections within a group of spatiotemporally colocated localizations.

Keywords: fluorescence microscopy, super-resolution, image analysis, computational modeling, single molecule techniques

1 INTRODUCTION

Fluorescence super-resolution methods have grown to be vital imaging techniques in many research areas, particularly in the biological sciences. Single Molecule Localization Microscopy (SMLM) methods take advantage of an extreme form of temporal independence where individual sources blink on and off with little spatial-temporal overlap from other "on" sources. Many of these techniques, such as (d)STORM (Rust et al., 2006; Heilemann et al., 2008), PALM (Betzig et al., 2006; Hess et al., 2006), and DNA-PAINT (Jungmann et al., 2010), are relatively easy to implement on common fluorescence microscopes with little to no modifications. By finding the center of distinct PSFs arising from independent "on" sources as observed on a camera, SMLM data is reduced to a set of PSF center coordinates, or localizations, and their associated precisions. The subsequent processing of these localizations can have significant impacts on the final interpretation of the data.

Despite extensive research into optimally localizing emitters (Small and Stahlheber, 2014; Deschout et al., 2014; Sage et al., 2019), little effort has been spent on what we will henceforth refer to as the frame-connection problem. SMLM methods produce data with multiple localizations in subsequent/near-subsequent frames which are likely the result of a single blinking event of a single emitter. Specifically, a single visible emitter may appear in multiple frames, with each frame potentially producing a new localization of that emitter. The frame-connection problem deals with combining these repeated localizations into a single localization with higher precision. To the best of our knowledge, only two solutions to the frame-connection problem are in use: 1) combining any localizations within N frames and d pixels of one another, as is done in the popular ThunderSTORM package (Ovesný et al., 2014) (we'll refer to this method as the "classical" approach); or 2) by a hypothesis test assuming Gaussian localization noise ("hypothesis test") (Wester et al., 2021). A modification to the classical approach involves setting the separation threshold d to be some multiple of the localization error, as is done in the PYMEVisualize package (Marin et al., 2021) (referred to as "chaining" in that work and as "revised classical" here). The classical approach has the benefit of simplicity: its implementation is straightforward and accessible. The hypothesis testing approach makes use of localization error to test the null hypothesis that localizations came from the same emitter, however it neglects a calculation and comparison to the low-probability alternative hypothesis that a new emitter could have appeared in the same location. Both of these methods implicitly make use of the prior knowledge that multiple blinking events within a small spatiotemporal volume is rare in SMLM data.

To ensure information about the underlying structure of emitters is retained, an optimal frame-connection solution should exhibit minimal over-clustering. In other words, a frame-connection algorithm prone to connecting localizations from distinct emitters may reduce the quality of SMLM data. However, if a frame-connection algorithm is prone to under-clustering localizations from a single blinking event, it's addition to the analysis pipeline may not represent much value. In that view, an optimal frame-connection solution must be capable of clustering those localizations which are very likely to have arisen from a single blinking event of a single emitter, all the while remaining sufficiently conservative in its connection assignments to minimize over-clustering.

The analysis of SMLM localizations can be classified into two categories: pre- and post-processing. Broadly speaking, pre-processing is a clean-up stage during which raw localizations are filtered without destroying the information they carry. Frame-connection should be considered pre-processing in the sense that its goal is to combine repeated localizations without destroying the temporal information carried by emitter blinking. In contrast, post-processing methods aim to condense/summarize the information carried by the localizations into descriptors of the underlying structure or process being observed. More general post-processing clustering methods, such as DBSCAN (Daszykowski et al., 2001), Voronoi tesselation (Levet et al., 2015), and BaGoL (Fazel et al., 2019b), differ from pre-clustering frame-connection in that they are not restricted to grouping observations of a single blinking event. Rather, post-processing clustering methods attempt to associate or make inference from all localizations of a single emitter.

The analysis of single-particle tracking (SPT) data aims to achieve a similar goal to frame-connection: associating multiple localizations over time to a single emitter. The ideal solution to the SPT problem is global across all connection possibilities; however, such a solution is not computationally feasible for realistic experiments. A locally greedy solution is prone to incorrect/missed connections, a problem exacerbated by emitter blinking and detection failure. As a result, many SPT analysis methods approximate a global solution by performing a locally greedy (in time) step to reduce the computational complexity. For example, the multiple target tracing (MTT) method (Sergé et al., 2008) considers only those connection hypotheses corresponding to a sliding spatiotemporal window. The method presented in (Jaqaman et al., 2008) performs an initial frame-to-frame connection followed by a global gap closing procedure.

In this work, we present a novel solution to the single blinking event frame-connection problem which accounts for local emitter densities, fluorescent emission kinetics, and localizations missed in processing, which we refer to as linear assignment problem frame-connection (LAP-FC). Motivated by the success and robustness of the cost matrix method to solving the linear assignment problem (LAP) in SPT (Jaqaman et al., 2008), we formulate the frame-connection problem in terms of the costs of connecting/not connecting localizations. Our algorithm effectively groups all reasonable connection hypotheses in a pre-processing step (enabled by the typical brevity of blinking events in SMLM data), which allows us to find a globally optimal solution to the single blinking event frame-connection problem. We demonstrate that our algorithm outperforms the classical and hypothesis test methods in several situations typical of SMLM data with no to minimal evidence of over-clustering. Furthermore, our algorithm is in practice parameter-free, making it the ideal method for use by end users of SMLM data.

2 MATERIALS AND METHODS

Our solution to the frame-connection problem consists of three primary components: 1) pre-clustering of localizations into sets of connection candidates, 2) estimating local densities and kinetic rates from preclusters, and 3) making a maximum likelihood assignment of localizations to clusters, which is implemented as a LAP. In this section, we will describe our formulation of the frame-connection problem before describing the three components of our algorithm. A description of some commonly used variables used throughout this text is provided in **Table 1**.

2.1 Pre-Clustering

For a typical SMLM dataset, the number of localizations $n \sim 10^6$ makes finding a global solution to the LAP across all localizations computationally infeasible. As such, we perform a pre-clustering of localizations in a manner similar to the revised classical frame-connection solution as presented in (Marin et al., 2021). For a given localization, the spatial nearest neighbor within some frame gap and within some multiplier of its localization error (typically chosen to be five frames and 5, respectively) is found. If that nearest neighbor is already part of a cluster, the localization is incorporated into that same cluster. Otherwise, the localization and its nearest neighbor (if one exists) are defined as a new cluster. To ensure localizations aren't excluded from their ideal precluster, pre-clustering allows incorporation of multiple localizations within the same frame to the same cluster.

2.2 Estimating Local Emitter Densities and Kinetic Rates

To estimate local emitter densities and kinetic rates, we assume that each precluster will on average be representative of a single blinking event. That is, we assume that most preclusters consists

TABLE 1 | Description of commonly used variables.

Variable	Description	Units
k_{on}	transition rate from the emitter dark state to the on (visible) state	frame^{-1}
k_{off}	transition rate from the emitter on state to the reversible off state	frame^{-1}
k_{bleach}	transition rate from the emitter on state to the irreversible bleached state	frame^{-1}
p_{miss}	probability of failing to localize a visible emitter	
n	total number of (pre-frame connection) localizations in the data	
n_c	number of localizations in a given precluster	
N_{emitters}	underlying number of emitters in the data	
ρ_0	initial underlying density of emitters in the first frame of data	$\mathrm{emitters/pixel}^2$
ρ	underlying density of non-bleached emitters	$\mathrm{emitters/pixel}^2$
ρ_{on}	density of emitters in the “on” state	$\mathrm{emitters/pixel}^2$
ρ_{off}	density of emitters in the “off” state	$\mathrm{emitters/pixel}^2$
N	number of spatial dimensions	
$\mathbf{x}$	vector of Cartesian coordinates $[x_1, x_2, \ldots, x_N]$	pixels
Δx_i	separation between two localizations along the i-th dimension	pixels
$\sigma^2_{x_i,1}$	variance of the first localization in the i-th dimension	pixels^2
$\sigma^2_{x_i,2}$	variance of the second localization in the i-th dimension	pixels^2
$\sigma^2_{x_i}$	sum of the variances $\sigma^2_{x_i,1} + \sigma^2_{x_i,2}$	pixels^2
f	integer frame number	frames
f_{end}	frame number corresponding to the last frame of the data	frames
N_p	number of candidate frames that have elapsed by the appearance of a localization	frames
N_f	number of candidate frames remaining after the appearance of a localization	frames
τ	approximate duty cycle of an emitter	
F	CDF of the nearest-neighbor distribution of localizations within 5 frames of one another	
δ	deviation of a nearest-neighbor distribution CDF F from the ideal CDF F_{ideal}	

of localizations of a single emitter blinking once with a duration of multiple frames. The rate parameters k_{on}, k_{off}, and k_{bleach}, and the probability of missing a localization p_{miss} are estimated from the pre-clustered data as follows. The sum of the off rate and the bleaching rate $k_{\mathrm{off}} + k_{\mathrm{bleach}}$ is estimated from the cluster durations N (in frames) as

$$\widehat{k_{\mathrm{off}} + k_{\mathrm{bleach}}} = -\log\left(1 - \frac{1}{\overline{N}}\right) \tag{1}$$

where $\overline{\ldots}$ denotes the mean value. The expression given in **Eq. 1** is derived assuming that cluster durations are geometrically distributed with the probability of turning off given by $1 - \exp[-(k_{\mathrm{off}} + k_{\mathrm{bleach}})]$ (the probability of turning off within $\Delta t = 1$ frames). The probability of missing a localization p_{miss} is estimated from the ratio of the number of localizations in a cluster n_c to the cluster's duration N as

$$\hat{p}_{\mathrm{miss}} = 1 - \overline{n_c/N}$$

The expected cumulative number of localizations observed by frame f is given by

$$\langle n_{\mathrm{cumulative}}\rangle(f) \approx N_{\mathrm{emitters}}(1 - p_{\mathrm{miss}}) \tau\left\{\frac{1 - \exp[-\lambda_1(f-1)]}{\lambda_1} - \frac{1 - \exp[-\lambda_2(f-1)]}{\lambda_2}\right\} \tag{2}$$

with

$$\lambda_1 = k_{\mathrm{bleach}}\frac{k_{\mathrm{on}}}{k_{\mathrm{on}} + k_{\mathrm{off}} + k_{\mathrm{bleach}}} \equiv k_{\mathrm{bleach}}\tau$$

$$\lambda_2 = k_{\mathrm{on}} + k_{\mathrm{off}} + k_{\mathrm{bleach}} - \lambda_1$$

where N_{emitters} is the total number of emitters present at the beginning of the experiment. **Eq. 2** was derived from the results presented in (Nino and Milstein, 2021) by assuming $k_{\mathrm{on}} \ll k_{\mathrm{off}}$ with no restriction on k_{bleach} and by accounting for p_{miss}. Similarly, the cumulative number of preclusters observed over time is of the form

$$\langle n_{\mathrm{clusters\ cumulative}}\rangle(f) \approx k_{\mathrm{off}}\langle n_{\mathrm{cumulative}}\rangle(f) \tag{3}$$

According to **Eqs. 2**, **3**, the off rate k_{off} can be estimated as n_{clusters}/n where n_{clusters} is the total number of preclusters and n is the total number of localizations. The bleaching rate k_{bleach} is then found by subtracting the estimate for k_{off} from **Eq. 1**. The on rate k_{on} and the underlying number of emitters N_{emitters} are then estimated by fitting the cumulative number of localizations to the model given in **Eq. 2**. Additional details about the parameter estimation procedures can be found in **Supplementary Text 1**.

The local pre-cluster density corresponding to each pre-cluster is estimated by finding the k (chosen to be two in this study) nearest pre-clusters and then computing $\rho_c = (k+1)/\pi r_k^2$ where r_k is the distance to the kth nearest pre-cluster. The underlying local emitter density present at the beginning of the experiment is then estimated for each pre-cluster as

$$\hat{\rho}_{0,\mathrm{local}} = \rho_c \frac{1}{\hat{k}_{\mathrm{off}}\hat{\tau}} \frac{1}{1 - \hat{p}_{\mathrm{miss}}} \left\{\frac{1 - \exp[-\hat{\lambda}_1(f_{\mathrm{end}} - 1)]}{\hat{\lambda}_1} - \frac{1 - \exp[-\hat{\lambda}_2(f_{\mathrm{end}} - 1)]}{\hat{\lambda}_2}\right\}^{-1}$$

where f_{end} is the last frame containing localizations in the experiment. The density of on emitters ρ_{on} and the density of off emitters ρ_{off} are then estimated as

$$\hat{\rho}_{\mathrm{on}}(f) = \hat{\rho}_{0,\mathrm{local}} \hat{\tau} \left\{ \exp\left[-\hat{\lambda}_1 (f-1)\right] - \exp\left[-\hat{\lambda}_2 (f-1)\right] \right\}$$

$$\hat{\rho}_{\mathrm{off}}(f) = \hat{\rho}_{\mathrm{on}}(f) \frac{\hat{k}_{\mathrm{off}}}{\hat{k}_{\mathrm{on}}}$$

2.3 Frame-Connection via Minimization of Costs

The frame-connection problem can be thought of as a spatiotemporal clustering problem in which only one localization is allowed admittance to each cluster in each frame. In terms of the LAP, frame-connection concerns assigning each observed localization to one and only one cluster, with each assignment having an associated cost. In particular, frame-connection consists of "connection" costs, "birth" costs, and "death" costs. The connection costs are the costs for assigning a localization to an existing cluster. The birth costs are the costs for birthing a new emitter with the candidate localization being its first observation. The death costs are the costs for prohibiting assignment of any future localizations to an existing localization cluster. The costs are arranged in a square matrix such that the LAP solution permits only one assignment per row and column. We define each of these costs by assuming a three-state kinetic model for emitter blinking. The transition rates are defined as k_{on}, the rate from the (reversible) off state to the visible on state; k_{off}, the rate from the on state to the off state; and k_{bleach}, the rate from the on state to the (irreversible) bleached state. We additionally assume a constant probability of missing a localization (i.e., failing to localize a visible emitter) which we designate p_{miss}. Furthermore, the costs account for the local density of emitters $\rho(\mathbf{x}, f)$ where $\mathbf{x} = [x, y]$ is the precluster location and f is the frame number. Our procedure for estimating k_{on}, k_{off}, k_{bleach}, p_{miss}, and $\rho(\mathbf{x}, f)$ directly from the data is described in **section 2.2**.

The connection, birth, and death costs are defined to be the negative logarithm of the probabilities associated with the prescribed actions. The cost c_c of connecting two localizations is defined as follows:

$$c_c = -\log\left\{ \prod_{i=1}^{N} p\left(\Delta x_i | \sigma_{x_i}^2\right) \cdot p\left(\text{observe after missing localizations} | p_{\mathrm{miss}}, \Delta f\right) \cdot p\left(\text{not turning off} | \Delta f\right) \right\}$$

where N is the number of dimensions (taken to be 2 for the present study), Δx_i is the separation between the two localizations along the i-th dimension, $\sigma_{x_i}^2 \equiv \sigma_{x_i,1}^2 + \sigma_{x_i,2}^2$ is the sum of the localization variances $\sigma_{x_i,1}^2$ for localization 1 and $\sigma_{x_i,2}^2$ for localization 2 in the i-th dimension, and $\Delta f > 0$ is the temporal separation between the two localizations. The probability terms are given by

$$p\left(\Delta x_i | \sigma_{x_i}^2\right) = \frac{1}{\sqrt{2\pi\sigma_{x_i}^2}} \exp\left(\frac{\Delta x_i^2}{2\sigma_{x_i}^2}\right)$$

$$p\left(\text{observe after missing localizations} | p_{\mathrm{miss}}, \Delta f\right) = \left(1 - p_{\mathrm{miss}}\right) p_{\mathrm{miss}}^{\Delta f - 1}$$

$$p\left(\text{not turning off} | \Delta f\right) = \exp\left[-\left(k_{\mathrm{off}} + k_{\mathrm{bleach}}\right)\Delta f\right]$$

where the rate parameters are given in units of frame^{-1}. The cost of introducing a new emitter in frame M after N_p candidate frames ("birth" cost) is given by

$$\begin{aligned} c_b &= -\log\left\{ p\left(\text{new emitter turning on} | k_{\mathrm{on}}, \rho_{\mathrm{off}}(\mathbf{x}, f), N_p\right) \cdot p\left(\text{not missing localization} | p_{\mathrm{miss}}\right) \right. \\ &\quad \left. + \; p\left(\text{observe after missing localizations} | p_{\mathrm{miss}}, N_p, \rho_{\mathrm{on}}(\mathbf{x}, f)\right) \right\} \\ &= -\log\left\{ \rho_{\mathrm{off}}(\mathbf{x}, M)\left[1 - \exp\left(-k_{\mathrm{on}}\right)\right] \exp\left(-k_{\mathrm{on}} N_p\right)\left(1 - p_{\mathrm{miss}}\right) \right. \\ &\quad \left. + \; \rho_{\mathrm{on}}\left(\mathbf{x}, M - N_p\right)\left(1 - p_{\mathrm{miss}}\right) p_{\mathrm{miss}}^{N_p} \right\} \end{aligned}$$

where $\rho_{\mathrm{off}}(\mathbf{x}, f)$ is the local density of emitters in the off state, and $\rho_{\mathrm{on}}(\mathbf{x}, f)$ is the local density of emitters in the on state (see **section 2.2**). The cost of not observing an emitter for the remaining N_f candidate frames ("death" cost) is given by

$$\begin{aligned} c_d &= -\log\left\{ p\left(\text{bleaching} | k_{\mathrm{bleach}}\right) + p\left(\text{turn off} | k_{\mathrm{off}}\right) + p\left(\text{missing localizations} | p_{\mathrm{miss}}, N_f\right) \right\} \\ &= -\log\left\{ \left[1 - \exp\left(-k_{\mathrm{bleach}}\right)\right] + \left[1 - \exp\left(-k_{\mathrm{off}}\right)\right] + p_{\mathrm{miss}}^{N_f} \right\} \end{aligned}$$

As in (Jaqaman et al., 2008), we arrange our LAP costs in a square block matrix composed of four equal sized square sub-matrices, with each sub-matrix being $n_c \times n_c$ for n_c localizations within a given precluster. The upper-left block matrix contains the connection costs between a localization identified by its row index with a localization identified by its column index, arranged as an upper-triangular matrix (to prohibit selection pairs of row m to column n and row n to column m) and divided by two to account for the definition of the bottom-right auxiliary block costs (see below). The bottom-left block contains the birth costs for the localizations identified by the column index. The upper-right block contains the death costs for the localizations identified by the row index. The bottom-right block, to which we attribute no physical significance, is defined to be the transpose of the upper-left connection block, as assignments in the upper-left block lead to the same assignments in the (transposed) lower-right block. All cost matrix entries containing a prohibited selection (e.g., main diagonal terms, which represent connection of a localization to itself) are set to a non-link marker, which tells the LAP solver not to select those entries. Costs that are infinite or otherwise invalid (i.e., not a number) are set to twice the sum of all valid costs to ensure they are only selected when no other assignment is available. The LAP is then solved using the Jonker-Volgenant algorithm (Jonker and Volgenant, 1987), which assigns each localization to a single cluster of localizations. This process is then repeated for each pre-cluster of localizations to yield the final frame-connected set of localizations.

Localizations connected by the frame-connection algorithm are combined assuming they each represent independent samples from a Gaussian distribution. The resulting position of the m frame-connected localizations is taken to be the maximum-likelihood estimate for the position $\mathbf{x}$

$$\hat{\mathbf{x}} = \frac{\sum_{i=1}^{m} \mathbf{x}_i / \sigma_i^2}{\sum_{i=1}^{m} 1/\sigma_i^2} \qquad (4)$$

and the localization error for the frame-connected localization is taken to be the inverse of the Fisher information

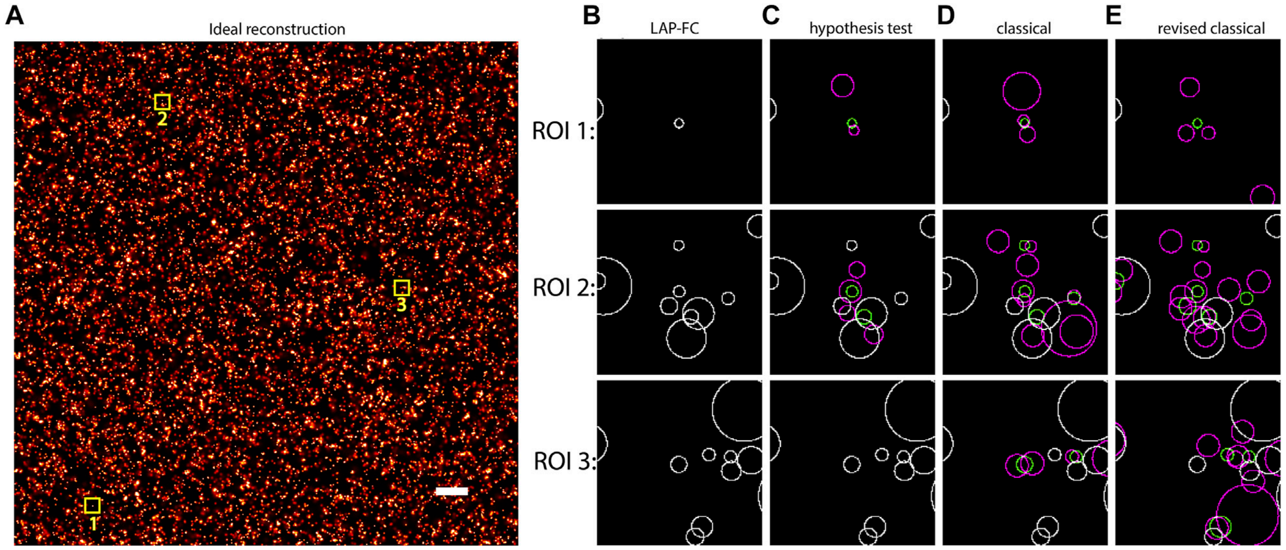

FIGURE 1 | Uniformly distributed emitters with initial density ρ_0 = 10 emitter/pixel^2, k_{on} = 0.005/frame, k_{off} = 0.5/frame, k_{bleach} = 0.2/frame, p_{miss} = 0.01, photon emission rate of 1,000 photons/frame, additional Gaussian noise with σ = 0.05 pixels, and 10,000 total frames. **(A)** "Ideal" frame-connection solution, scale bar = 2 pixels. **(B)–(E)** Results for the three sub-ROIs marked with yellow squares in **(A)** using **(B)** LAP-FC with a maximum pre-clustering frame gap of five frames and a maximum separation of 5 times the localization error; **(C)** the hypothesis test algorithm with a maximum frame gap of five frames, a maximum separation of 1 pixel, and a level-of-significance of 0.05; **(D)** the classical algorithm with a maximum frame gap of 1 frame and a maximum separation of 0.2 pixels; and **(E)** the revised classical algorithm with a maximum frame gap of five frames and a maximum separation of 2 times the localization error. The circles in **(B)–(E)** are centered at the localization position with radii equal to the localization error. Green circles represent localizations from the ideal results from **(A)**. Magenta circles represent the results of the frame-connection algorithm. White circles correspond to frame-connection results matching the ideal results.

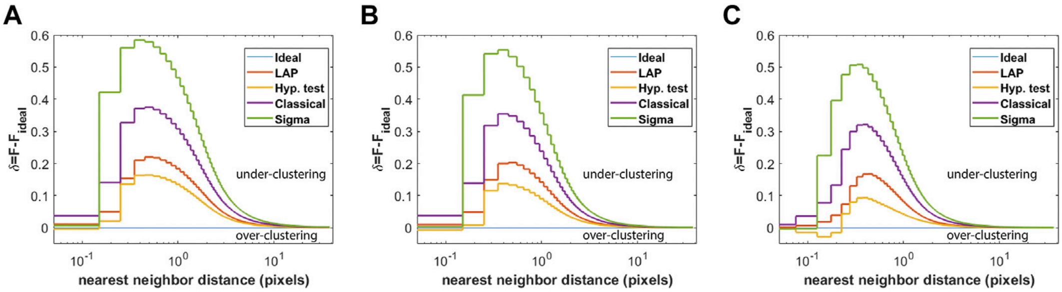

FIGURE 2 | Deviation of the nearest-neighbor distance CDF from that of the ideal frame-connection result ensembled over multiple uniform emitter simulations, where nearest-neighbors are restricted to appear within five frames of one another. The green line corresponds to the revised classical method, the purple line to the classical method, the yellow line to the hypothesis test method, the red-orange line to the LAP-FC method, and the blue line is the δ = 0 baseline. The number of simulations and initial densities were varied as **(A)** 40 simulations with ρ_0 = 5 emitters/pixel^2, **(B)** 20 simulations with ρ_0 = 10 emitters/pixel^2, and **(C)** 10 simulations with ρ_0 = 20 emitters/pixel^2.

$$\hat{\sigma}^2 = \frac{1}{\sum_{i=1}^{m} 1/\sigma_i^2} \tag{5}$$

2.4 Simulated SMLM Data

Simulated SMLM localizations were generated to test the frame-connection algorithms. A uniformly distributed point target was simulated by scattering emitters uniformly across a square region of interest (ROI). Dimerized emitters were simulated by placing emitters at varying separations from one another with sufficient inter-dimer spacing to ensure localizations from distinct dimers will not be connected by any of the algorithms. To generate localizations from simulated emitter positions, the frames in which each emitter was observed were simulated by the Gillespie algorithm (Gillespie, 1976) as prescribed by the transition rates k_{on} = 0.005 frame^{-1}, k_{off} = 0.5 frame^{-1}, and k_{bleach} = 0.2 frame^{-1}. Localizations corresponding to the emitter being on the entire frame were assigned a fixed photon count I. For frames in which the emitter turned on, turned off, or bleached, the number of photons was reduced to I (1 − u) where u is sampled from the standard uniform distribution. Gaussian noise was added to each localization

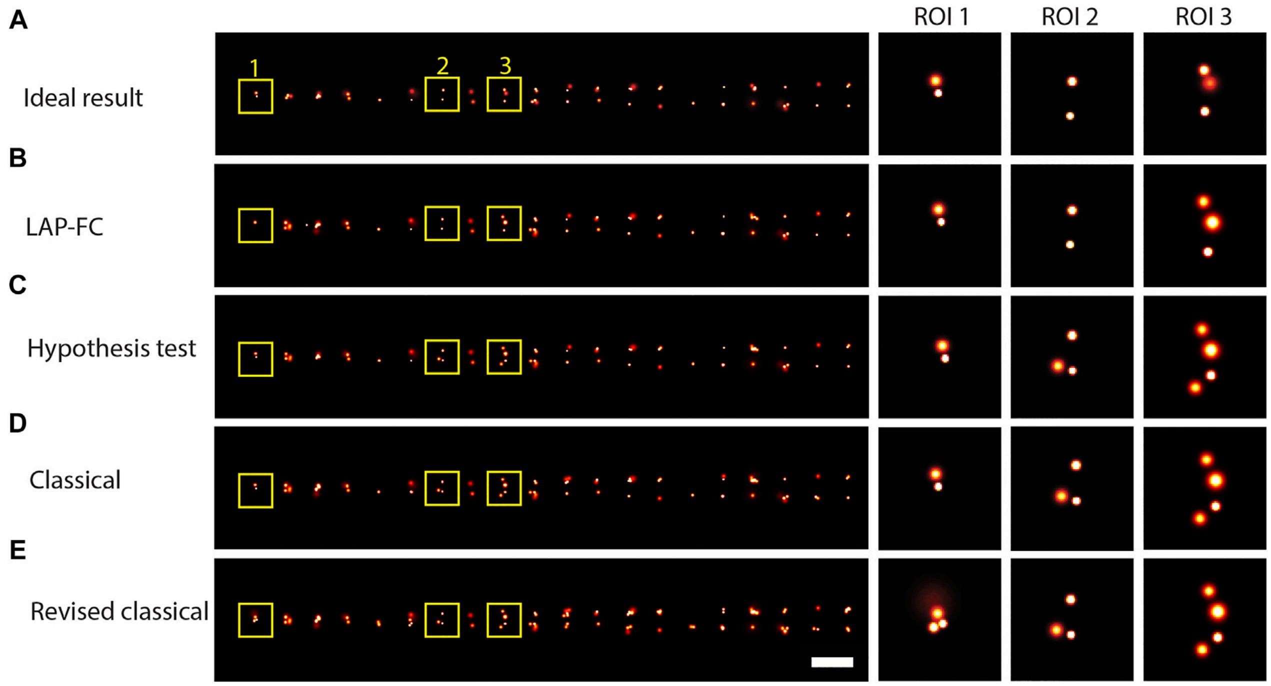

FIGURE 3 | Gaussian reconstruction images for frame-connection results on simulated dimer emitters with spatial separations ranging from 0.1-1 pixel, k_{on} = 0.005/frame, k_{off} = 0.5/frame, k_{bleach} = 0.2/frame, p_{miss} = 0.01, photon emission rate of 1,000 photons/frame, and 10,000 total frames. **(A)** "Ideal" frame-connection solution, scale bar = 2 pixels. **(B)–(E)** Results for the three sub-ROIs marked with yellow squares in **(A)** using **(B)** LAP-FC with a maximum pre-clustering frame gap of five frames and a maximum separation of 5 times the localization error; **(C)** the hypothesis test algorithm with a maximum frame gap of five frames, a maximum separation of 1 pixel, and a level-of-significance of 0.05; **(D)** the classical algorithm with a maximum frame gap of 1 frame and a maximum separation of 0.2 pixels; and **(E)** the revised classical algorithm with a maximum frame gap of five frames and a maximum separation of 2 times the localization error. Scale bar = 2 pixels.

with a standard deviation given by the Cramér-Rao lower bound corresponding to fitting a Gaussian to the emitter PSF given the background intensity and a finite pixel size (Smith et al., 2010). To mimic noise sources not accounted for by localization errors, such as residual, uncorrected sample drift, an additional source of Gaussian noise with standard deviation 0.05 pixels was added to each localization. A constant probability of missing a localization p_{miss} was applied to the final results by randomly removing $p_{\text{miss}}n$ (rounded to the nearest integer) localizations from the n total localizations.

2.5 Comparison to "Ideal" Results

The "ideal" frame-connection results are specified as follows. For a given simulation, the underlying emitter generating each localization is noted. Localizations arising from the same emitter that occur within five frames of one another are then combined using **Eqs. 4**, **5**. These frame-connected localizations are considered to be the "ideal" frame-connection result.

The cumulative distribution function (CDF) of the nearest-neighbor distance distribution between frame-connected localizations was computed as follows. For a given set of frame-connected localizations, the nearest-neighbor to each localization within five frames (in the past or into the future, but excluding same frame neighbors) was found and their separation was stored. The binned CDF was then computed from the resulting set of nearest-neighbor distances. Comparisons to the "ideal" frame-connection CDF F_{ideal} were made by subtracting F_{ideal} from the binned CDF F of the results being compared. The difference $\delta \equiv F - F_{\text{ideal}}$ provides a visual tool for comparing frame-connection results. A deviation $\delta < 0$ suggests that localizations were connected that should not have been, since such over-connection would increase the expected nearest-neighbor distance. Similarly, a difference $\delta > 0$ suggests that frame-connection did not connect localizations which should have ideally been connected. Although this trend for δ may not necessarily hold for exceptionally high localization densities (e.g., for very high localization densities, incorrect connections may in fact cause the mean nearest-neighbor distance to decrease), we don't expect such data to be relevant in SMLM.

3 RESULTS

3.1 Uniformly Distributed Emitters

Simulated SMLM data for uniformly distributed emitters was generated as described in **section 2.4**. The frame-connection results from each of the algorithms (LAP-FC, hypothesis test, classical, and revised classical) are shown in **Figure 1**. ROI selections were made to highlight the performance of LAP-FC in comparison to the other algorithms. For the sole emitter blink present in **Figure 1** ROI 1, the LAP-FC algorithm was the only

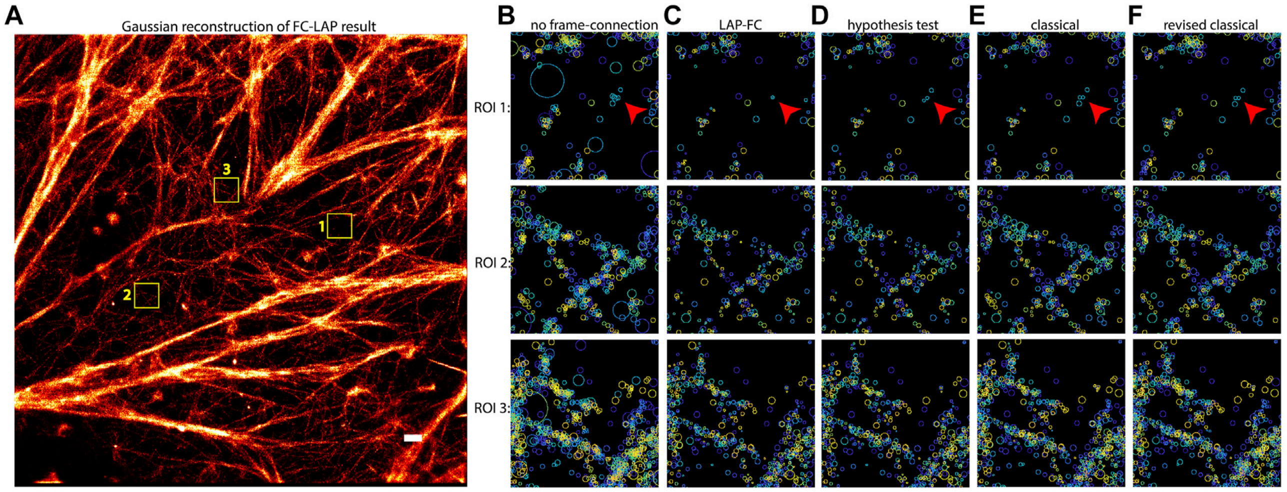

FIGURE 4 | Frame-connection results for actin microfilament localizations generated by multi-emitter fitting. **(A)** Gaussian reconstruction image of the LAP-FC frame-connection results. Selected ROIs indicated by numbered yellow boxes in (A) are shown for the frame-connection results using **(C)** LAP-FC with a maximum pre-clustering frame gap of five frames and a maximum separation of 5 times the localization error; **(D)** the hypothesis test algorithm with a maximum frame gap of five frames, a maximum separation of 1 pixel, and a level-of-significance of 0.05; **(E)** the classical algorithm with a maximum frame gap of 1 frame and a maximum separation of 0.2 pixels; and **(F)** the revised classical algorithm with a maximum frame gap of five frames and a maximum separation of 2 times the localization error. Scale bar = 0.5 μm. Localizations in **(B)**–**(F)** are displayed as circles of radius equal to the localization error centered on the estimated position and color-coded to indicate time, with dark blue indicating the start of the experiment and yellow indicating the end of the experiment. The red arrows in **(B)**–**(F)** ROI 1 point to a qualitatively interesting set of localizations.

method to completely connect all observed localizations. For **Figure 1** ROI 2, the hypothesis test, classical, and revised classical algorithms correctly connected most of the localizations. For **Figure 1** ROI 3, the classical and revised classical algorithms again connected most localizations correctly while failing to connect some others.

To compare the frame-connection algorithms for data with varying densities, a total of 40, 20, and 10 independent uniform emitter simulations were generated for initial emitter densities of $\rho_0 = 5$ emitters/pixel^2, $\rho_0 = 10$ emitters/pixel^2, and $\rho_0 = 20$ emitters/pixel^2, respectively, with the parameters otherwise matching those described in **section 2.4**. The deviation δ of the nearest-neighbor distance CDF from the ideal CDF was computed as described in **section 2.5**. The results are shown in **Figure 2**. For a relatively low initial emitter density of 5 emitters/pixel^2, all of the algorithms tend to under-cluster localizations, with LAP-FC showing closer correspondence to the ideal case; however, the hypothesis-test may slightly over-cluster as indicated by the dip of $\delta < 0$ in **Figure 2A**. For an initial density of 10 emitters/pixel^2, the hypothesis test algorithm shows the closest correspondence to the ideal frame-connection results, however the dip $\delta < 0$ seen in **Figure 2B** suggestive of over-clustering is more prominent than in **Figure 2A**. The LAP-FC algorithm shows the closest correspondence to the ideal result without indication of over-clustering. For an initial emitter density of 20 emitters/pixel^2, **Figure 2C** suggests that the hypothesis testing method is largely over-clustering localizations. The LAP-FC algorithm otherwise shows the closest correspondence to the ideal frame-connection results without significant over-clustering, however a small dip of $\delta < 0$ was present at a scale not visible in the figure.

For the simulations described in the preceding paragraph, histograms of the durations of frame-connected localizations were generated and are shown in **Supplementary Figure S2**. Comparing to the expected distribution (geometric with probability $p = 1 - \exp(-k)$, where $k \equiv k_{\text{off}} + k_{\text{bleach}}$) of frame-connected durations, all methods appear to have an overabundance of short durations, with the trend being similar at each tested density. LAP-FC and the hypothesis test method more closely reproduce the expected distribution than the classical and revised classical methods, with the hypothesis test showing the closest correspondence.

To test the robustness of LAP-FC with respect to its estimates of k_{on}, k_{off}, k_{bleach}, and p_{miss}, LAP-FC was repeated for the 20 $\rho_0 = 10$ emitters/pixel^2 simulations described above with varying values of each parameter. For each of the 20 simulations, LAP-FC was applied and the internally estimated values $\hat{k}_{\text{on}}$, $\hat{k}_{\text{off}}$, $\hat{k}_{\text{bleach}}$, and $\hat{p}_{\text{miss}}$ were noted (see **Supplementary Table S1**). LAP-FC was then applied to each simulation with externally prescribed values of k_{on}, k_{off}, k_{bleach}, and p_{miss}, with each parameter being varied individually with the other parameters held fixed at their true simulated value. Each parameter was varied to their upper and lower bound (see **Supplementary Text 1**) as well as to the maximum and minimum values estimated in the original LAP-FC application described above. The resulting values of δ were computed as described in 2.5 and plotted in **Supplementary Figure S1**. According to the results in **Supplementary Figure S1**, even large deviations in parameter estimates from the true values rarely lead to over-clustering by LAP-FC, and in all observed cases (i.e., excluding the upper and lower bound demonstrations), the results show little deviation from those when all parameters are set to their simulated value.

3.2 Simulated Dimer Emitters

Dimerized emitters were simulated at 20 spatial separations ranging uniformly from 0.1-1 pixel to investigate frame-connection performance for closely spaced emitters. Gaussian reconstruction images are shown for the results of each of the frame-connection algorithms in **Figure 3**. Overall, each of the tested algorithms performed well enough to observe the general trend in the data clear from the ideal result in **Figure 3A** (that is, pairs of closely spaced emitters with an increasing pair separation from left to right). The classical and the revised classical methods (**Figure 3D,E**, respectively) did not correctly connect as many localizations as the LAP-FC and hypothesis test methods (**Figure 3B,C**, respectively), however no over-clustering was apparent. Overall, the LAP-FC performed better than the other methods tested. No apparent over-clustering artifacts were introduced by any of the four algorithms tested.

3.3 High Duty Cycle Actin With Multi-Emitter Fitting

An SMLM dataset resulting from Bayesian multi-emitter fitting (Fazel et al., 2019a) of actin data with a relatively high localization density was used to compare the performance of the tested frame-connection algorithms. The results are shown in **Figure 4**. Inspecting the ROI selections made in **Figures 4C–F** and comparing to the non-frame connected results in **Figure 4B**, each of the algorithms appear to make reasonable connections based on localization spatiotemporal proximity. The LAP-FC and hypothesis testing algorithms made the most connections as is noticeable by the feature sharpness in **Figures 4C,D**. The classical and revised classical methods both fail to connect a pair of relatively isolated nearby emitters on the right hand side of ROI 1 (shown as blue circles and pointed to by small red arrows), which when compared to **Figure 4B** seem to be arising from the same emitter.

4 DISCUSSION

SMLM is rapidly becoming a commonplace tool for researchers in need of nanoscale spatial resolution in fluorescence microscopy. The expansion of SMLM outside of dedicated research labs necessitates reliable analyses which can be trusted without expert intervention. Quantitative analysis of the resulting super-resolved localizations requires, in many cases, a well-characterized correspondence between localizations and emitters. That is to say, many analyses of super-resolved localizations require a one-to-one relationship between localization and emitter. While recent techniques have largely solved this localization clustering problem (Fazel et al., 2019b), any such method will be limited by the reliability of the input localizations. If the input localizations contain a very large proportion of repeated localizations, such post-processing tools may be pushed to their practical limits, for example leading to infeasible computational costs. Alternatively, localizations which have been over-clustered (i.e., localizations from distinct emitters that were connected together) represent a loss of information unlikely to be captured by any post-processing analysis.

Many steps in SMLM data analysis have been refined and validated (e.g., fitting the localizations and determining the error in their positions), however the frame-connection problem has received little attention. Known existing methods for solving the frame-connection problem have not reached an optimal solution. We have shown that the classical and the revised classical methods are perhaps too conservative in their assignment of connections to make optimal use of the data. On the other hand, the hypothesis testing method is perhaps too liberal in its assignment of connections. We have shown that the hypothesis testing method for frame-connection, which typically provides more appealing results than the classical and revised classical methods, is susceptible to over-clustering at high densities. Furthermore, results of the classical, revised classical, and the hypothesis test algorithms rely heavily on the selection of arbitrary thresholds. We have shown that, by formulating the frame-connection problem as a linear assignment problem with statistically motivated assignment costs, these common artifacts can largely be reduced, with the added benefit that arbitrary thresholds are used only in a pre-processing step. Our algorithm accounts for the local emitter densities, the kinetic rates of blinking, and the possibility of missing localizations of a visible emitter. By combining all of this knowledge, our algorithm exceeds the performance of other known frame-connection problems with minimal to no over-clustering.

DATA AVAILABILITY STATEMENT

The raw data supporting the conclusions of this article will be made available by the authors, without undue reservation.

AUTHOR CONTRIBUTIONS

DS and KL were jointly involved in all aspects of the paper including conception of the algorithm and preparation of the article.

FUNDING

DS and KL were supported by NIH grants R21GM132716 and R01CA248166. KL was additionally supported by NIH grant P30CA118100.

ACKNOWLEDGMENTS

We thank Dr. Michael J. Wester for providing feedback during article preparation. We would also like to thank Dr. Hanieh Mazloom-Farsibaf for the actin dataset and Dr. Mohamadreza Fazel for Bayesian multi-emitter fitting analysis of the actin dataset.

SUPPLEMENTARY MATERIAL

The Supplementary Material for this article can be found online at: https://www.frontiersin.org/articles/10.3389/fbinf.2021.724325/full#supplementary-material

REFERENCES

Betzig, E., Patterson, G. H., Sougrat, R., Lindwasser, O. W., Olenych, S., Bonifacino, J. S., et al. (2006). Imaging Intracellular Fluorescent Proteins at Nanometer Resolution. *Science* 313, 1642–1645. doi:10.1126/science.1127344

Daszykowski, M., Walczak, B., and Massart, D. L. (2001). Looking for Natural Patterns in Data. *Chemometrics Intell. Lab. Syst.* 56, 83–92. doi:10.1016/S0169-7439(01)00111-3

Deschout, H., Cella Zanacchi, F., Mlodzianoski, M., Diaspro, A., Bewersdorf, J., Hess, S. T., et al. (2014). Precisely and Accurately Localizing Single Emitters in Fluorescence Microscopy. *Nat. Methods* 11, 253–266. doi:10.1038/nmeth.2843

Fazel, M., Wester, M. J., Mazloom-Farsibaf, H., Meddens, M. B. M., Eklund, A. S., Schlichthaerle, T., et al. (2019a). Bayesian Multiple Emitter Fitting Using Reversible Jump Markov Chain Monte Carlo. *Sci. Rep.* 9, 13791. doi:10.1038/s41598-019-50232-x

Fazel, M., Wester, M. J., Rieger, B., Jungmann, R., and Lidke, K. A. (2019b). Sub-Nanometer Precision Using Bayesian Grouping of Localizations. *bioRxiv*, 752287. doi:10.1101/752287

Gillespie, D. T. (1976). A General Method for Numerically Simulating the Stochastic Time Evolution of Coupled Chemical Reactions. *J. Comput. Phys.* 22, 403–434. doi:10.1016/0021-9991(76)90041-3

Heilemann, M., Van De Linde, S., Schüttpelz, M., Kasper, R., Seefeldt, B., Mukherjee, A., et al. (2008). Subdiffraction-resolution Fluorescence Imaging with Conventional Fluorescent Probes. *Angew. Chem. Int. Ed. Engl.* 47, 6172–6176. doi:10.1002/anie.200802376

Hess, S. T., Girirajan, T. P., and Mason, M. D. (2006). Ultra-high Resolution Imaging by Fluorescence Photoactivation Localization Microscopy. *Biophys. J.* 91, 4258–4272. doi:10.1529/biophysj.106.091116

Jaqaman, K., Loerke, D., Mettlen, M., Kuwata, H., Grinstein, S., Schmid, S. L., et al. (2008). Robust Single-Particle Tracking in Live-Cell Time-Lapse Sequences. *Nat. Methods* 5, 695–702. doi:10.1038/nmeth.1237

Jonker, R., and Volgenant, A. (1987). A Shortest Augmenting Path Algorithm for Dense and Sparse Linear Assignment Problems. *Computing* 38, 325–340. doi:10.1007/bf02278710

Jungmann, R., Steinhauer, C., Scheible, M., Kuzyk, A., Tinnefeld, P., and Simmel, F. C. (2010). Single-molecule Kinetics and Super-resolution Microscopy by Fluorescence Imaging of Transient Binding on DNA Origami. *Nano Lett.* 10, 4756–4761. doi:10.1021/nl103427w

Levet, F., Hosy, E., Kechkar, A., Butler, C., Beghin, A., Choquet, D., et al. (2015). SR-tesseler: a Method to Segment and Quantify Localization-Based Super-resolution Microscopy Data. *Nat. Methods* 12, 1065–1071. doi:10.1038/nmeth.3579

Marin, Z., Graff, M., Barentine, A. E. S., Soeller, C., Chung, K. K. H., Fuentes, L. A., et al. (2021). PYMEVisualize: an Open-Source Tool for Exploring 3D Super-resolution Data. *Nat. Methods* 18, 582–584. doi:10.1038/s41592-021-01165-9

Nino, D. F., and Milstein, J. N. (2021). Estimating the Dynamic Range of Quantitative Single-Molecule Localization Microscopy. *bioRxiv*. doi:10.1101/2021.05.24.445502

Ovesný, M., Křížek, P., Borkovec, J., Švindrych, Z., and Hagen, G. M. (2014). ThunderSTORM: A Comprehensive ImageJ Plug-In for PALM and STORM Data Analysis and Super-resolution Imaging. *Bioinformatics* 30, 2389–2390. doi:10.1093/bioinformatics/btu202

Rust, M. J., Bates, M., and Zhuang, X. (2006). Sub-diffraction-limit Imaging by Stochastic Optical Reconstruction Microscopy (STORM). *Nat. Methods* 3, 793–795. doi:10.1038/nmeth929

Sage, D., Pham, T. A., Babcock, H., Lukes, T., Pengo, T., Chao, J., et al. (2019). Super-resolution Fight Club: Assessment of 2D and 3D Single-Molecule Localization Microscopy Software. *Nat. Methods* 16, 387–395. doi:10.1038/s41592-019-0364-4

Sergé, A., Bertaux, N., Rigneault, H., and Marguet, D. (2008). Dynamic Multiple-Target Tracing to Probe Spatiotemporal Cartography of Cell Membranes. *Nat. Methods* 5, 687–694. doi:10.1038/nmeth.1233

Small, A., and Stahlheber, S. (2014). Fluorophore Localization Algorithms for Super-resolution Microscopy. *Nat. Methods* 11, 267–279. doi:10.1038/nmeth.2844

Smith, C. S., Joseph, N., Rieger, B., and Lidke, K. A. (2010). Fast, Single-Molecule Localization that Achieves Theoretically Minimum Uncertainty. *Nat. Methods* 7, 373–375. doi:10.1038/nmeth.1449

Wester, M. J., Schodt, D. J., Mazloom-Farsibaf, H., Fazel, M., Pallikkuth, S., and Lidke, K. A. (2021). Robust, Fiducial-free Drift Correction for Super-resolution Imaging. *bioRxiv*. doi:10.1101/2021.03.26.437196

Conflict of Interest: The authors declare that the research was conducted in the absence of any commercial or financial relationships that could be construed as a potential conflict of interest.

frontiers in Bioinformatics

CORRECTION
published: 25 January 2022
doi: 10.3389/fbinf.2021.836606

Corrigendum: Spatiotemporal Clustering of Repeated Super-Resolution Localizations via Linear Assignment Problem

*David J. Schodt and Keith A. Lidke**

Department of Physics and Astronomy, University of New Mexico, Albuquerque, NM, United States

Keywords: fluorescence microscopy, super-resolution, image analysis, computational modeling, single molecule techniques

A Corrigendum on

Spatiotemporal Clustering of Repeated Super-Resolution Localizations via Linear Assignment Problem
by Schodt D. J and Lidke K. A (2021). Front. Bioinform. 1:724 325. doi: 10.3389/fbinf.2021.724325

In the original article, there was an error. **Eq. (2)** was written incorrectly. A correction has been made to *MATERIALS AND METHODS*, *Estimating Local Emitter Densities and Kinetic Rates*, *Paragraph Number 2*:

The expected cumulative number of localizations observed by frame f is given by

$$\langle n_{\text{cumulative}} \rangle (f) \approx N_{\text{emitters}} (1 - p_{\text{miss}}) \tau \left\{ \frac{1 - \exp[-\lambda_1 (f - 1)]}{\lambda_1} - \frac{1 - \exp[-\lambda_2 (f - 1)]}{\lambda_2} \right\} \tag{2}$$

In the original article, there was an error. An unlabeled equation was written incorrectly. Additionally, a line of text in the associated paragraph was written incorrectly. A correction has been made to *MATERIALS AND METHODS*, *Estimating Local Emitter Densities and Kinetic Rates*, *Paragraph Number 4*:

The local pre-cluster density corresponding to each pre-cluster is estimated by finding the k (chosen to be two in this study) nearest pre-clusters and then computing $\rho_c = (k+1)/\pi r_k^2$ where r_k is the distance to the kth nearest pre-cluster. The underlying local emitter density present at the beginning of the experiment is then estimated for each pre-cluster as

$$\hat{\rho}_{0,\text{local}} = \rho_c \frac{1}{\hat{k}_{\text{off}} \hat{\tau}} \frac{1}{1 - \hat{p}_{\text{miss}}} \left\{ \frac{1 - \exp[-\hat{\lambda}_1 (f_{\text{end}} - 1)]}{\hat{\lambda}_1} - \frac{1 - \exp[-\hat{\lambda}_2 (f_{\text{end}} - 1)]}{\hat{\lambda}_2} \right\}^{-1}$$

where f_{end} is the last frame containing localizations in the experiment.

The authors apologize for this error and state that this does not change the scientific conclusion of the article in any way. The original article has been updated.

OPEN ACCESS

Edited and reviewed by:
Thomas Pengo,
University of Minnesota Twin Cities,
United States

****Correspondence:***
Keith A. Lidke
klidke@unm.edu

Specialty section:
This article was submitted to Computational BioImaging, a section of the journal Frontiers in Bioinformatics

Received: *15 December 2021*
Accepted: *21 December 2021*
Published: *25 January 2022*

Citation:
Schodt DJ and Lidke KA (2022) Corrigendum: Spatiotemporal Clustering of Repeated Super-Resolution Localizations via Linear Assignment Problem. Front. Bioinform. 1:836606. doi: 10.3389/fbinf.2021.836606

frontiers in Bioinformatics

METHODS
published: 28 October 2021
doi: 10.3389/fbinf.2021.740342

3D Structure From 2D Microscopy Images Using Deep Learning

Benjamin Blundell[1], Christian Sieben[2], Suliana Manley[3], Ed Rosten[4], QueeLim Ch'ng[1] and Susan Cox[5]*

[1]Centre for Developmental Biology, Institute of Psychiatry, Psychology and Neuroscience, King's College London, London, United Kingdom, [2]Nanoscale Infection Biology Lab (NIBI), Helmholtz Centre for Infection Research, London, Germany, [3]École Polytechnique Fédérale de Lausanne, Lausanne, Switzerland, [4]Snap, Inc., London, United Kingdom, [5]Randall Centre for Cell and Molecular Biophysics, King's College London, London, United Kingdom

Understanding the structure of a protein complex is crucial in determining its function. However, retrieving accurate 3D structures from microscopy images is highly challenging, particularly as many imaging modalities are two-dimensional. Recent advances in Artificial Intelligence have been applied to this problem, primarily using voxel based approaches to analyse sets of electron microscopy images. Here we present a deep learning solution for reconstructing the protein complexes from a number of 2D single molecule localization microscopy images, with the solution being completely unconstrained. Our convolutional neural network coupled with a differentiable renderer predicts pose and derives a single structure. After training, the network is discarded, with the output of this method being a structural model which fits the data-set. We demonstrate the performance of our system on two protein complexes: CEP152 (which comprises part of the proximal toroid of the centriole) and centrioles.

Keywords: SMLM, deep-learning, structure, storm, AI

OPEN ACCESS

Edited by:
Thomas Pengo,
University of Minnesota Twin Cities,
United States

Reviewed by:
Paul Henderson,
Institute of Science and Technology Austria (IST Austria), Austria
Jan Egger,
Graz University of Technology, Austria
Søren Hauberg,
Technical University of Denmark, Denmark

***Correspondence:**
Susan Cox
susan.cox@kcl.ac.uk

Specialty section:
This article was submitted to Computational BioImaging, a section of the journal Frontiers in Bioinformatics

Received: *12 July 2021*
Accepted: *12 October 2021*
Published: *28 October 2021*

Citation:
Blundell B, Sieben C, Manley S, Rosten E, Ch'ng Q and Cox S (2021) 3D Structure From 2D Microscopy Images Using Deep Learning. Front. Bioinform. 1:740342. doi: 10.3389/fbinf.2021.740342

1 INTRODUCTION

Imaging mesoscale 3D biological structures (that is, those between the nano- and the micro-scale) is a critical problem in biology, as many processes of biological interest rely on collections of proteins or other molecules arranged into a distinct architecture. Currently two major techniques can provide data on the shape of such aggregates: electron microscopy and light (particularly fluorescence) microscopy. Electron microscopy (EM) offers resolution below 1 nm, but is limited in the thickness of the samples it can observe, and analysis is relatively complex, generally requiring multiple particle averaging (Milne et al., 2013). Fluorescence microscopy is experimentally relatively simple and can deal with larger samples, but generally yields only single images which are limited in resolution to about 250 nm (Schermelleh et al., 2010).

Super-resolution techniques allow this limit to be broken, pushing the achievable resolution down to 20–100 nm. In particular, single molecule localisation microscopy (SMLM) yields high resolution images (around 20–30 nm), while allowing large amounts of data to be collected (Schermelleh et al., 2010; Holden et al., 2014) and being relatively experimentally simple. SMLM imaging has a trade off between the x, y and z resolution: gaining information in the z direction is possible, but generally at the expense of in-plane information quality (Badieirostami et al., 2010). Therefore, 2D images will have the highest localisation quality, but clearly limit information on 3D structure.

The challenge of how to infer 3D information from 2D images has been tackled both from the perspective of synthesising EM images to create a 3D structural model (Milne et al., 2013), and in the

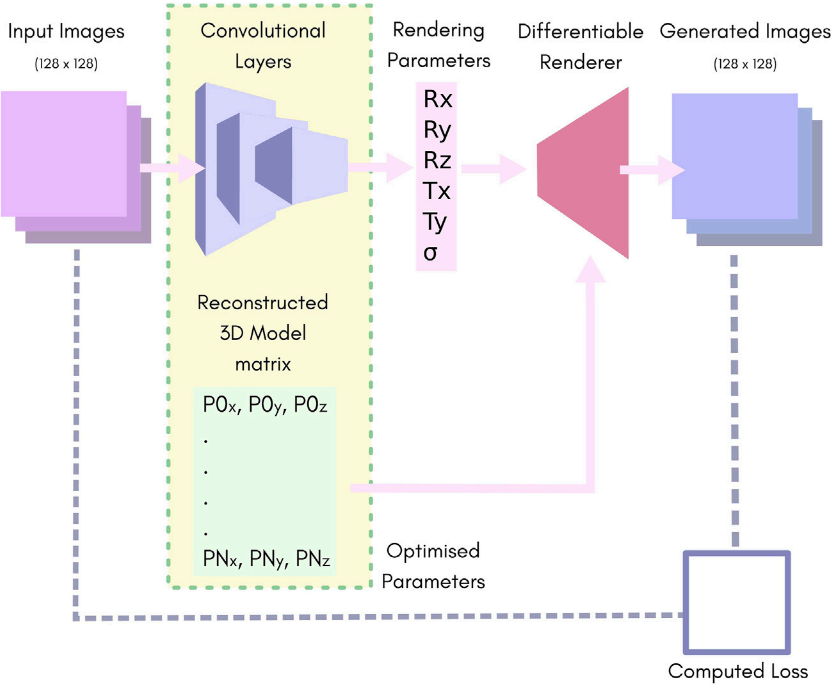

FIGURE 1 | An overview of our network. Batches of images of size 128 × 128 pixels are fed to the convolution layers, which reduce the batch down to 6 parameters. These are passed to the rendering pipeline along with the 3D reconstruction matrix to produce a batch of output images. The rendering parameters Rx, Ry and Rz represent the rotation in "Angle-Axis" form. Tx and Ty represent translation in the X, Y plane. S represents the predicted output-sigma. The 3D reconstruction matrix contains a list of vertices representing the predicted point-cloud.

computer vision field to infer a 3D structure from a single image of a single object (Fan et al., 2017). In recent years, deep learning has emerged as a promising approach to improve structural fitting.

Convolutional neural networks are one of the most well known forms of Deep Learning - convolving the data with a kernel (Goodfellow et al., 2016). This process reduces the size of the principal data dimensions, creating a number of feature maps or filters, each sensitive to a particular, local aspect of the data. Through training, the network parameters adjust to produce the required output.

Here, we use a deep learning network to infer the pose of point cloud data and 3D structure. Our algorithm HOLLy (Hypothesised Object from Light Localisations) allows us to perform a completely unconstrained model fit from 2D SMLM images.

2 METHODS

2.1 Modelling Pose Using Deep Learning

HOLLy fits a 3D model against a set of 2D images of the same biological structure. The input images are typically super-resolved SMLM reconstructions, each of which is a z projection of the structure being imaged from some unknown rotational orientation and translation. The goal is to deduce the pose (rotation and translation) for each input image and infer a single 3D model for the entire data-set.

The 3D model is a collection of points (with their co-ordinates represented by a matrix) which are initiated at random positions. The current positions of the points, and the pose corresponding to each input image, are used to generate a simulated microscopy image corresponding to each input image (with the image being projected in z into a single x-y plane). The image is rendered with a Gaussian at each point, as is standard for SMLM. Each Gaussian has the same sigma, which is a parameter of the renderer, and the resulting image is differentiable with respect to the point coordinates and sigma. Our renderer is designed to efficiently and accurately render SMLM point clouds. This is in contrast to existing state of the art such as OpenDR (Loper and Black, 2014), DiRT (Henderson and Ferrari, 2020), PyTorch3D (Ravi et al., 2020), Pulsar (Lassner and Zollhöfer, 2020) and DWDR (Han et al., 2020) which are designed primarily to render illuminated, textured meshes with perspective cameras (or in the case of Pulsar and Insafutdinov and Dosovitskiy (2018), rendering with spheres), our renderer is simpler and more closely models SMLM. Rather than rendering rasterised triangles, HOLLy converts the final 2D points to Gaussians.

We used a simple convolutional neural network (CNN) consisting of 10 layers of strided convolutions and Leaky-ReLU (Aggarwal, 2018), followed by two fully connected layers. **Figure 1** highlights the major components (further

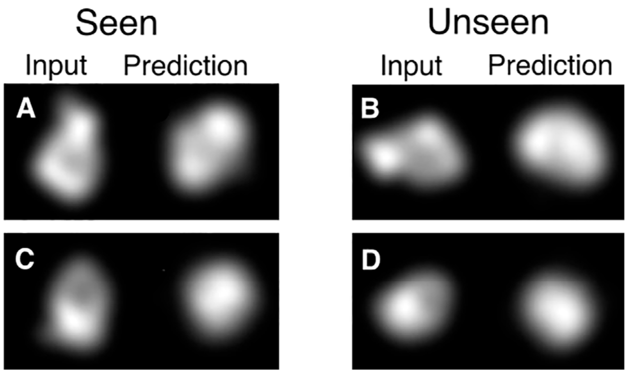

FIGURE 2 | Demonstration of information sharing between different poses with the CNN. HOLLy was stopped half-way through the first epoch of training, meaning only half of the data has been used for training. Note that for the half of the data which has been seen, this corresponds to a single step of gradient descent per image, and half of the data has not yet been used at all. Already it can be observed that in many cases on seen data (illustrated in **A, C**) there is correspondence between the input and output shapes (albeit imperfect as it is very early in the optimization process). The advantage of the CNN can be observed in the results on unseen data where this correspondence also exists **(B, D)**. This partial convergence on unseen data shows that the CNN allows earlier data to assist in the convergence of data seen later, which provides a very substantial improvement over modelling poses separately.

information can be found in **Supplementary Material**: HOLLy technical details).

The CNN yields six outputs. The position and orientation of the model are described by the translation in X and Y, and three rotation parameters for which we used the axis-angle formulation. The sixth parameter is the output-sigma value which is used as the sigma for the renderer. Note that the output-sigma explicitly differs from the resolution of the input images, i.e., in the case where input images are themselves reconstructions of SMLM data, the sigma used for their reconstruction (*input-sigma*) is not the same as output-sigma.

In principle, if the input data were perfect, the output sigma could be fixed to be equal to the input sigma. Since this is not the case, allowing the model to predict output-sigma allows it to account for some of the noise in the data. For example, consider the case of scatter (noise in the position of fluorophores). That is essentially a stochastic blur of the model structure, so when the reconstructed 3D model (which has no scatter) is rendered, the sigma needs to be higher in order for the output to be a good match to the input. This is discussed further in **Section 2.6**.

The key element of our system is the use of a CNN to predict the pose for each input image. Allowing for a pose per image is a significant advantage over techniques such as template matching based Cryo-EM (Milne et al., 2013), or classification of the images by view (Salas et al., 2017) since the system is not limited to a small number of orientations, and views do not have to be determined a-priori on unknown structure in order to build a classifier.

Additionally, using a CNN to predict the pose has a big advantage in modelling a pose per image as it makes the overall optimization much more tractable. The reason for this is that the space is in some sense smooth and images that are close in appearance will usually also be close in pose. This allows the network to aggregate information from similar images in order to get a better prediction of the pose for all of them. It also allows for fast convergence because an improvement on one image can cause an improvement in many others. We illustrate this in **Figure 2**, where data that is not seen during training can generate outputs that correspond to the input.

The advantage of using a CNN can be illustrated by attempting to solve the same problem by direct optimisation. We removed the convolutional layers from the architecture shown in **Figure 1**, replacing them with a single $5 \times N$ matrix (N being the size of the training set). A training batch consists of a batch of images and their corresponding poses from that $5 \times N$ matrix. These differentiable render is used to render the model with these poses. This rendered images are compared to the corresponding input image creating a loss as before. The loss is back-propagated through the diffentiable renderer and used to update the model and the poses. Various learning rates, models and optimisers were tested.

This direct optimisation approach could not reproduce 3D sample structure or model the pose correctly. We suspect this is due to both a lack of shared rotational model between data and the difficulty of modelling rotation. The results can be found in **Supplementary Material**: Direct Optimisation. These results demonstrate the advantages of using a CNN in this scenario.

2.2 The Output Is a Structural Model Rather Than a Trained Network

Often, the value of a neural network is the network itself that can be used to predict, discriminate or otherwise solve a particular problem once trained. Our approach ignores the network once it has been trained; the value in our approach is the 3D model stored in the Reconstructed 3D Model matrix.

This 3D model gradually improves as training continues. The user can stop training at any time, typically when the loss stops improving. The final positions of the points in the 3D reconstruction matrix represent the final structure, whereupon the network is no longer required.

2.3 Simulated Data Models

In order to evaluate HOLLy, we selected a number of ground-truth point-clouds with different characteristics: a reduced version of the Stanford Bunny[1], the Utah Teapot[2] and an approximation of the CEP152/HsSAS-6 complex (Sieben et al., 2018).

All of the models consist of a relatively small number of vertices (fewer than 400). Each have unique characteristics, such as different numbers of vertices, symmetries and voids (see **Section 3** - Results). The Stanford Bunny and Utah Teapot are standard in computer vision tests as they have properties

---

[1] http://graphics.stanford.edu/data/3Dscanrep/\#bunny

[2] https://www.computerhistory.org/collections/catalog/102710359

that are likely to prove challenging. The Utah teapot is close to, but not quite, symmetric, and the Stanford bunny has fine structure (ears) but also relatively large areas of smooth structure (back). These properties showcase the potential of the method to yield results as experimental data improves.

As we have complete control of data-set generation from synthetic models, we must choose the distribution of data across the translation and rotation space. We uniformly sampled the 3D rotation group—SO(3)—which consists of all rotations in Euclidean $\mathfrak{R}^3$ space, centred at the origin, using the equation presented by[3] Kirk (1994). The models used in the simulated data are small enough to be rendered "on-the-fly" into images as the network trains.

2.4 Experimental Data From Biological Structures

Our main biological targets were a centriolar complex comprised of the CEP152 protein, and purified centrioles.

The first dataset was a super-resolution (STORM) microscopy data-set of CEP152, obtained and analysed as described in Sieben et al. (2018). The structure of this centro-symmetric complex has been fitted with a toroid and found to be 400 nm in diameter (Sieben et al., 2018), which subsequent work confirmed (Kim et al., 2019). This yielded a list of localisations for each identified CEP152 structure which were reconstructed localisations into 2D images, rendering with a Gaussian. Since the number of localisations in the experimental SMLM data-sets outnumber the modelled point-cloud by a factor of 20, this process is computationally intensive, and so these images are pre-rendered and stored on disk.

This data-set consists of 4,663 individual images. Some of these show incomplete labelling or are not centriole structures (such as all the fluorophores converging on a single, bright spot). Erroneous data were removed manually, reducing the data-set size to 2055. Data was augmented by a factor of 20 rotating the entire centriole within the field of view using a 2D rotational matrix, giving a final training set size of around 40,000. As the data is represented by points and not a bitmap, it can be rotated by an arbitrary angle without introducing additional artefacts. Examples of the STORM CEP152 training images can be found in the **Supplementary Figure S2**.

The second data-set is derived from expansion microscopy experiments to image labelled glutamylated tubulin in centrioles purified from *Chlamydomoanas reinhardtii* (Mahecic et al., 2020). The images are segmented and presented as tiff stacks of size 128 × 128 × 84 in xyz. A sum projection is carried out to eliminate the information in z, creating a 2D image of an unknown blur. Each image was cropped to 60 × 60 pixels centred on the protein complex.

As the data are represented by pixels and not a list of localisations, augmentation is limited to the four cardinal directions to avoid the creation of artefacts. The resulting data-set is 14,612 items in size. As the point-spread function is not modelled, there is no base input-sigma. A Gaussian blur of decreasing sigma is applied "on-top-of" the existing image (see **Supplementary Figure S3**).

2.5 Input Images

The input to the network consists of a batch of 2D images, each of the same target object from different viewpoints. These images may be simulated (rendered from a known ground-truth 3D model) or derived from experimental data.

For both simulated and real SMLM data, rendering with a Gaussian generates a 2D image, with the resolution of the reconstruction being determined by the input-sigma. For the simulated data the 2D point cloud is generated by applying a random rotation and translation, adding noise and projecting away Z. For data in the form of images were blurred with a Gaussian, with input-sigma as the width.

Before being passed into the network, the input images were normalised to ensure that the pixel values fall within boundaries usable by the network (see **Section 2.8**).

Deep learning requires a large, representative training set for results to be accurate. For accurate 3D reconstruction, it is important to sample diverse angles since areas of the object not represented in the training data will not be reconstructed. In the simulated case, data-sets of any size can be generated (time permitting). However, this is not the case for the experimental data.

2.6 Sigma

The input-sigma value, which defines the level of blur (i.e., resolution) in the input images, is initialised at a high value (one which would produce an image with around diffraction limited resolution). The value is then decreased on a curve as the network trains. By starting with a larger input-sigma, the loss between the input and output images is smaller, with shallower gradients over larger distances. This allows the network to broadly optimise the points in the 3D reconstructed model matrix, refining finer detail as the input-sigma is reduced.

The lowest value for sigma can be set to the expected localization error for a particular SMLM experiment. The input-sigma curve can be found in the **Supplementary Figure S1**. The output-sigma (that is, the sigma used by the differentiable renderer to create images from the hypothesised model) is predicted by the network. The output-sigma can be set to match the known input-sigma, but early experiments suggest that predicting the output-sigma increases the network's tolerance to scattered or missing fluorophores. By increasing the output-sigma the blur increases, accommodating the scattered points.

In experimental data, we would expect around an ~8 nm scatter in position due to the antibody used and an additional ~12 nm degradation in precision due to the localisation accuracy. Such values suggest an expected resolution around 20nm, with an expected sigma around 10 nm. For our STORM CEP152 experiments we set the lower-bound of the input-sigma to a value of ~3.2 pixels, which equates to 30 nm using the scale provided with the data. The input-sigma changes at the end of each epoch, rather than continuously, giving a "stepped-curve"

---

[3] https://demonstrations.wolfram.com/SamplingAUniformlyRandomRotation/

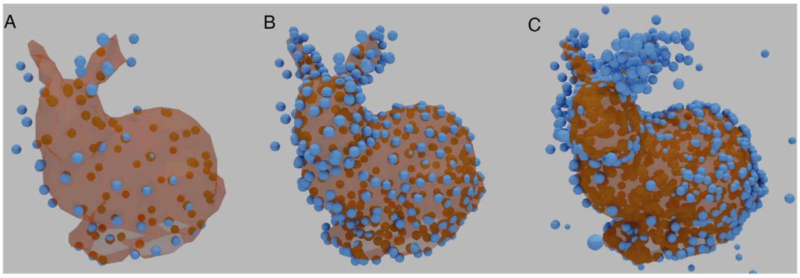

FIGURE 3 | Examples of a reconstructed Stanford Bunny using different sizes of 3D reconstruction matrices. **(A)** contains 100 vertices. **(B)** contains 350 vertices, the same number as the underlying ground truth. **(C)** contains 1,000 vertices. HOLLy manages to reproduce the basic shape throughout.

(see **Supplementary Material**: Note 3 - input-sigma Hyper-parameter and **Supplementary Figure S1**) This is due to the images being pre-rendered before training begins. This decision was made for performance reasons.

The expansion microscopy centriole data-set has a scale of 14 nm per pixel. The additional input sigma curve begins at 2.8 pixels (~ 40 nm), reducing to zero. The smaller initial input sigma attempts to account for the smaller image size and the unknown resolution of the data.

2.7 Loss Function

The loss is calculated directly between images by comparing the pixel values between the input data and the predicted result, using the PyTorch L1 Reduction option[4] with the 'sum' reduction. Rather than use the L1 loss between entire images, a mask was generated from target image. The loss was calculated only for these pixels that are within the mask, with areas outside the mask set to zero for both input and output images.

2.8 Reconstructed 3D Model Matrix and Normalisation

As training progresses, the matrix of 3D points that represents the reconstructed 3D model moves from a random positions to yield a recognisable structure. The size of this matrix (the number of points to optimise) is ultimately limited by the amount of memory and time available to the end user. The matrix size is chosen by the user before training starts. In simulated tests, the number of points responsible for generating the input image is generally known, except when multiple fluorophore reappearances per point are simulated.

Since the number of points affects the integrated intensity of the image, and thus the loss, the number of points is linked to the appropriate learning rate. Normalisation was therefore required to bring the training data into numerical ranges the network can process without generating extreme gradients. The image tensor was divided by the integrated intensity, followed with a multiplication by a fixed scalar. **Figure 3** shows three examples of Stanford Bunny Reconstructions, each with a different size of 3D reconstruction matrix, with normalisation applied. In each case, the basic shape is recognisable, with increasing detail.

2.9 Hyper-Parameter Choices

Hyper-parameters are the user-chosen settings (Goodfellow et al., 2016), rather than the learned parameters. Our parameters were chosen using a combination of existing defaults and explorations within reasonable ranges.

To verify that the learning rate selected was appropriate the suggested value of 0.004 for the Adam Optimizer (Kingma and Ba, 2017) was varied by a factor of 10 in both directions, stopping when structure reproduction began to fail, with a score of 0.0004.

The simulated data-sets used comprised 40,000 images, generated from an initial set of 2000 images. Each image was augmented 20 times by a random rotation around the *Z* axis to better match the experimental data.

The number of images presented to the network at each training step (the batch-size) can affect the final accuracy of the network (Kandel and Castelli, 2020). A batch-size of 32 was selected as appropriate. Decreasing the batch size too far caused reproduction to suffer and increasing too far caused memory usage to become computationally limiting.

The final parameter considered was the number of epochs (that is, the training time). An epoch is completed when the network has processed the entire training set once. A range of number of epochs were tested, with a value of 40 being found to be an acceptable trade-off between accuracy and time.

This baseline for training with simulated data was chosen after a number of results from earlier tests, with the restrictions of the final experimental data in mind. The most important of these is the training set size and construction. Experiments with increasing the size of the simulated training set gave improved results, but we are restricted in the size of the real, experimental data. Therefore we chose to match the size of the experimental data-set when performing the simulated experiments.

Further details of these hyper-parameters used in our experiments are listed in **Supplementary Material**: Note 5.

2.10 Implementation

Experiments were carried out with a nVidia GeForce 2080Ti GPU. Training duration was around 8 h with the settings given as the baseline. Larger numbers of points in the reconstructed 3D model dramatically increased memory usage.

---

[4] https://pytorch.org/docs/stable/generated/torch.nn.L1Loss.html

The estimated energy use to train a model is 2.1 kWh based on a measurement of 623.4 kWh over 166 days. In this period, 298 models were trained and evaluated. This was confirmed by cross-checking against the wattage of the GPU and the time spent to generate a model.

Further technical details may be found in **Supplementary Material**: HOLLy Technical Details.

3 RESULTS

3.1 Evaluation Criteria

The 3D structure which the network attempts to reconstruct is represented as a point cloud with the coordinates of each point stored in the 3D reconstruction matrix. The network attempts to learn the orientation over time, and simultaneously improves its own internal representation of the 3D structure by comparing 2D renders of the point cloud against the training images.

The effectiveness of our approach was assessed by measuring the similarity between the input point-cloud and the resulting point-cloud stored in the model's 3D reconstruction matrix. Finding the absolute best match between two structures is an NP-hard problem, and therefore a definitive score is not possible. Given this, we selected the root mean squared distance (RMSD) between two equivalent vertices in each point-cloud as an acceptable measure. Equivalence is determined by finding the closest neighbour with the Iterative Closest Point (ICP) (Arun et al., 1987) algorithm within CloudCompare[5].

ICP relies on an rough, initial alignment. We performed this step manually, then applied ICP to obtain our RMSD score, independent of the pose predicted by the network. To find an RMSD score baseline to compare against we attempted to match two random clouds covering the same world-space as our model.

The parameters used in these experiments can be found in **Supplementary Material**: Experiment parameters.

3.2 Simulated Results

To assess the accuracy of our proposed method, a set of commonly used 3D models were chosen to evaluate the approach. The availability of a ground-truth structure allowed us to measure how well our network performs under different conditions. To validate our approach, we first performed a set of baseline experiments to determine how well the network could infer the 3D structure when only presented with 2D renders of these models.

3.2.1 Baseline Experiments - Stanford Bunny

The first model tested was the Stanford Bunny. This model has no symmetry, contains fine detail, protrusions and a homogeneous distribution of vertices across its surface. It contains considerably more points than the other point-clouds used, though the version in our experiments is in the order of hundreds of vertices as opposed to tens of thousands in the original point-cloud.

All results from baseline experiments were noise free (i.e., every generated fluorophore was exactly at an existing vertex position, there was only one per vertex position, and every vertex position was occupied). The baseline results all had low RMSD scores, considerably less than 0.17, the average score when aligning two random point clouds of the same size (**Figure 4**). However, three of the runs showed a mirroring error, where the network mirrors the point-cloud in the dorsal plane. This is due to the lack of depth information in the training images (**Figure 4**), and is a fundamental ambiguity.

3.2.2 Baseline Experiments - Utah Teapot

Our second choice of model was the Utah Teapot, which posed several challenges for our method: the similarity of the handle and spout (when rendered using points), the bilateral symmetry and the large voids between the layers of points in the central body.

It was reconstructed well and the pose was well predicted. However, the handle appeared to be the same as the spout. Both of these areas are low in information with few ground truth points. The predicted structure therefore has an additional transverse plane of symmetry not present in the ground-truth (**Figure 5**). From the tip of the spout, to the edge of the handle, the distance is 1036nm, using the CEP152 experiment scale.

3.2.3 Baseline Experiments - Approximation of the CEP152/HsSAS-6 Complex

The third point-cloud used in these experiments is an approximation of the CEP152/HsSAS-6 complex (Sieben et al., 2018). The approximation consisted of two cylinders, one smaller and perpendicular to the other. This point-cloud is somewhat smaller than the others and is extremely regular with large gaps between the columns of points.

The smaller, cylindrical structure is offset towards the top of the larger structure in the ground-truth; this is not reflected in the reconstruction. This is likely due to the size of the point-cloud in the view - fine detail is hard to discern when the point-cloud is small (**Figure 6**). From the end of the small cylinder to the furthest edge of the larger cylinder, the distance is roughly 415 nm.

Together, these baseline experiments indicate that our approach is suitable for reconstructing the overall 3D structure from a series of 2D images. Most results showed low RMSD scores and produced structures that are a good match to the original 3D models.

3.3 Modelling Experimental Noise in Simulated Results

Our method aims to discern structure from fluorescence microscopy images, particularly super-resolution. We therefore focused on the kinds of problems often encountered in such experiments. Fluorophores are offset from the object they are labelling, they may not bind to certain areas, or might bind multiple times. They may not illuminate consistently or they may not be separable from their neighbours. We modelled three forms of experimental noise: missing fluorophores (where no fluorophores appear for a particular ground-truth point), scatter (where a fluorophore appears at a varying distance from its ground-truth point), and multiple binding (where multiple fluorophores appear for a single ground-truth point).

---

[5] http://www.cloudcompare.org/

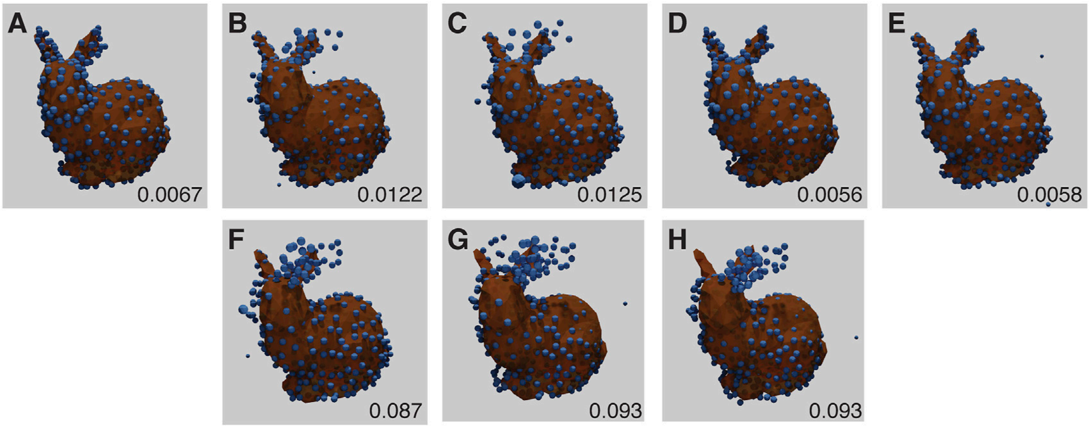

FIGURE 4 | Baseline Stanford Bunny experiment results for each run **(A–E)** with RMSD score in the lower right corner of each panel. The ground truth model is shown in orange, with the inferred structure shown as blue spheres, overlaid and aligned. **(B–D)** have the models mirrored for display and RMSD computation, and show high quality fitting. **(F–H)** correspond to results for **(B–D)** as the original reconstructions (without mirroring). Note that under this imaging modality, the presence or absence of mirroring cannot be determined. The parameters for this experiment can be found in **Supplementary Table S5.1**.

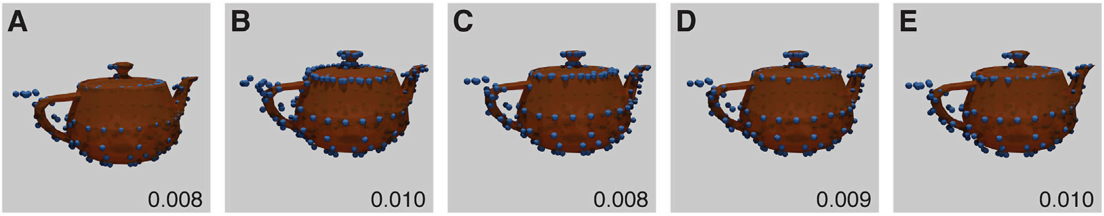

FIGURE 5 | Baseline Utah Teapot Experiment results for each run **(A–E)** with RMSD score. The inferred structure shown as blue spheres, overlaid and aligned against the ground truth model shown in orange. Each model shows incorrect symmetry with non-differentiated spout and handle. The parameters for this experiment can be found in **Supplementary Table S5.2**.

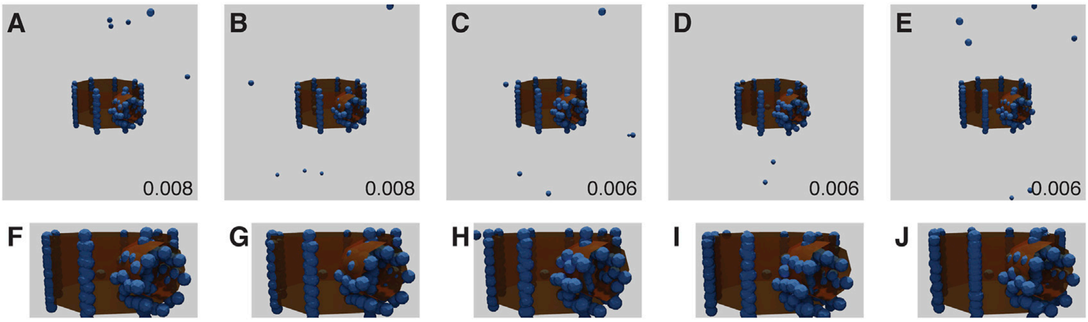

FIGURE 6 | Baseline CEP152/HsSAS-6 approximation experiment results for each run (**(A–E)**, **top row**) with RMSD score. The ground truth model is shown in orange, with the inferred structure shown as blue spheres, overlaid and aligned. Bottom row **(F–J)**: close up of the **top** row. Note the slight offset of the smaller, reconstructed cylinder from the ground-truth. The parameters for this experiment can be found in **Supplementary Table S5.3**.

3.3.1 Scatter

Two factors can lead to scatter in fluorophore positions: the inaccuracy of the fitted position due to the limited number of photons collected, and the offset between the protein of interest and the label, with the largest effect arising from primary/secondary antibody labelling. This noisy change of position (scatter) is modelled using a random Gaussian distribution with a particular scatter-sigma value. The scatter-sigma ranges from 0.03 to 0.15 pixels (9–44 nm, given the scale in the CEP152 experimental data).

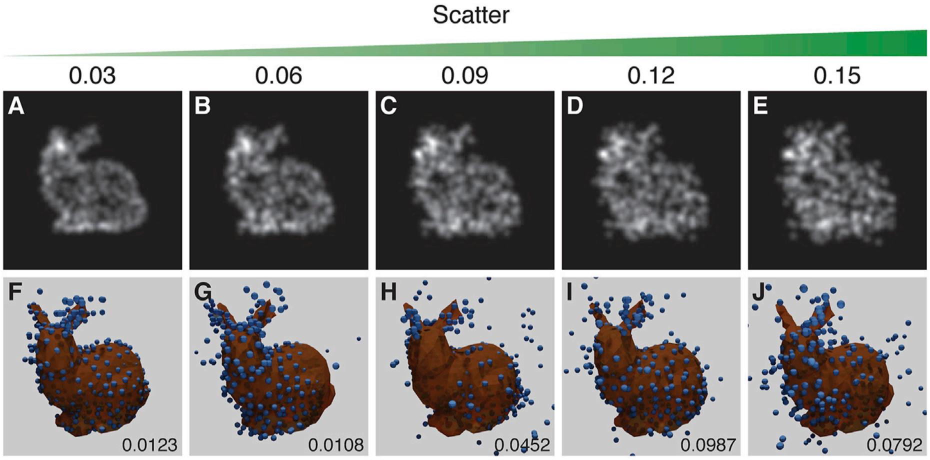

FIGURE 7 | The results of the experiment into the effect of scatter. Top row **(A–E)**: examples of training images treated with increasing scatter, as indicated by the scatter value above each panel. Bottom row **(F–J)**: the corresponding results with the inferred structure shown as blue spheres, overlaid and aligned with the ground truth model shown in orange. RSMD scores are indicated for each run in the lower right corner of **(F–J)**. Runs in **(F)** and **(C)** respectively showed an incorrect symmetry in structure and mirroring in a vertical plane. The parameters for this experiment can be found in **Supplementary Table S5.4**.

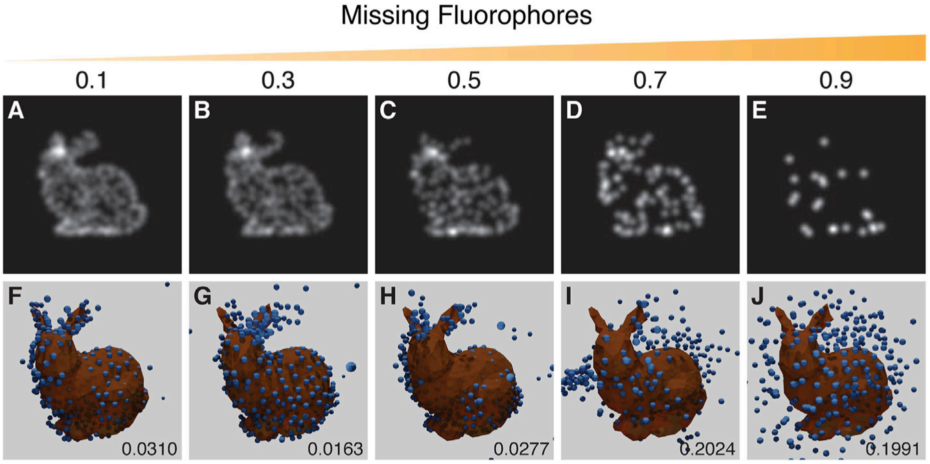

FIGURE 8 | Results from the experiment on the effect of missing fluorophores. Top row **(A–E)**: examples of training images with increasing probability of removing points as indicated by the value above each panel. Bottom row **(F–J)**: the corresponding results with the inferred structure shown as blue spheres, overlaid and aligned with the ground truth model in orange. Resulting RSMD scores for each run are indicated in the lower right corner of (F–J). The run in **(G)** showed an incorrect symmetrical structure whereas the run in **(H)** showed mirroring in a vertical plane. The parameters for this experiment can be found in **Supplementary Table S5.5**.

The results suggest that a scatter-sigma value between 0.06 pixels and 0.09 pixels (20–29 nm) is the cut-off point for acceptable reproduction of the structure. The run in **Figure 7F** shows a rare error where the structure is symmetrical along the dorsal plane - effectively giving the structure two heads. **Figure 7C** suffers from the mirroring problem (**Figure 7**).

3.3.2 Missing Fluorophores

When a fluorescence microscopy sample is labelled, not every potential site is labelled, and not all fluorophores will fluoresce. The degree of labelling and the performance of fluorophores strongly impacts image quality. To simulate this effect a random selection of vertex positions are not labelled with fluorophores. Results suggest that a recognizable reproduction with a good RMSD score can be obtained with up to ~30% of the points removed (**Figure 8**).

3.3.3 Multiple Binding and Scatter

Our final noise experiment randomly chooses up to a maximum number of bound fluorophores per ground-truth point, each with a random scatter. A single ground-truth point may "spawn" up-to a maximum of individual fluorophores (*max-spawn*) using a user-set probability (*spawn-rate*). In these experiments we chose a number of parameters for "max-spawn," "spawn-rate" and scatter.

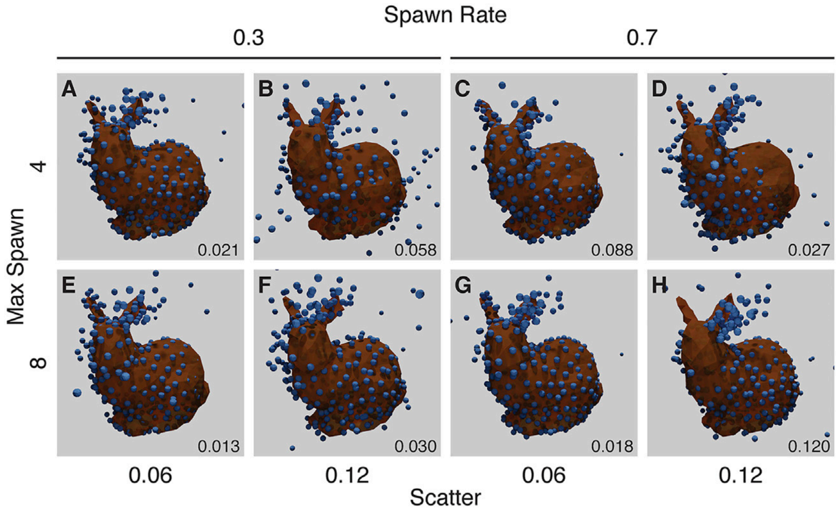

FIGURE 9 | Results from the Noise Experiment for each run **(A–H)**, with resulting RMSD shown in the lower right corner of each panel. The ground truth model is shown in orange, with the created structure shown as blue spheres, overlaid and aligned. The top row **(A–D)** shows runs with a maximum number of flurophores per ground-truth point of 4, while the bottom row **(E–H)** shows runs with a maximum of 8. The left two columns **(A, B, E, F)** have a spawn-rate of 0.3, with the right two columns (C, D, G, H) have a spawn-rate of 0.7. Runs in **(A, C, D, E, F, G)** have incorrect symmetry whereas the run in **(H)** has mirroring in a vertical plane. The parameters for this experiment can be found in **Supplementary Table S5.6**.

Many of these runs show symmetrical structure where none should occur (**Figure 9**), in a manner similar to the missing fluorophores experiment (**Figure 8**).

These results provide additional confidence that HOLLy can produce accurate structures from experimental data. The majority of results have low RMSD scores, with identifiable structures and some tolerance to noise.

3.4 SMLM Dataset of the CEP152 Complex

Having optimized our approach with different 3D models, we next applied it to experimental SMLM data collected on the CEP152 complex, which is part of the centriole. One important factor with this data is that the integrated intensity varies considerably across the CEP152 data-set, with the number of localisations ranging from 5,000 to 30,000. Normalisation plays a key part in making sure this intensity range can be modelled by our network. Additionally, since this data-set is limited by the number of feasible experiments, data-augmentation plays a key role in increasing both the absolute number of training images and the variety of orientations. This training data-set consists of approximately 40,000 images, augmented from an experimental data-set of approximately 2000 images. See **Supplementary Figure S2** for representative images that illustrate the range of orientations and experimental noise in this training data-set.

After training with these images, our network converged on a central torus for the CEP152 complex (**Figures 10**, **11**). This inferred structure is consistent with the confirmed structure of this protein complex (Sieben et al., 2018; Kim et al., 2019).

Figure 10 in particular, shows examples of the network attempting to match the training images, both in terms of structure and the input-sigma. The input images are not completely static; recall they are generated with a particular input-sigma, which decreases as training progresses. However, the output-sigma predicted by the network does not continuously decrease as the input-sigma does—rather the rate begins to flatten towards the end of training. Indeed, certain images are rendered with a higher blur than others, suggesting that certain images are being compensated for with a higher output-sigma.

The final 3D structures in **Figure 11** can be seen more easily in the videos which accompany this paper (see **Supplementary Video S1, 2**). When rendering these predicted structures in 2D based on the inferred orientations, they show significant blurring due to a large predicted output-sigma, even when the input-sigma was low (**Figure 10**). There was some noise in the inferred structure, with two “fringe-like” structures in some of the runs (**Figure 11**). Some points still appear in the middle of the toroidal structure, likely because the network has been unable to optimise these points as any direction they might now move in would result in an increasing error. The density appears to be lower for a small arc on the torus, reflective of the input images that also show a similar effect. These final structures are not exact as some noise still remains. Nonetheless, the consensus result that emerges from multiple runs is a toroidal structure that matches that of the CEP152 complex.

3.5 SIM/Expansion Microscopy Dataset of Glutamylated Tubulin in Centrioles

To validate our method, we also applied it to a separate experimental data-set (Mahecic et al., 2020) obtained using a different imaging technique. We analysed SIM/expansion

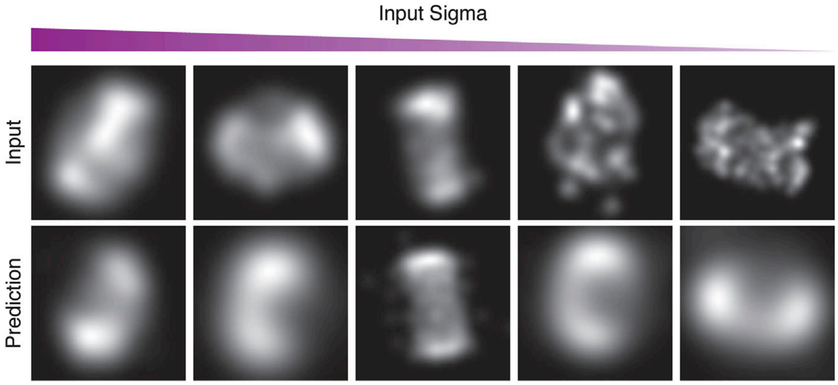

FIGURE 10 | Examples from the first run of the STORM CEP152 data-set, rendered at different points during training as input-sigma values decreased. The top row shows input images from the test set. The bottom row shows the corresponding prediction.

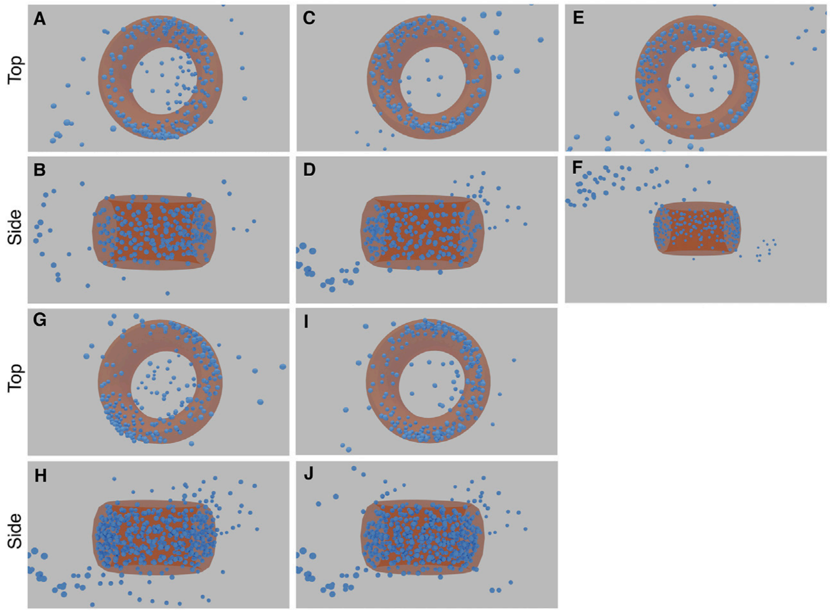

FIGURE 11 | Results of the five STORM CEP152 experiments (each with a top and side view image pair). The first experiment comprises image **(A)** and **(B)**, the second experiment **(C)** and **(D)**, and so forth. The torus structure within the blue point cloud is highlighted with an orange ring. See **Supplementary Material Video S1, 2** for greater clarity.

microscopy images of glutamylated tubulin in purified centrioles. After training on the SIM/expansion microscopy images, our network converged on a central cylinder for this complex (**Figure 12**). The density of points is highest in the centre of each image, with a tube-like structure visible. These 3D aspects are clearer in the **Supplementary Video S3, 4**. There appears to be a "frill-like" structure around the top to middle of the cylinder, which may reflect a particular characteristic of the input data. Many of the images show a spike like protrusion, emanating from the top of the central cylinder (see **Supplementary Figure S3**).

The consensus elongated cylindrical structure produced by our method is also consistent with the known structure of glutamylated tubulin in centrioles (Mahecic et al., 2020) (See **Supplementary Figure S2**).

3.6 Handedness

Often when reconstructing 3D shapes from macroscopic images, perspective projection and occlusion effects can be used to infer depth. Neither of these are present in 2D fluorescence microscopy images. Without perspective projection, there is an unknown reflection of the final 3D geometry which cannot be determined from the data. This is known as the affine ambiguity (Hartley, 2004). Examples of this effect can bee seen in **Figure 4**.

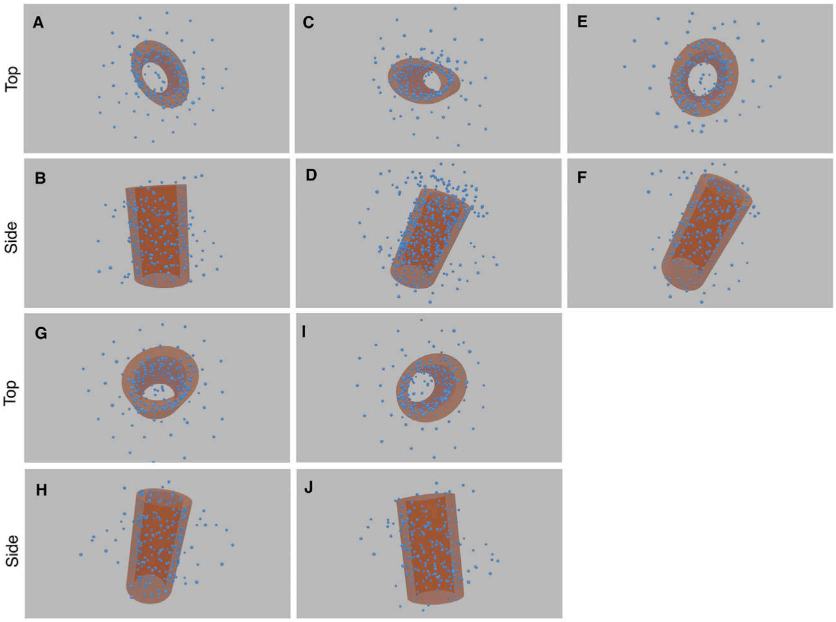

FIGURE 12 | Results of the five experiments on SIM/expansion Microscopy of glutamylated tubulin in purified centrioles (each with a top and side view image pair). The first experiment comprises image **(A)** and **(B)**, the second experiment **(C)** and **(D)**, and so forth. The cylinder structure within the blue point cloud is highlighted with an orange cylinder. See **Supplementary Video S3, 4** for greater clarity.

4 DISCUSSION

We have demonstrated a method that enables 3D structures to be reconstructed from sets of 2D SMLM or fluorescence microscopy images without any template or symmetry constraints. Our method, HOLLy, can tolerate both scatter and the limited labelling efficiency of experimental fluorescence images. The training process results in a 3D model of the structure encoded as a point-cloud in the 3D reconstruction matrix. Based on estimates of RMSD values against ground-truth and visual inspection of the results, we find that our approach can create accurate reconstructions of 3D macro-molecular structures.

Our results also demonstrate the limitations of the technique. Because of the use of 2D images, the technique is unable to resolve the chirality of the model. In addition, when the data quality is poor small structures are not reproduced. As a result when the structure is close to symmetric, the final model may become actually symmetric. On experimental data, the presence of these issues could potentially be identified by training on the same data-set multiple times and examining the differences between the results.

The value of reconstructing multiple images of a structure into a single hypothesised structure has been demonstrated in cryo-EM. In SMLM such approaches exist Heydarian et al. (2019), and show an improvement in the signal to noise ratio when combining multiple images, but performing such fits on complex structures with no constraints is extremely challenging. Here we show that, by building a 3D model and using a neural network for predicting rotation, HOLLy can discern structure from localisations with a data-set of 2000 unique images. With the increased popularity of high throughput SMLM techniques (Holden et al., 2014; Barentine et al., 2019), HOLLy provides a way to extract structural information from large volumes of super-resolution microscopy data without assumptions.

DATA AVAILABILITY STATEMENT

The program HOLLy can be found at https://github.com/OniDaito/Holly.git. The simulated data results presented in the paper can be reproduced with the configuration files found in that repository. The STORM CEP152 complex data used in our experiments can be found on Zenodo at https://doi.org/10.5281/zenodo.4751056. Once downloaded and extracted, our results can be reproduced using the configuration file found in the HOLLy project. The GT335 tublin, centriole data can be found at https://doi.org/10.5281/zenodo.3613906. The results from out CEP152 experiments we have presented can be downloaded from Zenodo at https://zenodo.org/record/4836173.

AUTHOR CONTRIBUTIONS

Initial conception and design: SC and ER. Acquired high-throughput SMLM images: CS and SM. Performed data cleaning, deep learning implementation, experiments: BB. Supervised the research: SC, ER, and QC. Interpreted and discussed results: BB, SC, ER, QC, CS, and SM. Comments on the article: CS, and SM. Wrote the paper: BB, SC, ER, and QC.

FUNDING

BB is funded by a studentship from the UKRI/BBSRC National Productivity Investment Fund (BB/S507519/1) and is part of the London Interdisciplinary Doctoral Programme funded by UKRI/BBSRC (BB/M009513/1).

SUPPLEMENTARY MATERIAL

The Supplementary Material for this article can be found online at: https://www.frontiersin.org/articles/10.3389/fbinf.2021.740342/full#supplementary-material.

REFERENCES

Aggarwal, C. C. (2018). *Neural Networks and Deep Learning: A Textbook*. Cham: Springer International Publishing. doi:10.1007/978-3-319-94463-0

Arun, K. S., Huang, T. S., and Blostein, S. D. (1987). Least-Squares Fitting of Two 3-D Point Sets. *IEEE Trans. Pattern Anal. Mach Intell.* 9, 698–700. doi:10.1109/tpami.1987.4767965

Badieirostami, M., Lew, M. D., Thompson, M. A., and Moerner, W. E. (2010). Three-dimensional Localization Precision of the Double-helix point Spread Function versus Astigmatism and Biplane. *Appl. Phys. Lett.* 97, 161103. doi:10.1063/1.3499652

[Dataset] Barentine, A. E. S., Lin, Y., Liu, M., Kidd, P., Balduf, L., Grace, M. R., et al. (2019). 3D Multicolor Nanoscopy at 10,000 Cells a Day. *bioRxiv*. doi:10.1101/606954

D. Kirk (Editor) (1994). *Graphics Gems 3*. 1st edn (Amsterdam: Morgan Kaufmann).

Fan, H., Su, H., and Guibas, L. J. (2017). "Point Set Generation Network for 3D Object Reconstruction From a Single Image," in Proceedings of the IEEE Conference on Computer Vision and Pattern Recognition, Honolulu, HI, 605–613. doi:10.1109/cvpr.2017.264

Goodfellow, I., Bengio, Y., and Courville, A. (2016). *Deep Learning*. MIT Press.

Han, Z., Chen, C., Liu, Y.-S., and Zwicker, M. (2020). "DRWR: A Differentiable Renderer without Rendering for Unsupervised 3D Structure Learning from Silhouette Images," in InInternational Conference on Machine Learning 2020.

Hartley, R. (2004). *Multiple View Geometry in Computer Vision*. 2nd edn. Cambridge, UK ; New York: Cambridge University Press.

Henderson, P., and Ferrari, V. (2020). Learning Single-Image 3D Reconstruction by Generative Modelling of Shape, Pose and Shading. *Int. J. Comput. Vis.* 128, 835–854. doi:10.1007/s11263-019-01219-8

Heydarian, H., Przybylski, A., Schueder, F., Jungmann, R., van Werkhoven, B., Keller-Findeisen, J., et al. (2019). Three Dimensional Particle Averaging for Structural Imaging of Macromolecular Complexes by Localization Microscopy. *bioRxiv* 837575. doi:10.1101/837575

Holden, S. J., Pengo, T., Meibom, K. L., Fernandez Fernandez, C., Collier, J., and Manley, S. (2014). High Throughput 3D Super-resolution Microscopy Reveals *Caulobacter crescentus In Vivo* Z-Ring Organization. *Proc. Natl. Acad. Sci. U S A.* 111, 4566–4571. doi:10.1073/pnas.1313368111

Insafutdinov, E., and Dosovitskiy, A. (2018). *Unsupervised Learning of Shape and Pose with Differentiable Point Clouds*.

Kandel, I., and Castelli, M. (2020). The Effect of Batch Size on the Generalizability of the Convolutional Neural Networks on a Histopathology Dataset. *ICT Express* 6, 312–315. doi:10.1016/j.icte.2020.04.010

Kim, T. S., Zhang, L., Il Ahn, J., Meng, L., Chen, Y., Lee, E., et al. (2019). Molecular Architecture of a Cylindrical Self-Assembly at Human Centrosomes. *Nat. Commun.* 10, 1151. doi:10.1038/s41467-019-08838-2

Kingma, D. P., and Ba, J. (2017). "Adam: A Method for Stochastic Optimization," in 3rd International Conference on Learning Representations,{ICLR} 2015, San Diego, CA, USA.

Lassner, C., and Zollhöfer, M. (2020). "Pulsar: Efficient Sphere-Based Neural Rendering," in Proceedings of the IEEE/CVF Conference on Computer Vision and Pattern Recognition, 1440–1449.

Loper, M. M., and Black, M. J. (2014). "OpenDR: An Approximate Differentiable Renderer," in *Computer Vision – ECCV 2014*. Editors D. Fleet, T. Pajdla, B. Schiele, and T. Tuytelaars (Cham: Springer International Publishing), 154–169. Lecture Notes in Computer Science. doi:10.1007/978-3-319-10584-0_11

Mahecic, D., Gambarotto, D., Douglass, K. M., Fortun, D., Banterle, N., Ibrahim, K. A., et al. (2020). Homogeneous Multifocal Excitation for High-Throughput Super-resolution Imaging. *Nat. Methods* 17, 726–733. doi:10.1038/s41592-020-0859-z

Milne, J. L., Borgnia, M. J., Bartesaghi, A., Tran, E. E., Earl, L. A., Schauder, D. M., et al. (2013). Cryo-electron Microscopy-Aa Primer for the Non-microscopist. *FEBS J.* 280, 28–45. doi:10.1111/febs.12078

Ravi, N., Reizenstein, J., Novotny, D., Gordon, T., Lo, W.-Y., Johnson, J., et al. (2020). *Accelerating 3D Deep Learning with PyTorch3D*. arXiv:2007.08501.

Salas, D., Le Gall, A., Fiche, J. B., Valeri, A., Ke, Y., Bron, P., et al. (2017). Angular Reconstitution-Based 3D Reconstructions of Nanomolecular Structures from Superresolution Light-Microscopy Images. *Proc. Natl. Acad. Sci. U S A.* 114, 9273–9278. doi:10.1073/pnas.1704908114

Schermelleh, L., Heintzmann, R., and Leonhardt, H. (2010). A Guide to Super-resolution Fluorescence Microscopy. *J. Cel Biol* 190, 165–175. doi:10.1083/jcb.201002018

Sieben, C., Banterle, N., Douglass, K. M., Gönczy, P., and Manley, S. (2018). Multicolor Single-Particle Reconstruction of Protein Complexes. *Nat. Methods* 15, 777–780. doi:10.1038/s41592-018-0140-x

Conflict of Interest: Author ER is employed by Snap Incorporated.

The remaining authors declare that the research was conducted in the absence of any commercial or financial relationships that could be construed as a potential conflict of interest.

frontiers
in Bioinformatics

METHODS
published: 04 November 2021
doi: 10.3389/fbinf.2021.739769

Efficient Cross-Correlation Filtering of One- and Two-Color Single Molecule Localization Microscopy Data

Angel Mancebo[1†], *Dushyant Mehra*[1,2†], *Chiranjib Banerjee*[1], *Do-Hyung Kim*[3] and *Elias M. Puchner*[1]*

[1]*School of Physics and Astronomy, University of Minnesota, Minneapolis, MN, United States,* [2]*Department of Physiology and Biomedical Engineering, Mayo Clinic, Rochester, MN, United States,* [3]*Department of Biochemistry, Molecular Biology, and Biophysics, University of Minnesota, Minneapolis, MN, United States*

Edited by:
Christian Franke,
Friedrich Schiller University Jena,
Germany

Reviewed by:
Zoltan Cseresnyes,
Leibniz Institute for Natural Product
Research and Infection Biology,
Germany
Anna Medyukhina,
St. Jude Children's Research Hospital,
United States

***Correspondence:**
Elias M. Puchner
epuchner@umn.edu

[†]*These authors have contributed equally to this work*

Specialty section:
This article was submitted to
Computational BioImaging,
a section of the journal
Frontiers in Bioinformatics

Received: *11 July 2021*
Accepted: *14 October 2021*
Published: *04 November 2021*

Citation:
Mancebo A, Mehra D, Banerjee C,
Kim D-H and Puchner EM (2021)
Efficient Cross-Correlation Filtering of
One- and Two-Color Single Molecule
Localization Microscopy Data.
Front. Bioinform. 1:739769.
doi: 10.3389/fbinf.2021.739769

Single molecule localization microscopy has become a prominent technique to quantitatively study biological processes below the optical diffraction limit. By fitting the intensity profile of single sparsely activated fluorophores, which are often attached to a specific biomolecule within a cell, the locations of all imaged fluorophores are obtained with ~20 nm resolution in the form of a coordinate table. While rendered super-resolution images reveal structural features of intracellular structures below the optical diffraction limit, the ability to further analyze the molecular coordinates presents opportunities to gain additional quantitative insights into the spatial distribution of a biomolecule of interest. For instance, pair-correlation or radial distribution functions are employed as a measure of clustering, and cross-correlation analysis reveals the colocalization of two biomolecules in two-color SMLM data. Here, we present an efficient filtering method for SMLM data sets based on pair- or cross-correlation to isolate localizations that are clustered or appear in proximity to a second set of localizations in two-color SMLM data. In this way, clustered or colocalized localizations can be separately rendered and analyzed to compare other molecular properties to the remaining localizations, such as their oligomeric state or mobility in live cell experiments. Current matrix-based cross-correlation analyses of large data sets quickly reach the limitations of computer memory due to the space complexity of constructing the distance matrices. Our approach leverages k-dimensional trees to efficiently perform range searches, which dramatically reduces memory needs and the time for the analysis. We demonstrate the versatile applications of this method with simulated data sets as well as examples of two-color SMLM data. The provided MATLAB code and its description can be integrated into existing localization analysis packages and provides a useful resource to analyze SMLM data with new detail.

Keywords: single-molecule localization microscopy, photo-activated localization microscopy, cross-correlation, colocalization, clustering

INTRODUCTION

The subcellular localization of proteins and their interaction with other biomolecules is a critical determinant of their function. For instance, proteins have been shown to form clusters in nuclear condensates which affect chromatin organization and gene regulation (Cisse et al., 2013; Larson et al., 2017; Cho et al., 2018; Chong et al., 2018; Sabari et al., 2018; Cai et al., 2019; McSwiggen et al., 2019). Cell surface receptors such as TNFα, EGFR, and TLR4 have been shown to form functional clusters in the cell membrane that enhance signaling (Krüger et al., 2017, 4; van Lengerich et al., 2017; Karathanasis et al., 2020). In the immunological synapse, various receptors and signaling proteins are co-clustered or excluded in supramolecular activation clusters (Hartman et al., 2009; Pageon et al., 2016b). In most contexts, the fraction of the proteins that cluster or co-cluster with other proteins have different biophysical and biochemical properties compared to the non-clustered ones.

Fluorescence microscopy has become a prominent technique to study the sub-cellular distribution and colocalization of specifically labeled proteins in cells. However, many intracellular structures and proteins clusters are too small or too closely spaced to be resolved below the optical diffraction limit of conventional fluorescence microscopy. Super-resolution microscopy techniques such as single molecule localization microscopy (SMLM) (Betzig et al., 2006; Rust et al., 2006) overcome these challenges. Instead of imaging all fluorophores at the same time, SMLM employs fluorophores that are predominantly in a dark state but switch to a fluorescent state either intrinsically or induced by irradiation of a certain wavelength of light (Patterson and Lippincott-Schwartz, 2002; Betzig et al., 2006; Rust et al., 2006). In this way, only sparse and spatially well separated single molecules are in a fluorescent state and are detected in a single imaging frame. By recording many frames, all individual fluorophores are then imaged over time. A super-resolution image is then constructed by fitting all sparse fluorophores in each frame with a point-spread function (PSF) or Gaussian and by superimposing the center coordinates of all localizations that typically have a precision of ~20 nm.

In contrast to pixel-intensity information of conventional fluorescence microscopy, SMLM data is based on coordinates, widths, heights etc., of all fitted single fluorophores and therefore presents unique opportunities for secondary data analysis. For instance blink-correction algorithms have been developed to correct repeated localizations of the same fluorophore that arise from the complicated photophysics (Lee et al., 2012; Rollins et al., 2015; Hummer et al., 2016; De Zitter et al., 2020) and to count the number of molecules on an organelle or cluster (Puchner et al., 2013). Various clustering algorithms have been developed to quantify the degree or variability of clustering of a protein of interest under various conditions. Examples include local clustering algorithms that define boundaries of dense localizations (Ester et al., 1996; Perry, 2004; Owen et al., 2010; Pageon et al., 2016a; Griffié et al., 2016; Levet et al., 2019; Khater et al., 2020; Nino et al., 2020; Simoncelli et al., 2020; Williamson et al., 2020; Marenda et al., 2021; Nieves et al., 2021) or bulk metrics based on the radial distribution or pair-correlation function that quantify the density of localization pairs as a function of their distance to each other (Ripley, 1979; Kiskowski et al., 2009; Sengupta et al., 2011; Veatch et al., 2012; Stone and Veatch, 2015). Importantly, these analysis methods can be expanded to two-color SMLM data to quantify the colocalization and structural relation of two proteins. For instance, cross-correlation and pair correlation analysis has been used to study co-localization among synaptic membrane receptors (Malkusch et al., 2012; Pageon et al., 2016a, 2016b; Krüger et al., 2017; Khater et al., 2018, 2019; Lagache et al., 2018; Kennedy et al., 2019; Karathanasis et al., 2020; Simoncelli et al., 2020) and quantify the density of accessible DNA domains colocalized with nuclear condensates and other nuclear landmarks (Lee, 2019; Xie et al., 2020).

For the analysis of any SMLM data set that exhibits clustering or colocalization of two different proteins, it would be desirable to separate the molecule list based on the proximity of proteins to each other. In this way localizations from clustered or colocalized proteins can be separately visualized and analyzed to study how their properties such as molecule number or their structure differs from the rest of localizations that are not clustered or colocalized. While pair-or cross-correlation analysis in principle allows to make this separation based on a distance threshold, the calculation of the distance matrix is memory intensive and can't be use over entire field of view of a typical mammalian cell due to the large number of N localizations. Both the memory requirement and calculation time scales as N^2. An approach to generate a cross correlation curve is to use small sections of data (Kennedy et al., 2019), however, most of the localizations are discarded. Fourier transformations are also used to calculate the cross-correlation curve across the full field of view (Kiskowski et al., 2009; Liu et al., 2014, 2; Xie et al., 2020) but these methods discard localizations that generate pairwise distances during analysis. Therefore, localizations that are within specific distances or are colocalized with a protein of interest cannot be separated and further analyzed. These existing methods provide a coarse-grained representation of the cross-correlation curve and may miss relevant transitions occurring at smaller differences in distances that could provide insight into protein oligomerization.

Here, we address these limitations by developing a memory efficient approach using k-dimensional trees (Bentley, 1975) to efficiently calculate the distance matrix for the pair- or cross-correlation of SMLM data across the entire field of view (**Figure 1**). Based on the cross-correlation, a distance cutoff can be defined to separate localizations that cluster or colocalize with a second protein of interest. These separated molecule lists can then be separately visualized and further analyzed with any existing secondary analysis algorithm to e.g. determine the number of molecules in and the size of a cluster, their diffusive state in live-cell data, or their degree of cross-correlation (Owen et al., 2010; Sengupta et al., 2011; Veatch et al., 2012; Puchner et al., 2013; Stone and Veatch, 2015; Pageon et al., 2016a, 2016b; Hummer et al., 2016; Lagache et al., 2018; Banerjee et al., 2020; Heydarian et al., 2021; Marenda et al., 2021). We first demonstrate the performance and application of this method with simulated data sets to allow a comparison of the results to a

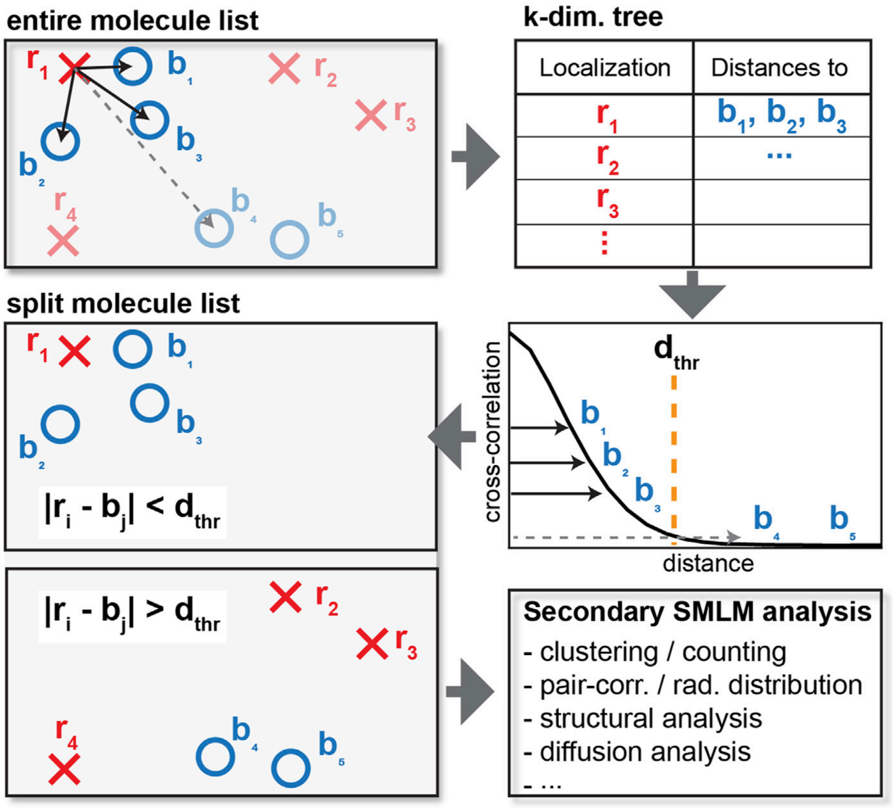

FIGURE 1 | Schematics of cross-correlation. For each localization of one type (red crosses), the distance to each of the other type (blue circles) is computed and tabulated. Instead of calculating the distance of every pair of red crosses and blue circles, a distance cutoff is applied to only consider interparticle distances within relevant length scales. When the distance exceeds the cutoff as shown by the dashed line, the distance is not tabulated, resulting in reduced memory requirements. The list of localization can then be split into localization that do and do not colocalize or appear within the specified distance cutoff for further downstream analysis.

known ground truth. We also show the application to two-color SMLM data of ULK1 and Atg13, two proteins that have been recently shown to be involved in the initiation of autophagy when co-clustered. Since our described method can be paired with any existing downstream SMLM data analysis algorithm, it presents a useful and modular way to improve SMLM analysis results e.g. by suppressing randomly localized noise localizations and by providing a refined comparison between clustered and non-clustered localization.

MATERIALS AND METHODS

Workflow

In our code, available at https://github.com/PuchnerLab/cross-correlation-filtering, the point of entry is the MATLAB function “cc_graphic_pipeline”, which accepts as arguments each list of coordinates (as x-y columns), the maximum distance used for the pair- and cross-correlation calculations, the area of the field of view of the localization data (for correct normalization of the cross-correlation), and the units in which the data is provided. This function outputs the pair-correlation of each dataset and the cross-correlation between the two datasets. From the generated graphs, the user can determine appropriate cutoff distances for cross-correlation filtering and for the optional clustering. As an aid, the pair-correlations indicate the distance to the 99% drop in correlation, and the cross-correlation indicates the distance to both the 50 and 99% drop in correlation.

The second step is the function “cc_separation_pipeline”, which accepts as arguments each list of coordinates, a vector of cutoff distances for clustering for each dataset [(0, 0) if no clustering is to be performed], the cutoff distance for the cross-correlation filtering, and a vector of minimum stoichiometries considered for colocalization for each dataset [(1, 1) for no minimum]. The primary output is a cell with each element containing a logical vector of colocalized localizations of each dataset, which can be used to select the colocalized and non-colocalized localizations from the original datasets or from the indices provided by another cluster assignment algorithm, such as DBSCAN (Ester et al., 1996). Additionally, “cc_separation_pipeline” outputs a cell of the colocalized coordinates and a cell of non-colocalized coordinates.

In this second step, localizations from the two coordinate lists that lie within the cutoff distance are assigned as colocalized. If the optional clustering is performed prior to colocalization, then two clusters are assigned as colocalized if any of their constituent

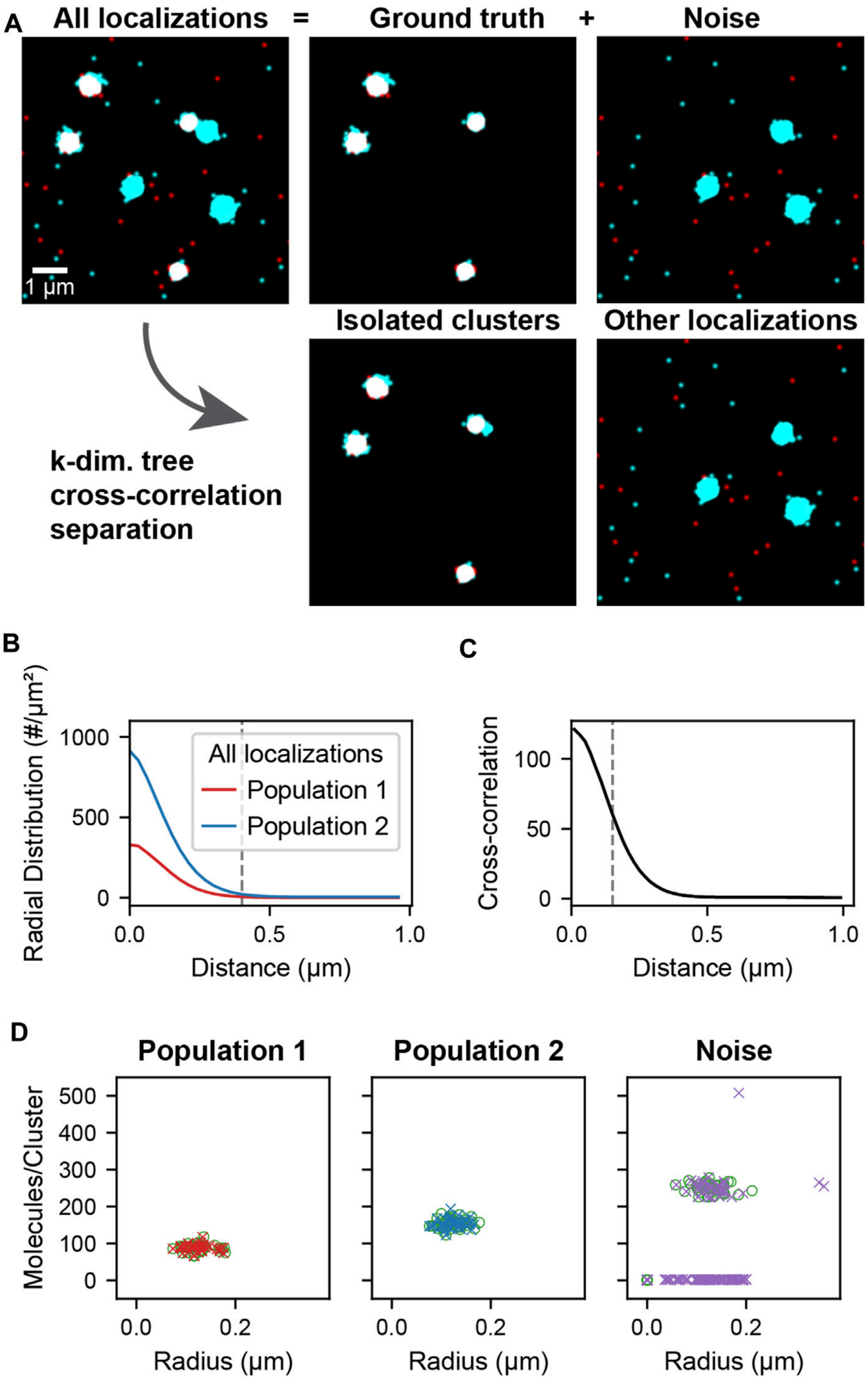

FIGURE 2 | Cluster separation on simulated data. A data set was simulated consisting of two types of localizations as well as added noise. Population 1 (red) and 2 (cyan) consists of 40 clusters of size 0.1 ± 0.02 µm and stoichiometries of Poisson (90) and Poisson (150) respectively and represents the ground truth. Noise localizations include non-colocalized clusters of size 0.1 ± 0.02 µm and stoichiometry Poisson (250) (cyan) as well as randomly distributed localizations (red) to measure the performance of the cluster separation. **(A)** Super-resolution reconstruction of all localizations, the ground truth clusters of population 1 and 2, and the noise localizations (upper). After applying the distance-based cutoff, the two molecule lists can be separated into the colocalized clusters and all other remaining noise localizations (lower). **(B)** Pair correlation functions of each of the two ground truth populations showing the relevant length scale of cluster sizes used to identify clusters. **(C)** Cross-correlation functions of all localizations between the two populations for all localizations. The dashed line indicates the maximum separation two localizations can have to be classified as colocalized. If two localizations that belong to clusters as identified in B are closer than this maximum separation, all localizations from the entire clusters are classified as colocalized. **(D)** Stoichiometry and size of ground truth (circles) and recovered clusters (crosses) for each of the populations.

localizations are within the cutoff distance and if the number of localizations in the cluster is at least the specified minimum number of localizations for each cluster.

A schematic of the organization of the code is shown in **Supplementary Figure S1**.

Simulated Data

The simulated localization data used in cross-correlation filtering (**Figure 2A**, All localizations) is composed of two parts: the ground truth clusters (**Figure 2A**, Ground truth) and noise clusters and localizations (**Figure 2A**, Noise). The clusters were generated by randomly distributing cluster centers throughout the field of view. Localizations were placed by generating coordinates from a normal distribution around each cluster center. Localizations were generated in this way for both populations of clusters using the same cluster centers so that colocalized clusters have complete overlap (**Figure 2A**, Ground truth). Randomly distributed localizations were mixed into each population to simulate localizations that are not clustered or colocalized. Additional clusters of higher stoichiometry were mixed into the second population to simulate non-colocalized clusters that should be separated by the analysis (**Figure 2A**, Noise). A schematic of the simulated data construction is show in **Supplementary Figure S2**. The recovery of the underlying colocalized ground truth and noise rejection was quantified by computing the F-score as a function of the colocalization cutoff distance (**Supplementary Figure S3A**). The recovery of the correct radii and stoichiometries was quantified in **Supplementary Figure S3B** and **Supplementary Figure S3C**, respectively.

Cross-Correlation and Cluster Separation Analysis

In each population of simulated data, localizations appearing within a distance of 0.4 μm from each other were first assigned to clusters. Next, a cross-correlation analysis was performed by using a k-dimensional tree for fast querying and to limit the memory consumption of the distance tabulation. A range search was then performed to compute the distances between each localization of one population and those of the other population up to a specified maximum separation distance, which was chosen to be 1 μm. The indices and distances from the range search are used to determine which clusters from one population are colocalized with clusters from the other population. A maximum separation of 150 nm between the constituent molecules of two clusters was used for determining their colocalization and at the same time a requirement of a minimum of two localizations per cluster was imposed to filter out individual non-colocalized localizations. The resulting lists of colocalized clusters (and complementary list of excluded clusters and localizations) were then further analyzed to determine their stoichiometry and size compared to the ground truth clusters. The performance of the colocalization analysis was also quantified on lines and rings (**Supplementary Figure S6**).

Benchmarks

To test the memory and time efficiency of the k-dimensional tree-based cross-correlation compared to full distance matrix approach, we simulated two populations of completely colocalized clusters of stoichiometries of 200 and 300 localizations normally distributed about the centroid with standard deviation 100 nm and 10,000 individual noise localizations in each population within a 40.96 μm field of view. We varied the total number of clusters within the field of view to increase the memory requirements of the cross-correlation.

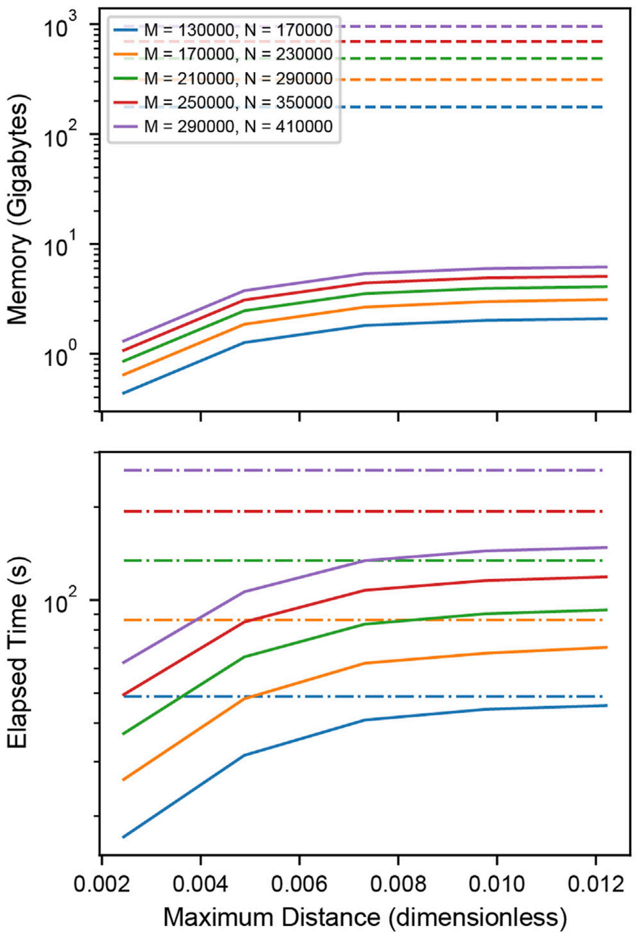

FIGURE 3 | Performance of distance tabulation using a k-d tree and range search vs. a full distance matrix. **(A)** Simulated data sets as in **Figure 2** with varying numbers of localizations were analyzed to measure the memory needs for calculating the full distance matrix (dashed) and k-dimensional tree (solid) with distance cutoff. For matrices that could not explicitly be allocated into memory, a linear extrapolation was applied to estimate the allocation time (dot-dashed). The total number of clusters is increased with an increasing number of localizations to increase the memory requirements of the distance tabulation. The distance is expressed as a fraction of the field of view. For relevant length scales, the tree uses significantly less memory than the matrix. **(B)** Elapsed time for calculating the full distance matrix (dashed) vs. the k-dimensional tree (solid). When a realistic number of localizations is included in the distance tabulation, the distance tabulation for the tree takes less time than the full matrix.

Memory Efficiency

Memory requirements in **Figure 3** A were determined by calculating the total number of bytes of memory needed for

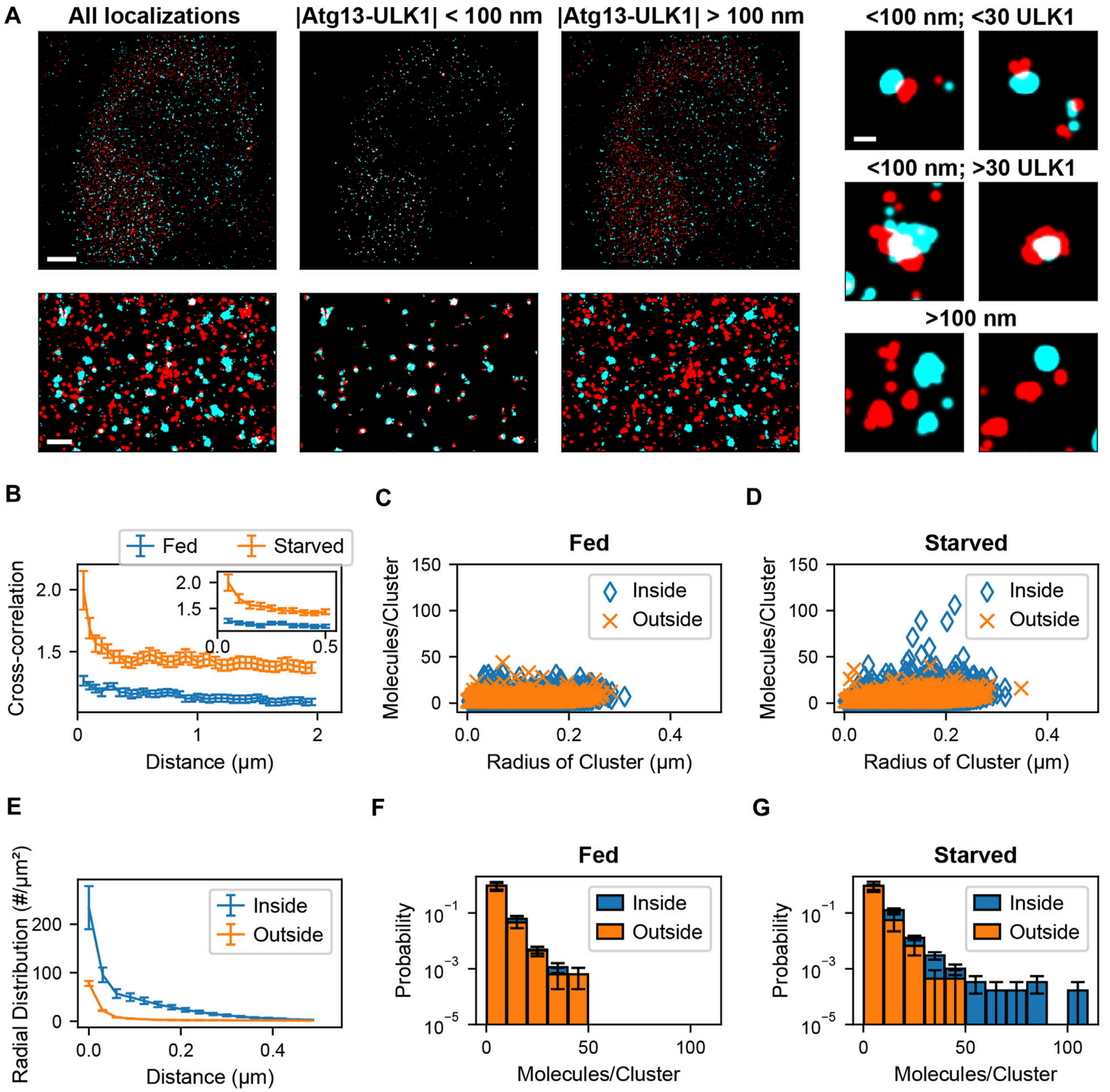

FIGURE 4 | Colocalization analysis of ULK1 and ATG13 via cross correlation. **(A)** Left shows a two-color overlay of PALM images of mEos2-ULK1 (red) and HaloTag-ATG13 bound to JF646 (cyan) with a corresponding magnified image (bottom left) taken from a representative starved cell (Scale bar top left: 5 μm; bottom left: 1 μm). Middle represents the ATG13 localizations that are within 100 nm of ULK1 molecules and considered colocalized with ULK1 clusters. The corresponding magnified image (bottom middle) highlights the increased visibility of colocalized ULK1 clusters after filtering out non colocalized molecules using the cross-correlation analysis framework. Right represents ULK1 and ATG13 localizations that are further than 100 nm away from each other and are not considered colocalized. Examples of individual clusters that are and are not colocalized with ATG13 localizations are also displayed (scale bar: 150 nm). **(B)** Cross-correlation plot between ULK1 molecules and ATG13 localizations in fed (blue) and starved (red) cells. The cross correlation plot was calculated by using k dimensional trees to obtain ATG13 localizations within 2 μm of ULK1 molecules across the entire field of view. The inset graph represents the onset of leveling of the cross correlation plot around 100 nm. The error bar corresponds to SEM from five fed and five starved cells. **(C,D)** show the quantification of the number of molecules and radii of ULK1 clusters colocalized with ATG13 (inside, blue) and not colocalized with ATG13 (outside, orange) in fed **(C)** and starved **(D)** cells. ULK1 localizations that are and are not colocalized with ATG13 exhibited similar distributions in fed cells while ULK1 localizations that colocalized with ATG13 in starved cells formed structures that contained more molecules and were interpreted to be forming autophagosomes. **(E)** The radial distribution function further quantifies the local density difference between ULK1 colocalized (inside, blue) vs. non ATG13 colocalized (outside, red) ULK1 molecules in starved cells. The error bar represents SEM from five starved cells. Figure **(F)** and **(G)** display a normalized histogram of the number of ULK1 molecules in a cluster colocalized with ATG13 (inside, blue) and not colocalized with ATG13 (outside, orange) in fed **(F)** and starved **(G)** cells. The error bar corresponds to SEM from five fed and five starved cells. While there was no noticeable difference in ATG13 colocalized and non ATG13 colocalized distributions in fed cells, there was a significant difference in both distributions in starved cells where ATG13 colocalized clusters contained the highest number of ULK1 molecules.

storing the distances between the localizations. For the matrix-based analysis, this is MNB, which corresponds to the number of elements in the distance matrix, where M and N are the number of localizations in each population and B is the number of bytes corresponding to the floating-point precision used. For the k-dimensional tree-based analysis, the total amount of memory is bounded from above by MNB, gradually approaching it as the range is increased. For structure sizes much smaller than the field of view, the k-dimensional tree distance tabulation outperforms the distance matrix when including only the relevant distances and excluding potentially less relevant long-range distances. In the cases where the matrix memory requirements did not exceed the system memory (as in **Supplementary Figure S5A**), the memory consumption was measured directly.

Time Efficiency

Elapsed times in **Figure 3** B and **Supplementary Figure S5B** were determined by measuring the time needed to construct either the full distance matrix or the range search on the k-dimensional tree for various distances. For matrices with a memory allocation that would exceed the available system memory, the allocation time was extrapolated from the allocation rate determined by fitting the matrix allocation vs memory for moderate data (**Supplementary Figure S5D**).

Mammalian Cell Analysis

Sample preparation, imaging methods, and blink correction analysis are described in Banerjee et al., 2020 (Banerjee et al., 2020). After identification of blink corrected ULK1 molecules, molecules were assigned to clusters. The radial distribution (or pair correlation) among all blink corrected ULK1 molecules with respect to each other was calculated. The leveling of the pair correlation plot approached zero at around 400 nm (Banerjee et al., 2020). Nearby ULK1 molecules whose distances lie within the cutoff distance of 400 nm were assigned to the same ULK1 cluster. After this, a spatial cross-correlation between the blink corrected ULK1 molecules and ATG13 localizations was calculated to determine the pairwise distance distribution between the two protein populations. To overcome memory limitations associated with existing methods, the ATG13 dataset was converted into a k-dimensional tree structure as described in the results section. Then, a nearest neighbor search was used to obtain pairwise distances between ULK1 and ATG13 molecules up to a specified distance cutoff of 2 μm. A cross correlation function was then calculated between the obtained ATG13 and ULK1 pairwise distances using previously described methods (Veatch et al., 2012; Banerjee et al., 2020). Since the cross-correlation curve remained constant at distances larger than 100 nm, which indicates no clustering beyond this distance, this number was used as the colocalization distance cutoff (**Figure 4B**). ATG13 localizations within the 100 nm distance cutoff of ULK1 molecules were therefore considered colocalized with ULK1 molecules. ULK1 and ATG13 molecules were segregated into colocalized and non-colocalized groups. Cell and matrix array computations were parallelized to increase computational speed. Next, ULK1 clusters that contained at least one molecule colocalized with an ATG13 localization was identified as a colocalized cluster. These clusters were separated from non-ATG13 colocalized clusters and further analyzed. Cluster properties such as radius and the number of molecules for both ULK1 clusters were then obtained. Radial distribution functions of various sub ULK1 cluster populations were calculated (ATG13 colocalized vs non-ATG13 colocalized molecules) by normalizing the separated pairwise distances by the bin area and the number of molecules in those individual datasets. Cluster properties and pairwise distance distributions from the full cell and isolated sub-populations within the cell were pooled together to compare how these metric change between fed and starved cells. The analysis codes were written in MATLAB 2018b and run on a Dell PowerEdge T440 server with 94GB RAM, an Intel Xeon 2.68 GHz CPU, and 14.5 TB of disk space.

RESULTS

Cluster Separation to Remove Noise From Simulated Data

The cross-correlation and cluster separation analysis can provide information about the stoichiometry and size of colocalized clusters while filtering out localizations that do not belong to clusters or are not colocalized. To demonstrate the application and to measure the performance of this analysis, we first simulated localization data, allowing us to compare the processed results to the ground truth. **Figure 2** shows the simulated cluster data for two populations of localizations. The ground truth consists of randomly distributed clusters of population 1 with a mean number of 90 localizations that colocalize with clusters of population 2 that have a mean number of 150 localizations. Superimposed to the ground truth are randomly distributed localization of population 1 as well as randomly distributed localizations and clusters of population 2 with a mean of 250 localizations. In this way, non-colocalized localizations and clusters are introduced as noise, which is meant to be filtered by our analysis pipeline. First, localizations in each population are assigned to a cluster if they appear within 0.4 μm of each other, which corresponds to the peak-width of the pair-correlation and reflects the average cluster size (**Figure 2B**). Next, colocalized clusters from both populations were identified based on the cross-correlation if two localizations were separated by less than 150 nm (**Figure 2C**, **Supplementary Note S1**, **Supplementary Figure S4**). As can be seen in **Figure 2A**, the isolated clusters and remaining localizations reflect to a large degree the original ground truth and noise localizations. By determining the number of localizations in each of the colocalized cluster, the original distribution that was used for the simulation is recovered to above 98% for population 1 and above 93% for population 2 (**Figure 2D**, **Supplementary Figure S4**). Likewise, further structural analysis of the isolated clusters such as the determination of cluster radii recovers the same results from the ground truth. Overall, 100% of the 40 ground truth clusters in each population were recovered and most deviations arose from noise localizations and clusters that are coincidentally in proximity to the ground truth. These results demonstrate that our cross-correlation based approach is effective in separating noise localizations and clusters from colocalized clusters for further downstream analysis.

Benchmarks

For large enough SMLM datasets, constructing a full distance matrix for a cross-correlation analysis can approach or even exceed the available system memory. This is because distances between all localizations across the field of view are tabulated, including distances that are well beyond relevant length scales of clusters or structures under investigation. Using the k-dimensional tree-based approach to compute the cross-correlation can significantly reduce the memory requirements by orders of magnitude when an appropriate cutoff distance is selected for tabulating the distances. **Figure 3A** shows how the memory requirements of the k-dimensional tree-based method increase with the cutoff distance and remain orders of magnitude below the full matrix for relevant length scales. As the cutoff distance increases up to the full field of view, the memory consumption approaches that of the full distance matrix. **Figure 3B** shows that the computation time is worse for the k-dimensional tree-based method when applied to smaller datasets but eventually shows improved runtime performance as the size of the dataset increases and reaches more realistic numbers in the range of thousands of localizations. When extrapolating the memory consumption to 100 GB, which is at the order of magnitude where the calculation becomes infeasible, a number of 112,000 localization is obtained for the full distance matrix and 44, 200, 000 for k-dimensional trees at a distance cutoff of 0.5 μm (**Supplementary Note S2**, **Supplementary Figure S5C**). This result demonstrates that typical SMLM data sets cannot be analyzed with a full cross-correlation and that significantly larger data sets can be analyzed using k-dimensional trees.

Isolating Co-clustered ULK1 and Atg13 Structures That Form Phagophores

In the following we demonstrate the isolation of co-clustered structures in real two-color PALM data that recently led to the identification of signaling clusters involved in autophagy (Banerjee et al., 2020). Autophagy is a subcellular process in eukaryotic cells in which macromolecules and organelles are engulfed by a double membrane and then degraded by fusion with lysosomes (Mercer et al., 2009; Jung et al., 2010; Roach, 2011; Park et al., 2018). Autophagy can be induced by amino acid starvation and the resulting inhibition of mechanistic target of rapamycin complex 1 (mTORC1) (Kamada et al., 2000; Chang and Neufeld, 2009, 1), which in turn leads to the formation of autophagy initiation cluster composed of activated UNC51-like kinase 1 (ULK1), Atg13, FIP200 (FAK family kinase interacting protein 200 kDa), and Atg101 (Hosokawa et al., 2009). In a recent study we employed CRISPR/Cas9 based genome editing to endogenously tag ULK1 with the photoswitchable fluorescent protein mEos2 in HeLa cells and to perform a quantitative PALM colocalization analysis with Atg13, a critical interaction partner of ULK1 in activation cluster (Banerjee et al., 2020). Our results showed that amino acid starvation induced the formation of a small fraction of arc shaped and spherical structures containing more than 30 ULK1 molecules that all colocalized with Atg13 in proximity to the Endoplasmic Reticulum. Therefore, a threshold number of ULK1 is required to initiate the formation of autophagosomes. Here, we demonstrate the application of our cross-correlation approach to a modified data sets similar to the ones shown in (Banerjee et al., 2020).

Two-color PALM data was recorded using endogenously tagged ULK1-mEos2 and transiently transfected Atg13-HaloTag in conjunction with the PALM compatible JF646 dye as described in (Banerjee et al., 2020). As can be seen in **Figure 4** A in both fed and starved cells ULK1 and Atg13 formed puncta that did and did not colocalize. However, in starved cells a few larger structures with a higher number of ULK1 molecules are visible. Due to the large number of localizations in the 5 data sets (9,589 ± 904 ULK1 molecules, 1,270,045 ± 420,310 Atg13 localizations), a traditional cross-correlation across the entire fields of view is not feasible with commonly used computers or servers (our server (2.68 GHz CPU, 94 GB RAM)—typical computer (2.7 GHz CPU and 8–20 GB RAM) since it would require up to 95 GB of RAM memory. We therefore employed k-dimensional trees to efficiently calculate the distance matrix for the cross-correlation across the entire field of view (**Figure 4B**). The cross-correlation between ULK1 and Atg13 was significantly larger in starved cells and exhibited a pronounced peak up to distances of ~100 nm, indicating the formation of more densely colocalized structures. Using the cross-correlation matrix, it is now possible to separate the molecule list of ULK1 and Atg13 localizations that are closer than 100 nm and considered to be colocalized. All remaining localizations that are separated by more than 100 nm are accumulated in a separate molecule list (**Figure 4C**). Importantly, these separated molecule lists can now be further processed with any secondary SMLM data analysis approach. For instance, when plotting the number of ULK1 molecules in clusters against the radius of structures, it becomes apparent that under starvation a unique but rare population of structures with a large number of ULK1 molecules emerges (**Figure 4D**). Importantly, this population of structures is not present in fed cells and always colocalizes with Atg13. Based on this result and further evidence provided in (Banerjee et al., 2020), these structures are identified to be involved in autophagy and the formation of autophagosomes.

Another commonly used secondary data analysis approach is the use of pair-correlation or radial distribution functions to determine the average density of pairs of localization with respect to their distance (Puchner et al., 2013; van Lengerich et al., 2017; Banerjee et al., 2020). We therefore calculated the radial distribution function of ULK1 localizations that did and did not colocalize with Atg13. ULK1 localizations that did not

TABLE 1 | Performance Comparison of existing methods. This table compares our proposed kd-tree approach to three existing approaches, Clus-DoC, Coloc-Tesseler, and full matrix approach. Clus-DoC utilizes Ripley's K analysis and density based clustering using DBSCAN to segment localizations into clusters and separate colocalized from non-colocalized clusters. Coloc-Tesseler uses Voronoi tessellations to assess whether molecules are co localized and uses the tessellation diagram to draw boundaries around colocalized clusters. Datasets were simulated in a similar manner to those shown in **Figure 2** and described in the methods section. Time was measured as the entire time required to run program after data files were load. An F-score (described in the methods section) was used to compare colocalization accuracy among all datasets. Since localization lists cannot be outputted from Coloc-Tesseler, the colocalization accuracy of this method cannot be calculated. Furthermore, due to large memory requirement, Clus-DoC and the full matrix method cannot analyze datasets above 94 GB. Memory use by Coloc-Tesseler was estimated from task manager since it is a GUI based executable program with no available source code but all simulated molecule lists could be analyzed in an efficient time window (seconds) while only requiring between 0.2 and 1.5 GB of memory.

Number of localizations in population 1	Number of localizations in population 2	Full matrix memory (GB)	Clus-DoC memory (GB)	Coloc-Tessler memory (GB)	k-d tree memory (GB)
20,000	25,000	4	4	0.21	0.15
30,000	40,000	9.6	9.6	0.22	0.31
50,000	70,000	28	28	0.43	0.61
70,000	100,000	56	56	0.58	0.91
170,000	250,000	340	Not possible to compute	0.78	2.45
250,000	370,000	740	Not possible to compute	0.85	3.74
310,000	460,000	1,140	Not possible to compute	1.42	4.70

Number of localizations in population 1	Number of localizations in population 2	Full matrix time (s)	Clus-DoC time (s)	Coloc-Tessler time (s)	k-d tree time (s)
20,000	25,000	30.5	48.26	1.35	7.11
30,000	40,000	63.7	103.42	1.53	8.47
50,000	70,000	138.2	340.26	2.57	15.88
70,000	100,000	289.2	739.30	3.54	23.36
170,000	250,000	Not possible to compute	Not possible to compute	9.72	70.45
250,000	370,000	Not possible to compute	Not possible to compute	25.3	95.39
310,000	460,000	Not possible to compute	Not possible to compute	42.54	120.38

Number of localizations in population 1	Number of localizations in population 2	Full matrix accuracy	Clus-DoC accuracy	Coloc-Tessler accuracy	K-d tree accuracy
20,000	25,000	0.99	0.98	Not possible to compute	0.98
30,000	40,000	0.99	0.99	Not possible to compute	0.99
50,000	70,000	0.99	0.99	Not possible to compute	0.99
70,000	100,000	0.99	0.99	Not possible to compute	0.99
170,000	250,000	Not possible to compute	Not possible to compute	Not possible to compute	0.99
250,000	370,000	Not possible to compute	Not possible to compute	Not possible to compute	0.99
310,000	460,000	Not possible to compute	Not possible to compute	Not possible to compute	0.99

colocalize with Atg13 exhibited the lowest density and only a small peak at short distances up to ~74 molecules/μm^2 in starved and fed cells, indicating a small degree of basal clustering in the absence of Atg13 (**Figure 4E**). Since no significant difference is observed between fed and starved cell, these clusters are interpreted to be passive and not involved in autophagy initiation. ULK1 structures that did colocalize with Atg13 exhibited a significantly larger ULK1 density up to ~234 molecules/μm^2 in starved cells (**Figure 4E**). Since this density is also significantly larger than in fed cells, these clusters are interpreted to be dense initiation clusters that form in response to starvation and aid in the formation of phagophores (Banerjee et al., 2020) for details. Histograms of the ULK1 stoichiometry show that ULK1 clusters colocalized and not colocalized with Atg13 have identical stoichiometries in the fed case (**Figure 4F**) but colocalized ULK1 clusters have a higher stoichiometry in the starved case (**Figure 4G**). These results demonstrate that our presented SMLM analysis approach is powerful to isolate protein clusters and nanoscopic structures that are rare but of biological significance. Furthermore, any secondary SMLM data analysis such as quantification of molecule numbers, densities or sizes of structures can be applied to the isolated molecule lists to gain further insight into the nanoscopic characteristic and differences between different populations.

Comparison to Existing Colocalization Methods

To demonstrate the advantages k-d tree-based cross-correlation, we performed a comparison to existing methods that employ radial threshold-based colocalization, density-based cluster detection, and tessellation-based cluster detection/colocalization. The MATLAB based Clus-DoC program (Pageon et al., 2016a) combines a radial threshold-based method to characterize colocalization with a density-based cluster detection to identify colocalized molecules. This method first utilizes Ripley's K analysis to calculate the radial distance distribution between the colocalized molecule populations and then assigns each localization a normalized score based on its proximity to surrounding localizations of the opposite molecule population. The algorithm sets a score cutoff that is akin to a radial distance threshold to determine whether individual molecules are colocalized. Then, Clus-DoC uses the density-based clustering algorithm DBSCAN to segment localizations into individual clusters. Both techniques are commonly used in a variety of other clustering and colocalization algorithms (Ester et al., 1996; Owen et al., 2010; Malkusch et al., 2012; Lagache et al., 2018). The algorithm then combines both approaches to separate colocalized clusters with a minimum number of localizations from non-colocalized clusters. Finally, the algorithm calculates size and density metrics of colocalized clusters. This algorithm is most similar to our approach as it employs a radial distance distribution analysis to characterize the degree of colocalization between two protein populations and defines a threshold based on the radial distance to isolate colocalized molecules/cluster for downstream analysis. When validated against simulated datasets shown in **Figure 2** and described in the methods section, we find that the accuracy metrics are similar to ours since cross-correlation analysis is similar to Ripley's K analysis (**Table 1**) and since both methods rely in part on a distance threshold derived from the distance distribution. The main advantage our method compared to the Clus-DoC approach is the efficient analysis of the entire field of view of large datasets. Though Clus-DoC employs k-d trees to calculate the Ripley's K distribution, it requires the calculation of the full distance matrix to segment molecules into clusters and to isolate colocalized clusters. Therefore, Clus-DoC cannot analyze the full field of view for large 340 gigabyte-1.1 terabyte datasets due to large memory requirement (**Table 1**). In contrast, our method is able to efficiently analyze the full field of view of 340 gigabyte-1.1 terabyte sized datasets while needing a fraction of the available memory (**Table 1**). The memory required for our largest 1.1 TB simulated dataset is 4.7 GB which is similar to the memory available on laptops. Furthermore, using k-d trees for pair correlation analysis allows us to efficiently calculate the distance distribution across the full field of view to make an accurate assessment of the cutoff distances needed to segment molecules into clusters. Our k-d tree-based colocalization analysis also has an improved run time when compared to Clus-DoC (**Table 1**).

We also compared our method to colocalization analysis approaches based on Voronoi tessellation. These approaches have gained popularity since the detection of colocalized localizations does not require as a radial distance threshold, Ripley's K score, or density threshold (Levet et al., 2015, 2019; Andronov et al., 2016). Instead, these algorithms use Voronoi tessellations to determine cluster boundaries by using the relative similarities in the areas of polygons and densities of localizations. These techniques also allow for the direct calculation of Spearman's rank coefficients and Mander's coefficients to quantify the degree of clustering in the same molecule population and the degree of colocalization between multiple molecule populations. Coloc-Tesseler (Levet et al., 2019) is a graphical user interface (GUI) based C++ program that uses Voronoi tessellations to assess colocalization. Molecule lists from both molecule populations are directly inputted into the program through the GUI. The program then outputs colocalized molecules of one population, colocalized molecules of the other population, and non-colocalized molecules of both populations. The Voronoi diagram visually highlights the density difference between the colocalized and non colocalized population. Mander's and Spearman's rank coefficients can be calculated for a defined region of interest with the plot to quantify the degree of colocalization in that area. The user is also able to further refine co localization performance by altering relative density cutoffs used by the program to define cluster boundaries. This program can analyze large simulated datasets quickly while having a similar memory requirement as our k-d tree-based program (**Table 1**). The main drawback is that colocalized molecule lists or colocalized cluster lists cannot be outputted by the program which makes downstream analysis impossible. In addition, an accuracy analysis via an F-score, which requires true positives, false positives, false negatives, and true negatives cannot be calculated. The only other program outputs besides the color coded Voronoi plot are a quantification of colocalization via Mander's and Spearman rank coefficients. However, these metrics do not contain information about the distance dependent degree of colocalizations that the cross-correlation methods directly quantify. This distance dependent degree of-colocalization is particularly useful when comparing datasets across different states such as comparing the degree of colocalization between fed and starved cells at various distances (**Figure 4**).

In summary, while Voronoi tessellation efficiently detects clustering and colocalization of SMLM data, it does not contain the distance dependent density information of cross-correlation methods, which is useful for comparing data sets and for separating colocalized molecule lists for further downstream analysis. Our implementation of k-d trees for calculating the auto- or cross-correlation significantly lowers the computational time and memory needs, which allows for the analysis of large SMLM data sets that cannot be analyzed with existing cross-correlation methods. The modular code can be interfaced from existing SMLM data analysis packages for up- and downstream analysis and therefore enables the detection of otherwise hidden features such as the critical number of ULK1 molecules in rare clusters that initiate autophagy.

DATA AVAILABILITY STATEMENT

The data analyzed in this study is subject to the following licenses/restrictions: Simulated data from Figure 2 is available in the code repository located at https://github.com/PuchnerLab/cross-correlation-filtering Due to the large size of the SMLM data sets, they will not be uploaded but made available upon request. Requests to access these datasets should be directed to EMP, epuchner@umn.edu.

AUTHOR CONTRIBUTIONS

AM and DM wrote the manuscript, simulated and analyzed all data and made figures. CB recorded two-color SMLM data of ULK1 and Atg13. DHK constructed the endogenously tagged cell line and provided funding. EMP conceptualized and supervised research, provided funding and helped write the manuscript and make figures.

FUNDING

Research reported in this publication was supported by the National Institute of General Medical Sciences of the National Institutes of Health under Award number R21GM127965 (EMP) and R35GM130353 (DHK). DM was also supported by the Mayo Clinic Graduate School of Biomedical Sciences and the Mayo Foundation.

ACKNOWLEDGMENTS

We thank Yu Xu for her valuable help and input in the blink correction code and Ragnar Stefansson for the distance-based clustering code.

SUPPLEMENTARY MATERIAL

The Supplementary Material for this article can be found online at: https://www.frontiersin.org/articles/10.3389/fbinf.2021.739769/full#supplementary-material

REFERENCES

Andronov, L., Orlov, I., Lutz, Y., Vonesch, J. L., and Klaholz, B. P. (2016). ClusterViSu, a Method for Clustering of Protein Complexes by Voronoi Tessellation in Super-Resolution Microscopy. *Sci. Rep.* 6, 24084. doi:10.1038/srep24084

Banerjee, C., Song, D., Mehra, D., Mancebo, A., Kim, D.-H., and Puchner, E. M. (2020). Quantitative Super-Resolution Microscopy Reveals Distinct ULK1 Oligomeric States and Nanoscopic Morphologies during Autophagy Initiation. *bioRxiv*. doi:10.1101/2020.07.03.187336

Bentley, J. L. (1975). Multidimensional Binary Search Trees Used for Associative Searching. *Commun. ACM* 18, 509–517. doi:10.1145/361002.361007

Betzig, E., Patterson, G. H., Sougrat, R., Lindwasser, O. W., Olenych, S., Bonifacino, J. S., et al. (2006). Imaging Intracellular Fluorescent Proteins at Nanometer Resolution. *Science* 313, 1642–1645. doi:10.1126/science.1127344

Cai, D., Feliciano, D., Dong, P., Flores, E., Gruebele, M., Porat-Shliom, N., et al. (2019). Phase Separation of YAP Reorganizes Genome Topology for Long-Term YAP Target Gene Expression. *Nat. Cel Biol.* 21, 1578–1589. doi:10.1038/s41556-019-0433-z

Chang, Y. Y., and Neufeld, T. P. (2009). An Atg1/Atg13 Complex with Multiple Roles in TOR-Mediated Autophagy Regulation. *Mol. Biol. Cel* 20, 2004–2014. doi:10.1091/mbc.e08-12-1250

Cho, W. K., Spille, J. H., Hecht, M., Lee, C., Li, C., Grube, V., et al. (2018). Mediator and RNA Polymerase II Clusters Associate in Transcription-Dependent Condensates. *Science* 361, 412–415. doi:10.1126/science.aar4199

Chong, S., Dugast-Darzacq, C., Liu, Z., Dong, P., Dailey, G. M., Cattoglio, C., et al. (2018). Imaging Dynamic and Selective Low-Complexity Domain Interactions that Control Gene Transcription. *Science* 361, eaar2555. doi:10.1126/science.aar2555

Cisse, I. I., Izeddin, I., Causse, S. Z., Boudarene, L., Senecal, A., Muresan, L., et al. (2013). Real-Time Dynamics of RNA Polymerase II Clustering in Live Human Cells. *Science* 341, 664–667. doi:10.1126/science.1239053

De Zitter, E., Ridard, J., Thédié, D., Adam, V., Lévy, B., Byrdin, M., et al. (2020). Mechanistic Investigations of Green mEos4b Reveal a Dynamic Long-Lived Dark State. *J. Am. Chem. Soc.* 142, 10978–10988. doi:10.1021/jacs.0c01880

Ester, M., Kriegel, H. P., Sander, J., and Xiaowei, X. (1996). A Density-Based Algorithm for Discovering Clusters in Large Spatial Databases with Noise. Available at: https://www.osti.gov/biblio/421283 (Accessed June 9, 2021).

Griffié, J., Shannon, M., Bromley, C. L., Boelen, L., Burn, G. L., Williamson, D. J., et al. (2016). A Bayesian Cluster Analysis Method for Single-Molecule Localization Microscopy Data. *Nat. Protoc.* 11, 2499–2514. doi:10.1038/nprot.2016.149

Hartman, N. C., Nye, J. A., and Groves, J. T. (2009). Cluster Size Regulates Protein Sorting in the Immunological Synapse. *Proc. Natl. Acad. Sci. U S A.* 106, 12729–12734. doi:10.1073/pnas.0902621106

Heydarian, H., Joosten, M., Przybylski, A., Schueder, F., Jungmann, R., Werkhoven, B. V., et al. (2021). 3D Particle Averaging and Detection of Macromolecular Symmetry in Localization Microscopy. *Nat. Commun.* 12, 2847. doi:10.1038/s41467-021-22006-5

Hosokawa, N., Hara, T., Kaizuka, T., Kishi, C., Takamura, A., Miura, Y., et al. (2009). Nutrient-Dependent mTORC1 Association with the ULK1-Atg13-Fip200 Complex Required for Autophagy. *Mol. Biol. Cel* 20, 1981–1991. doi:10.1091/mbc.e08-12-1248

Hummer, G., Fricke, F., and Heilemann, M. (2016). Model-Independent Counting of Molecules in Single-Molecule Localization Microscopy. *Mol. Biol. Cel* 27, 3637–3644. doi:10.1091/mbc.E16-07-0525

Jung, C. H., Ro, S. H., Cao, J., Otto, N. M., and Kim, D. H. (2010). mTOR Regulation of Autophagy. *FEBS Lett.* 584, 1287–1295. doi:10.1016/j.febslet.2010.01.017

Kamada, Y., Funakoshi, T., Shintani, T., Nagano, K., Ohsumi, M., and Ohsumi, Y. (2000). Tor-Mediated Induction of Autophagy via an Apg1 Protein Kinase Complex. *J. Cel Biol.* 150, 1507–1513. doi:10.1083/jcb.150.6.1507

Karathanasis, C., Medler, J., Fricke, F., Smith, S., Malkusch, S., Widera, D., et al. (2020). Single-Molecule Imaging Reveals the Oligomeric State of Functional TNFα-Induced Plasma Membrane TNFR1 Clusters in Cells. *Sci. Signal.* 13, eaax5647. doi:10.1126/scisignal.aax5647

Kennedy, P. R., Barthen, C., Williamson, D. J., Pitkeathly, W. T. E., Hazime, K. S., Cumming, J., et al. (2019). Genetic Diversity Affects the Nanoscale Membrane Organization and Signaling of Natural Killer Cell Receptors. *Sci. Signal.* 12, eaaw9252. doi:10.1126/scisignal.aaw9252

Khater, I. M., Aroca-Ouellette, S. T., Meng, F., Nabi, I. R., and Hamarneh, G. (2019). Caveolae and Scaffold Detection from Single Molecule Localization Microscopy Data Using Deep Learning. *PLOS ONE* 14, e0211659. doi:10.1371/journal.pone.0211659

Khater, I. M., Meng, F., Wong, T. H., Nabi, I. R., and Hamarneh, G. (2018). Super Resolution Network Analysis Defines the Molecular Architecture of Caveolae and Caveolin-1 Scaffolds. *Sci. Rep.* 8, 9009. doi:10.1038/s41598-018-27216-4

Khater, I. M., Nabi, I. R., and Hamarneh, G. (2020). A Review of Super-Resolution Single-Molecule Localization Microscopy Cluster Analysis and Quantification Methods. *Patterns (N Y)* 1, 100038. doi:10.1016/j.patter.2020.100038

Kiskowski, M. A., Hancock, J. F., and Kenworthy, A. K. (2009). On the Use of Ripley's K-Function and its Derivatives to Analyze Domain Size. *Biophys. J.* 97, 1095–1103. doi:10.1016/j.bpj.2009.05.039

Krüger, C. L., Zeuner, M. T., Cottrell, G. S., Widera, D., and Heilemann, M. (2017). Quantitative Single-Molecule Imaging of TLR4 Reveals Ligand-Specific Receptor Dimerization. *Sci. Signal.* 10, eaan1308. doi:10.1126/scisignal.aan1308

Lagache, T., Grassart, A., Dallongeville, S., Faklaris, O., Sauvonnet, N., Dufour, A., et al. (2018). Mapping Molecular Assemblies with Fluorescence Microscopy and Object-Based Spatial Statistics. *Nat. Commun.* 9, 698. doi:10.1038/s41467-018-03053-x

Larson, A. G., Elnatan, D., Keenen, M. M., Trnka, M. J., Johnston, J. B., Burlingame, A. L., et al. (2017). Liquid Droplet Formation by HP1α Suggests a Role for Phase Separation in Heterochromatin. *Nature* 547, 236–240. doi:10.1038/nature22822

Lee, M. Y. (2019). Single-Molecule Localization Microscopy and Applications to Visualize the Accessible Genome with ATAC-See. Available at: https://www.proquest.com/docview/2508881084/abstract/3148C56746F645DFPQ/1 (Accessed June 9, 2021).

Lee, S. H., Shin, J. Y., Lee, A., and Bustamante, C. (2012). Counting Single Photoactivatable Fluorescent Molecules by Photoactivated Localization Microscopy (PALM). *Proc. Natl. Acad. Sci. U. S. A.* 109, 17436–17441. doi:10.1073/pnas.1215175109

Levet, F., Hosy, E., Kechkar, A., Butler, C., Beghin, A., Choquet, D., et al. (2015). SR-Tesseler: A Method to Segment and Quantify Localization-Based Super-resolution Microscopy Data. *Nat. Methods* 12, 1065–1071. doi:10.1038/nmeth.3579

Levet, F., Julien, G., Galland, R., Butler, C., Beghin, A., Chazeau, A., et al. (2019). A Tessellation-Based Colocalization Analysis Approach for Single-Molecule Localization Microscopy. *Nat. Commun.* 10, 2379. doi:10.1038/s41467-019-10007-4

Liu, Z., Legant, W. R., Chen, B. C., Li, L., Grimm, J. B., Lavis, L. D., et al. (2014). 3D Imaging of Sox2 Enhancer Clusters in Embryonic Stem Cells. *eLife* 3, e04236. doi:10.7554/eLife.04236

Malkusch, S., Endesfelder, U., Mondry, J., Gelléri, M., Verveer, P. J., and Heilemann, M. (2012). Coordinate-Based Colocalization Analysis of Single-Molecule Localization Microscopy Data. *Histochem. Cel Biol.* 137, 1–10. doi:10.1007/s00418-011-0880-5

Marenda, M., Lazarova, E., van de Linde, S., Gilbert, N., and Michieletto, D. (2021). Parameter-Free Molecular Super-Structures Quantification in Single-Molecule Localization Microscopy. *J. Cel Biol.* 220, e202010003. doi:10.1083/jcb.202010003

McSwiggen, D. T., Mir, M., Darzacq, X., and Tjian, R. (2019). Evaluating Phase Separation in Live Cells: Diagnosis, Caveats, and Functional Consequences. *Genes Dev.* 33, 1619–1634. doi:10.1101/gad.331520.119

Mercer, C. A., Kaliappan, A., and Dennis, P. B. (2009). A Novel, Human Atg13 Binding Protein, Atg101, Interacts with ULK1 and Is Essential for Macroautophagy. *Autophagy* 5, 649–662. doi:10.4161/auto.5.5.8249

Nieves, D. J., Pike, J. A., Levet, F., Griffié, J., Sage, D., Cohen, E. A. K., et al. (2021). A Framework for Evaluating the Performance of SMLM Cluster Analysis Algorithms. *bioRxiv*. doi:10.1101/2021.06.19.449098

Nino, D. F., Djayakarsana, D., and Milstein, J. N. (2020). FOCAL3D: A 3-Dimensional Clustering Package for Single-Molecule Localization Microscopy. *PLOS Comput. Biol.* 16, e1008479. doi:10.1371/journal.pcbi.1008479

Owen, D. M., Rentero, C., Rossy, J., Magenau, A., Williamson, D., Rodriguez, M., et al. (2010). PALM Imaging and Cluster Analysis of Protein Heterogeneity at the Cell Surface. *J. Biophotonics* 3, 446–454. doi:10.1002/jbio.200900089

Pageon, S. V., Nicovich, P. R., Mollazade, M., Tabarin, T., and Gaus, K. (2016a). Clus-DoC: A Combined Cluster Detection and Colocalization Analysis for Single-Molecule Localization Microscopy Data. *Mol. Biol. Cel* 27, 3627–3636. doi:10.1091/mbc.E16-07-0478

Pageon, S. V., Tabarin, T., Yamamoto, Y., Ma, Y., Nicovich, P. R., Bridgeman, J. S., et al. (2016b). Functional Role of T-Cell Receptor Nanoclusters in Signal Initiation and Antigen Discrimination. *Proc. Natl. Acad. Sci. U S A.* 113, E5454–E5463. doi:10.1073/pnas.1607436113

Park, J. M., Seo, M., Jung, C. H., Grunwald, D., Stone, M., Otto, N. M., et al. (2018). ULK1 Phosphorylates Ser30 of BECN1 in Association with ATG14 to Stimulate Autophagy Induction. *Autophagy* 14, 584–597. doi:10.1080/15548627.2017.1422851

Patterson, G. H., and Lippincott-Schwartz, J. (2002). A Photoactivatable GFP for Selective Photolabeling of Proteins and Cells. *Science* 297, 1873–1877. doi:10.1126/science.1074952

Perry, G. L. W. (2004). SpPack: Spatial point Pattern Analysis in Excel Using Visual Basic for Applications (VBA). *Environ. Model. Softw.* 19, 559–569. doi:10.1016/j.envsoft.2003.07.004

Puchner, E. M., Walter, J. M., Kasper, R., Huang, B., and Lim, W. A. (2013). Counting Molecules in Single Organelles with Superresolution Microscopy Allows Tracking of the Endosome Maturation Trajectory. *Proc. Natl. Acad. Sci. U. S. A.* 110, 16015–16020. doi:10.1073/pnas.1309676110

Ripley, B. D. (1979). Tests of 'Randomness' for Spatial Point Patterns. *J. R. Stat. Soc. Ser. B (Methodological)* 41, 368–374. doi:10.1111/j.2517-6161.1979.tb01091.x

Roach, P. J. (2011). AMPK -> ULK1 -> Autophagy. *Mol. Cel. Biol.* 31, 3082–3084. doi:10.1128/MCB.05565-11

Rollins, G. C., Shin, J. Y., Bustamante, C., and Pressé, S. (2015). Stochastic Approach to the Molecular Counting Problem in Superresolution Microscopy. *Proc. Natl. Acad. Sci. U S A.* 112, E110–E118. doi:10.1073/pnas.1408071112

Rust, M. J., Bates, M., and Zhuang, X. (2006). Sub-Diffraction-Limit Imaging by Stochastic Optical Reconstruction Microscopy (STORM). *Nat. Methods* 3, 793–795. doi:10.1038/nmeth929

Sabari, B. R., Dall'Agnese, A., Boija, A., Klein, I. A., Coffey, E. L., Shrinivas, K., et al. (2018). Coactivator Condensation at Super-Enhancers Links Phase Separation and Gene Control. *Science* 361, eaar3958. doi:10.1126/science.aar3958

Sengupta, P., Jovanovic-Talisman, T., Skoko, D., Renz, M., Veatch, S. L., and Lippincott-Schwartz, J. (2011). Probing Protein Heterogeneity in the Plasma Membrane Using PALM and Pair Correlation Analysis. *Nat. Methods* 8, 969–975. doi:10.1038/nmeth.1704

Simoncelli, S., Griffié, J., Williamson, D. J., Bibby, J., Bray, C., Zamoyska, R., et al. (2020). Multi-Color Molecular Visualization of Signaling Proteins Reveals How C-Terminal Src Kinase Nanoclusters Regulate T Cell Receptor Activation. *Cell Rep* 33, 108523. doi:10.1016/j.celrep.2020.108523

Stone, M. B., and Veatch, S. L. (2015). Steady-State Cross-Correlations for Live Two-Colour Super-Resolution Localization Data Sets. *Nat. Commun.* 6, 7347. doi:10.1038/ncomms8347

van Lengerich, B., Agnew, C., Puchner, E. M., Huang, B., and Jura, N. (2017). EGF and NRG Induce Phosphorylation of HER3/ERBB3 by EGFR Using Distinct Oligomeric Mechanisms. *Proc. Natl. Acad. Sci. U S A.* 114, E2836–E2845. doi:10.1073/pnas.1617994114

Veatch, S. L., Machta, B. B., Shelby, S. A., Chiang, E. N., Holowka, D. A., and Baird, B. A. (2012). Correlation Functions Quantify Super-Resolution Images and Estimate Apparent Clustering Due to Over-Counting. *PLOS ONE* 7, e31457. doi:10.1371/journal.pone.0031457

Williamson, D. J., Burn, G. L., Simoncelli, S., Griffié, J., Peters, R., Davis, D. M., et al. (2020). Machine Learning for Cluster Analysis of Localization Microscopy Data. *Nat. Commun.* 11, 1493. doi:10.1038/s41467-020-15293-x

Xie, L., Dong, P., Chen, X., Hsieh, T. S., Banala, S., De Marzio, M., et al. (2020). 3D ATAC-PALM: Super-Resolution Imaging of the Accessible Genome. *Nat. Methods* 17, 430–436. doi:10.1038/s41592-020-0775-2

Conflict of Interest: The authors declare that the research was conducted in the absence of any commercial or financial relationships that could be construed as a potential conflict of interest.

frontiers in Bioinformatics

ORIGINAL RESEARCH
published: 19 November 2021
doi: 10.3389/fbinf.2021.740281

Advanced Data Analysis for Fluorescence-Lifetime Single-Molecule Localization Microscopy

Jan Christoph Thiele[1]*, *Oleksii Nevskyi*[1], *Dominic A. Helmerich*[2], *Markus Sauer*[2] and *Jörg Enderlein*[1,3]*

[1]*Third Institute of Physics—Biophysics, Georg August University, Göttingen, Germany,* [2]*Department of Biotechnology and Biophysics, Biocenter, Julius-Maximilians-Universität Würzburg, Würzburg, Germany,* [3]*Cluster of Excellence "Multiscale Bioimaging: from Molecular Machines to Networks of Excitable Cells" (MBExC), Georg August University, Göttingen, Germany*

Edited by:
Christian Franke,
Friedrich Schiller University Jena,
Germany

Reviewed by:
Zoltan Cseresnyes,
Leibniz Institute for Natural Product
Research and Infection Biology,
Germany
Hanieh Mazloom-Farsibaf,
University of Texas Southwestern
Medical Center, United States

***Correspondence:**
Jan Christoph Thiele
jan.christoph.thiele@phys.uni-goettingen.de
Jörg Enderlein
jenderl@gwdg.de

Specialty section:
This article was submitted to Computational BioImaging, a section of the journal Frontiers in Bioinformatics

Received: *12 July 2021*
Accepted: *04 October 2021*
Published: *19 November 2021*

Citation:
Thiele JC, Nevskyi O, Helmerich DA, Sauer M and Enderlein J (2021) Advanced Data Analysis for Fluorescence-Lifetime Single-Molecule Localization Microscopy. Front. Bioinform. 1:740281. doi: 10.3389/fbinf.2021.740281

Fluorescence-lifetime single molecule localization microscopy (FL-SMLM) adds the lifetime dimension to the spatial super-resolution provided by SMLM. Independent of intensity and spectrum, this lifetime information can be used, for example, to quantify the energy transfer efficiency in Förster Resonance Energy Transfer (FRET) imaging, to probe the local environment with dyes that change their lifetime in an environment-sensitive manner, or to achieve image multiplexing by using dyes with different lifetimes. We present a thorough theoretical analysis of fluorescence-lifetime determination in the context of FL-SMLM and compare different lifetime-fitting approaches. In particular, we investigate the impact of background and noise, and give clear guidelines for procedures that are optimized for FL-SMLM. We do also present and discuss our public-domain software package "Fluorescence-Lifetime TrackNTrace," which converts recorded fluorescence microscopy movies into super-resolved FL-SMLM images.

Keywords: FLIM (fluorescence lifetime imaging microscopy), CRLB (Cramér-Rao lower bound) analysis, fluoresence lifetime fitting, super-resolution microscopy, lifetime uncertainty, SMLM (single molecule localisation microscopy)

1 INTRODUCTION

The advent of super-resolution microscopy (Hell, 2007; Huang et al., 2009) has revolutionized optical microscopy over the last ca. 30 years, pushing the limits of spatial resolution by three orders of magnitude down to the molecular length scale. The first of these super-resolution methods was STimulated Emission Depletion (STED) microscopy (Hell and Wichmann, 1994; Klar et al., 2000), developed by Stefan Hell and co-workers since the nineties of the last century, and later extended to Ground State Depletion IMaging (GSDIM) (Fölling et al., 2008; Hell, 2009) and REversible Saturable OpticaL Fluorescence Transitions (RESOLFT) imaging (Keller et al., 2007; Schwentker et al., 2007). This spurred also the development of alternative methods that use single-molecule localization in wide-field images (Single-Molecule Localization Microscopy or SMLM) (Klein et al., 2014). Among these methods are PhotoActivated Localization Microscopy (PALM) (Betzig et al., 2006), Stochastic Optical Reconstruction Microscopy (STORM) (Rust et al., 2006), fluorescence PALM (fPALM) (Hess et al., 2006), direct STORM (dSTORM) (Van de Linde et al., 2011), Point Accumulation for Imaging in Nanoscale Topography (PAINT) microscopy (Sharonov and Hochstrasser, 2006), and its most common variant DNA-PAINT (Schnitzbauer et al., 2017; Auer et al., 2018). These methods rely on the fact that one can localize the center position of an emitting molecule with much higher accuracy than the width of the molecule's image, the latter being defined by the optical resolution of the used microscope. Roughly speaking, this localization accuracy scales as the diffraction-limited resolution divided by the square root of the number of detected photons, so that, for example, a molecule that delivers 10^4 detectable photons can be localized ca. 100 times better than the classical resolution limit (neglecting here, for simplicity, all kinds of details such as noise, background, or detector pixelation) (Ram et al., 2006). By recording many images of well-separated molecules (by using fluorescent labels that can be switched between non-fluorescent and fluorescent states), one can generate a super-resolved image, the resolution of which is only limited by the number of photons detectable from a single molecule.

One powerful extension of fluorescence microscopy is fluorescence lifetime imaging microscopy (FLIM) (Bastiaens and Squire, 1999; van Munster and Gadella, 2005; Chang et al., 2007) which measures, besides the intensity of the fluorescence signal, also its lifetime. This lifetime information can be, for example, used for multiplexing by using fluorophores with different lifetimes (Niehörster et al., 2016), for Förster Resonance Energy Transfer (FRET) imaging (Llères et al., 2017), or to probe different environmental characteristics when using fluorophores that change their lifetime as function of specific parameters (e.g. pH, ion concentration, viscosity) (Klymchenko, 2017). The two most common FLIM techniques are based on a confocal microscope equipped with a pulsed laser source, single-photon sensitive detectors and electronics for Time-Correlated Single Photon Counting (TCSPC) (Becker, 2005; O'Connor, 2012), or on phase fluorometry using a time-modulated excitation source and a wide-field detector with time-modulated detection gain (Venetta, 1959; Spencer and Weber, 1969; Dong et al., 1995). However, both these approaches are usually not suitable for SMLM: Confocal microscopy was until recently rarely used for SMLM due to the limited frame rate, and phase-fluorometry systems are by far to insensitive for single-molecule imaging. In contrast, single-molecule sensitive wide-field detectors such as emCCD or sCMOS cameras that are generally used for SMLM do not provide any lifetime information. Only recently, it has been shown that one can use rapid-scanning confocal TCSPC microscopy for fluorescence-lifetime SMLM (FL-SMLM) (Thiele et al., 2020). In this case, one rapidly records confocal images with single-molecule sensitivity and then analyses the stack of recorded scan images in the same way as is done in conventional wide-field SMLM. A drawback is that the light-throughput (or dwell-time per position) in a confocal microscopy is much lower than that of a camera-equipped wide-field microscope, but the advantage is that one can obtain the lifetime information for each imaged and registered molecule, and that the z-sectioning capability of the confocal microscope can help to do SMLM even deeper into a sample, where out-of-focus background light becomes a problem. Alternatively to confocal TCSPC microscopy, new single-photon sensitive wide-field cameras that can measure lifetime information with TCSPC are more and more emerging. One type of such cameras is based on an array of single-photon avalanche diodes (Ulku et al., 2018; Morimoto et al., 2020) and shows great promise for future SMLM applications. A second type of wide-field TCSPC detectors is the commercially available LINCam (PhotonScore GmbH, Magdeburg, Germany), that has been successfully used for FL-SMLM (Oleksiievets et al., 2020). Although this system has a relatively low quantum yield of detection (5–15%), it shows nearly complete absence of any readout or other camera noise, thus assuring sufficient high signal-to-background ratios for successful single-molecule imaging.

Thus, with the advent of FL-SMLM, the question arises what is the most optimal and efficient way of TCSPC-based fluorescence-lifetime determination for SMLM. Within the context of single-molecule spectroscopy, different fitting methods have been discussed and evaluated with experimental data, indicating that maximum likelihood estimations outperform least-square minimization techniques (Maus et al., 2001; Santra et al., 2016), and theoretical limits have been derived analytically (for background-free case) (Köllner and Wolfrum, 1992) and numerically (for a large range of experimental parameters) (Bouchet et al., 2019; Trinh et al., 2021). Here, we compare the performance of different commonly used fit algorithms by using simulated and experimental data, and we derive an analytic expression for their theoretical limits. With experimental data, we analyze the impact of sample inhomogeneity (intrinsic fluorescence lifetime variation of dye molecules) on obtained lifetime distributions, and we finally demonstrate that pattern-matching algorithms can be much more efficient than full lifetime-fitting in lifetime-based multiplexing.

2 THEORY OF LIFETIME DETERMINATION

In a TCSPC lifetime measurement, the sample is excited with a train of sufficiently short laser pulses (ca. 100 femtoseconds to few dozen picoseconds) with fixed inter-pulse time period T (repetition period). For each detected photon, the arrival time t with respect to the last excitation pulse is recorded. The fluorescence lifetime τ can then be directly estimated from these arrival times as the mean (or standard deviation) of these t-values. However, this is only exact for a background-free measurement and for sufficiently large values of the repetition period T ($T \gg \tau$). For a precise lifetime determination with background and finite T, photon detection events are aggregated according to their arrival times, yielding the so-called TCSPC histogram, which is then fitted with a suitable model. Most fluorophores show a mono-exponential fluorescent decay behavior, so that one used a mono-exponential decay function with single decay time for fitting the TCSPC histogram (Lakowicz, 2006). In that case, the probability p for a photon to be detected at the time t is given by

$$p(t) = (1-b)\frac{\exp(-t/\tau)}{\tau(1-\exp(-T/\tau))} + \frac{b}{T} \tag{1}$$

where b is the relative background amplitude (constant background). Experimentally, photon arrival times are grouped into K discrete TCSPC time channels t_i of finite width Δt. In modern TCSPC systems, this time resolution Δt of measuring photon detection times is usually much smaller than both the lifetime τ and the width of the so-called instrument response function (IRF) σ_{IRF}, which is the experimentally measured TCSPC histogram for an ideal sample with infinitely fast fluorescence decay time. Therefore, any error that may be introduced by the TCSPC channel width is negligible, and the probability to detect a photon within one TCSPC channel is given by

$$p_i = \Delta t\ (1-b)\frac{\exp(-t_i/\tau)}{\tau(1-\exp(-T/\tau))} + \frac{b}{K}. \tag{2}$$

For a total number $\hat{N}$ of expected photons, the expectation value for each bin is then given by

$$\hat{m}_i = \hat{N} p_i = \hat{N}\Delta t\ (1-b)\frac{\exp(-t_i/\tau)}{\tau(1-\exp(-T/\tau))} + \hat{N}\frac{b}{K}. \tag{3}$$

Here, $\hat{m}_i$ denotes the expected number of photons falling into the ith detection channel. It is important to note that the above equation is only correct for an infinitely narrow, delta-function like IRF, or when considering only TCSPC channels after a cut off of the part containing the IRF (TCSPC histogram starting some time t_{cut} after the peak of the IRF). This cut off eliminates the impact of the IRF on a TCSPC histogram and is a common approach when working with IRFs sufficiently narrow compared to the fluorescence lifetime. The values of τ, b, and, depending on the method, $\hat{N}$ are fitted by minimizing a suitable score function. **Table 1** summarizes the defined symbols.

2.1 Least-Square Estimators

The default score function for curve fitting with unknown error distribution is the sum of least-squares, i.e. the sum of the squared difference between data and estimate (L2-norm):

$$\chi^2_{\mathrm{LS}} = \sum_{i=1}^{K} (\hat{m}_i - m_i)^2 \tag{4}$$

For single-photon detection, the number m_i of detected photons in channel i follows a Poissonian statistics, so that its variance is equal to its mean value (expectation value). In a weighted least-square minimization, each value in the χ^2-sum is weighted by the inverse of its variance, which requires to estimate, from the experimental data, the value of this variance. Pearson's χ^2 used the model-fitted values $\hat{m}_i$ as an estimate for the variance, which leads to

$$\chi^2_{\mathrm{P}} = \sum_{i=1}^{K} \frac{(\hat{m}_i - m_i)^2}{\hat{m}_i}. \tag{5}$$

In contrast, Neyman's χ^2 directly uses the experimentally measured values m_i as an estimate of the variance,

$$\chi^2_{\mathrm{N}} = \sum_{i=1}^{K} \frac{(\hat{m}_i - m_i)^2}{m_i}. \tag{6}$$

However, this expression becomes infinite whenever one of the values m_i becomes zero. Therefore, the denominator is either set to one in these cases (χ^2_{N1}), or the sum skips all i where $m_i = 0$ (χ^2_{N2}). In this work, we exclusively use χ^2_{N1}, because we observed that χ^2_{N2} leads to unstable fit results.

2.2 Maximum Likelihood Estimator

Unlike measurement in bulk or on densely labeled structures, single molecule measurements are always limited by the number of detected photons. Especially for low photon count numbers, the variance of these numbers significantly deviates from a Gaussian distribution which is, however, the basic assumption behind all least-square estimators. A maximum likelihood estimator (MLE) solves this problem by calculating the probability that a given set of parameters leads to an experimentally measured photon detection distribution. When assuming that the probability of detecting a photon in the ith channel of a TCSPC histogram is p_i, then the likelihood of measuring a TCSPC histogram $\{m_i\}$ is given by (Baker and Cousins, 1984)

$$L = N! \prod_{i=1}^{K} \frac{(p_i)^{m_i}}{m_i!}. \tag{7}$$

This likelihood function takes extremely small values that are numerically difficult to handle and not very practical for comparing different parameter sets. To facilitate computation, constant factors are neglected, and one uses the negative logarithm of L instead of L itself. This leads to the negative log-likelihood function λ defined by

$$\lambda = -\sum_{i=1}^{K} m_i \ln p_i. \tag{8}$$

A similar estimator is the Poisson deviance which is derived from the likelihood ratio and relies on the estimated (fitted) values $\hat{m}_i$ instead of the probability (Baker and Cousins, 1984):

$$\chi^2_{\lambda} = 2\sum_{i=1}^{K}\left(m_i \ln\frac{m_i}{\hat{m}_i} - (m_i - \hat{m}_i)\right) \tag{9}$$

By minimizing λ, the estimated number of photons $\hat{N}$ is implicitly fixed to the detected number of photons N. When replacing $\hat{m}_i = \hat{N} p_i$ and fixing $\hat{N} = N$, **Eq. 9** becomes **Eq. 8** with a constant offset.

In the limit of high photon detection numbers N, both weighted least-square methods as well as the MLE give similar results (Bajzer et al., 1991).

2.3 Goodness of Fit

A widely used parameter for estimating the goodness of a fit is the reduced χ^2/ν with degrees of freedom $\nu = K$—3 (minus three because we have the three fit parameters τ, b, and $\hat{N}$). For a perfect fit, χ^2/ν should be close to one. Smaller values indicate over-fitting, which is in the case of a mono-exponential model unlikely, and larger values indicate that the model does not describe the data completely. Both Pearson's χ^2_{P} and the MLE χ^2_{λ} asymptotically approach the χ^2 distribution. However, for low number of counts per time bin ($\langle m_i \rangle_i \lesssim 1$), the expectation value of χ^2_{λ}/ν deviates from the value one while the expectation value of χ^2_{P}/ν stays close to one at the cost of an increased variance. In practice, an increased variance is usually preferable over a count-dependent expectation value. The bias of the expectation value of χ^2_λ/ν can be reduced by grouping adjacent time bins and thus decreasing the time resolution.

2.4 Lifetime Uncertainty

The Cramér-Rao lower bound (CRLB) uses the Fisher information of a measurement to calculate a lowest bound for the variance that an unbiased estimator can have. The amount of information conveyed by a measurement is shared between all unknown parameters $\boldsymbol{\theta}$. For a mono-exponential decay with N photons and the probability distribution $p(t)$ of **Eq. 1**, the Fisher matrix is given by:

$$[\mathcal{I}(\boldsymbol{\theta})]_{j,k} = \int_0^T \frac{\partial \ln(Np(t))}{\partial \theta_j} \frac{\partial \ln(Np(t))}{\partial \theta_k} Np(t)\, \mathrm{d}t \tag{10}$$

The CRLB for each parameter is then given by the corresponding diagonal element of the inverse Fisher matrix:

$$\sigma_j^2 = \left[\mathcal{I}(\boldsymbol{\theta})^{-1}\right]_{jj} \tag{11}$$

For TCSPC-measurements, typically both the lifetime and background need to be estimated: $\boldsymbol{\theta} = \{\tau, b\}$. As discussed by Köllner and Wolfrum (1992), an unknown number of photons does not affect the uncertainty as off-diagonal elements $\mathcal{I}_{N,k\neq N}$ become zero. A step-by-step derivation of the CRLB σ_τ^2 for the lifetime is provided in the supplemental information.

2.5 Pattern Matching

Pattern matching is an alternative to lifetime fitting when the core task is to determine to which species a detected molecule belongs, among a discrete number of different species. Unlike lifetime fitting, pattern matching does not make any assumptions about the shape of the decay, and the only prerequisite is that reference decays of the separate species are available. To identify the most likely species to which a molecule belongs, the different negative log-likelihood values λ_α are calculated according to **Eq. 8** by setting $\{p_i\}$ equal to the normalized probability distributions $\{p_{i,\alpha}\}$ for each species α. The species with the lowest value of λ is then chosen as the most likely species. The rate of misidentifications depends on the number of photons N and the similarity of the patterns, see discussion in Enderlein and Sauer (2001) for details. The relative probability f_α for species α among a total of S species is given by

$$f_\alpha = \frac{\exp(-\lambda_\alpha)}{\sum_{\beta=1}^{S} \exp\left(-\lambda_\beta\right)}. \tag{12}$$

This equation is useful for rejecting molecules that cannot be classified with a high probability (Thiele et al., 2020). The relative probability is equivalent to the posterior probability of a Bayesian model comparison when assuming equal prior probabilities. In contrast to likelihoods or Bayes factors, the posterior probability can be averaged over multiple molecules or many time points.

Unlike the situation in usual fitting, the $\{p_{i,\alpha}\}$ are the same for all TCSPC histograms. Therefore, the logarithms can be calculated in advance, and **Eq. 8** can be implemented as a simple matrix multiplication. For this purpose, first the $K \times S$-dimensional pattern matrix $\mathbf{P}_{\ln}$ is calculated which contains the logarithm of the normalized patterns as row vectors. Second, the negative log-likelihood matrix $\boldsymbol{\Lambda}$ is obtained by multiplication with matrix $\mathbf{M}$, which is the $J \times K$-dimensional matrix constructed from the J TCSPC histograms (column vectors):

$$\boldsymbol{\Lambda} = -\mathbf{M} \cdot \mathbf{P}_{\ln} \tag{13}$$

The resulting $J \times S$-dimensional matrix $\boldsymbol{\Lambda}$ with entries $\lambda_{j,\alpha}$ allows for a fast calculation of the relative probabilities $f_{j,\alpha}$ with **Eq. 12**, or to directly determine the most likely pattern x_j for each TCSPC histogram with

$$x_j = \underset{\alpha}{\arg\min}\ \lambda_{j,\alpha}. \tag{14}$$

The *a priori* calculation of $\mathbf{P}_{\ln}$, together with the single matrix multiplication step, enables efficient calculation of $\lambda_{j,\alpha}$ for thousands of TCSPC histograms in parallel and for many species. By employing a library of calculated decays $\{p_{i,\alpha}\}$, this approach allows for quick determination of the most likely parameter set using a grid-based search. We provide example code of pattern matching for classification and as well as for grid-based fitting in the supplementary material (Thiele, 2021b).

2.6 Fitting Using the Instrument Response Function

For lifetime values similar or shorter than the width of the IRF, it can be necessary to explicitly take the shape of the IRF into account. This is achieved by convolving the probability distribution $\{p_i\}$ (**1**) or expectation values $\{\hat{m}_i\}$ (**Eq. 3**) with the normalized IRF $\{q_i\}$:

$$\hat{p}_i^* = \hat{p}_i \circledast q_i, \quad \hat{m}_i^* = \hat{m}_i \circledast q_i \tag{15}$$

Here, $\circledast$ denotes a discrete, circular convolution. Subsequently, the score function is minimized with the convolved probability distributions $\{\hat{p}_i^*\}$ or expectation values $\{\hat{m}_i^*\}$, respectively. This can be either performed for the tail of the decay only, or, more commonly, for the entire decay curve.

The IRF can be measured experimentally, or it can be approximated with a model. Typically, a Gaussian distribution or a shifted Gamma distribution, which reflects a potential asymmetry of the IRF, are used as parametric models. In this work, we employed a shifted Gamma distribution of the form

$$q_i = \begin{cases} 0 & t_i \leq t_0 \\ \Delta t \kappa^\rho (t_i - t_0)^{\rho-1} \exp[-\kappa(t_i - t_0)]/\Gamma(\rho) & t_i > t_0 \end{cases} \tag{16}$$

where the distribution depends on the following three parameters: starting time of the peak t_0, shape parameter ρ, and rate parameter κ.

3 METHODS

3.1 Simulations

The different least-square estimators and the maximum-likelihood estimator were tested on simulated data. If not stated otherwise, the following parameters were used: lifetime

$\tau = 2$ ns, background $b = 0.2$, repetition period $T = 25$ ns, TCSPC time resolution $\Delta t = 0.016$ ns. Using these parameters and the average total number N of detected photons, the expectation values $\{\hat{m}_i\}$ were calculated for each time bin following **Eq. 3**. To generate a simulated decay $\{m_i\}$, Poisson-distributed random variables with expectation value $\{\hat{m}_i\}$ were drawn. The simulated data was fitted with the model function (**Eq. 3**) by minimizing each estimator (**Eqs 5**, **6** and **8**) with a Nelder-Mead simplex algorithm. Initial fit values were calculated by multiplying the true value with a random number between 0.5 and 1.5 to obtain a low-precision initial guess value. Simulation and fitting was repeated 10^5 times to obtain a sufficiently large distribution of fit results. The simulation was implemented in Matlab (R2020a, The MathWorks Inc.).

To investigate the influence of the IRF on the fitted lifetime, a dedicated simulation was performed. First, the experimental IRF of the confocal microscope described in (Thiele et al., 2020) was determined by measuring backscattering from a coverglass coated with a 10 nm gold film. The substrate preparation is described in detail in (Ghosh et al., 2021). A normalized experimental IRF is obtained from the measured TCSPC histogram by subtracting the background, defined as the average count level in the second half of the TCSPC histogram, and dividing by its sum. A parametric IRF was obtained by fitting the TCSPC histogram with $(1-b)q_i + b/K$, where q_i is defined as in **Eq. 16**, by minimizing the negative log-likelihood (**Eq. 8**) for the parameters t_0, ρ, κ, and b with a Nelder-Mead simplex algorithm. Subsequently, the parametric IRF was calculated with these t_0, ρ, and κ.

Similar to the previous simulation, a decay with background $b = 0.2$, repetition period $T = 25$ ns, and time resolution $\Delta t = 0.016$ ns was calculated, while its lifetime was varied from 0.025 ns to 2.0 ns in 0.025 ns increments. The calculated decay was convolved with the experimental IRF, and 10^5 TCSPC histograms with a mean value of 2000 photons were simulated. From the TCSPC histograms, the lifetime values were determined by an MLE grid search based on the pattern matching described in **Section 2.4** with 500 lifetime values linearly spaced from 0.01 ns to 3.00 ns and 60 different background values. The reference decays were calculated in three different ways: (1) mono-exponential decay without IRF, (2) mono-exponential decay convolved with the experimental IRF, and mono-exponential decay convolved with the parametric IRF. For case (1), the likelihood was calculated using the tail of the decay starting $t_{\text{cut}} = 0.2$ ns after the maximum of the sum of all decays. The correspondingly shortened reference decays were normalized prior to calculating the likelihood values. For case (2) and (3), the likelihood was calculated with the entire TCSPC histogram.

3.2 Experimental Data

For checking the different lifetime-fitting approaches on real experimental data, we used dSTORM images of three different structures: Alexa 647-labeled microtubules, Atto 655-labeled clathrin pits in fixed COS7 cells, and 3 μm polystyrene beads decorated with Alexa 647-labeled DNA. All experimental data were taken from (Thiele et al., 2020), where details on the sample preparation and measurement can be found. The data was processed with TrackNTrace (see below) to extract single-molecule TCSPC histograms. The tail of the single-molecule decay curves, starting 0.2 ns after the maximum in the sum of all decays, were fitted by minimizing the negative log-likelihood function (**Eq. 8**) with a Nelder-Mead simplex algorithm. Initial fit values were determined by using a pattern matching of the decay curves. For this purpose, 500 lifetime values linearly spaced from 0.01 to 5.00 ns and 60 different background values were used.

For the analysis of the experimentally obtained lifetime distributions (**Figure 3**), the single molecule data was sorted according to the number of photons per TCSPC histogram, and then divided into 30 equally-sized groups. Only molecules with an image size (standard deviation) between 100 and 180 nm, with at least 25 photons in the TCSPC histogram, and with a reduced Pearson's χ^2_{P}/ν of their lifetime fit between 0.8 and 1.2 were included in the final analysis.

For each group, the standard deviation σ of the single molecule lifetimes and the analytic CRLB based on the average number of photons $\langle N\rangle$, the lifetime $\langle\tau\rangle$ and the background $\langle b\rangle$, was calculated. The width of the sample-intrinsic lifetime variation σ_{sample} was determined by fitting the σ for $\langle N\rangle > 100$ with an decay of the form $\sigma = a\langle N\rangle^{-k} + \sigma_{\text{sample}}$ with empirical fit parameters a, k, and intrinsic sample-related variance σ_{sample} by minimizing χ^2_{LS} with a Nelder-Mead simplex algorithm.

For exemplifying and checking the pattern-matching algorithm, we used data obtained from COS7 cells labeled with either Alexa 647 or Atto 655, from which synthetic data with mixed labeling were generated. Only molecules with an image size between 100 and 180 nm and at least 50 photons in the TCSPC histogram were used for further analysis. As reference patterns, we used normalized decay curves of pure samples of Alexa 647 and Atto 655, respectively. With these reference patterns, the relative probability that a localized molecule was either Alexa 647 or Atto 655 was calculated, following **Eq. 12**. Based on these relative probabilities and the known identities of the samples, the receiver operating characteristic (ROC) and the area under curve (AUC) were calculated. As comparison, the same curves were calculated using MLE fitted lifetime values as classification score.

4 RESULTS

4.1 Simulations and Analytical Results

The CRLB yields the minimum variance that can be attained by an unbiased estimator. For a mono-exponential decay with background and an infinite time resolution, an analytical expression for the CRLB can be given. It has recently been shown numerically that the TCSPC channel discretization does not considerably affect the CRLB as long as the time bins are much narrower than the lifetime (Trinh et al., 2021). In contrast, background substantially affects a CRLB (Köllner and Wolfrum, 1992). The full expression of the CRLB for the variance σ^2_τ of the lifetime τ as function of τ itself, the number of photons N, the background fraction b, and the repetition period T, is given in the supplementary information (see **Supplementary Equation S1**). It is, however, useful to analyze some limiting cases. In the limiting case of an infinitely large repetition period T, the estimator is only limited by Poisson noise:

$$\lim_{T\to\infty} \sigma_\tau^2 = \frac{\tau^2}{N}\frac{1}{1-b} \tag{17}$$

Here, $N(1-b)$ photons correspond to the fluorescence signal while the Nb background photons do not carry any lifetime information. Since the off-diagonal elements of the Fisher matrix vanish ($[\mathcal{I}(\boldsymbol{\theta})]_{\tau,b} = 0$) for $T \to \infty$, the knowledge of the background does not affect the result. For a finite value of T, these off-diagonal elements become non-zero and do increase the value of σ_τ^2. Therefore, it makes a difference whether the background level needs to be estimated independently as an additional fit parameter, or whether it is known in advance. If it is known that the background is zero one finds

$$\lim_{b\to 0} \sigma_\tau^2 = \frac{\tau^2}{N}\frac{2(1-\cosh(\chi))}{2+\chi^2-2\cosh(\chi)} \quad \text{with } \chi = \frac{T}{\tau} \tag{18}$$

while for an unknown but zero background one finds the generally larger value

$$\lim_{b\to 0} \sigma_\tau^2 = \frac{\tau^2}{N}\frac{4\sinh\left(\frac{\chi}{2}\right)\left(\chi^2-2\cosh(\chi)+2\right)}{\left(\chi^4+12\chi^2+12\right)\sinh\left(\frac{\chi}{2}\right)-4\chi^3\cosh\left(\frac{\chi}{2}\right)-4\sinh\left(\frac{3\chi}{2}\right)}. \tag{19}$$

A comparison between known and unknown background levels and calculations for different combinations of background and repetition period T are provided in **Supplementary Figure S1**.

To validate the performance of the different estimators, simulated TCSPC histograms were fitted and the fit results compared to the ground truth. Especially at low photon counts, there is a striking difference between the estimators. In **Figure 1A**, it is apparent that weighted least-square estimators are biased and do not reproduce the correct decay curve. The distribution of fitted lifetime values (**Figure 1B**) emphasizes this count-dependent bias. In contrast, the median lifetime value recovered by the unweighted LSQ and the MLE are very close to the ground truth. However, the MLE achieves this with much less uncertainty. The distribution of the fitted number of photons, background level, and bias of median lifetime values in dependence of the number of counts are given in **Supplementary Figure S2**. As shown in **Figure 1C**, the standard deviation of the lifetime values obtained with weighted LSQ and MLE do approach the theoretical limit of the CRLB. However, solely MLE provides a performance close to the CRLB with no substantial bias of the lifetime values, even for photon detection numbers of only a few hundred. This behavior is not specific for the chosen simulation parameters. In the supplementary material, see **Supplementary Table S1**, we present additional simulations for lower lifetimes, for shorter repetition rates, and for higher and lower background values, confirming our results described above. In good agreement with our results, Santra et al. (2016) found no bias for MLE but substantial bias for least-square estimators when fitting solution measurements and neglecting background.

4.1.1 Influence of the Instrument Response Function

The simulations so far neglected the influence of the IRF which is equivalent to assuming a dirac-like IRF. In reality, the IRF has a finite width and can influence the fitted lifetime. **Figure 2** shows an experimental IRF obtained by recording the back-scattered light form a gold-covered coverslip, together with its parametric fit. The parametric IRF was obtained by fitting the scattering measurement and has a full width at half maximum (FWHM) of 0.58 ns. The good fit quality confirms that the shifted Gamma distribution is an excellent model for the true IRF.

To evaluate the effect of the IRF, we simulated TCSPC measurements using the experimental IRF and for sample lifetimes (ground-truth) between 0.025 and 2.0 ns. The computed TCSPC curves were then fitted with and without IRF using an MLE grid search. **Figure 2B** shows that the tail fit leads to a bias towards larger lifetime values when the actual lifetime comes closer to the width of the IRF. For lifetime values close to zero, the bias reaches 0.2 ns. This bias can be eliminated by taking the IRF explicitly into account. Fits with the IRF, both with the experimental IRF (which was used for the TCSPC simulation) as well as with its parametric form, lead to negligible bias for all tested lifetimes.

With a FWHM of above 0.5 ns, the IRF we used for the simulation was rather broad due to the employed diode laser. For a narrower IRF, e.g. with a typical white light laser, the influence of the IRF will be even less pronounced and the bias of tail-fit results reduced.

4.2 Experimental Results

4.2.1 Estimation of the Intrinsic Lifetime Distribution

In real measurements, single-molecule lifetime values are not only affected by Poisson noise but also by intrinsic sample inhomogeneity (variation of intrinsic lifetime values). **Figure 3** compares two samples: Alexa 647 in a cellular environment exhibits a broader lifetime distribution that cannot be explained solely by the CRLB, while the lifetime distribution of DNA-conjugated Alexa 647 on a polymer bead surface is close to the CRLB. Unlike the CRLB, this sample-dependent contribution to the lifetime variance does not dependent on the number of detected photons. Therefore, it can be estimated as the asymptotic limit of the standard deviation of the lifetimes as a function of the number of detected photons, as shown in **Figures 3C,F**. When taking this additional intrinsic sample-related variance into account, the theoretical estimate (green line in **Figures 3B,E**) does closely match the measured lifetime distribution. By simulating a sample with a known lifetime inhomogeneity (**Supplementary Figure S13**), we can confirm this method recovers the intrinsic variance. In the cellular environment, we observe a small dependence of the average lifetime on photon number (**Supplementary Figure S14**). This adds to the overall width of the lifetime distribution (**Figure 3B**), but does not affect our estimation of the intrinsic variance as the standard deviation is independent of the mean.

The clear difference between the average lifetimes in the two different samples matches results in the literature that the lifetime of cyanines like Alexa 647 sensitively depends on the environment (Buschmann et al., 2003; Klehs et al., 2014).

For experimental data, all lifetimes in this work are determined with mono-exponential tail-fits. The interval of the TCSPC

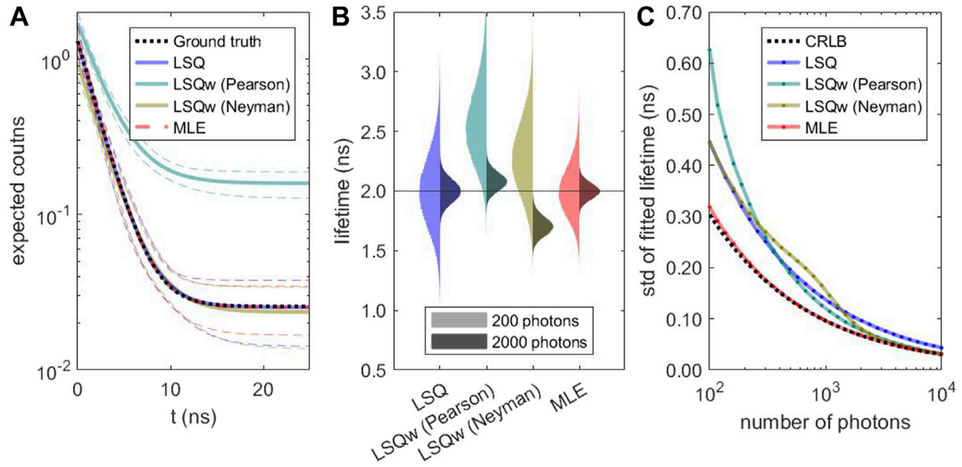

FIGURE 1 | Performance of different lifetime estimators: Based on a calculated decay with 2 ns lifetime and 20% background photons, 10^5 decay curves with Poissonian noise were simulated for different numbers of photons and fitted using different estimators. **(A)** Ground truth (black) and fit results of simulated decays with 200 photons (expectation value). The thick, colored lines indicate the median, and the thin, dashed lines the 5 and 95% quantiles. **(B)** Distribution of fitted lifetime values for decays with 200 photons **(left half)** and 2000 photons **(right half)**. **(C)** Standard deviation of the lifetime distributions and calculated CRLB as a function of the number of photons in the decay.

TABLE 1 | Definitions of frequently used symbols.

Parameter	Description
τ	fluorescence lifetime
b	background fraction
N	total number of photons
T	repetition period
t	time since last pulse
K	number of TCSPC time bins
Δt	width of TCSPC time bins
p	photon detection probability
m_i	counts in time bin i
$\hat{m}_i$	expected counts in time bin i
$\hat{N}$	expected total number of counts
t_{cut}	cut-off time for tail-fits
χ^2_{LS}	least square error
ν	degrees of freedom (here, $K-3$)
λ	negative log-likelihood
σ^2_τ	lifetime uncertainty (CRLB)
t_0, ρ, κ	parameters of model IRF

histogram which is used for lifetime fitting starts at or short time (cut off t_{cut}) after the maximum of the TCSPC histogram. **Figure 4C** illustrates that the cut off does not notably affect the resulting lifetime distribution for a mono-exponential sample.

4.2.2 Pattern Matching

A pattern matching compares the TCSPC histogram with a library of reference patterns. This allows one to classify single molecules without fitting their lifetime and setting a lifetime threshold. **Figure 4** compares the performance of pattern matching (A) with lifetime-fitting based classification (B). Pattern matching offers a higher sensitivity and specificity which is reflected in the larger area under the curve (AUC) as compared to lifetime-fitting based classification. The reference patterns, shown in **Supplementary Figure S15A**, reveal that the decay curves are not strictly mono-exponential. Therefore, overlapping lifetime distributions (**Supplementary Figure S15B**) can be separated better by pattern matching than by lifetime fitting. The specificity can be improved by removing molecules with low number of photons.

Pattern matching is also useful for quickly finding good guess values over a limited parameter space using a parallel grid search. **Figure 4C** shows that the lifetimes obtained by pattern matching closely resemble the distribution obtained from MLE fitting. For highest precision, the lifetime values could be refined with a subsequent precise MLE fit.

5 DISCUSSION AND CONCLUSION

Using Monte-Carlo simulations, we have demonstrated that MLE-based fitting outperforms common LSQ-based fitting and achieves close to shot-noise limited accuracy. An analytic expression for this limit, the CRLB for a mono-exponential decay with unknown background and finite repetition period was derived. In SMLM, the localization uncertainty derived from the CRLB has become an indispensable parameter for data filtering. We suggest to use the lifetime uncertainty in a similar fashion for filtering lifetime-resolved single-molecule data, to improve separation between different species or states, and to estimate experimental limitations. To facilitate its application, we provide a Python implementation of the CRLB calculation (Thiele, 2021a).

Our simulations confirmed that the fit uncertainties originating from photon statistics, background, and finite repetition period can be well estimated by the CRLB. However, in actual single-molecule lifetime experiments, additional sources of uncertainty need to be considered. Many

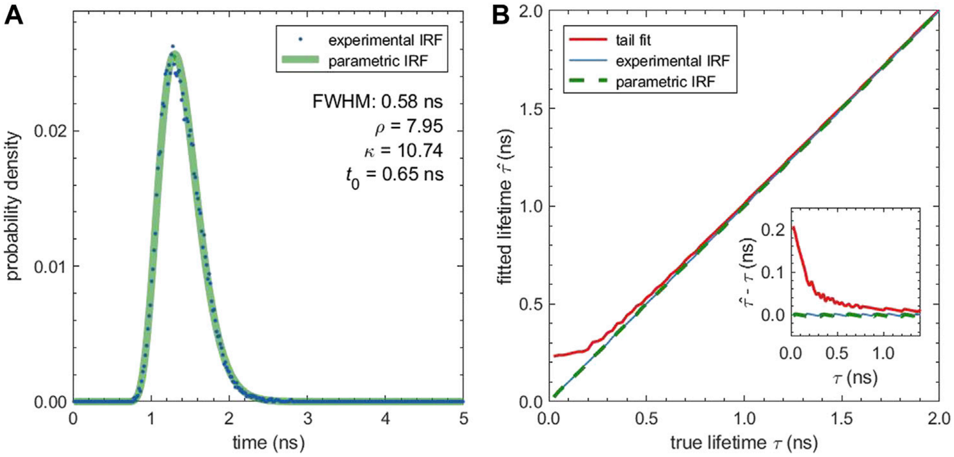

FIGURE 2 | Influence of a non-ideal IRF on the fitted lifetime: **(A)** Experimental IRF measured from gold scattering (blue dots) and parametric IRF (green line). The parametric IRF is described by a shifted Gamma distribution with the parameters given in the plot. **(B)** Median fitted lifetime for simulated decays with the experimental IRF and different lifetimes. The fitted lifetime was determined by fitting the tail of the decays with a mono-exponential function (tail fit) and by fitting the entire decay curve using either the experimental IRF or the parametric IRF. The inset shows the absolute difference between the fitted and the true lifetime in dependence of the true lifetime. All fits are grid-based MLE fits, and tail fits use a cut off t_{cut} = 0.2 ns.

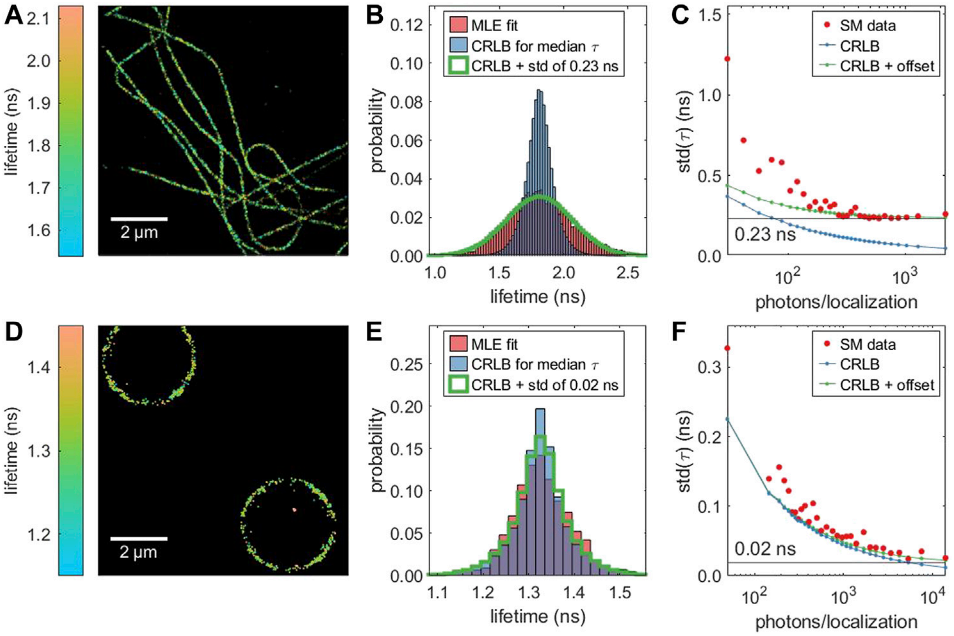

FIGURE 3 | Lifetime-resolved dSTORM of two different samples with Alexa 647: **(A, B, C)** immunostained microtubules in fixed COS7 cells and **(D, E, F)** DNA-functionalized micro-beads. **(A,D)** Super-resolved FL-SMLM image. **(B, E)** Distribution of the single molecule lifetime values (red), CRLB-limited distribution assuming equal lifetime values for all molecules, and CRLB-limited distribution with an additional broadening. **(C, F)** Dependence of the standard deviation of the fitted lifetime on the number of photons. With an increasing number of photons, the standard deviation (red) approaches a limit which is caused by sample inhomogeneity (intrinsic variation of lifetime values). In contrast, the corresponding CRLB (blue) approaches zero. The green line represents the square root of the sum of the variance as predicted by the CRLB and the intrinsic variance of the sample.

fluorophores are known to be sensitive to their local environment. This can be a desired effect, e.g. for lifetime-based environmental sensing (Klymchenko, 2017). However, for many applications, including lifetime-based multiplexing or FRET, the intrinsic lifetime variation should be as narrow as possible because any broadening increases final uncertainties of the results. Therefore, it is important to quantify the intrinsic lifetime variation across a single species of labels/dyes which is, unlike the CRLB,

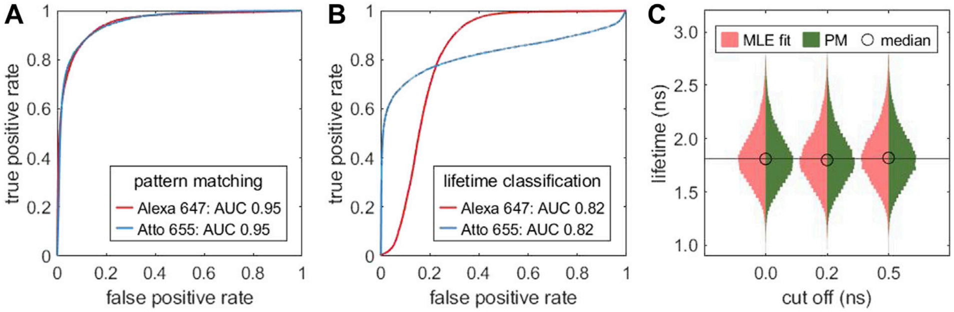

FIGURE 4 | Pattern matching as alternative to lifetime fitting: Receiver operating characteristic (ROC) curve for classifying a mixture of two different fluorophores (Alexa 647, Atto 655) with different lifetimes. In **(A)**, the classification is based on pattern matching, in **(B)** on the MLE fitted single molecule lifetimes. The data was generate by combining measurements of two samples, each labeled with one fluorophore. **(C)** Comparison of the lifetime distribution obtained by MLE lifetime fitting (red) and an MLE grid search based on pattern matching (dark green) for different cut off values t_{cut} relative to the TCSPC maximum. Based on the same measurement as **Figure 3A**.

independent on the number of detected photons. We have shown that this intrinsic lifetime variation can be extracted from the photon-number dependence of the experimentally determined lifetime distribution. As presented in **Figure 3**, the same fluorophore but in different samples can show very different lifetime variation, with measurements in cells exhibiting a considerably broader variation. This suggests that single-molecule lifetime measurements in cells might not always be limited only by the instrument response function or the photon statistics, but can be also limited by intrinsic lifetime variations of a sample itself.

In FLIM experiments, the fluorescence lifetime is often used to identify different states, e.g. high or low FRET efficiency, or distinguish between different species with different lifetimes. FL-SMLM extracts this information from single molecules and allows for a discrete classification of imaged molecules based on their lifetimes. For such an application, full lifetime fitting is not always the most efficient way for classification. As demonstrated in **Figure 4**, pattern matching outperforms lifetime-based classification. Pattern matching compares a measured TCSPC histogram with reference histograms, which can be done extremely fast, and which does not require any specific knowledge about the character of a fluorescence decay (e.g. mono-exponential decay) while utilizing all photons of a TCSPC histogram. When using a large number of calculated decays, pattern matching can serve as a way of unbiased lifetime estimation within a fixed parameter space. Since this is very fast, it is attractive for initial parameter guesses and might be useful when many thousands of lifetimes need to be determined, e.g. in pixel-wise time-resolved data.

To facilitate the analysis of FL-SMLM data, we have amended our open source software package TrackNTrace (Stein and Thiart, 2016) with the ability to extract TCSPC histograms and to fit lifetime values. It conveniently covers all required computational steps, from reading raw data to reconstructing FLIM images, all within a single GUI-based app. In this app, lifetime values can be determined with fast pattern matching and, optionally, by subsequent refinement with precise MLE-based fitting.

DATA AVAILABILITY STATEMENT

Publicly available datasets were analyzed in this study. This data can be found here: https://projects.gwdg.de/projects/cfl-smlm/repository. The supplemental scripts are available at https://doi.org/10.5281/zenodo.5093591 and example code for pattern matching at https://doi.org/10.5281/zenodo.5423457. Our analysis software TrackNTrace can be found at https://github.com/scstein/TrackNTrace.

AUTHOR CONTRIBUTIONS

JT and JE conceived the project. JT performed theoretical derivations, simulations, and data analysis. JT and ON acquired the data. ON prepared the bead sample. DH prepared the cell samples under the supervision of MS. JT and JE wrote the manuscript. All authors edited and approved the final manuscript.

FUNDING

This work was financially supported by funding from the European Research Council (ERC) under the European Union's Horizon 2020 research and innovation program (AdR ERC Grant "smMIET" No. 884488), the ERC Synergy Grant "ULTRARESOLUTION" (951275—GAP-951275), and by the Deutsche Forschungsgesellschaft (DFG) through Germany's Excellence Strategy EXC 2067/1–390729940.

ACKNOWLEDGMENTS

We are grateful to Alexey Chizhik and Roman Tsukanov for many fruitful discussions.

SUPPLEMENTARY MATERIAL

The Supplementary Material for this article can be found online at: https://www.frontiersin.org/articles/10.3389/fbinf.2021.740281/full#supplementary-material

REFERENCES

Auer, A., Schlichthaerle, T., Woehrstein, J. B., Schueder, F., Strauss, M. T., Grabmayr, H., et al. (2018). Nanometer-scale Multiplexed Super-resolution Imaging with an Economic 3d-Dna-Paint Microscope. *ChemPhysChem* 19, 3024–3034. doi:10.1002/cphc.201800630

Bajzer, e., Therneau, T. M., Sharp, J. C., and Prendergast, F. G. (1991). Maximum Likelihood Method for the Analysis of Time-Resolved Fluorescence Decay Curves. *Eur. Biophys. J.* 20, 247–262. doi:10.1007/BF00450560

Baker, S., and Cousins, R. D. (1984). Clarification of the Use of CHI-Square and Likelihood Functions in Fits to Histograms. *Nucl. Instr. Methods Phys. Res.* 221, 437–442. doi:10.1016/0167-5087(84)90016-4

Bastiaens, P. I., and Squire, A. (1999). Fluorescence Lifetime Imaging Microscopy: Spatial Resolution of Biochemical Processes in the Cell. *Trends Cel Biol* 9, 48–52. doi:10.1016/s0962-8924(98)01410-x

Becker, W. (2005). *Advanced Time-Correlated Single Photon Counting Techniques, Vol. 81*. Berlin, Germany: Springer Science & Business Media.

Betzig, E., Patterson, G. H., Sougrat, R., Lindwasser, O. W., Olenych, S., Bonifacino, J. S., et al. (2006). Imaging Intracellular Fluorescent Proteins at Nanometer Resolution. *Science* 313, 1642–1645. doi:10.1126/science.1127344

Bouchet, D., Krachmalnicoff, V., and Izeddin, I. (2019). Cramér-Rao Analysis of Lifetime Estimations in Time-Resolved Fluorescence Microscopy. *Opt. Express* 27, 21239–21252. doi:10.1364/OE.27.021239

Buschmann, V., Weston, K. D., and Sauer, M. (2003). Spectroscopic Study and Evaluation of Red-Absorbing Fluorescent Dyes. *Bioconjug. Chem.* 14, 195–204. doi:10.1021/bc025600x

Chang, C. W., Sud, D., and Mycek, M. A. (2007). Fluorescence Lifetime Imaging Microscopy. *Methods Cel Biol* 81, 495–524. doi:10.1016/S0091-679X(06)81024-1

Dong, C. Y., So, P. T., French, T., and Gratton, E. (1995). Fluorescence Lifetime Imaging by Asynchronous Pump-Probe Microscopy. *Biophys. J.* 69, 2234–2242. doi:10.1016/S0006-3495(95)80148-7

Enderlein, J., and Sauer, M. (2001). Optimal Algorithm for Single-Molecule Identification with Time-Correlated Single-Photon Counting. *J. Phys. Chem. A.* 105, 48–53. doi:10.1021/jp002358n

Fölling, J., Bossi, M., Bock, H., Medda, R., Wurm, C. A., Hein, B., et al. (2008). Fluorescence Nanoscopy by Ground-State Depletion and Single-Molecule Return. *Nat. Methods* 5, 943–945. doi:10.1038/nmeth.1257

Ghosh, A., Chizhik, A. I., Karedla, N., and Enderlein, J. (2021). Graphene- and Metal-Induced Energy Transfer for Single-Molecule Imaging and Live-Cell Nanoscopy with (Sub)-nanometer Axial Resolution. *Nat. Protoc.* 16, 3695–3715. doi:10.1038/s41596-021-00558-6

Hell, S. W. (2007). Far-field Optical Nanoscopy. *Science* 316, 1153–1158. doi:10.1126/science.1137395

Hell, S. W. (2009). Microscopy and its Focal Switch. *Nat. Methods* 6, 24–32. doi:10.1038/nmeth.1291

Hell, S. W., and Wichmann, J. (1994). Breaking the Diffraction Resolution Limit by Stimulated Emission: Stimulated-Emission-Depletion Fluorescence Microscopy. *Opt. Lett.* 19, 780–782. doi:10.1364/ol.19.000780

Hess, S. T., Girirajan, T. P., and Mason, M. D. (2006). Ultra-high Resolution Imaging by Fluorescence Photoactivation Localization Microscopy. *Biophys. J.* 91, 4258–4272. doi:10.1529/biophysj.106.091116

Huang, B., Bates, M., and Zhuang, X. (2009). Super-resolution Fluorescence Microscopy. *Annu. Rev. Biochem.* 78, 993–1016. doi:10.1146/annurev.biochem.77.061906.092014

Keller, J., Schönle, A., and Hell, S. W. (2007). Efficient Fluorescence Inhibition Patterns for Resolft Microscopy. *Opt. Express* 15, 3361–3371. doi:10.1364/oe.15.003361

Klar, T. A., Jakobs, S., Dyba, M., Egner, A., and Hell, S. W. (2000). Fluorescence Microscopy with Diffraction Resolution Barrier Broken by Stimulated Emission. *Proc. Natl. Acad. Sci. U S A.* 97, 8206–8210. doi:10.1073/pnas.97.15.8206

Klehs, K., Spahn, C., Endesfelder, U., Lee, S. F., Fürstenberg, A., and Heilemann, M. (2014). Increasing the Brightness of Cyanine Fluorophores for Single-Molecule and Superresolution Imaging. *ChemPhysChem* 15, 637–641. doi:10.1002/cphc.201300874

Klein, T., Proppert, S., and Sauer, M. (2014). Eight Years of Single-Molecule Localization Microscopy. *Histochem. Cel Biol* 141, 561–575. doi:10.1007/s00418-014-1184-3

Klymchenko, A. S. (2017). Solvatochromic and Fluorogenic Dyes as Environment-Sensitive Probes: Design and Biological Applications. *Acc. Chem. Res.* 50, 366–375. doi:10.1021/acs.accounts.6b00517

Köllner, M., and Wolfrum, J. (1992). How many Photons Are Necessary for Fluorescence-Lifetime Measurements? *Chem. Phys. Lett.* 200, 199–204. doi:10.1016/0009-2614(92)87068-Z

Lakowicz, J. R. (2006). "Time-Domain Lifetime Measurements," in *Principles of Fluorescence Spectroscopy*. Editor J. R. Lakowicz (Berlin, Germany: Springer US), 97–155. doi:10.1007/978-0-387-46312-4_4

Llères, D., Bailly, A. P., Perrin, A., Norman, D. G., Xirodimas, D. P., and Feil, R. (2017). Quantitative FLIM-FRET Microscopy to Monitor Nanoscale Chromatin Compaction *In Vivo* Reveals Structural Roles of Condensin Complexes. *Cell Rep* 18, 1791–1803. doi:10.1016/j.celrep.2017.01.043

Maus, M., Cotlet, M., Hofkens, J., Gensch, T., De Schryver, F. C., Schaffer, J., et al. (2001). An Experimental Comparison of the Maximum Likelihood Estimation and Nonlinear Least-Squares Fluorescence Lifetime Analysis of Single Molecules. *Anal. Chem.* 73, 2078–2086. doi:10.1021/ac000877g

Morimoto, K., Ardelean, A., Wu, M.-L., Ulku, A. C., Antolovic, I. M., Bruschini, C., et al. (2020). Megapixel Time-Gated Spad Image Sensor for 2d and 3d Imaging Applications. *Optica* 7, 346–354. doi:10.1364/optica.386574

Niehörster, T., Löschberger, A., Gregor, I., Krämer, B., Rahn, H. J., Patting, M., et al. (2016). Multi-target Spectrally Resolved Fluorescence Lifetime Imaging Microscopy. *Nat. Methods* 13, 257–262. doi:10.1038/nmeth.3740

O'Connor, D. (2012). *Time-correlated Single Photon Counting*. Cambridge, Massachusetts: Academic Press.

Oleksiievets, N., Thiele, J. C., Weber, A., Gregor, I., Nevskyi, O., Isbaner, S., et al. (2020). Wide-Field Fluorescence Lifetime Imaging of Single Molecules. *J. Phys. Chem. A.* 124, 3494–3500. doi:10.1021/acs.jpca.0c01513

Ram, S., Ward, E. S., and Ober, R. J. (2006). Beyond Rayleigh's Criterion: a Resolution Measure with Application to Single-Molecule Microscopy. *Proc. Natl. Acad. Sci. U S A.* 103, 4457–4462. doi:10.1073/pnas.0508047103

Rust, M. J., Bates, M., and Zhuang, X. (2006). Sub-diffraction-limit Imaging by Stochastic Optical Reconstruction Microscopy (Storm). *Nat. Methods* 3, 793–795. doi:10.1038/nmeth929

Santra, K., Zhan, J., Song, X., Smith, E. A., Vaswani, N., and Petrich, J. W. (2016). What Is the Best Method to Fit Time-Resolved Data? A Comparison of the Residual Minimization and the Maximum Likelihood Techniques as Applied to Experimental Time-Correlated, Single-Photon Counting Data. *J. Phys. Chem. B* 120, 2484–2490. doi:10.1021/acs.jpcb.6b00154

Schnitzbauer, J., Strauss, M. T., Schlichthaerle, T., Schueder, F., and Jungmann, R. (2017). Super-resolution Microscopy with Dna-Paint. *Nat. Protoc.* 12, 1198–1228. doi:10.1038/nprot.2017.024

Schwentker, M. A., Hofmann, M., Jakobs, S., Bewersdorf, J., Eggeling, C., Hell, S. W., et al. (2007). Wide-field Subdiffraction Resolft Microscopy Using Fluorescent Protein Photoswitching. *Microsc. Res. Tech.* 70, 269–280. doi:10.1002/jemt.20443

Sharonov, A., and Hochstrasser, R. M. (2006). Wide-field Subdiffraction Imaging by Accumulated Binding of Diffusing Probes. *Proc. Natl. Acad. Sci. U S A.* 103, 18911–18916. doi:10.1073/pnas.0609643104

Spencer, R. D., and Weber, G. (1969). Measurements of Subnanosecond Fluorescence Lifetimes with a Cross-Correlation Phase Fluorometer. *Ann. NY Acad. Sci.* 158, 361–376. doi:10.1111/j.1749-6632.1969.tb56231.x

Stein, S. C., and Thiart, J. (2016). TrackNTrace: A Simple and Extendable Open-Source Framework for Developing Single-Molecule Localization and Tracking Algorithms. *Sci. Rep.* 6, 37947. doi:10.1038/srep37947

Thiele, J. C., Helmerich, D. A., Oleksiievets, N., Tsukanov, R., Butkevich, E., Sauer, M., et al. (2020). Confocal Fluorescence-Lifetime Single-Molecule Localization Microscopy. *ACS Nano* 14, 14190–14200. doi:10.1021/acsnano.0c07322

[Dataset] Thiele, J. C. (2021a). *CRLB for Mono-Exponential Fitting*. doi:10.5281/zenodo.5093591

[Dataset] Thiele, J. C. (2021b). *FL-SMLM Pattern-Matching*. doi:10.5281/zenodo.5423457

Trinh, A. L., Esposito, A., Esposito, A., and Esposito, A. (2021). Biochemical Resolving Power of Fluorescence Lifetime Imaging: Untangling the Roles of the

Instrument Response Function and Photon-Statistics. *Biomed. Opt. Express* 12, 3775–3788. doi:10.1364/BOE.428070

Ulku, A. C., Bruschini, C., Antolovic, I. M., Charbon, E., Kuo, Y., Ankri, R., et al. (2018). A 512×512 SPAD Image Sensor with Integrated Gating for Widefield FLIM. *IEEE J. Sel Top. Quan. Electron* 25, 1–12. doi:10.1109/JSTQE.2018.2867439

Van de Linde, S., Löschberger, A., Klein, T., Heidbreder, M., Wolter, S., Heilemann, M., et al. (2011). Direct Stochastic Optical Reconstruction Microscopy with Standard Fluorescent Probes. *Nat. Protoc.* 6, 991–1009. doi:10.1038/nprot.2011.336

van Munster, E. B., and Gadella, T. W. (2005). Fluorescence Lifetime Imaging Microscopy (Flim). *Adv. Biochem. Eng. Biotechnol.* 95, 143–175. doi:10.1007/b102213

Venetta, B. D. (1959). Microscope Phase Fluorometer for Determining the Fluorescence Lifetimes of Fluorochromes. *Rev. Scientific Instr.* 30, 450–457. doi:10.1063/1.1716652

Conflict of Interest: The authors declare that the research was conducted in the absence of any commercial or financial relationships that could be construed as a potential conflict of interest.

frontiers
in Bioinformatics

OPINION
published: 15 December 2021
doi: 10.3389/fbinf.2021.801115

A Tribute to Professor Katharina Gaus

*Marek Cebecauer**

J. Heyrovsky Institute of Physical Chemistry of the Czech Academy of Sciences, Prague, Czechia

Keywords: tribute, single molecule localisation microscopy, Laurdan, cluster analysis, membrane biophysics

"With new single-molecule tools, and our formidable team, the only limit to what we can achieve is our imagination."

It is with great sadness that I report that Professor Dr. Katharina (Kat) Gaus, aged 48, passed away on March 3, 2021. She left with all her energy and enthusiasm, which she constantly devoted to us, her friends, and a broad spectrum of scientific questions. I would like to share with you some brief and personal memories of Katharina Gaus.

I met Kat in Sydney in 2011. She had invited me to stay for 1 month in her lab to learn about single-molecule localization microscopy (SMLM), a modern super-resolution microscopy technique that was already well-established in her laboratory a mere 6 years after appearing in the literature, demonstrating the beauty of biological imaging beyond the diffraction limit. Commercial super-resolution microscopes had just appeared on the market. Her young and productive team was already extensively using SMLM to characterise molecular processes associated with the activation of T lymphocytes (Williamson et al., 2011; Rossy et al., 2013). They were among the very few laboratories that had managed to employ super-resolution microscopy to address key biological questions in such a short time. In fact, this was a typical feature of Kat's research. She was one of those bold thinkers, who kept bringing new (imaging) technologies into a number of fields, such as immunology, cell biology and virology, to name just a few. To illustrate the impact of Kat's drive for new technologies, I will mention the two main directions of her research: plasma membrane biophysics and the organisation of signalling molecules on T cells.

Laurdan, a fluorescent membrane probe that is able to sense changes in its environment, was only sparsely used in the community of biophysicists studying synthetic lipid bilayers when Kat harnessed its properties to measure the physical heterogeneity of cellular membranes (Gaus et al., 2003; Gaus et al., 2006). Although the results have been later superseded, Kat and her colleagues continued to improve the Laurdan imaging technology, and the current images certainly are impressive (Ma et al., 2018). Similarly, she pioneered the use of statistical analysis designed for geoinformation studies to characterise surface topography of key players involved in the activation of immune cells (Williamson et al., 2011; Rossy et al., 2013). Cluster analysis used in these early SMLM studies seems a little outdated now and is limited to certain shapes and density levels, but Kat's team together with her alumni students kept developing more appropriate and advanced cluster analysis methods to achieve more precise information about processes in immune cells (Pageon et al., 2016; Griffié et al., 2017; Hinde et al., 2017; Williamson et al., 2020). Such a continuous effort to improve available technologies underlines Kat's dedication to advancing the field while delivering excellent science.

Looking back at her publication history and her current team, it is apparent how Kat was able to attract great talent to her laboratory. She built a lab with a mix of biologists, chemists, and physicists at just the right ratio to attack, thanks to this scientific and cultural mixture, important unresolved questions that required unconventional approach(es). This led to several great discoveries and technological improvements, which will serve the community for many years to follow. To highlight contributions to the field of SMLM, it is especially noteworthy how Kat's team adapted this technique for the quantitative analysis of receptor stoichiometry (Baker et al., 2019), the measurements of intermolecular distances (Coelho et al., 2020), the three-dimensional distribution of molecules (Coelho et al., 2021) and diffusional analysis (Hilzenrat et al., 2020). In collaboration with her

Edited by:
Thomas Pengo,
University of Minnesota Twin Cities,
United States

Reviewed by:
Ricardo Henriques,
University College London,
United Kingdom

****Correspondence:***
Marek Cebecauer
marek.cebecauer@jh-inst.cas.cz

Specialty section:
This article was submitted to
Computational BioImaging,
a section of the journal
Frontiers in Bioinformatics

Received: *24 October 2021*
Accepted: *09 November 2021*
Published: *15 December 2021*

Citation:
Cebecauer M (2021) A Tribute to
Professor Katharina Gaus.
Front. Bioinform. 1:801115.
doi: 10.3389/fbinf.2021.801115

partner's group (Prof. Justin Gooding), they developed a variety of nanostructures for functional and super-resolution imaging and contributed to the application of "click chemistry" in SMLM (Laxman et al., 2021). And I have probably forgotten to refer to several other improvements to this field. However, this long list emphasizes the special position of Kat Gaus in the hearts of microscopists, especially those studying surface molecules on lymphocytes like me. I would like to finish by mentioning that I have never seen Kat frowning. She kept smiling constantly, at least in my presence. I hope that many of you have similar memories. She will be missed, certainly by her collaborators, and the microscopy and SMLM community.

AUTHOR CONTRIBUTIONS

The author confirms being the sole contributor of this work and has approved it for publication.

REFERENCES

Baker, M. A. B., Nieves, D. J., Hilzenrat, G., Berengut, J. F., Gaus, K., and Lee, L. K. (2019). Stoichiometric Quantification of Spatially Dense Assemblies with qPAINT. *Nanoscale* 11, 12460–12464. doi:10.1039/c9nr00472f

Coelho, S,, Baek, J,, Walsh, J,, Gooding, J. J., and Gaus, K. (2021). 3D Active Stabilization for Single-Molecule Imaging. *Nat. Protoc.* 16, 497–515. doi:10.1038/s41596-020-00426-9

Coelho, S., Baek, J., Graus, M. S., Halstead, J. M., Nicovich, P. R., Feher, K., et al. (2020). Ultraprecise Single-Molecule Localization Microscopy Enables *In Situ* Distance Measurements in Intact Cells. *Sci. Adv.* 6, eaay8271. doi:10.1126/sciadv.aay8271

Gaus, K., Gratton, E., Kable, E. P., Jones, A. S., Gelissen, I., Kritharides, L., et al. (2003). Visualizing Lipid Structure and Raft Domains in Living Cells with Two-Photon Microscopy. *Proc. Natl. Acad. Sci. U S A.* 100, 15554–15559. doi:10.1073/pnas.2534386100

Gaus, K., Le Lay, S., Balasubramanian, N., and Schwartz, M. A. (2006). Integrin-mediated Adhesion Regulates Membrane Order. *J. Cel Biol* 174, 725–734. doi:10.1083/jcb.200603034

Griffié, J., Shlomovich, L., Williamson, D. J., Shannon, M., Aaron, J., Khuon, S., et al. (2017). 3D Bayesian Cluster Analysis of Super-resolution Data Reveals LAT Recruitment to the T Cell Synapse. *Sci. Rep.* 7, 4077. doi:10.1038/s41598-017-04450-w

Hilzenrat, G., Pandžić, E., Yang, Z., Nieves, D. J., Goyette, J., Rossy, J., et al. (2020). Conformational States Control Lck Switching between Free and Confined Diffusion Modes in T Cells. *Biophys. J.* 118, 1489–1501. doi:10.1016/j.bpj.2020.01.041

Hinde, E., Thammasiraphop, K., Duong, H. T., Yeow, J., Karagoz, B., Boyer, C., et al. (2017). Pair Correlation Microscopy Reveals the Role of Nanoparticle Shape in Intracellular Transport and Site of Drug Release. *Nat. Nanotechnol* 12, 81–89. doi:10.1038/nnano.2016.160

Laxman, P., Ansari, S., Gaus, K., and Goyette, J. (2021). The Benefits of Unnatural Amino Acid Incorporation as Protein Labels for Single Molecule Localization Microscopy. *Front. Chem.* 9, 641355. doi:10.3389/fchem.2021.641355

Ma, Y., Benda, A., Kwiatek, J., Owen, D. M., and Gaus, K. (2018). Time-Resolved Laurdan Fluorescence Reveals Insights into Membrane Viscosity and Hydration Levels. *Biophys. J.* 115, 1498–1508. doi:10.1016/j.bpj.2018.08.041

Pageon, S. V., Nicovich, P. R., Mollazade, M., Tabarin, T., and Gaus, K. (2016). Clus-DoC: a Combined Cluster Detection and Colocalization Analysis for Single-Molecule Localization Microscopy Data. *Mol. Biol. Cel* 27, 3627–3636. doi:10.1091/mbc.E16-07-0478

Rossy, J., Owen, D. M., Williamson, D. J., Yang, Z., and Gaus, K. (2013). Conformational States of the Kinase Lck Regulate Clustering in Early T Cell Signaling. *Nat. Immunol.* 14, 82–89. doi:10.1038/ni.2488

Williamson, D. J., Burn, G. L., Simoncelli, S., Griffié, J., Peters, R., Davis, D. M., et al. (2020). Machine Learning for Cluster Analysis of Localization Microscopy Data. *Nat. Commun.* 11, 1493. doi:10.1038/s41467-020-15293-x

Williamson, D. J., Owen, D. M., Rossy, J., Magenau, A., Wehrmann, M., Gooding, J. J., et al. (2011). Pre-existing Clusters of the Adaptor Lat Do Not Participate in Early T Cell Signaling Events. *Nat. Immunol.* 12, 655–662. doi:10.1038/ni.2049

Conflict of Interest: The author declares that the research was conducted in the absence of any commercial or financial relationships that could be construed as a potential conflict of interest.

frontiers in Bioinformatics

TECHNOLOGY AND CODE
published: 01 February 2022
doi: 10.3389/fbinf.2021.817254

Raw Data to Results: A Hands-On Introduction and Overview of Computational Analysis for Single-Molecule Localization Microscopy

*Koen J. A. Martens[1,2], Bartosz Turkowyd[1,2,3] and Ulrike Endesfelder[1,2,3]**

[1]Department of Physics, Carnegie Mellon University, Pittsburgh, PA, United States, [2]Institute for Microbiology and Biotechnology, Rheinische-Friedrich-Wilhelms-Universität Bonn, Bonn, Germany, [3]Department of Systems and Synthetic Microbiology, Max Planck Institute for Terrestrial Microbiology, LOEWE Center for Synthetic Microbiology (SYNMIKRO), Marburg, Germany

Single-molecule localization microscopy (SMLM) is an advanced microscopy method that uses the blinking of fluorescent molecules to determine the position of these molecules with a resolution below the diffraction limit (~5–40 nm). While SMLM imaging itself is becoming more popular, the computational analysis surrounding the technique is still a specialized area and often remains a "black box" for experimental researchers. Here, we provide an introduction to the required computational analysis of SMLM imaging, post-processing and typical data analysis. Importantly, user-friendly, ready-to-use and well-documented code in Python and MATLAB with exemplary data is provided as an interactive experience for the reader, as well as a starting point for further analysis. Our code is supplemented by descriptions of the computational problems and their implementation. We discuss the state of the art in computational methods and software suites used in SMLM imaging and data analysis. Finally, we give an outlook into further computational challenges in the field.

Keywords: SMLM Python and MATLAB code, temporal median filtering, SMLM localization and localization merging, drift and chromatic aberration correction, SMLM image formation, single-particle tracking, SMLM clustering, SMLM localization precision and structural image resolution

Edited by:
Thomas Pengo,
University of Minnesota Twin Cities,
United States

Reviewed by:
Jonas Ries,
European Molecular Biology
Laboratory, Germany
Christian Franke,
Friedrich Schiller University Jena,
Germany

****Correspondence:***
Ulrike Endesfelder
endesfelder@uni-bonn.de

Specialty section:
This article was submitted to
Computational BioImaging,
a section of the journal
Frontiers in Bioinformatics

Received: *17 November 2021*
Accepted: *28 December 2021*
Published: *01 February 2022*

Citation:
Martens KJ, Turkowyd B and Endesfelder U (2022) Raw Data to Results: A Hands-On Introduction and Overview of Computational Analysis for Single-Molecule Localization Microscopy.
Front. Bioinform. 1:817254.
doi: 10.3389/fbinf.2021.817254

INTRODUCTION

Single-molecule localization microscopy (SMLM) is a collective term for microscopy techniques that generate localization data of individual fluorescent molecule emission events, and can achieve ~5–40 nm resolution at ~10–100 Hz (Betzig et al., 2006; Rust et al., 2006; Sage et al., 2019). Localization-based microscopy can be performed with relatively standard, albeit sensitive, wide-field fluorescence microscopes. The key requirement is that the fluorescent molecules used are able to switch between *on* and *off* states, ensuring that all molecules are read out individually (Endesfelder et al., 2011). dSTORM (direct stochastic optical reconstruction microscopy) achieves this *on/off*-switching *via* chemical equilibria of organic fluorophores, often assisted *via* (near-)UV light and/or reactive chemicals (Rust et al., 2006; Heilemann et al., 2008). For *in vivo* SMLM imaging, PALM (photo-activated localization microscopy) is a conceptually similar technique as dSTORM, but relies on photo-induced chemical transitions of fluorescent proteins (Betzig et al., 2006; Manley et al., 2008). Alternatively, the *on/off*-switching can be accomplished by repetitive binding/unbinding of the fluorophore as done by PAINT microscopy (points accumulation for imaging in nanoscale topography) (Sharonov and Hochstrasser, 2006). As long as the fluorophore is unbound, it diffuses too rapidly to produce a well-formed point-spread function (PSF). This binding/unbinding is often, but not exclusively, induced via DNA complementarity, i.e. DNA-PAINT (Schnitzbauer et al., 2017).

A further increase in spatiotemporal resolution can be achieved by various improvements in sample, fluorophores, instrument, or computational design. For instance, increasing labeling density and specificity, increasing emitter fluorescence, or decreasing the distance between fluorophore to structure of interest will result in a better observed resolution (Grimm et al., 2016; Virant et al., 2018; Vojnovic and Endesfelder, 2020; Geertsema et al., 2021). Accurate axial drift correction and experimental PSF descriptions also have an influence (Li et al., 2018; Vojnovic and Endesfelder, 2020). Instrumentally, the *on/off*-switching of organic fluorophores or photo-activatable fluorescent proteins can be combined with structured illumination profiles, reaching up to 2–3 nm spatial resolution (Balzarotti et al., 2017; Gu et al., 2019; Cnossen et al., 2020; Jouchet et al., 2021).

All SMLM methods fundamentally result in an identical output: a movie of individual fluorophore emissions from which a coordinate list, containing at least time, x, and y positions of individual emitters, often complemented by information on localization uncertainty, emitter intensity, and axial (z) position, can be extracted. This output can principally be used to explore two main avenues: super-resolution imaging or single-particle tracking (spt).

In super-resolution imaging, the sample of interest is usually chemically fixed. Resolving all fluorophores' positions, the fluorescently-tagged structure of interest can be visualized with a resolution about 10–20-fold lower than the classical diffraction limit [~250 nm (Abbe, 1873)]. With the help of super-resolution imaging several unknown molecular arrangements in structural biology could be revealed and quantified and many review articles summarize these findings and achievements in detail (Huang et al., 2009; Patterson et al., 2010; Turkowyd et al., 2016; Baddeley and Bewersdorf, 2018; Sigal et al., 2018).

Alternatively, in spt, a natural biological sample (i.e. single living cells) with fluorophore-tagged proteins of interest are imaged (Manley et al., 2008). The behaviour of the individual intracellular biomolecules can be quantified, providing detailed information on molecular dynamics and interactions (Shen et al., 2017; Kapanidis et al., 2018; Elf and Barkefors, 2019). Spt can also be applied in *ex vivo* settings, such as membrane proteins in synthetic membranes or material science (Schütz et al., 1997; Martens et al., 2020).

Clearly, applications of SMLM imaging are highly diverse. Nevertheless, all of them inherently make use of similar computational analysis tools - from localization software, drift correction or color channel overlays to clustering or tracking routines. Over the past decades, a multitude of analysis methods and tools for localization data have evolved. Understanding the obligate computational details of SMLM imaging and knowing which tools to apply (when), and how to expand or modify them for a specific use case can be overwhelming, especially for researchers without a background in computer science. In this manuscript, we provide an overview of the most common computational analysis procedures in single-molecule localization microscopy and supply code written in Python and MATLAB. The structure of this work focuses on understanding of the problems and their solutions, rather than providing the most efficient or theoretically best solution. Wherever possible, information about less intuitive, but state-of-the-art alternatives is provided, as well as references to relevant software suites.

MATERIALS AND METHODS

Samples

The *E. coli* RNA polymerase (RNAP) data for fiducial drift correction, image generation, clustering and Nearest Neighbor based Analysis (NeNA, (Endesfelder et al., 2014)) were taken from our previous work (Virant et al., 2017). Briefly, RNAPs were tagged with mEos3.2-A69T at their β'-subunit. Red, photoconverted mEos3.2-A69T fluorescence was read out using primed photoconversion. Movies were recorded with 16.67 Hz image acquisition until no new spots appeared. Localizations were obtained using RapidSTORM (Wolter et al., 2012).

The vimentin-BC2-tag data for the Fourier Ring Correlation (FRC) analysis were taken from our previous work (Virant et al., 2018). Briefly, vimentin, transiently expressed from a plasmid in HeLa cells, was tagged by the BC2 peptide tag sequence. After chemical fixation, cells were stained with the bivalent anti-BC2 nanobody labeled by AlexaFluor 647. The region of interest was imaged for 20,000 frames using the dSTORM imaging buffer (van de Linde et al., 2011) and localizations were obtained using RapidSTORM.

DNA-PAINT nanoruler SMLM data was recorded for the temporal median filter, localization, chromatic aberration and cross correlation drift correction modules. The GATTA-PAINT 80RG nanoruler was obtained from Gattaquant, Germany. 10.000 frames were recorded with 100 ms interval under 561 nm (1.5 kW/cm^2) and 640 nm (1 kW/cm^2) excitation, using a ZET405/488/561/640m dichroic, ZT405/488/561/640rpc rejection filter, and respectively ET610/75 or ET655LP bandpass filter.

For the single-particle tracking analysis, we prepared 20 nm diameter red and 200 nm diameter dark-red fluorescent beads (FluoSphere Thermo Fisher; 580 nm excitation/605 nm emission and 660 nm excitation/680 nm emission, respectively) in respectively a 1:1,000 and 1:10,000 dilution from the original stock in milli-Q water. ~10 µL solution was placed on a coverslip and covered with another coverslip. Coverslips were gently pressed together to remove excess liquid and air bubbles and placed on the microscope. 10,000 frames were recorded with 15 ms interval, and 1 ms stroboscopic 488 and 561 nm laser illumination set at 3 and 0.3 kW/cm^2, respectively. No bandpass filter was used. Localizations were obtained using ThunderStorm (Ovesny et al., 2014).

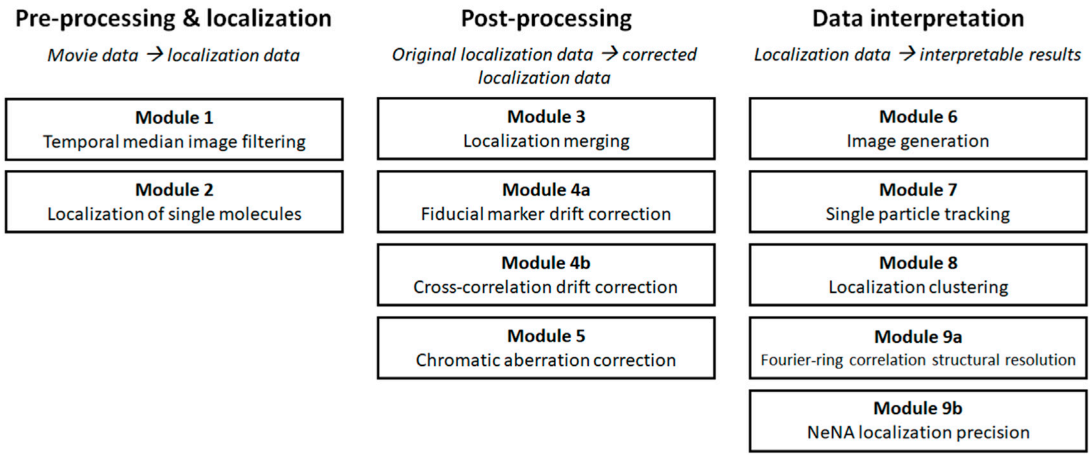

SCHEME 1 | Overview of the modules.

All movie and localization datasets used in the computational modules can be found on https://github.com/Endesfelder-Lab/SMLMComputational.

SMLM Imaging

Imaging was performed on a custom build setup based on an automated Nikon Ti Eclipse microscope equipped with appropriate dichroic and filters (ET dapi/Fitc/cy3 or ZET405/488/561/640m dichroic, ZT405/488/561rpc or ZT405/488/561/640rpc rejection filter, ET610/75 or ET655LP bandpass, all AHF Analysentechnik, Germany), and a CFI Apo TIRF ×100 oil objective (NA 1.49, Nikon). The 488 nm, 561 nm, and 637 nm lasers (Coherent) was modulated via an acousto-optical tunable filter (AOTF) (Gooch and Housego, United States). Fluorescence was detected by an emCCD (iXON Ultra 888; Andor, United Kingdom). The *z*-focus was controlled by a commercial perfect focus system (Nikon, Germany). The sample was placed on a heating stage and kept at the constant temperature 25°C. Acquisitions were controlled by µManager (Edelstein et al., 2010).

Code

All code, sub-divided into modules (**Scheme 1**) is provided both as Python code and as MATLAB code (https://drive.google.com/drive/u/0/folders/1lOKvC_L2fb78–uwz3on4lBzDGVum8Mc and https://github.com/Endesfelder-Lab/SMLMComputational) and is further documented by Pseudo-code (Supplementary information) and descriptions in the main text. The interactive environment of the google colab implementation (https://colab.research.google.com/) allows for direct, user-based testing and adaptation on our example data.

RESULTS

SMLM data is typically analyzed in several, mostly consecutive steps. The different analysis procedures in this manuscript follow this workflow are thus subdivided in three major groups: "pre-processing and localization", "post-processing", and "data interpretation" modules (**Scheme 1**). The modules of the first group "pre-processing and localization" all work on SMLM movie data and concern analysis steps which are used to properly translate the recorded movie material into localization data. In the second group, called "post-processing", those raw localization lists are typically further refined in several routines that raise the quality of the data or combine different parts of data into final SMLM localization lists. These data sets then are visualized, characterized and interpreted by analysis routines which are grouped in "data interpretation", and provide additional data (images, parameters, bionumbers and measurements etc.,) as output.

The order of our modules follows standard analysis practices, but some modules can be skipped or performed in a different order, and two modules (4 and 9) are subdivided into variant a and b as they present alternatives for similar tasks (i.e. drift correction and determination of structural resolution or localization precision). For every module, well-documented Pseudo-code, Python code, and MATLAB code is provided (https://drive.google.com/drive/u/0/folders/1lOKvC_L2fb78–uwz3on4lBzDGVum8Mc and https://github.com/Endesfelder-Lab/SMLMComputational, **Supplementary Pseudocode S1–S9**), which is accompanied by explanatory text and illustrations, as well as software alternatives, in the following text. We stress that this code is designed as "teaching material" rather than best-practice software, especially relating to speed optimization. An overview of existing SMLM analysis software that implement at least one of this manuscript's modules is presented in **Supplementary Table S1**.

We encourage users of the codebase to not only run the analysis with the provided raw data, but also to apply it on their own data, and change the code accordingly and appropriately. To further assist users new to programming language, we have included a Supplemental Code environment (https://colab.research.google.com/drive/1Ht-WL-W3tpFfavDMZjDofLOR9HKP-nVV), where we show how to perform basic data handling, and include region-of-interest selection, pixel size conversion and intensity level correction. These little helper code snippets can be easily

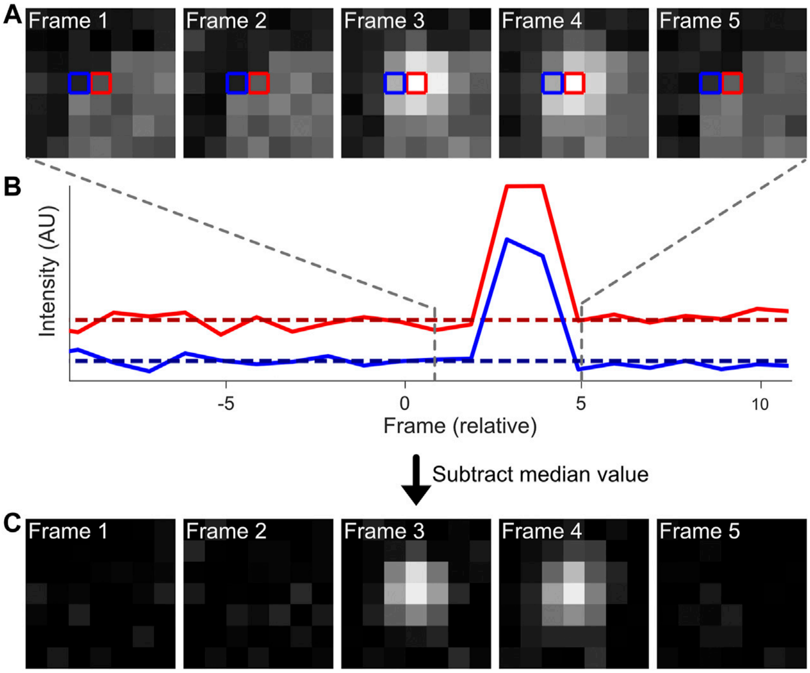

FIGURE 1 | Computational workflow of a temporal median filter. Fluorescence emissions from individual, blinking fluorophores are often present on top of an inhomogeneous background **(A)**. The intensities of individual pixels can be analysed over a period of time [**(B)**, solid lines]. The median intensity value per pixel (dotted lines) can be extracted and subtracted from the original intensity data to adequately remove the background from the dataset **(C)**.

combined with the modules to filter, select and modify raw data as input for the chosen module.

Within our modules we focus on intuitive solutions to common SMLM analysis routines, and references to e.g. more complex or less intuitive state-of-the-art alternatives are provided. Specific analysis routines for highly specialized tasks - mostly for the third module group "data interpretation"- are out of scope of this work. These analysis procedures are not covered within our modules but the interested reader is pointed towards them in the discussion.

Module 1: Temporal Median Image Filtering

Raw single-molecule microscopy movie data often contains non-structured background noise with different photophysical characteristics as the fluorophores of interest, caused by for example residual out-of-focus fluorophores e.g. in the immersion oil or sample buffer, or by autofluorescence within the biological sample itself (Turkowyd et al., 2019, 2020). Additionally, out-of-focus fluorophores under HiLo or TIRF illumination will display different blinking characteristics compared to in-focus fluorophores, and can therefore also be filtered out. It can have a detrimental effect on localization efficiency (i.e. minimizing false positive and false negative localizations) and accuracy when identifying single-molecule emissions from the imaging data. The impact of background noise can be lowered by globally subtracting average background levels from the raw movie data. This, nevertheless, does not adequately capture temporal changes. Temporal median image filtering provides a solution to this problem (**Figure 1**).

Briefly, because *on/off*-switching of fluorophores in SMLM is equilibrated towards the *off*-state, the median intensity of a pixel is a good approximation of the background noise. Thus, the operating principle of temporal median image filtering is that for each pixel at time t, the median value of the pixel in the time interval t−i/2 to t + i/2 is computed and subtracted at time t (**Figure 1B**) (Hoogendoorn et al., 2014). The value i is user-defined, and should be substantially higher than the longest *on*-period of single emitters (at least twice; normally a value of ~50 frames can be used), and is capped at high ends by unreasonable analysis times or temporal fluctuations in background intensity. A fast version of this algorithm is implemented as an ImageJ plugin (Jabermoradi et al., 2021). Temporal median image filtering should be avoided if the equilibrium of blinking is favored towards the *on*-state (i.e. > 50% of the time fluorescently active), since this would result in active removal of fluorescent signal rather than background. Additionally, this pre-processing step does not accurately reduce temporal heterogeneous background fluctuations (i.e. non-specific binding events).

Our code corresponding to module 1 can be found here: (https://colab.research.google.com/drive/1XKMP5BQWhUkQuKAjTkBgkaHy9bGjR23H or https://github.com/Endesfelder-Lab/SMLMComputational, also **Supplementary Pseudocode S1**). The required input is a raw SMLM movie, and the code module outputs a temporally-median-filtered movie with identical dimensions. Looping over every pixel in every frame, the pixel intensity values from i/2 before the current frame to i/2 after the current frame are extracted. Alternatively, if the frame is

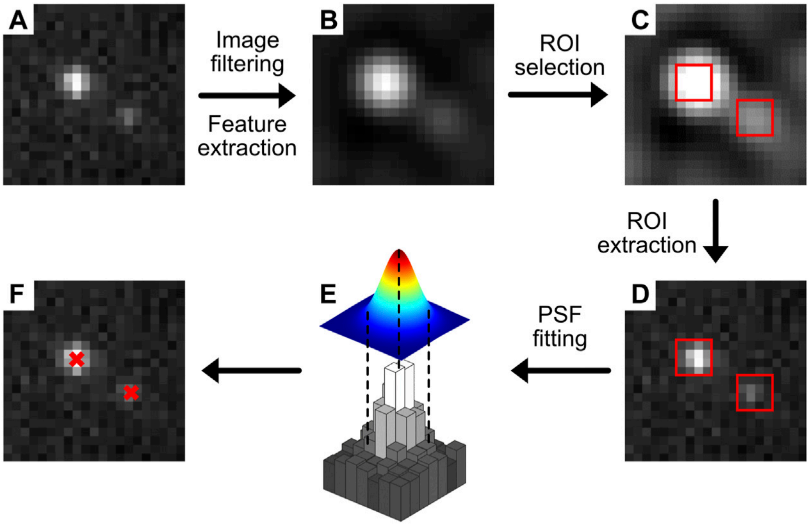

FIGURE 2 | Typical localization methodology. A raw image **(A)** is filtered to enhance features that likely contain emitters **(B)**. From this filtered image, ROIs (red squares) are selected **(C)** and used to extract the PSF data from the original image **(D)**. This region is then fitted by a PSF model (e.g. commonly a 2-dimensional Gaussian) **(E)**, and the localizations with sub-pixel precision are displayed or used for further analysis **(F)**.

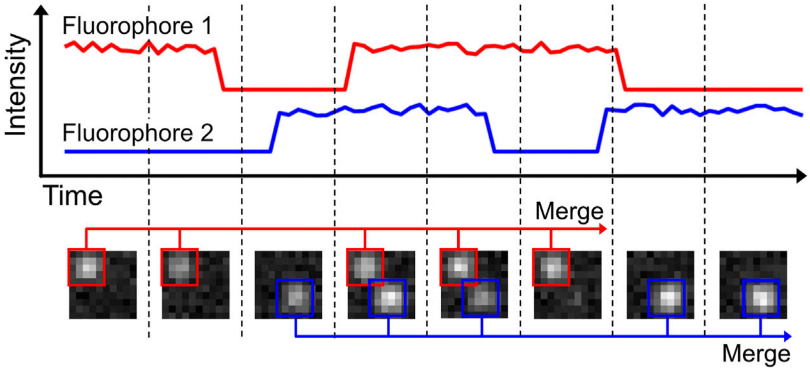

FIGURE 3 | Localization merging. In the shown example, two fluorophores are present. Both fluorophores are emitting for multiple frames, but are also blinking during this period. The localization merging routine identifies emitters that emit over multiple frames, accounting for possible blinking periods. Merging the individual localizations into one increases accuracy of fluorophore quantification and emitter localization precision.

at the beginning of the movie, the pixel values are extracted from frame 0 onwards, and expanded further than i/2 after the current frame (and similar at the end of the movie). The median value is determined from this range, subtracted from the current pixel intensity, and stored in a new data array. These steps are then repeated for all pixels and all frames.

This concept can be taken one step further by first determining a localization and then calculating the local background from the spatiotemporal voxels in which no fluorescence of this emitter is present, followed by repeating the localization step. This has been realized by the SMALL-LABS software package (Isaacoff et al., 2019; Martens et al., 2021). Alternatively, temporal filtering can be based on minimum values to have a robust estimator at high fluorophore densities (Ma et al., 2021), or heterogeneous background can be assessed and restored via a neural network (Krull et al., 2019; Möckl et al., 2020). sCMOS-induced noise should be addressed separately (Diekmann et al., 2021; Zhang et al., 2021).

Module 2: Localization

Determining the positions of individual fluorescent emitters to translate the SMLM movie data into SMLM localization data is the primary computational effort in SMLM imaging. Here, localization algorithms determine the sub-pixel accurate position of each point-spread function (PSF) of single fluorophores in the raw movie data (**Figure 2**). Principally, these localization routines consist of two steps, although methods are developed that merge these steps: 1) region-of-interest (ROI) selection, in which the presence or absence of a PSF is determined; and 2) sub-pixel localization of the emitter in the ROI. These steps are the basis of many user-friendly, open access software packages, such as ThunderSTORM, rapidSTORM, SMAP, Picasso, QuickPALM and GDSC SMLM (Henriques et al., 2010; Wolter et al., 2012; Ovesny et al., 2014; Schnitzbauer et al., 2017; Ries, 2020; Herbert, 2021).

Sub-pixel localization fitting procedures can benefit from fitting raw SMLM movie input, rather than a temporal-median-corrected movie (Module 1), if they e.g. take camera noise models into account that are effectively removed by temporal median image filtering. Thus, step 1 can be performed on the output of Module 1, while step 2 should be performed on ROIs extracted from the input of Module 1 (i.e. raw SMLM movie). However, in certain cases, such as when encountering hot pixels or patterned background fluorescence, the increased localization precision from running localization on raw movie data does not offset the removal of background.

The code belonging to this module can be found here: (https://colab.research.google.com/drive/1Jir3HxTZ-au8L56ZrNHGxfBD0XlDkOMl or https://github.com/Endesfelder-Lab/SMLMComputational, also **Supplementary Pseudocode S2**). A raw SMLM movie, or alternatively the output from Module 1 should be supplied as input, and a localization list with (frame*, x, y,* intensity) columns will be stored as output. Briefly, every frame in the temporal-median-corrected movie undergoes a difference-of-Gaussian (DoG) filtering to highlight PSFs. Local maximum positions are then found in the corresponding frame in the raw movie, which correspond to the approximate positions of PSFs. Looping over these local maxima, a small region of interest (7 × 7 pixels) is extracted, and the pSMLM code from (Martens et al., 2018) is used to extract the sub-pixel PSF position. This sub-pixel position is then added to the approximate PSF position, and added to the localization list.

Commonly, the ROI selection is performed *via* image filtering or feature enhancement. DoG filtering, like applied in this module's code, is a common method used for edge detection (Marr et al., 1980). Alternatives to the DoG filter are the Laplacian of Gaussians [LoG; (Tinevez et al., 2017)] or a β-spline wavelet filter (Izeddin et al., 2012a).

Sub-pixel localization has seen many improvements in the past decades and several localization software challenges benchmarked different algorithms for different data scenarios (Sage et al., 2019). Because a 2-dimensional Gaussian function is a good approximation for the PSF of in-focus fluorophores, iterative algorithms based on fitting a Gaussian function are often used (Mortensen et al., 2010; Stallinga and Rieger, 2010), providing good accuracy especially when using a maximum likelihood estimator (MLE) fitting procedure (Smith et al., 2010). Possible fast analysis methods are centroid-based (Cheezum et al., 2001), phasor-based (Martens et al., 2018, 2021), which is used here because of the low computation time and good accuracy, or radial-symmetry-based (Parthasarathy, 2012). Another type of algorithms that more accurately simulate and localize PSFs also exists, based on theoretical or measured optical wavefronts (Liu et al., 2013; Shechtman et al., 2014; Aristov et al., 2018; Xu et al., 2020) or on measured PSFs (Babcock and Zhuang, 2017; Li et al., 2018). Recently, deep-learning-based methods combine the ROI selection and sub-pixel localization with excellent results (Nehme et al., 2020; Speiser et al., 2021).

The sub-pixel localization step can additionally be used to obtain information about the 3-dimensional position of individual emitters. This requires additional optical elements in the microscope's emission path such as elliptical lenses (Huang et al., 2008), deformable mirrors (Izeddin et al., 2012b; Martens et al., 2021), or custom phase masks (Shechtman et al., 2014), or is based on simultaneously imaging slices at different depths (Juette et al., 2008; Louis et al., 2020). In all cases, information about the *z*-position is encoded in the shape of the PSF, and thus more complex localization analysis needs to be performed (Aristov et al., 2018; Li et al., 2018).

Importantly, it is assumed that every ROI only contains a single fluorophore for most of these implementations. This is not always the case, especially in high-density samples. While the common approach in the SMLM community is to prevent these high densities experimentally, there are computational approaches designed specifically for high density and multi-emitter fitting (Holden et al., 2011; Zhu et al., 2012; Marsh et al., 2018; Nehme et al., 2020; Speiser et al., 2021). Additionally, the localization result should be checked for inhomogeneous distribution artefacts (e.g. bias towards the center of a camera pixel), which can be especially important when the experiment requires quantification of repeating patterns.

Module 3: Localization Merging

The movie acquisition speed (i.e. time per imaging frame) during SMLM imaging has to be optimized based on the method (i.e. STORM, PALM, etc.,) and dependent on technical and biological sample factors, e.g. whether a static or dynamic sample is imaged (i.e. super-resolution imaging or single-particle tracking). During imaging of static samples, fluorophores switched to their *on*-state normally remain in this state for ~10–50 ms (STORM) or ~100–500 ms (PAINT), depending on the experimental set-up. Additionally, the fluorophores can go in various temporary dark-states (blinking), meaning that no emission can be detected for several frames (Dickson et al., 1997; van de Linde and Sauer, 2014; Berardozzi et al., 2016). Because SMLM acquisition speed is static, it is likely that a single fluorophore can be in its *on*-state for more than one imaging frame. This means that the same fluorescent event is recorded multiple times over consecutive frames, but could be "skipping" one or multiple frames due to fluorophore blinking.

It can be advantageous to merge these multiple recordings of a single emission down to a single event (**Figure 3**). First, this will provide a more quantitative overview of the sample, which can help with e.g. counting of fluorophores. Secondly, merging multiple events allows for *de facto* higher photon levels (N) per localization, which scales with localization precision by $1/\sqrt{N}$ (Rieger and Stallinga, 2014). Merging is readily available in the post-processing of many SMLM software packages, such as ThunderSTORM, SMAP and Rapidstorm (Wolter et al., 2012; Ovesny et al., 2014; Ries, 2020). In Rapidstorm, the merging is implemented as a Kalman-filter, which improves the merging quality. Care should be taken when performing localization merging on high-density datasets, as this could result in linking different fluorophores to each other, rather than linking multiple emissions from a single fluorophore.

Our code belonging to this module can be found here: (https://colab.research.google.com/drive/16ooyjTonAP3xvsQKCv_uxWcUp1hB8msC or https://github.com/Endesfelder-Lab/SMLMComputational, also **Supplementary Pseudocode S3**). It requires a localization list (at least containing frame, *x*, *y* position) as input, and stores a corrected localization list as output. The code itself loops over all localizations on a given frame. For every localization, it is checked whether there are localizations in the next 1 or 2 frames that are closer than a user-defined maximum distance. This pair of localizations is then given an identical "trajectory-id". After looping over all localizations, the localizations that have the same trajectory-id and do not belong to special cases [e.g., on purpose placed fiducial markers for drift correction (see Module 4a)] are merged. This is performed by taking their collective, intensity-weighted mean position, minimum frame value, and summed intensity. The original localizations are then replaced by this merged localization.

Localization merging can be reasonably expanded to work on the level of the movie data. This would involve re-performing the localization module on the summed raw data of merging events.

Module 4: Drift Correction

SMLM data is recorded in movies (and not in single image snapshots), and thus the data is acquired over substantial time periods, typically in the order of tens of minutes. The obtained localization precision in the final reconstructed image, that summarizes all localizations from all imaging frames, is in the order of nanometers. But high image resolutions can only be achieved and the results are only interpretable if some technical criteria are fulfilled, e.g. sufficient fluorophore labeling density and detection efficiency as well as an absence of temporal drift during the movie acquisition (Vojnovic and Endesfelder, 2020). For the latter, it thus is important that the sample itself moves only very minimally with respect to the detector throughout the acquisition. However, this is challenging, if not impossible, to achieve via merely stabilizing hardware (even if the setup has good heat dissipation and a vibration-damping module). Therefore, additional drift correction procedures are used, either on-line (directly during acquisition) or off-line (post-processing and correcting the localization data after acquisition).

A distinction should be made between axial (i.e. in the *z*-direction) and lateral (i.e. in the *xy*-direction) drift for two reasons. First, axial drift is much more detrimental to the acquisition, because the emitters are only in focus in an axial slice of about 600 nm (Franke et al., 2017). Second, many microscopes have axial stages equipped with piezo-stages that provide accurate and repeatable precision of ~1–5 nm, while the lateral stage is usually not equipped with a piezo-stage, which limits on-line correction of lateral drift to a micrometer-accuracy. For these two reasons, axial drift correction is often performed on-line *via* a hardware add-on based on the internal reflection of an (infra) red laser (Liron et al., 2006), while lateral drift correction is performed off-line using one of the numerous variations of the methodology that we outline below. Briefly, fiducial marker drift correction (Module 4a) can be used for any sample, but requires introduction of steady-fluorescent markers in the sample, while cross-correlation drift correction (Module 4b) calculates and corrects for drift directly from the samples' features, but requires static data and thus cannot be used for highly dynamic samples or particle tracking studies.

Module 4a: Drift Correction by Fiducial Markers

A conceptually simple way to measure and correct sample drift is to introduce stable fluorescent fiducial markers (Balinovic et al., 2019). These markers are bright, non-blinking emitters [often nanoparticles that have many individual fluorophores bound to a support structure such as polystyrene beads, possibly excited away from their absorption maximum (Balinovic et al., 2019)] that emit stable and bright fluorescence throughout the acquisition time. By incorporating and tracing the signal of multiple fiducial markers in every field of view (FoV) that is recorded, the drift of the sample can be assessed (**Figure 4**). The displacement of this drift trace from its original position at time point zero can then be subtracted from all localization data, allowing for effective drift suppression that in practice achieves a precision of about 3–5 nm (Balinovic et al., 2019). In case the fluorescence of the fiducial markers is not stable, if the fiducial markers cannot be distinguished from sample signal, or if the marker moves separately from the sample, this method will provide inaccurate results. Moreover, with high intensity fiducial markers, camera oversaturation will result in bad fitting, causing artefacts. Finally, if a marker with multiple fluorophores is used, bleaching of a single fluorophore can bias localization, if only a small number of fluorophores are remaining on the marker (Balinovic et al., 2019).

The code belonging to this module can be found here: (https://colab.research.google.com/drive/1U-yiO56r4uG92hnq1KKAKAjy4IeW8n_I or https://github.com/Endesfelder-Lab/SMLMComputational, also **Supplementary Pseudocode S4**). For fiducial marker-based drift correction, the fiducial localizations must be selected and isolated. In our module, we identify the fiducials by their constant signal: appropriately chosen fiducial markers will be present throughout the entire movie acquisition. Alternatively, the fiducial markers can be isolated based on higher fluorescence intensity compared to dSTORM, PALM, or PAINT fluorophores, or selected based on their position by hand (i.e. based on coordinates). After performing a single-particle tracking routine (see Module 3), the position of each marker is compared to the position of the same marker in the first frame of the movie. This yields time traces of the drift for every single fiducial marker that have a temporal resolution of one frame. These time traces of individual fiducial markers are averaged to obtain a single drift trace. This averaged drift trace usually has better accuracy than the individual traces because inaccuracies in localization are averaged out. The drift trace is

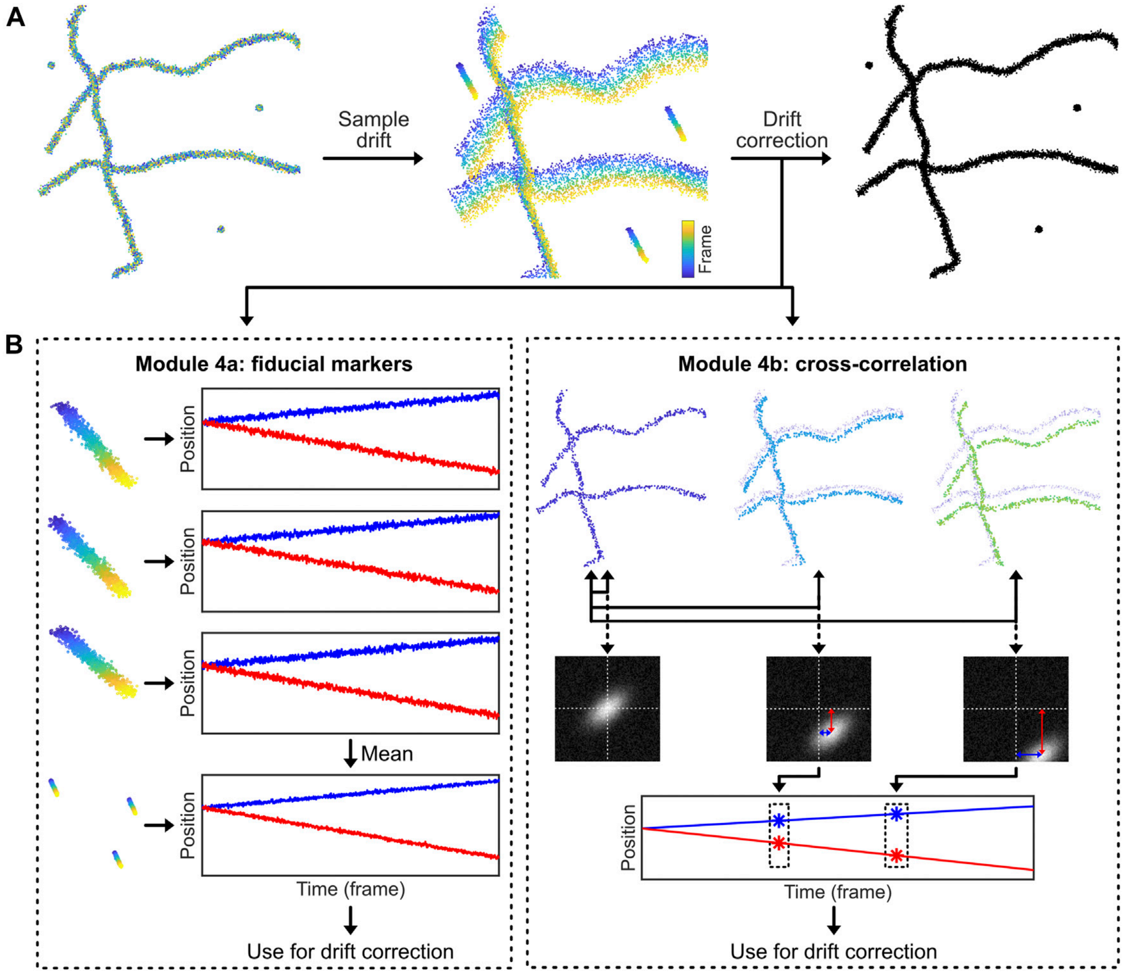

FIGURE 4 | Drift correction methodologies. Most SMLM experiments exhibit sample drift, so the localizations obtained from each fluorophore depend on their detection time within the SMLM acquisition. The reconstructed SMLM image, which combines all localizations from the SMLM experiment, is therefore affected by the overall drift, which directly affects the structural resolution and as such can introduce misleading artifacts (e.g. smearing clusters to filaments). Drift correction methods correct this. **(A)**: Drift can be corrected by introducing fiducial markers that can be tracked with high precision. **(B)**: Alternatively, the displacement of the biological structure at different time points can be analysed *via* temporally cross-correlating the data.

then subtracted from all localizations in the whole dataset, which effectively removes the effects of sample drift. Fiducial marker drift correction is normally applied to 2-dimensional data only, but can easily be expanded to include axial drift, assuming that a 3-dimensional localization procedure is used.

Module 4b: Drift Correction by Cross-Correlation Methods

Data belonging to structural samples that do not change themselves during the acquisition (i.e. SMLM images of immobilized, non-dynamic samples as being obtained by dSTORM or PAINT imaging), can effectively be drift-corrected by visualising the data at different time points and comparing these visualisations (Mlodzianoski et al., 2011) (**Figure 4**). In principle, drift correction by cross-correlation methods is based on the fact that the image generated by the localizations is identical throughout the acquisition time. This means that e.g. for a dataset comprised of 1,000 frames, a visualisation of the structure can be generated from imaging frames 1–100, which can be compared with a visualisation generated from imaging frames 101–200, etc. If drift is present, the second visualisation will be offset from the first. Measuring this offset over time using consecutive data subsets, the overall drift trace can be obtained and corrected for. Drift correction via cross-correlation requires stable, unmoving datasets. In case the structure itself is flexible or moves throughout the data acquisition, this method will silently fail. In addition, heterogeneous sample drift or sample rotation (i.e. caused by uneven matrix contraction) should be prevented.

In our module 4b found here: (https://colab.research.google.com/drive/1DUhUxeCnYXxD7ZkL9NcIDxE6VV7fnzvQ or https://github.com/Endesfelder-Lab/SMLMComputational, also **Supplementary Pseudocode S4**), we therefore generate

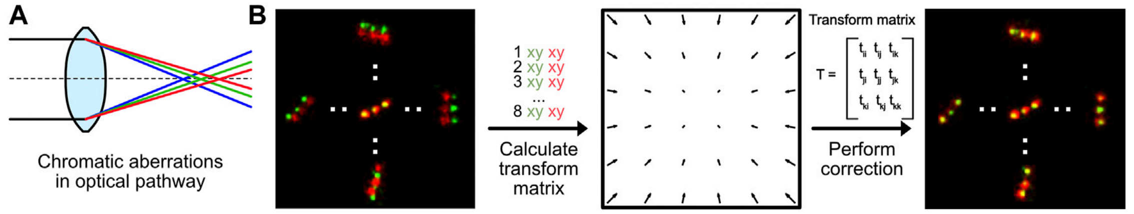

FIGURE 5 | Chromatic aberration correction. (A) Optical elements in any microscope will refract light of different wavelengths differently, causing chromatic aberrations. **(B)** Chromatic aberrations can be corrected by calculating a transformation matrix based on pairwise positions of fluorescent markers measured at different wavelengths. This transformation can be used to correct the instrument-specific chromatic aberration.

multiple images from different time bins. We then calculate cross-correlations between the visualisations at each time bin and the visualisation at the start of the SMLM acquisition (= first time bin). The spatial position of the intensity maximum of each cross-correlation provides a good measure for the drift. This position is identified and attributed to the temporal centre of each bin. The drift trace is based on these points, and—in our module as well as for most cross correlation implementations—non-linearly interpolated to smooth the trajectory. The drift trace is subtracted from the original localizations. This can additionally be expanded to three-dimensional data by taking *z*-slices, and comparing those similarly.

This technique can be expanded to redundant cross-correlation (RCC) (Wang et al., 2014), in which the temporal bins are not only compared to the first, but to all bins. This increases computational effort, but results in higher accuracy. Alternatively, the positions of the emitters at different time points can be compared with each other. The mean shift of the localizations over time is a measure for the drift, similar to the shift of the maximum position of the cross-correlation images, (Cnossen et al., 2021; Fazekas et al., 2021).

Module 5: Chromatic Aberration Correction

All optical components in a microscope experience chromatic aberrations: light is refracted slightly differently based on its wavelength (**Figure 5A**) (Erdelyi et al., 2013). Today, almost every optical element in a fluorescence microscope is corrected for chromatic aberrations. Thus, standard diffraction-limited fluorescence microscopy can be performed without further chromatic aberration corrections. Nevertheless, even for high-quality optics, a residual chromatic shift in the nanometer range shift remains. This is enough to hamper multicolor super-resolution imaging and creates a mismatch of images generated by fluorophores with different emission wavelengths (Zessin et al., 2013) (**Figure 5B**, left). This chromatic aberration is microscope-specific and directly dependent on the optical path and individual components. It thus has to be measured for each setup individually. Nevertheless, it is a static shift (as long as no components change), so it does not need to be repeatedly measured for every new experiment.

In our module 5 (https://colab.research.google.com/drive/1UH0BIuHUJFjF_hXtO3rwdOLTl45LkzLz or https://github.com/Endesfelder-Lab/SMLMComputational, also **Supplementary Pseudocode S5**), we correct the chromatic aberration by comparing data with identical ground-truth positions emitted at two different wavelengths. For the data-pairs, an affine 2-dimensional transform matrix is estimated. For microscopes with more than two color channels, such a matrix has to be estimated for all channels in relation to one reference channel. These transformation matrices can then be used to correct the chromatic aberration from all datasets measured with the same microscope and color channels.

As mentioned, a requirement for chromatic aberration correction is a sample that is identical for multiple emission wavelengths. In this module, we have used a so-called "DNA-PAINT nanoruler" which has identical "docking positions" for both, ATTO542 and ATTO655 fluorophore DNA oligos used as reporters (emission peaks at 561 nm ("green") and 680 nm ("red"), respectively). Those reporters can repeatedly bind and unbind during the SMLM acquisition. The chromatic aberrations in our microscope results in green positions that are localized slightly further to the outside of the image than the red positions (**Figure 5B**, left). We then hand-picked green and red DNA-PAINT position pairs, and used their relative positional shifts to calculate the affine transformation matrix (**Figure 5B**, middle). This transformation is then applied on either the image created from the red localizations, or directly on the red localizations. This effectively reduces the experienced chromatic aberration (**Figure 5B**, right). We note that this analysis method can also be applied for translational offsets, introduced in e.g. dual-view camera systems.

Module 6: Image Generation

A main goal of SMLM, but especially of structural super-resolution imaging, is the generation of super-resolved images from the localization data. However, this is not as straightforward as it may sound, since ultimately the dataset of SMLM localizations are essentially 0-dimensional points. While plotting these localizations as a scatter plot may provide some information (Rust et al., 2006), the symbol size and shape can be arbitrary and the scatter plot does not adequately visualise local emitter density (**Figure 6A**). Thus, it should normally not be used. Generally, it must be noted that all forms of image visualisation decrease the resolution (as every pixelation variant, even when adjusted to the experimental localization precision of the data, ultimately sorts the data in bins), but are often very useful for human interpretation. It is therefore recommended that downstream quantitative efforts are focused on the localization list rather than generated images.

One could reason that each localization can be visualised as the central point of a 2-dimensional Gaussian function with a full-width half maximum determined by the localization precision.

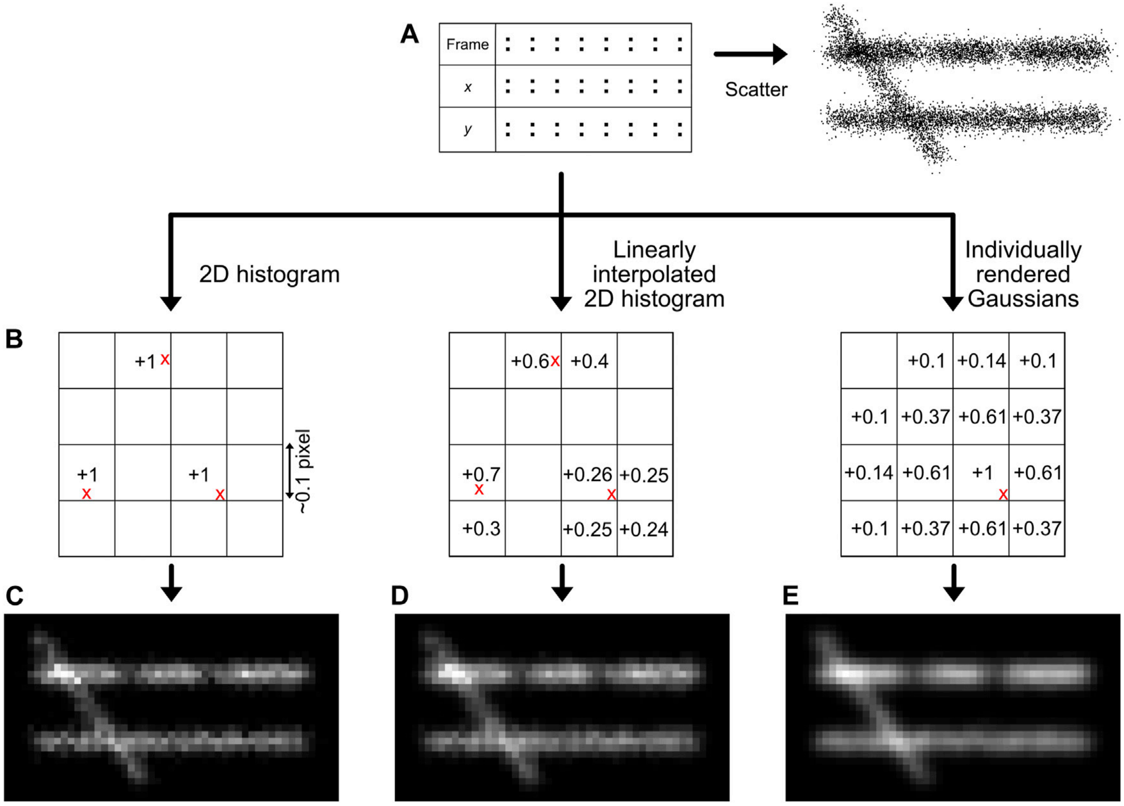

FIGURE 6 | Image generation methods. The simplest way for image generation is a scatter plot, although this does not reflect the localization density accurately **(A)**. The localizations (red crosses) can also be placed on a sub-pixel grid **(B)**, and the bin intensities can be increased based on the position of the localizations. The methods described in this manuscript are the creation of a 2D histogram **(C)**, a linearly interpolated 2D histogram **(D)**, or individually rendered Gaussians **(E)**. Note the regions with lower density (66% lower density compared to the surrounding) and the different intensity between the two horizontal lines (30% lower density) that are more clearly interpreted by histogram images compared to a scatter visualisation.

This procedure would be conceptually very similar to the physical representation of regular brightfield microscopy, which can be interpreted as many simultaneous localizations generating PSFs with a width determined by the optical resolution. However, this methodology actually results in a loss of visual resolution, as it effectively blurs the original structure by the visualization method in addition to blurring caused by the localization error, resulting in a $\sqrt{2}$ resolution loss (Baddeley et al., 2010). Moreover, the rendering of several thousands to millions of 2-dimensional Gaussian functions is computationally expensive and thus unrealistic *via* a computation processing unit (CPU) only (and instead requires e.g. using a graphical processing unit (GPU) that works in a highly parallelized and optimized manner), unless well-optimized code and functions are used (Ries, 2020).

A quantitatively better way for localization visualisation is to place the localizations in user-defined sub-pixel bins, normally ~10–15 sub-bins per original imaging pixel in each dimension (**Figure 6C**) (Nieuwenhuizen et al., 2013). It is important to choose this sub-bin value cautiously, as the super-resolution image pixel size should be in the range of the localization precision (Nyquist-Shannon sampling theorem) (Nyquist, 1928; Shannon, 1949), also see Module 9 to determine the localization precision. If a smaller sub-bin value is chosen, it could lead to visualisation of non-existing details, hindering correct interpretation. This can additionally be subject to a pseudo-Gaussian kernel to spread the intensity to surrounding pixels, which is especially valuable on datasets with sparse signals. This is the approach taken in our module, but is also used standard in e.g. the ThunderSTORM software (Ovesny et al., 2014).

A more sophisticated method, also shown in our module and first published with the software Rapidstorm, is to linearly interpolate the localizations on a sub-pixel raster (**Figure 6D**) (Wolter et al., 2010). In the basis, this method is similar to localization binning in sub-pixel bins, but additionally, neighbouring pixels are also populated based on the distance from the localization to the center of the main sub-pixel bin, preventing discretization errors.

Our module (https://colab.research.google.com/drive/14OCvRUAUFp9JXK6HVyj18fndGY92-Dsx or https://github.com/Endesfelder-Lab/SMLMComputational, also **Supplementary Pseudocode S6**) implements all three methods. Regular 2-dimensional histogram visualisation is straightforward in Python and MATLAB, since this is a built-in function in both languages. For linearly interpolated histograms, for every localization, the correct sub-pixel bin is found, as well as the distance to the center of the sub-pixel bin. This distance in x and y is used to calculate the relative intensity in the neighbouring pixels. Image generation based on individual Gaussian reconstruction is done by looping over every emitter and over every sub-pixel in the reconstructed image, and increasing this value based on the distance to the emitter position.

More involved methods are investigated by Baddeley et al. (2010), and show that adaptive quad-tree histograms and visualisation based on Delaunay triangulation have distinct advantages for SMLM image generation, at the cost of computational complexity.

Module 7: Single-Particle Tracking (spt)

In contrast to structural SMLM imaging, spt is a methodology in which moving fluorescently-labeled objects are tracked over time. Rather than generating an image, assessing and interpreting this movement is the goal of spt. Computational efforts are therefore fundamentally different in spt from those in structural imaging (Chenouard et al., 2014). Analysis consists of three main computational efforts: 1) localizing moving PSFs, 2) linking the localizations of single particles from consecutive imaging frames into trajectories and 3) analysis of the dynamics and diffusional states of the particles from their trajectories.

Localization

Localization efforts required in spt are largely similar to localization efforts required in structural SMLM (Module 2). However, the inherent movement of fluorophores in spt causes deviations of the measured PSF from a theoretical PSF. Software explicitly designed to localize static PSFs can therefore fail when localizing moving PSFs. Downstream processing of spt also dictates that there is a higher priority on detecting the fluorescent emissions than there is on localization precision: because statistics from the fluorophore trajectories are averaged over many linkages, this effectively lessens the influence of localization errors. This results in localization efforts designed for spt to be robust (i.e. high accuracy on fluorophore detection) rather than precise, e.g. as implemented in Trackmate (Tinevez et al., 2017).

Linking of single Fluorescent Emissions Into Particle Trajectories

Linking single fluorescent emissions into particle trajectories is a conceptually simple problem: localizations in subsequent frames possibly belong to the same emitter, and these should be linked together to obtain a trajectory through time, which can be further analysed. In its easiest form, tracking can be performed by determining the nearest localization in the next frame for each localization. Then, as long as the jump distance (JD) between these localizations is lower than a user-defined value, the localizations are linked together and form a track. This methodology is commonly known as nearest-neighbour tracking.

However, nearest-neighbour tracking is not a final method due to several reasons. First, there could be several localizations within the search radius and the closer one could simply be the wrong choice (i.e. two trajectories are crossing each other, or localizations are found due to autofluorescence). Second, fluorophores can blink for one or multiple frames, which effectively means that a "gap" can be present in the trajectory, which should be accounted for. Third, since Brownian diffusion results in a noncentral chi (Rayleigh) distribution of jump distances, there is no well-defined maximum jump distance. Fourth, a population can consist of more than one diffusive state, meaning that the user-chosen maximum jump distance is even less well-defined. Last, nearest-neighbour tracking is prone to introduce artifacts as there is no way to end a trajectory if any localization is present within the defined radius. This will introduce false linkages within the trajectories (e.g. caused by autofluorescence or another molecule appearing in close proximity, e.g. in molecular clusters). These artifacts can be lessened by reducing the search radius, but this will lead to many truncated trajectories (see third and fourth argument). All that being said, nearest neighbor tracking in low density and low noise datasets will experience a neglectable effect from all these criticisms. Meanwhile, it does not introduce any algorithmic bias which easily happens the more *a priori* knowledge and assumptions are taken into account using more advanced methods.

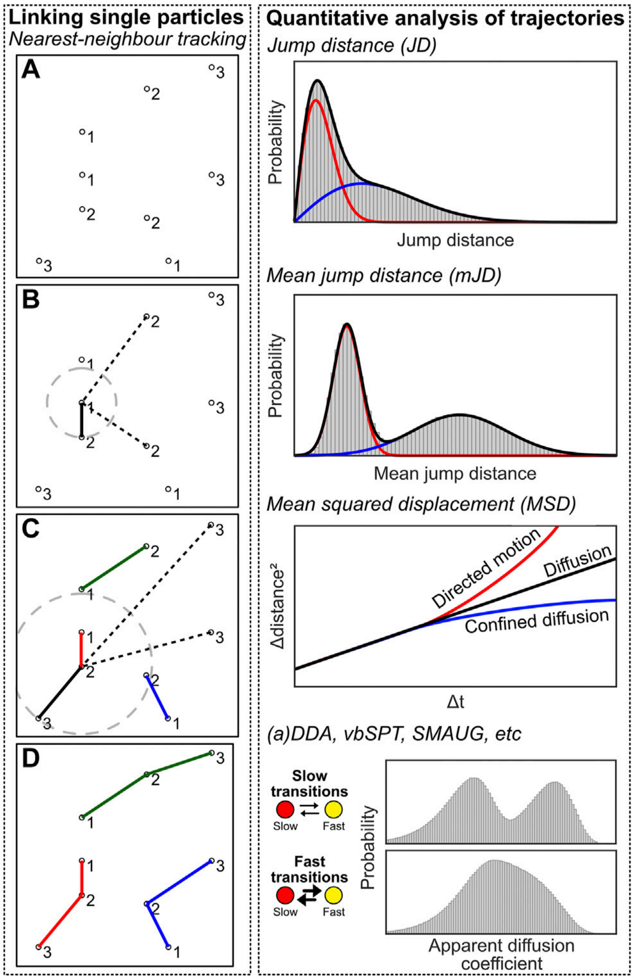

FIGURE 7 | Single-particle tracking computational approaches. Left: Individual emitters have to be linked to create trajectories. Individual emitters have been localized at multiple frames **(A)**, and the nearest neighbour localization in frame n+1 is determined for every localization at frame n, and a linkage is created between these localizations **(B,C)**. This creates trajectories that can be further analysed **(D)**. Right: quantification analysis of trajectory data. See the main text for details on the methods.

Still, solutions for more dense or background-intense spt are a field of on-going method development (Chenouard et al., 2014). All of those algorithms incorporate *a priori* knowledge. E.g. the Icy software (de Chaumont et al., 2012) uses a Bayesian model with multiple hypothesis tracking (MHT) that yields more accurate results especially for weak fluorescent signals (Chenouard et al., 2013). Or alternatively, in TrackMate (Tinevez et al., 2017), tracking is formulated as a linear assignment problem (LAP) (Jaqaman et al., 2008), in which a computational cost factor balances localization-to-localization linkages and track initialisation and termination (i.e. minimizing wrong linkages). Also, localization and tracking steps can be combined, e.g. alternatingly performing localization and tracking to verify each other, as implemented in multiple-target tracking (MTT) (Sergé et al., 2008).

Quantitative Analysis of Trajectories

After the localizations are linked into trajectories, the underlying dynamics can be analysed to interpret the data (**Figure 7**, right). The simplest method is to create a JD histogram, and fitting this histogram with one or multiple diffusive populations from which apparent diffusion coefficients (D*) can be extracted (Schütz et al., 1997; Vrljic et al., 2002). However, analysis of a JD histogram does not have sufficient resolving power if two or more populations with small differences are present; in this case, the mean jump distance (mJD) of every trajectory can be determined, which provides stronger differences, i.e. separated maxima, between populations (Turkowyd et al., 2019; Martens et al., 2020). An analytical correct solution of mJD histograms is impossible, as the underlying data has different statistical origins due to varying trajectory length. However, for sufficiently long trajectories, mJD values will approach, and thus can be well-approximated by, a Gaussian (central limit theorem) from which the diffusion coefficient can be extracted. In our module, we implemented both analyses.

In our module (https://colab.research.google.com/drive/1v4N6os8cdHqilDLguYUGrKmlRM8vcG_8 or https://github.com/Endesfelder-Lab/SMLMComputational, also **Supplementary Pseudocode S7**), we implemented nearest-neighbour tracking while taking blinking into account. This is identical code to the tracking performed in Module 3, albeit with a larger maximum jump distance. Next, the script loops over every trajectory, and consecutively over every localization in the trajectory, except for the last one. The Euclidean distance between this localization and the next localization is calculated and stored if there is 1 frame temporal distance between these localizations. Localizations that do not have a jump distance calculated like this get a value of −1 to easily filter out in later steps. Next, the mean jump distance for the complete trajectory is calculated for every trajectory. The jump distances or mean jump distances are then extracted and plotted in a histogram, after which a non-central chi distribution (JD) or Gaussian approximation (mJD) is fitted to the histogram. This analysis routine is performed on free diffusion of two populations of beads with different sizes, and we show that fitting the data with a single population does not provide satisfactory results. Please also note that the number of bins in the histogram can have an effect on the fitting procedure, and care should be taken to assure that fitting is robust with respect to the bin size.

Another popular method involves calculating the mean squared displacement (MSD) of the trajectories, by taking the squared displacements over time (at $\Delta t = 1, 2\ldots n\text{-}1$ for a trajectory with length n), averaged over all possible starting positions of the trajectory per Δt (Qian et al., 1991). These displacements are then plotted as a function of Δt, and yield 1) the diffusion coefficient D by the MSD curve slope; 2) the localization uncertainty by the intersection with the y-axis; and 3) the type of diffusion (i.e. pure diffusion, confined diffusion, directed motion, relatively) by the shape of the curve (i.e. linear, curved downwards, curved upwards) (Lee et al., 2017). However, the MSD is sensitive to noise in the case of short trajectories commonly obtained *via* sptPALM.

So far, these analysis methods assume that the diffusive state of the underlying trajectory does not change. However, this is commonly not the case in biological situations, e.g. in the case of DNA-binding proteins, where the proteins can be diffusing or be stably bound to the DNA. There are several software packages available that quantify transient states and their state-changing kinetics: (a)DDA [(analytical) diffusion distribution analysis] allows for analysis with a temporal resolution faster than the frametime (Martens et al., 2019; Vink et al., 2020a, 2020b), while vbSPT (Persson et al., 2013) and SMAUG (Karslake et al., 2021) specifically assume state-changing slower or on the same timescale as the frametime.

Module 8: Clustering

By cluster analysis methods, localizations are grouped into coherent structures which helps to visualize and interpret structural data. There are several clustering approaches which can be categorized by their clustering model, e.g. connectivity-based (hierarchical), centroid-based, distribution-based, or density-based methods. Generally, clustering algorithms can be extended to colocalization algorithms when taking a second color channel in consideration (Malkusch et al., 2012; Rossy et al., 2014).

A simple approach is Ripley's K-functions and its normalized variants (i.e. L- and H-functions), which measure the data density as a function of radius around every point in the dataset and compares it to random spatial distribution at same density (Ripley, 1977; Owen et al., 2010; Endesfelder et al., 2011). It does not require initial parameters but can only reveal whether clusters are formed and does not report cluster size accurately (Malkusch et al., 2013). Since the Ripley's functions provide a value that is non-straightforward to interpret, it is normally compared against a differing biological condition (Rossy et al., 2013).

A common clustering algorithm that defines individual clusters is the K-means algorithm (Hartigan and Wong, 1979). It is a centroid-based and unsupervised method that finds the centroids of clusters by minimizing the summed distance of all localizations to the nearest clusters' centroids. However, this approach requires the user to pre-determine how many clusters are expected, and is based on a spherical cluster model without considering noise.

Density-based algorithms can account for irregular shapes and noise. The most known algorithm of this kind in SMLM analyses is DBSCAN (Density-based spatial clustering of applications with noise), which is used in Module 8 (**Figure 8**) (Ester et al., 1996; Endesfelder et al., 2013). DBSCAN requires two parameters: 1)

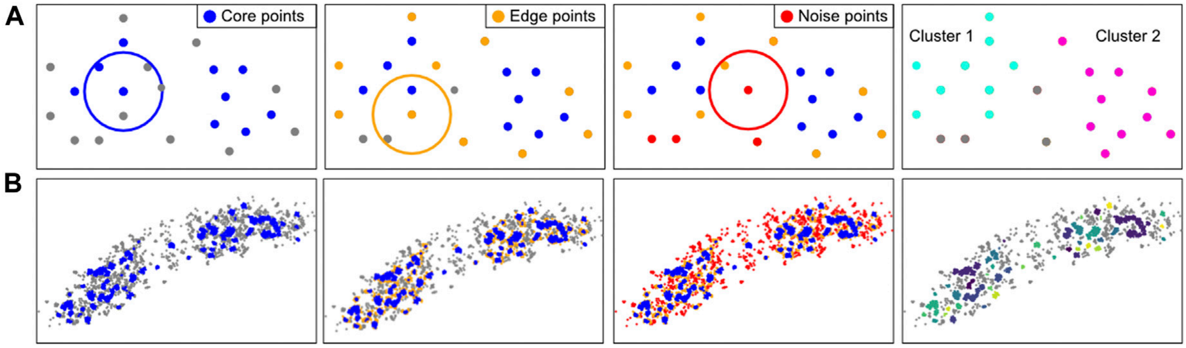

FIGURE 8 | Computational approach of the clustering method DBSCAN. **(A)**: DBSCAN explanation. For every localization in a given FoV, the number of neighbours in a user-defined radius are counted. If there are more neighboring points than a (by the user) set minimal number of points (left), these points are considered core points (blue). All localizations that are not core points, but have a neighbour that is a core point, are considered an edge point (orange, second panel). Localizations that have neither enough neighbours nor proximal core localizations are considered noise points (red, third panel). The core and edge localizations together are considered to form a cluster. The identified clusters can be visualised and characterized (right). In this example, at least 3 neighbours are required for a localization to be considered a core point in the radius indicated by the circle. **(B)**: Application of the DBSCAN steps on an *E. coli* cell with fluorescently-labeled RNA polymerase.

the radius in which adjacent localizations are considered as neighbours, and 2) the minimum number of points in this neighborhood required to initiate the cluster formation. Based on these criteria each point is labeled as a "core point", "edge point" or "noise point". Core and edge points belong to clusters, while noise points do not. This classification is then used to uniquely define the individual clusters.

Note that clustering methods require care (Khater et al., 2020), as all clustering algorithms tend to quantify clusters, even if these do not exist in the dataset, i.e. most methods lack a quality control and fail silently. Moreover, if blinking is not adequately corrected for (Module 2), this could influence clustering results. Next, non-spatially resolved clustering methods (i.e. Ripley's functions) can be influenced by edge effects, e.g. where a uniform distribution inside a single cell can be quantified as non-uniform, because higher localization density inside the cell is contrasting with lower density outside the cell. Finally, DBSCAN could provide quantitatively poor results when directional heterogeneity exists on a same scale as the search radius.

Our module (https://colab.research.google.com/drive/1ruLv02SWFtlEAlZTkWSgHnucoGAZPDcF or https://github.com/Endesfelder-Lab/SMLMComputational, also **Supplementary Pseudocode S8**) implements DBSCAN. The script loops over all localizations, and first finds, counts, and stores the neighbouring localizations (over all frames) in a table. Afterwards, the core and cluster localizations are found based on the procedure described earlier. Finally, a recursion algorithm is employed to determine the individual clusters. Briefly, a loop is started over all core or cluster points, which is set to the current label-id. Next, the same loop is started over all neighbouring core and cluster points, if the original point was a core point. Only if no more neighbours without an assigned label-id can be found, the label-id is increased.

DBSCAN is widely used in SMLM analysis (Endesfelder et al., 2013; Khater et al., 2020). However, as its input is a fixed density [given by the two user-defined parameters (minimal number of points) per (area defined by the input radius)] it is insensitive to different densities of data points and it is not possible to perform hierarchical clustering (e.g. identifying several dense clusters grouping together to form some larger, higher-order clusters). Data with varying cluster densities can be analysed by OPTICS (Ordering Points to Identify the Clustering Structure) (Ankerst et al., 1999) which returns clusters within their hierarchical structure. Compared to DBSCAN however, OPTICS is computationally demanding, especially for large datasets. These clustering algorithms are implemented in the software suites LAMA and PALMSiever (Pengo et al., 2015; Malkusch and Heilemann, 2016).

Alternatively, clustering can be based on Voronoi polygons (Levet et al., 2015; Voronoi, 1908a, 1908b). Based on the user-defined maximal area of polygons (i.e. dependent on the local density), localizations are assigned to clusters.

Module 9: Localization Precision and Image Resolution

SMLM imaging is sensitive to experimental conditions, such as the background noise, thermal drift of the sample, labeling strategy (e.g. movement of fluorophore with respect to the target) and imaging procedure (e.g. read-out intensities, camera settings, optics). As a result, the experimental localization precision is normally lower than the theoretically achievable localization precision, which itself scales with the square root of the number of photons emitted by the fluorophore (Mortensen et al., 2010; Turkowyd et al., 2016). Therefore, quantification of the experimental localization precision provides more accurate results, especially concerning the best achievable resolution (i.e. the optimum image resolution is at best twice the localization precision (Nyquist-Shannon sampling theorem) (Nyquist, 1928; Shannon, 1949). Two methods to compute either image resolution or localization precision are described here: Fourier-ring correlation (FRC) (Saxton and Baumeister, 1982; Van Heel et al., 1982; Unser et al., 1987; Banterle et al., 2013; Nieuwenhuizen et al., 2013) and nearest neighbor based analysis (NeNA) (Endesfelder et al., 2014).

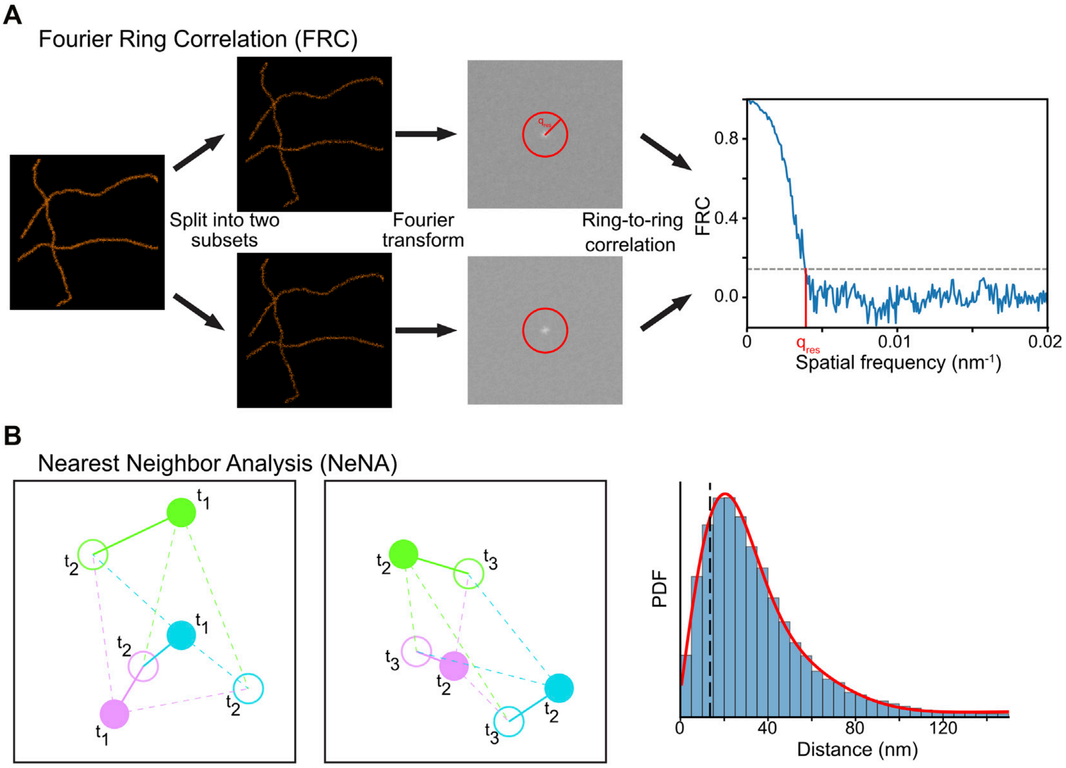

FIGURE 9 | Computational methods to determine resolution in SMLM. **(A)** In FRC, the localization data is split randomly in two subsets, and the correlation of the Fourier transforms of these images at rings with increasing radius is calculated. The resolution of the dataset can then be calculated by determining where the FRC crosses the value of 1/7. **(B)** In NeNA, positions of identical emitters localized in subsequent frames are compared with each other, and the distribution of these distances is fitted with a non-central chi distribution. This fit provides a measure for localization resolution.

Module 9a: Fourier Ring Correlation (FRC)

FRC is a method used to calculate image resolution by comparing two images taken from the same structure (Saxton and Baumeister, 1982; Van Heel et al., 1982). It can be reasonably applied to SMLM data by splitting the dataset into two halves and assuming that a structure rather than mobile fluorophores are imaged (Banterle et al., 2013; Nieuwenhuizen et al., 2013). The spatial frequency domain spectra of these images are computed via a Fourier transform and are correlated with each other at different distances from the frequency center of the image (**Figure 9A**). The image resolution is estimated by determining where the FRC value crosses a user-defined value, typically $1/7 \approx 0.143$ (Rosenthal and Henderson, 2003; Banterle et al., 2013; Nieuwenhuizen et al., 2013).

In our module (https://colab.research.google.com/drive/1svyAqyjpdo_hIG8FSCjAmhNznqDq2sFm or https://github.com/Endesfelder-Lab/SMLMComputational, also **Supplementary Pseudocode S9**), a localization list is randomly split into two arrays, and two images are created (see Module 6). Next, a "distance map" is created with the same size as the two images, which stores the distance to the center of the image. Three required Fourier-transform-based images are then calculated from the two generated images. Finally, the code loops over all distances found in the distance map, and extracts the pixels in the distance map that match this distance. The values in the Fourier-transform-based images belonging to these pixels are then extracted, and the FRC value at this distance is calculated. These distances are plotted in a graph, and the intersection with 1/7 is calculated.

Due to its simplicity, FRC is a widely implemented and used approach (Ovesny et al., 2014; Ries, 2020; Herbert, 2021). However, it can only be used on structural data, as it measures the image similarities via correlation. Also, FRC is sensitive to the non-random division of the data into two bins, e.g. splitting SMLM data into two sub-datasets with only odd or even frames is typically overestimating image resolution as fluorophores commonly fluoresce for more than one consecutive frame. Such effects can be counterbalanced by a correction factor (Nieuwenhuizen et al., 2013). Finally, FRC is affected by the image pixel size used for the visualization and Fourier transform, and additionally requires a structural density that is higher than the localization precision.

Module 9b: Nearest Neighbor Analysis (NeNA)

The localization precision of a SMLM (sub)dataset can be estimated directly from the localization data using NeNA (**Figure 9B**) (Endesfelder et al., 2014). As most nearest neighbor events in adjacent frames from non-merged localization data are originating from the same fluorophore which emits photons over several frames, the true distance between these events is zero (assuming a static dataset). To estimate the localization precision, NeNA estimates the apparent jump distances (and thus localization precision) with a non-central chi distribution for two or three dimensions, or a Gaussian for one dimension.

NeNA will only fail if the average lifetime of single fluorophores is (much) less than a single frame, but this is a setting that should be avoided in SMLM experiments to obtain optimal data (Diekmann et al., 2020).

In our module (https://colab.research.google.com/drive/1JbmbEL1XsF6ab4WmL96iLUijN8Tx0LCU or https://github.com/Endesfelder-Lab/SMLMComputational, also **Supplementary Pseudocode S9**), a two-dimensional localization dataset is loaded, and the distance to the nearest-neighbor in the next frame is calculated (see Module 3). Since the data contains fiducial markers (see Module 4a) and PALM localizations, the localizations are split by their emission intensity. Finally, the jump distance calculated via nearest-neighbor tracking for both PALM- and fiducial marker-localizations are plotted as a histogram, and the distributions are fitted.

DISCUSSION AND PERSPECTIVE

In the previous modules, we covered the most common computational analysis procedures. However, there are other approaches which can improve the efficiency of the analysis and the quality of results or provide new insights into SMLM data, but are not shown here, either due to their highly specific implementation, niche usage, or computational complexity.

A possibility for any SMLM data analysis is to confine the analysis to user-defined ROIs, i.e. only performing analysis in specific regions, or separating analysis based on these regions (e.g. per cell). This ROI selection can be performed on a variety of measures, but we will exemplify ROI selection via single-cell data analysis, where an outline of the cell is used to separate data analysis. This naturally requires (brightfield or phase-contrast) image data of the cells in addition to SMLM data. Additionally, the cells need to be segmented, either manually or *via* algorithms incorporated in e.g. MorphoLibJ, SplineDist, or Oufti (Legland et al., 2016; Paintdakhi et al., 2016; Berg et al., 2019; Mandal and Uhlmann, 2021). Recently, machine-learning approaches have been created to perform cell segmentation (Ronneberger et al., 2015; Berg et al., 2019; Falk et al., 2019). Machine-learning approaches can be especially powerful, considering it often provides good segmentation performance, and its fast computation could allow for real-time (on-line) segmentation. This opens up avenues for e.g. capturing only subsets of the FoV where cells are present, reducing storage size and downstream computational efforts.

If a structure of interest needs to be resolved with a resolution higher than normally achievable in SMLM, particle averaging is an interesting avenue. In particle averaging, the same structure (e.g. nuclear pore complexes Thevathasan et al., 2019) are visualised many times throughout the FoV. Then, their data is combined, traditionally by mapping the repeated structure to a template structure. Mapping onto a template nevertheless is biased towards the template (e.g. rare but biologically important deviations from the consensus structure will be not detected), is sensitive to insufficient labeling, and requires image generation rather than using the localization data directly (Henderson, 2013). Recently, new particle averaging approaches, namely "all-to-all" registrations and comparing relative localization distances to a model description, have arisen that circumvent these downsides (Curd et al., 2021; Heydarian et al., 2018; Heydarian et al., 2021).

An improvement that concerns all computational analysis procedures is to apply these in real-time; i.e. during the SMLM acquisition rather than during post-processing. However, rapid computations and feedback for online microscope control are non-trivial to achieve. Nonetheless, an increasing number of tools approaches real-time SMLM data analysis and online microscopic feedback (Henriques et al., 2010; Kechkar et al., 2013; Holden et al., 2014; Štefko et al., 2018; Li et al., 2019). These advancements can eventually pave the way for intelligent and fully autonomous live-cell, single-molecule microscopy.

DATA AVAILABILITY STATEMENT

All data required to run the modules can be obtained from https://github.com/Endesfelder-Lab/SMLMComputational. The data underlying the provided data are available upon reasonable request to the corresponding author.

AUTHOR CONTRIBUTIONS

UE conceived the idea; KM and BT designed the modules, wrote the code and designed the figures; all authors wrote the manuscript and approved the submitted version.

FUNDING

This work was supported by the DFG priority program SPP 2141 (En1171/1-1) in the frame of the DFG priority program SPP214 (BT and UE), start-up funds at Carnegie Mellon University (BT, KM, and UE), the NSF AI Institute: Physics of the Future (NSF PHY-2020295) (UE), start-up funds at Bonn University (BT, KM, and UE) and an Argelander Grant awarded by the University of Bonn (KM).

ACKNOWLEDGMENTS

The authors thank David Virant for the BC2 dataset and Laura Weber for testing the colab code.

SUPPLEMENTARY MATERIAL

The Supplementary Material for this article can be found online at: https://www.frontiersin.org/articles/10.3389/fbinf.2021.817254/full#supplementary-material

REFERENCES

Abbe, E. (1873). Beiträge zur Theorie des Mikroskops und der mikroskopischen Wahrnehmung. *Archiv F. Mikrosk. Anatomie* 9, 413–468. doi:10.1007/bf02956173

Ankerst, M., Breunig, M. M., Kriegel, H.-P., and Sander, J. (1999). OPTICS: Ordering Points to Identify the Clustering Structure. *SIGMOD Rec.* 28, 49–60. doi:10.1145/304181.304187

Aristov, A., Lelandais, B., Rensen, E., and Zimmer, C. (2018). ZOLA-3D Allows Flexible 3D Localization Microscopy over an Adjustable Axial Range. *Nat. Commun.* 9, 2409. doi:10.1038/s41467-018-04709-4

Babcock, H. P., and Zhuang, X. (2017). Analyzing Single Molecule Localization Microscopy Data Using Cubic Splines. *Sci. Rep.* 7, 552. doi:10.1038/s41598-017-00622-w

Baddeley, D., and Bewersdorf, J. (2018). Biological Insight from Super-resolution Microscopy: What We Can Learn from Localization-Based Images. *Annu. Rev. Biochem.* 87, 965–989. doi:10.1146/annurev-biochem-060815-014801

Baddeley, D., Cannell, M. B., and Soeller, C. (2010). Visualization of Localization Microscopy Data. *Microsc. Microanal.* 16, 64–72. doi:10.1017/S143192760999122X

Balinovic, A., Albrecht, D., and Endesfelder, U. (2019). Spectrally Red-Shifted Fluorescent Fiducial Markers for Optimal Drift Correction in Localization Microscopy. *J. Phys. D: Appl. Phys.* 52, 204002. doi:10.1088/1361-6463/ab0862

Balzarotti, F., Eilers, Y., Gwosch, K. C., Gynnå, A. H., Westphal, V., Stefani, F. D., et al. (2017). Nanometer Resolution Imaging and Tracking of Fluorescent Molecules with Minimal Photon Fluxes. *Science* 355, 606–612. doi:10.1126/science.aak9913

Banterle, N., Bui, K. H., Lemke, E. A., and Beck, M. (2013). Fourier Ring Correlation as a Resolution Criterion for Super-resolution Microscopy. *J. Struct. Biol.* 183, 363–367. doi:10.1016/j.jsb.2013.05.004

Berardozzi, R., Adam, V., Martins, A., and Bourgeois, D. (2016). Arginine 66 Controls Dark-State Formation in Green-to-Red Photoconvertible Fluorescent Proteins. *J. Am. Chem. Soc.* 138, 558–565. doi:10.1021/jacs.5b09923

Berg, S., Kutra, D., Kroeger, T., Straehle, C. N., Kausler, B. X., Haubold, C., et al. (2019). Ilastik: Interactive Machine Learning for (Bio)image Analysis. *Nat. Methods* 16, 1226–1232. doi:10.1038/s41592-019-0582-9

Betzig, E., Patterson, G. H., Sougrat, R., Lindwasser, O. W., Olenych, S., Bonifacino, J. S., et al. (2006). Imaging Intracellular Fluorescent Proteins at Nanometer Resolution. *Science* 313, 1642–1645. doi:10.1126/science.1127344

Cheezum, M. K., Walker, W. F., and Guilford, W. H. (2001). Quantitative Comparison of Algorithms for Tracking Single Fluorescent Particles. *Biophys. J.* 81, 2378–2388. doi:10.1016/S0006-3495(01)75884-5

Chenouard, N., Bloch, I., and Olivo-Marin, J. C. (2013). Multiple Hypothesis Tracking for Cluttered Biological Image Sequences. *IEEE Trans. Pattern Anal. Mach. Intell.* 35, 2736–3750. doi:10.1109/TPAMI.2013.97

Chenouard, N., Smal, I., de Chaumont, F., Maška, M., Sbalzarini, I. F., Gong, Y., et al. (2014). Objective Comparison of Particle Tracking Methods. *Nat. Methods* 11, 281–289. doi:10.1038/nmeth.2808

Cnossen, J., Hinsdale, T., Thorsen, R. Ø., Siemons, M., Schueder, F., Jungmann, R., et al. (2020). Localization Microscopy at Doubled Precision with Patterned Illumination. *Nat. Methods* 17, 59–63. doi:10.1038/s41592-019-0657-7

Cnossen, J., Cui, T. J., Joo, C., and Smith, C. (2021). Drift Correction in Localization Microscopy Using Entropy Minimization. *Opt. Express.* 29, 27961–27974.

Curd, A. P., Leng, J., Hughes, R. E., Cleasby, A. J., Rogers, B., Trinh, C. H., et al. (2021). Nanoscale Pattern Extraction from Relative Positions of Sparse 3D Localizations. *Nano Lett.* 21, 1213–1220. doi:10.1021/acs.nanolett.0c03332

de Chaumont, F., Dallongeville, S., Chenouard, N., Hervé, N., Pop, S., Provoost, T., et al. (2012). Icy: an Open Bioimage Informatics Platform for Extended Reproducible Research. *Nat. Methods* 9, 690–696. doi:10.1038/nmeth.2075

Dickson, R. M., Cubitt, A. B., Tsien, R. Y., and Moerner, W. E. (1997). On/off Blinking and Switching Behaviour of Single Molecules of green Fluorescent Protein. *Nature* 388, 355–358. doi:10.1038/41048

Diekmann, R., Kahnwald, M., Schoenit, A., Deschamps, J., Matti, U., and Ries, J. (2020). Optimizing Imaging Speed and Excitation Intensity for Single-Molecule Localization Microscopy. *Nat. Methods* 17, 909–912. doi:10.1038/s41592-020-0918-5

Diekmann, R., Deschamps, J., Li, Y., Tschanz, A., Kahnwald, M., Matti, U., et al. (2021). Photon-free (S)CMOS Camera Characterization for Artifact Reduction in High- and Super-resolution Microscopy. *BioRxiv*. doi:10.1101/2021.04.16.440125

Edelstein, A., Amodaj, N., Hoover, K., Vale, R., and Stuurman, N. (2010). Computer Control of Microscopes Using µManager. *Curr. Protoc. Mol. Biol.* Chapter 14, Unit14.20.1–14.20.17. doi:10.1002/0471142727.mb1420s92

Elf, J., and Barkefors, I. (2019). Single-Molecule Kinetics in Living Cells. *Annu. Rev. Biochem.* 88, 635–659. doi:10.1146/annurev-biochem-013118-110801

Endesfelder, U., Malkusch, S., Flottmann, B., Mondry, J., Liguzinski, P., Verveer, P. J., et al. (2011). Chemically Induced Photoswitching of Fluorescent Probes-Aa General Concept for Super-resolution Microscopy. *Molecules* 16, 3106–3118. doi:10.3390/molecules16043106

Endesfelder, U., Finan, K., Holden, S. J., Cook, P. R., Kapanidis, A. N., and Heilemann, M. (2013). Multiscale Spatial Organization of RNA Polymerase in *Escherichia coli*. *Biophys. J.* 105, 172–181. doi:10.1016/j.bpj.2013.05.048

Endesfelder, U., Malkusch, S., Fricke, F., and Heilemann, M. (2014). A Simple Method to Estimate the Average Localization Precision of a Single-Molecule Localization Microscopy experiment. *Histochem. Cel Biol.* 141, 629–638. doi:10.1007/s00418-014-1192-3

Erdelyi, M., Rees, E., Metcalf, D., Schierle, G. S., Dudas, L., Sinko, J., et al. (2013). Correcting Chromatic Offset in Multicolor Super-resolution Localization Microscopy. *Opt. Express* 21, 10978–10988. doi:10.1364/OE.21.010978

Ester, M., Kriegel, H.-P., Sander, J., and Xu, X. (1996). A Density-Based Algorithm for Discovering Clusters in Large Spatial Databases with Noise. *Kdd.* 96 (34), 226–231.

Falk, T., Mai, D., Bensch, R., Çiçek, Ö., Abdulkadir, A., Marrakchi, Y., et al. (2019). U-Net: Deep Learning for Cell Counting, Detection, and Morphometry. *Nat. Methods* 16, 67–70. doi:10.1038/s41592-018-0261-2

Fazekas, F. J., Shaw, T. R., Kim, S., Bogucki, R. A., and Veatch, S. L. (2021). A Mean Shift Algorithm for Drift Correction in Localization Microscopy. *Biophysical Rep.* 1 (1), 100008. doi:10.1016/j.bpr.2021.100008

Franke, C., Sauer, M., and van de Linde, S. (2017). Photometry Unlocks 3D Information from 2D Localization Microscopy Data. *Nat. Methods* 14, 41–44. doi:10.1038/nmeth.4073

Geertsema, H. J., Aimola, G., Fabricius, V., Fuerste, J. P., Kaufer, B. B., and Ewers, H. (2021). Left-handed DNA-PAINT for Improved Super-resolution Imaging in the Nucleus. *Nat. Biotechnol.* 39, 551–554. doi:10.1038/s41587-020-00753-y

Grimm, J. B., English, B. P., Choi, H., Muthusamy, A. K., Mehl, B. P., Dong, P., et al. (2016). Bright Photoactivatable Fluorophores for Single-Molecule Imaging. *Nat. Methods* 13, 985–988. doi:10.1038/nmeth.4034

Gu, L., Li, Y., Zhang, S., Xue, Y., Li, W., Li, D., et al. (2019). Molecular Resolution Imaging by Repetitive Optical Selective Exposure. *Nat. Methods* 16, 1114–1118. doi:10.1038/s41592-019-0544-2

Hartigan, J. A., and Wong, M. A. (1979). Algorithm AS 136: A K-Means Clustering Algorithm. *Appl. Stat.* 28, 100–108. doi:10.2307/2346830

Heilemann, M., van de Linde, S., Schüttpelz, M., Kasper, R., Seefeldt, B., Mukherjee, A., et al. (2008). Subdiffraction-resolution Fluorescence Imaging with Conventional Fluorescent Probes. *Angew. Chem. Int. Ed. Engl.* 47, 6172–6176. doi:10.1002/anie.200802376

Henderson, R. (2013). Avoiding the Pitfalls of Single Particle Cryo-Electron Microscopy: Einstein from Noise. *Proc. Natl. Acad. Sci. U S A.* 110, 18037–18041. doi:10.1073/pnas.1314449110

Henriques, R., Lelek, M., Fornasiero, E. F., Valtorta, F., Zimmer, C., and Mhlanga, M. M. (2010). QuickPALM: 3D Real-Time Photoactivation Nanoscopy Image Processing in ImageJ. *Nat. Methods* 7, 339–340. doi:10.1038/nmeth0510-339

Herbert, A. (2021). *GDSC Single Molecule Light Microscopy (SMLM) ImageJ Plugins*. Available at: http://www.sussex.ac.uk/gdsc/intranet/microscopy/UserSupport/AnalysisProtocol/imagej/smlm_plugins/.

Heydarian, H., Schueder, F., Strauss, M. T., van Werkhoven, B., Fazel, M., Lidke, K. A., et al. (2018). Template-free 2D Particle Fusion in Localization Microscopy. *Nat. Methods* 15, 781–784. doi:10.1038/s41592-018-0136-6

Heydarian, H., Joosten, M., Przybylski, A., Schueder, F., Jungmann, R., Werkhoven, B. V., et al. (2021). 3D Particle Averaging and Detection of Macromolecular Symmetry in Localization Microscopy. *Nat. Commun.* 12, 2847. doi:10.1038/s41467-021-22006-5

Holden, S. J., Uphoff, S., and Kapanidis, A. N. (2011). DAOSTORM: an Algorithm for High- Density Super-resolution Microscopy. *Nat. Methods* 8, 279–280. doi:10.1038/nmeth0411-279

Holden, S. J., Pengo, T., Meibom, K. L., Fernandez Fernandez, C., Collier, J., and Manley, S. (2014). High Throughput 3D Super-resolution Microscopy Reveals *Caulobacter crescentus In Vivo* Z-Ring Organization. *Proc. Natl. Acad. Sci. U S A.* 111, 4566–4571. doi:10.1073/pnas.1313368111

Hoogendoorn, E., Crosby, K. C., Leyton-Puig, D., Breedijk, R. M., Jalink, K., Gadella, T. W., et al. (2014). The Fidelity of Stochastic Single-Molecule Super-resolution Reconstructions Critically Depends upon Robust Background Estimation. *Sci. Rep.* 4, 3854. doi:10.1038/srep03854

Huang, B., Wang, W., Bates, M., and Zhuang, X. (2008). Three-Dimensional Super-resolution Imaging by Stochastic Optical Reconstruction Microscopy. *Science* 319, 810–813. doi:10.1126/science.1153529

Huang, B., Bates, M., and Zhuang, X. (2009). Super-Resolution Fluorescence Microscopy. *Annu. Rev. Biochem.* 78, 993–1016. doi:10.1146/annurev.biochem.77.061906.092014

Isaacoff, B. P., Li, Y., Lee, S. A., and Biteen, J. S. (2019). SMALL-LABS: Measuring Single-Molecule Intensity and Position in Obscuring Backgrounds. *Biophys. J.* 116, 975–982. doi:10.1016/j.bpj.2019.02.006

Izeddin, I., Boulanger, J., Racine, V., Specht, C. G., Kechkar, A., Nair, D., et al. (2012a). Wavelet Analysis for Single Molecule Localization Microscopy. *Opt. Express* 20, 2081–2095. doi:10.1364/OE.20.002081

Izeddin, I., El Beheiry, M., Andilla, J., Ciepielewski, D., Darzacq, X., and Dahan, M. (2012b). PSF Shaping Using Adaptive Optics for Three-Dimensional Single-Molecule Super-resolution Imaging and Tracking. *Opt. Express* 20, 4957–4967. doi:10.1364/OE.20.004957

Jabermoradi, A., Yang, S., Gobes, M., van Duynhoven, J. P. M., and Hohlbein, J. (2021). Enabling Single-Molecule Localization Microscopy in Turbid Food Emulsions. *Biorxiv*. doi:10.1101/2021.03.03.433739

Jaqaman, K., Loerke, D., Mettlen, M., Kuwata, H., Grinstein, S., Schmid, S. L., et al. (2008). Robust Single-Particle Tracking in Live-Cell Time-Lapse Sequences. *Nat. Methods* 5, 695–702. doi:10.1038/nmeth.1237

Jouchet, P., Cabriel, C., Bourg, N., Bardou, M., Poüs, C., Fort, E., et al. (2021). Nanometric Axial Localization of Single Fluorescent Molecules with Modulated Excitation. *Nat. Photon.* 15, 297–304. doi:10.1038/s41566-020-00749-9

Juette, M. F., Gould, T. J., Lessard, M. D., Mlodzianoski, M. J., Nagpure, B. S., Bennett, B. T., et al. (2008). Three-dimensional Sub-100 Nm Resolution Fluorescence Microscopy of Thick Samples. *Nat. Methods* 5, 527–529. doi:10.1038/nmeth.1211

Kapanidis, A. N., Uphoff, S., and Stracy, M. (2018). Understanding Protein Mobility in Bacteria by Tracking Single Molecules. *J. Mol. Biol.* 430, 4443–4455. doi:10.1016/j.jmb.2018.05.002

Karslake, J. D., Donarski, E. D., Shelby, S. A., Demey, L. M., DiRita, V. J., Veatch, S. L., et al. (2021). SMAUG: Analyzing Single-Molecule Tracks with Nonparametric Bayesian Statistics. *Methods* 193, 16–26. doi:10.1016/j.ymeth.2020.03.008

Kechkar, A., Nair, D., Heilemann, M., Choquet, D., and Sibarita, J. B. (2013). Real-Time Analysis and Visualization for Single-Molecule Based Super-resolution Microscopy. *PLOS ONE* 8, e62918. doi:10.1371/journal.pone.0062918

Khater, I. M., Nabi, I. R., and Hamarneh, G. (2020). A Review of Super-resolution Single-Molecule Localization Microscopy Cluster Analysis and Quantification Methods. *Patterns (N Y)* 1, 100038. doi:10.1016/j.patter.2020.100038

Krull, A., Buchholz, T.-O., and Jug, F. (2019). "Noise2Void - Learning Denoising from Single Noisy Images," in 2019 IEEE/CVF Conference on Computer Vision and Pattern Recognition (CVPR), Long Beach, CA, USA, 15-20 June 2019, 2129–2137. doi:10.1109/cvpr.2019.00223

Lee, A., Tsekouras, K., Calderon, C., Bustamante, C., and Pressé, S. (2017). Unraveling the Thousand Word Picture: An Introduction to Super-resolution Data Analysis. *Chem. Rev.* 117, 7276–7330. doi:10.1021/acs.chemrev.6b00729

Legland, D., Arganda-Carreras, I., and Andrey, P. (2016). MorphoLibJ: Integrated Library and Plugins for Mathematical Morphology with ImageJ. *Bioinformatics* 32, 3532–3534. doi:10.1093/bioinformatics/btw413

Levet, F., Hosy, E., Kechkar, A., Butler, C., Beghin, A., Choquet, D., et al. (2015). SR-Tesseler: a Method to Segment and Quantify Localization-Based Super-resolution Microscopy Data. *Nat. Methods* 12, 1065–1071. doi:10.1038/nmeth.3579

Li, Y., Mund, M., Hoess, P., Deschamps, J., Matti, U., Nijmeijer, B., et al. (2018). Real-time 3D Single-Molecule Localization Using Experimental point Spread Functions. *Nat. Methods* 15, 367–369. doi:10.1038/nmeth.4661

Li, L., Xin, B., Kuang, W., Zhou, Z., and Huang, Z. L. (2019). Divide and Conquer: Real-Time Maximum Likelihood Fitting of Multiple Emitters for Super-resolution Localization Microscopy. *Opt. Express* 27, 21029–21049. doi:10.1364/OE.27.021029

Liron, Y., Paran, Y., Zatorsky, N. G., Geiger, B., and Kam, Z. (2006). Laser Autofocusing System for High-Resolution Cell Biological Imaging. *J. Microsc.* 221, 145–151. doi:10.1111/j.1365-2818.2006.01550.x

Liu, S., Kromann, E. B., Krueger, W. D., Bewersdorf, J., and Lidke, K. A. (2013). Three Dimensional Single Molecule Localization Using a Phase Retrieved Pupil Function. *Opt. Express* 21, 29462–29487. doi:10.1364/OE.21.029462

Louis, B., Camacho, R., Bresolí-Obach, R., Abakumov, S., Vandaele, J., Kudo, T., et al. (2020). Fast-tracking of Single Emitters in Large Volumes with Nanometer Precision. *Opt. Express* 28, 28656–28671. doi:10.1364/OE.401557

Ma, H., Jiang, W., Xu, J., and Liu, Y. (2021). Enhanced Super-resolution Microscopy by Extreme Value Based Emitter Recovery. *Sci. Rep.* 11, 20417. doi:10.1038/s41598-021-00066-3

Malkusch, S., and Heilemann, M. (2016). Extracting Quantitative Information from Single-Molecule Super-resolution Imaging Data with LAMA - LocAlization Microscopy Analyzer. *Sci. Rep.* 6, 34486. doi:10.1038/srep34486

Malkusch, S., Endesfelder, U., Mondry, J., Gelléri, M., Verveer, P. J., and Heilemann, M. (2012). Coordinate-based Colocalization Analysis of Single-Molecule Localization Microscopy Data. *Histochem. Cel Biol.* 137, 1–10. doi:10.1007/s00418-011-0880-5

Malkusch, S., Muranyi, W., Müller, B., Kräusslich, H. G., and Heilemann, M. (2013). Single-molecule Coordinate-Based Analysis of the Morphology of HIV-1 Assembly Sites with Near-Molecular Spatial Resolution. *Histochem. Cel Biol.* 139, 173–179. doi:10.1007/s00418-012-1014-4

Mandal, S., and Uhlmann, V. (2021). "Splinedist: Automated Cell Segmentation with Spline Curves," in 2021 IEEE 18th International Symposium on Biomedical Imaging (ISBI), April 13–16, 2021, 1082–1086. doi:10.1109/isbi48211.2021.9433928

Manley, S., Gillette, J. M., Patterson, G. H., Shroff, H., Hess, H. F., Betzig, E., et al. (2008). High-density Mapping of Single-Molecule Trajectories with Photoactivated Localization Microscopy. *Nat. Methods* 5, 155–157. doi:10.1038/nmeth.1176

Marr, D., Hildreth, E., and Brenner, S. (1980). Theory of Edge Detection. *Proc. R. Soc. Lond. B Biol. Sci.* 207, 187–217. doi:10.1098/rspb.1980.0020

Marsh, R. J., Pfisterer, K., Bennett, P., Hirvonen, L. M., Gautel, M., Jones, G. E., et al. (2018). Artifact-free High-Density Localization Microscopy Analysis. *Nat. Methods* 15, 689–692. doi:10.1038/s41592-018-0072-5

Martens, K. J. A., Bader, A. N., Baas, S., Rieger, B., and Hohlbein, J. (2018). Phasor Based Single-Molecule Localization Microscopy in 3D (pSMLM-3D): An Algorithm for MHz Localization Rates Using Standard CPUs. *J. Chem. Phys.* 148, 123311. doi:10.1063/1.5005899

Martens, K. J. A., van Beljouw, S. P. B., van der Els, S., Vink, J. N. A., Baas, S., Vogelaar, G. A., et al. (2019). Visualisation of dCas9 Target Search *In Vivo* Using an Open-Microscopy Framework. *Nat. Commun.* 10, 3552. doi:10.1038/s41467-019-11514-0

Martens, K., van Duynhoven, J., and Hohlbein, J. (2020). Spatiotemporal Heterogeneity of κ-carrageenan Gels Investigated via Single-Particle-Tracking Fluorescence Microscopy. *Langmuir* 36, 5502–5509. doi:10.1021/acs.langmuir.0c00393

Martens, K. J. A., Jabermoradi, A., Yang, S., and Hohlbein, J. (2021). Integrating Engineered point Spread Functions into the Phasor-Based Single-Molecule Localization Microscopy Framework. *Methods* 193, 107–115. doi:10.1016/j.ymeth.2020.07.010

Mlodzianoski, M. J., Schreiner, J. M., Callahan, S. P., Smolková, K., Dlasková, A., Santorová, J., et al. (2011). Sample Drift Correction in 3D Fluorescence Photoactivation Localization Microscopy. *Opt. Express* 19, 15009–15019. doi:10.1364/OE.19.015009

Möckl, L., Roy, A. R., and Moerner, W. E. (2020). Deep Learning in Single-Molecule Microscopy: Fundamentals, Caveats, and Recent Developments [Invited]. *Biomed. Opt. Express* 11, 1633–1661. doi:10.1364/BOE.386361

Mortensen, K. I., Churchman, L. S., Spudich, J. A., and Flyvbjerg, H. (2010). Optimized Localization Analysis for Single-Molecule Tracking and Super-resolution Microscopy. *Nat. Methods* 7, 377–381. doi:10.1038/nmeth.1447

Nehme, E., Freedman, D., Gordon, R., Ferdman, B., Weiss, L. E., Alalouf, O., et al. (2020). DeepSTORM3D: Dense 3D Localization Microscopy and PSF Design by Deep Learning. *Nat. Methods* 17, 734–740. doi:10.1038/s41592-020-0853-5

Nieuwenhuizen, R. P., Lidke, K. A., Bates, M., Puig, D. L., Grünwald, D., Stallinga, S., et al. (2013). Measuring Image Resolution in Optical Nanoscopy. *Nat. Methods* 10, 557–562. doi:10.1038/nmeth.2448

Nyquist, H. (1928). Certain Topics in Telegraph Transmission Theory. *Trans. Am. Inst. Electr. Eng.* 47, 617–644. doi:10.1109/t-aiee.1928.5055024

Ovesný, M., Křížek, P., Borkovec, J., Švindrych, Z., and Hagen, G. M. (2014). ThunderSTORM: a Comprehensive ImageJ Plug-In for PALM and STORM Data Analysis and Super-resolution Imaging. *Bioinformatics* 30, 2389–2390. doi:10.1093/bioinformatics/btu202

Owen, D. M., Rentero, C., Rossy, J., Magenau, A., Williamson, D., Rodriguez, M., et al. (2010). PALM Imaging and Cluster Analysis of Protein Heterogeneity at the Cell Surface. *J. Biophotonics* 3, 446–454. doi:10.1002/jbio.200900089

Paintdakhi, A., Parry, B., Campos, M., Irnov, I., Elf, J., Surovtsev, I., et al. (2016). Oufti: an Integrated Software Package for High-Accuracy, High-Throughput Quantitative Microscopy Analysis. *Mol. Microbiol.* 99, 767–777. doi:10.1111/mmi.13264

Parthasarathy, R. (2012). Rapid, Accurate Particle Tracking by Calculation of Radial Symmetry Centers. *Nat. Methods* 9, 724–726. doi:10.1038/nmeth.2071

Patterson, G., Davidson, M., Manley, S., and Lippincott-Schwartz, J. (2010). Superresolution Imaging Using Single-Molecule Localization. *Annu. Rev. Phys. Chem.* 61, 345–367. doi:10.1146/annurev.physchem.012809.103444

Pengo, T., Holden, S. J., and Manley, S. (2015). PALMsiever: a Tool to Turn Raw Data into Results for Single-Molecule Localization Microscopy. *Bioinformatics* 31, 797–798. doi:10.1093/bioinformatics/btu720

Persson, F., Lindén, M., Unoson, C., and Elf, J. (2013). Extracting Intracellular Diffusive States and Transition Rates from Single-Molecule Tracking Data. *Nat. Methods* 10, 265–269. doi:10.1038/nmeth.2367

Qian, H., Sheetz, M. P., and Elson, E. L. (1991). Single Particle Tracking. Analysis of Diffusion and Flow in Two-Dimensional Systems. *Biophys. J.* 60, 910–921. doi:10.1016/S0006-3495(91)82125-7

Rieger, B., and Stallinga, S. (2014). The Lateral and Axial Localization Uncertainty in Super-resolution Light Microscopy. *ChemPhysChem* 15, 664–670. doi:10.1002/cphc.201300711

Ries, J. (2020). SMAP: a Modular Super-resolution Microscopy Analysis Platform for SMLM Data. *Nat. Methods* 17, 870–872. doi:10.1038/s41592-020-0938-1

Ripley, B. D. (1977). The point Processes of Stochastic Geometry. *Adv. Appl. Probab.* 9, 434–435. doi:10.1017/s0001867800028792

Ronneberger, O., Fischer, P., and Brox, T. (2015). "U-net: Convolutional Networks for Biomedical Image Segmentation," in International Conference on Medical Image Computing and Computer-Assisted Intervention, Munich, Germany, October 5–9, 2015 (Springer), 234–241. doi:10.1007/978-3-319-24574-4_28

Rosenthal, P. B., and Henderson, R. (2003). Optimal Determination of Particle Orientation, Absolute Hand, and Contrast Loss in Single-Particle Electron Cryomicroscopy. *J. Mol. Biol.* 333, 721–745. doi:10.1016/j.jmb.2003.07.013

Rossy, J., Owen, D. M., Williamson, D. J., Yang, Z., and Gaus, K. (2013). Conformational States of the Kinase Lck Regulate Clustering in Early T Cell Signaling. *Nat. Immunol.* 14, 82–89. doi:10.1038/ni.2488

Rossy, J., Cohen, E., Gaus, K., and Owen, D. M. (2014). Method for Co-cluster Analysis in Multichannel Single-Molecule Localisation Data. *Histochem. Cel Biol.* 141, 605–612. doi:10.1007/s00418-014-1208-z

Rust, M. J., Bates, M., and Zhuang, X. (2006). Sub-diffraction-limit Imaging by Stochastic Optical Reconstruction Microscopy (STORM). *Nat. Methods* 3, 793–795. doi:10.1038/nmeth929

Sage, D., Pham, T. A., Babcock, H., Lukes, T., Pengo, T., Chao, J., et al. (2019). Super-resolution Fight Club: Assessment of 2D and 3D Single-Molecule Localization Microscopy Software. *Nat. Methods* 16, 387–395. doi:10.1038/s41592-019-0364-4

Saxton, W. O., and Baumeister, W. (1982). The Correlation Averaging of a Regularly Arranged Bacterial Cell Envelope Protein. *J. Microsc.* 127, 127–138. doi:10.1111/j.1365-2818.1982.tb00405.x

Schnitzbauer, J., Strauss, M. T., Schlichthaerle, T., Schueder, F., and Jungmann, R. (2017). Super-resolution Microscopy with DNA-PAINT. *Nat. Protoc.* 12, 1198–1228. doi:10.1038/nprot.2017.024

Schütz, G. J., Schindler, H., and Schmidt, T. (1997). Single-molecule Microscopy on Model Membranes Reveals Anomalous Diffusion. *Biophys. J.* 73, 1073–1080. doi:10.1016/S0006-3495(97)78139-6

Sergé, A., Bertaux, N., Rigneault, H., and Marguet, D. (2008). Dynamic Multiple-Target Tracing to Probe Spatiotemporal Cartography of Cell Membranes. *Nat. Methods* 5, 687–694. doi:10.1038/nmeth.1233

Shannon, C. E. (1949). Communication in the Presence of Noise. *Proc. IRE* 37, 10–21. doi:10.1109/jrproc.1949.232969

Sharonov, A., and Hochstrasser, R. M. (2006). Wide-field Subdiffraction Imaging by Accumulated Binding of Diffusing Probes. *Proc. Natl. Acad. Sci. U S A.* 103, 18911–18916. doi:10.1073/pnas.0609643104

Shechtman, Y., Sahl, S. J., Backer, A. S., and Moerner, W. E. (2014). Optimal Point Spread Function Design for 3D Imaging. *Phys. Rev. Lett.* 113, 133902. doi:10.1103/PhysRevLett.113.133902

Shen, H., Tauzin, L. J., Baiyasi, R., Wang, W., Moringo, N., Shuang, B., et al. (2017). Single Particle Tracking: From Theory to Biophysical Applications. *Chem. Rev.* 117, 7331–7376. doi:10.1021/acs.chemrev.6b00815

Sigal, Y. M., Zhou, R., and Zhuang, X. (2018). Visualizing and Discovering Cellular Structures with Super-resolution Microscopy. *Science* 361, 880–887. doi:10.1126/science.aau1044

Smith, C. S., Joseph, N., Rieger, B., and Lidke, K. A. (2010). Fast, Single-Molecule Localization that Achieves Theoretically Minimum Uncertainty. *Nat. Methods* 7, 373–375. doi:10.1038/nmeth.1449

Speiser, A., Müller, L. R., Hoess, P., Matti, U., Obara, C. J., Legant, W. R., et al. (2021). Deep Learning Enables Fast and Dense Single-Molecule Localization with High Accuracy. *Nat. Methods* 18, 1082–1090. doi:10.1038/s41592-021-01236-x

Stallinga, S., and Rieger, B. (2010). Accuracy of the Gaussian point Spread Function Model in 2D Localization Microscopy. *Opt. Express* 18, 24461–24476. doi:10.1364/OE.18.024461

Štefko, M., Ottino, B., Douglass, K. M., and Manley, S. (2018). Autonomous Illumination Control for Localization Microscopy. *Opt. Express* 26, 30882–30900. doi:10.1364/OE.26.030882

Thevathasan, J. V., Kahnwald, M., Cieśliński, K., Hoess, P., Peneti, S. K., Reitberger, M., et al. (2019). Nuclear Pores as Versatile Reference Standards for Quantitative Super Resolution Microscopy. *Nat. Methods* 16, 1045–1053. doi:10.1038/s41592-019-0574-9

Tinevez, J. Y., Perry, N., Schindelin, J., Hoopes, G. M., Reynolds, G. D., Laplantine, E., et al. (2017). TrackMate: An Open and Extensible Platform for Single-Particle Tracking. *Methods* 115, 80–90. doi:10.1016/j.ymeth.2016.09.016

Turkowyd, B., Virant, D., and Endesfelder, U. (2016). From Single Molecules to Life: Microscopy at the Nanoscale. *Anal. Bioanal. Chem.* 408, 6885–6911. doi:10.1007/s00216-016-9781-8

Turkowyd, B., Müller-Esparza, H., Climenti, V., Steube, N., Endesfelder, U., and Randau, L. (2019). Live-cell Single-Particle Tracking Photoactivated Localization Microscopy of Cascade-mediated DNA Surveillance. *Methods Enzymol.* 616, 133–171. doi:10.1016/bs.mie.2018.11.001

Turkowyd, B., Schreiber, S., Wörtz, J., Segal, E. S., Mevarech, M., Duggin, I. G., et al. (2020). Establishing Live-Cell Single-Molecule Localization Microscopy Imaging and Single-Particle Tracking in the Archaeon Haloferax Volcanii. *Front. Microbiol.* 11, 583010. doi:10.3389/fmicb.2020.583010

Unser, M., Trus, B. L., and Steven, A. C. (1987). A New Resolution Criterion Based on Spectral Signal-To-Noise Ratios. *Ultramicroscopy* 23, 39–51. doi:10.1016/0304-3991(87)90225-7

van de Linde, S., and Sauer, M. (2014). How to Switch a Fluorophore: from Undesired Blinking to Controlled Photoswitching. *Chem. Soc. Rev.* 43, 1076–1087. doi:10.1039/c3cs60195a

van de Linde, S., Löschberger, A., Klein, T., Heidbreder, M., Wolter, S., Heilemann, M., et al. (2011). Direct Stochastic Optical Reconstruction Microscopy with Standard Fluorescent Probes. *Nat. Protoc.* 6, 991–1009. doi:10.1038/nprot.2011.336

Van Heel, M., Keegstra, W., Schutter, W., and Van Bruggen, E. J. F. (1982). Arthropod Hemocyanin Structures Studied by Image Analysis. *Life Chem. Rep. Suppl.* 1, 69–73.

Vink, J. N. A., Martens, K. J. A., Vlot, M., McKenzie, R. E., Almendros, C., Estrada Bonilla, B., et al. (2020a). Direct Visualization of Native CRISPR Target Search in Live Bacteria Reveals Cascade DNA Surveillance Mechanism. *Mol. Cel.* 77, 39–e10. doi:10.1016/j.molcel.2019.10.021

Vink, J. N. A., Brouns, S. J. J., and Hohlbein, J. (2020b). Extracting Transition Rates in Particle Tracking Using Analytical Diffusion Distribution Analysis. *Biophys. J.* 119, 1970–1983. doi:10.1016/j.bpj.2020.09.033

Virant, D., Turkowyd, B., Balinovic, A., and Endesfelder, U. (2017). Combining Primed Photoconversion and UV-Photoactivation for Aberration-free, Live-Cell Compliant Multi-Color Single-Molecule Localization Microscopy Imaging. *Int. J. Mol. Sci.* 18, 1524. doi:10.3390/ijms18071524

Virant, D., Traenkle, B., Maier, J., Kaiser, P. D., Bodenhöfer, M., Schmees, C., et al. (2018). A Peptide Tag-Specific Nanobody Enables High-Quality Labeling for dSTORM Imaging. *Nat. Commun.* 9, 930. doi:10.1038/s41467-018-03191-2

Vojnovic, I., and Endesfelder, U. (2020). Beginner's Guide to Producing Super-resolved Images on a Widefield Fluorescence Microscope. *Biochemist* 42, 52–56. doi:10.1042/bio20200045

Voronoi, G. (1908a). Nouvelles applications des paramètres continus à la théorie des formes quadratiques. Deuxième mémoire. Recherches sur les parallélloèdres primitifs. *J. Für Reine Angew. Math. Crelles J.* 1908, 198–287. doi:10.1515/crll.1908.134.198

Voronoi, G. (1908b). Nouvelles applications des paramètres continus à la théorie des formes quadratiques. Premier mémoire. Sur quelques propriétés des formes quadratiques positives parfaites. *J. Für Reine Angew. Math. Crelles J.* 1908, 97–102. doi:10.1515/crll.1908.133.97

Vrljic, M., Nishimura, S. Y., Brasselet, S., Moerner, W. E., and McConnell, H. M. (2002). Translational Diffusion of Individual Class II MHC Membrane Proteins in Cells. *Biophys. J.* 83, 2681–2692. doi:10.1016/S0006-3495(02)75277-6

Wang, Y., Schnitzbauer, J., Hu, Z., Li, X., Cheng, Y., Huang, Z. L., et al. (2014). Localization Events-Based Sample Drift Correction for Localization Microscopy with Redundant Cross-Correlation Algorithm. *Opt. Express* 22, 15982–15991. doi:10.1364/OE.22.015982

Wolter, S., Schüttpelz, M., Tscherepanow, M., Van De Linde, S., Heilemann, M., and Sauer, M. (2010). Real-time Computation of Subdiffraction-Resolution Fluorescence Images. *J. Microsc.* 237, 12–22. doi:10.1111/j.1365-2818.2009.03287.x

Wolter, S., Löschberger, A., Holm, T., Aufmkolk, S., Dabauvalle, M. C., van de Linde, S., et al. (2012). rapidSTORM: Accurate, Fast Open-Source Software for Localization Microscopy. *Nat. Methods* 9, 1040–1041. doi:10.1038/nmeth.2224

Xu, F., Ma, D., MacPherson, K. P., Liu, S., Bu, Y., Wang, Y., et al. (2020). Three-dimensional Nanoscopy of Whole Cells and Tissues with *In Situ* point Spread Function Retrieval. *Nat. Methods* 17, 531–540. doi:10.1038/s41592-020-0816-x

Zessin, P. J., Krüger, C. L., Malkusch, S., Endesfelder, U., and Heilemann, M. (2013). A Hydrophilic Gel Matrix for Single-Molecule Super-resolution Microscopy. *Opt. Nano* 2, 4. doi:10.1186/2192-2853-2-4

Zhang, Z., Wang, Y., Piestun, R., Huang, Z. L., Piestun, R., and Huang, Z. (2021). Characterizing and Correcting Camera Noise in Back-Illuminated sCMOS Cameras. *Opt. Express* 29, 6668–6690. doi:10.1364/OE.418684

Zhu, L., Zhang, W., Elnatan, D., and Huang, B. (2012). Faster STORM Using Compressed Sensing. *Nat. Methods* 9, 721–723. doi:10.1038/nmeth.1978

Conflict of Interest: The authors declare that the research was conducted in the absence of any commercial or financial relationships that could be construed as a potential conflict of interest.

frontiers in Bioinformatics

REVIEW
published: 04 March 2022
doi: 10.3389/fbinf.2022.811053

Don’t Be Fooled by Randomness: Valid *p*-Values for Single Molecule Microscopy

***Magdalena C. Schneider* and *Gerhard J. Schütz* ***

Institute of Applied Physics, TU Wien, Vienna, Austria

The human mind shows extraordinary capability at recognizing patterns, while at the same time tending to underestimate the natural scope of random processes. Taken together, this easily misleads researchers in judging whether the observed characteristics of their data are of significance or just the outcome of random effects. One of the best tools to assess whether observed features fall into the scope of pure randomness is statistical significance testing, which quantifies the probability to falsely reject a chosen null hypothesis. The central parameter in this context is the *p*-value, which can be calculated from the recorded data sets. In case of *p*-values smaller than the level of significance, the null hypothesis is rejected, otherwise not. While significance testing has found widespread application in many sciences including the life sciences, it is hardly used in (bio-)physics. We propose here that significance testing provides an important and valid addendum to the toolbox of quantitative (single molecule) biology. It allows to support a quantitative judgement (the hypothesis) about the data set with a probabilistic assessment. In this manuscript we describe ways for obtaining valid *p*-values in two selected applications of single molecule microscopy: (i) Nanoclustering in single molecule localization microscopy. Previously, we developed a method termed 2-CLASTA, which allows to calculate a valid *p*-value for the null hypothesis of an underlying random distribution of molecules of interest while circumventing overcounting issues. Here, we present an extension to this approach, yielding a single overall *p*-value for data pooled from multiple cells or experiments. (ii) Single molecule trajectories. Data from a single molecule trajectory are inherently correlated, thus prohibiting a direct analysis via conventional statistical tools. Here, we introduce a block permutation test, which yields a valid *p*-value for the analysis and comparison of single molecule trajectory data. We exemplify the approach based on FRET trajectories.

Keywords: single molecule microscopy, single molecule localization microscopy, FRET, statistical significance testing, nanoclustering

Edited by:
Christian Franke,
Friedrich Schiller University Jena,
Germany

Reviewed by:
Sjoerd Stallinga,
Delft University of Technology,
Netherlands
Zengyou He,
Dalian University of Technology, China

Correspondence:
Gerhard J. Schütz
schuetz@iap.tuwien.ac.at

Specialty section:
This article was submitted to
Computational BioImaging,
a section of the journal
Frontiers in Bioinformatics

Received: *08 November 2021*
Accepted: *12 January 2022*
Published: *04 March 2022*

Citation:
Schneider MC and Schütz GJ (2022)
Don’t Be Fooled by Randomness:
Valid p*-Values for Single*
Molecule Microscopy.
Front. Bioinform. 2:811053.
doi: 10.3389/fbinf.2022.811053

1 INTRODUCTION

One fundamental problem behind the interpretation of biological data relates to the question whether a specific data set agrees with a certain hypothesis or not. Typical examples include the comparative analysis of different subgroups, or the compatibility of data with a specified model. The basic problem arises from the fact that each reproduction of a biological experiment yields a slightly different outcome, irrespective of the quality and precision of the experiment. The reason can be

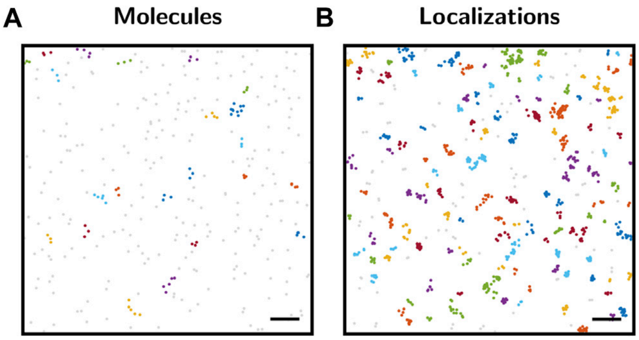

FIGURE 1 | Cluster analysis with DBSCAN. **(A)** Map of molecule positions. Positions were generated by a spatial Poisson point process with a density of 80 points per μm^2. The point pattern was analyzed by DBSCAN (Ester et al., 1996). Analysis parameters were set to $r = 50$ nm for the search radius and $n = 3$ for the minimum number of points constituting a cluster. The color code represents the cluster assignment. Unclustered points are shown in gray. Although the molecule point pattern represents complete spatial randomness, 22 clusters were identified by DBSCAN. **(B)** SMLM localization map simulated based on the molecule positions from panel **(A)**, including overcounting according to the blinking statistics of SNAP-AF647 (Arnold et al., 2020). The localization map was analyzed by DBSCAN as described in panel **(A)**, yielding 116 clusters. Scale bars: 200 nm.

measurement errors or stochastic variations underlying the physical processes. In consequence, it is the interpreter's problem to judge the compatibility of the data with the hypothesis.

Significance testing has been developed to provide an exact mathematical framework for this problem. The first step is to formulate a null hypothesis, against which the data is to be tested; a typical null hypothesis would be the absence of any effect or difference. Let us introduce as an example the question whether proteins are distributed randomly on a two-dimensional membrane. This question has become central in many fields of cellular biophysics (Garcia-Parajo et al., 2014; Goyette et al., 2019). In our case, the null hypothesis would be a purely random distribution. The idea is now to judge the validity of this hypothesis, based on a binary classifier, which either rejects the hypothesis or not. Naturally, one makes errors in this judgement. One misjudgement is the false rejection of the null hypothesis. The *p*-value together with significance testing is the attempt to quantitatively assess such misjudgements. In a nutshell, the lower the *p*-value, the likelier it is that the data set disagrees with the null hypothesis. Ideally, the researcher defines a significance level α before performing the experiment, which is taken as threshold criterion for the decision: any *p*-value below α is considered as a rejection of the null hypothesis, whereas any *p*-value greater than α would count as agreement.

Significance testing can hence be considered as a powerful tool for a quantitative assessment of a particular experimental outcome. In this context, quantification does not relate to a determination of the magnitude of certain biological parameters, but to a probabilistic assessment of the likelihood of the chosen null hypothesis or the deviation of it. Indeed, as **Figure 1A** indicates, even random spatial protein distributions contain accumulations that would be picked up as clusters by standard clustering algorithms. Therefore, we consider it important to first globally assess a data set via significance testing before using more detailed analysis tools for a quantification of the biological parameters of interest.

In this manuscript, we provide a guideline how to use *p*-values for the analysis of single molecule microscopy data. In particular, we address the following questions:

- What is the probabilistic basis of the significance level α and the *p*-value?
- How can one handle situations in which the distribution of the test statistic under the null hypothesis is not known analytically?
- How can multiple experimental outcomes be combined into one global *p*-value?
- How can one account for correlated data in significance testing?

After a brief introduction into significance testing, we provide the reader of this paper with instructions how to use significance testing in two specific settings:

(i) Detection of protein nanoclusters in membranes. The spatial organization of membrane proteins can be studied in unprecedented detail via single molecule localization microscopy (SMLM). In this superresolution technique, the diffraction limit of light is circumvented by separating the emission of individual fluorophores in time (Sigal et al., 2018; Schermelleh et al., 2019; Lelek et al., 2021; Schütz and Schneider, 2021). After recording and post-processing of thousands of frames, a localization map is obtained. This map is a list of coordinates representing the observed molecule positions. Early studies conducting SMLM experiments on cellular plasma membrane proteins have consistently reported nanoclustering to different degrees (Lillemeier et al., 2010; Rossy et al., 2013; Garcia-Parajo et al., 2014). However, due to blinking of fluorophores the same biomolecule of interest can be detected multiple times during the image acquisition. In combination with localization errors, this leads to localization clusters in the localization maps, which can be easily mistaken for true molecular nanoclustering. Here, we want to address the question of biomolecular nanoclustering in the framework of significance testing.

(ii) Comparative analysis of single molecule trajectories. In SMLM, the high spatial resolution is traded for temporal resolution. To complement this approach, cellular dynamics can be investigated based on the recording of single particle trajectories (Wieser and Schütz, 2008). Similar to SMLM, the density of fluorescent molecules needs to be low enough to distinguish individual molecules. A single molecule is then imaged and tracked over a certain time span, yielding the evolution of a recorded parameter over time. As observed quantity, we considered here the Förster Resonance Energy Transfer (FRET) (Roy et al., 2008). The FRET efficiency corresponds to the non-radiative energy transfer between a

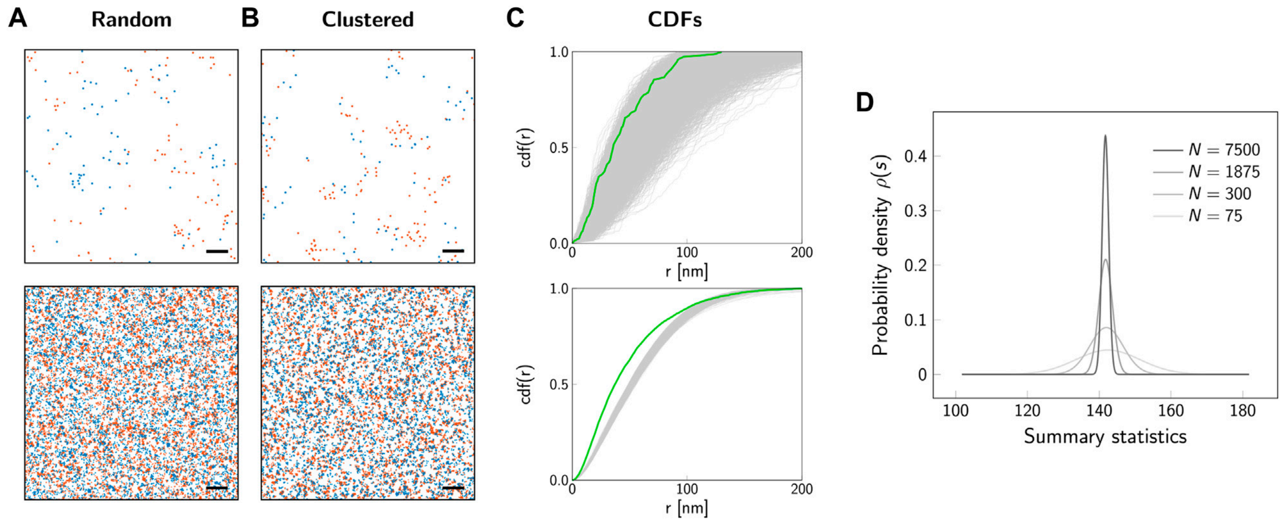

FIGURE 2 | Sampling distribution and influence of sample size. Representative localization maps of an underlying random **(A)** and clustered **(B)** distribution of biomolecules. The simulated regions comprise a number of $N = 75$ underlying molecules (top row) or $N = 7500$ molecules (bottom row). For the clustered scenario, we simulated dimers. The degree of labeling was set to 100%. Scale bars: 100 nm (top row), 1 μm (bottom row). **(C)** Cumulative distribution functions (CDFs) of cross-nearest neighbor distances between localizations of the red and blue color channel. Gray lines show the CDFs for 10 000 simulations of random biomolecular distributions. The green line indicates the CDF for the clustered scenario from panel **(B)**. **(D)** Probability distribution of the summary statistic, i.e. the *sampling distribution*. As a summary statistic the integral of the CDF from 0 nm to 200 nm was calculated. The sampling distribution is shown for sample sizes corresponding to a number of molecules from $N = 75$ (light gray line) to $N = 7500$ (black line). The larger the sample size, the narrower is the sampling distribution.

donor and acceptor fluorophore, which is directly related to the distance between the two fluorophores. Thus, distances between molecules can be determined at a length scale of a few nanometers. When performing a comparative analysis of recorded samples, one difficulty relates to the correlation within single trajectories. Here, we show how this problem can be solved via a block permutation testing approach.

2 STATISTICAL SIGNIFICANCE

In the following, we discuss the concept of significance testing for the analysis of biophysical data. As guiding example we will use hypothetical data from SMLM experiments, which shall be analyzed by a 2-color localization microscopy and significance testing approach (2-CLASTA), which we recently developed (Arnold et al., 2020). 2-CLASTA is based on competitive labeling of the same type of biomolecule with labels of two different colors, yielding a 2-color localization map. As the method does not analyze the distribution of localizations directly, but possible correlations between the two color channels, it is independent of the blinking behavior and, in particular, is compatible with any SMLM technique, including PALM, STORM and PAINT [see Supplementary Figure S3 in (Arnold et al., 2020)].

Let us start by considering a pattern generated by a spatial Poisson point process, i.e., complete spatial randomness (**Figure 1A**), which could correspond to the 2D positions of single protein molecules in a cell membrane. As is apparent from the image, several points will be in close spatial proximity due to random chance alone. This can be easily seen when analyzing the point pattern with clustering methods such as DBSCAN (Ester et al., 1996). Although the point pattern is purely random, multiple clusters were detected by the method.

The situation becomes more severe when considering SMLM-inherent overcounts which arise from repetitive detections due to the blinking kinetics of single dye molecules. **Figure 1B** shows the same underlying biomolecular distribution as **Figure 1A**, but now including overcounting which was simulated using typical experimental blinking data. Obviously, more apparent localization clusters arise and are detected by the DBSCAN approach. Thus, a mere analysis of clustering without considering its statistical significance in the context of the global point pattern distribution may yield misleading results.

In a statistical analysis, the characteristics of a whole population are estimated based on the analysis of a subsample (**Figure 2A**); for example, the overall spatial distribution of biomolecules is investigated based on the localization map obtained from a subregion of a cell. The population follows an underlying unknown spatial distribution, which shall be characterized by the statistical test. The *sample* is a data subset which should be representative of the population. For our example of 2-color SMLM data, **Figure 2A** shows two samples simulated with different sizes of the selected region of interest. The key step now is to identify a sample *summary statistic*, which will be used to infer information about the whole population. In our previous publication, we analyzed the cross-nearest neighbor distances between the two color channels (Arnold et al., 2020). **Figure 2C** shows the empirical cumulative density function (CDF) for a number of 10 000 different subsamples. In principle, if an analytical and parameterized model of the underlying spatial distribution was available, the empirical

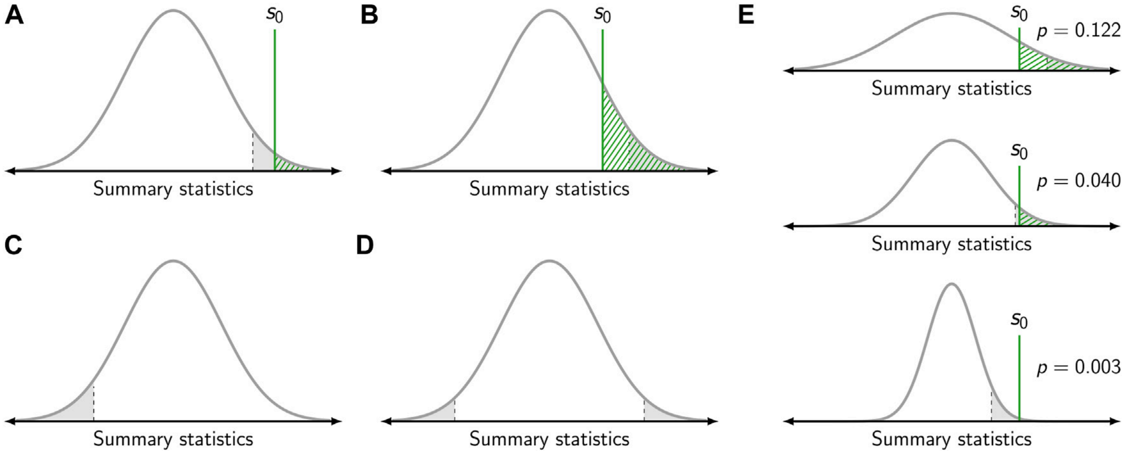

FIGURE 3 | Calculation of the *p*-value. **(A,B)** Gray curves show the sampling distribution of the summary statistic under the null hypothesis. The value of the summary statistic s_0 obtained for one specific sample is shown as green vertical line. The *p*-value corresponds to the dashed green area. The gray area corresponds to the level of significance, which was set to $\alpha = 0.05$. If the *p*-value falls below the level of significance (i.e., s_0 falls within the gray area), the null hypothesis is rejected **(A)**. Otherwise, the null hypothesis is kept **(B)**. In panels **(A)** and **(B)** a right-sided test is depicted. **(C)** Left-sided test. **(D)** Two-sided test. **(E)** Influence of sample size. The same value s_0 of the summary statistics yields a different *p*-value dependent on the sample size (top to bottom). For a small sample size, the sampling distribution is broad and the null hypothesis is kept (top). For a large sample size, the sampling distribution is narrow and the null hypothesis is rejected (bottom).

CDFs could be fitted and the parameters determined. However, in practice such a model is difficult to establish, making statistical tools a valid choice for approaching this problem. What is apparent at first glance is the rather large spread between the different curves, which is particularly pronounced for smaller subsample sizes. The large spread reflects random effects which lead to variations between subsamples, also if they are drawn from the same underlying population. In the following, we did not use the empirical CDFs directly, but reduced them to the integral over the curve, which was taken as a summary statistics for the subsequent analysis. The sample summary statistics is a random variable that follows a probability distribution (**Figure 2D**). This probability distribution of the sample summary statistic over all possible random samples of given size n is called the *sampling distribution* $\rho(s)$. The shape of the sampling distribution depends both on the underlying population and the sample size. For increasing sample sizes, the distribution becomes narrower.

Let us apply the analysis *via* summary statistics to characterize a simple model, which becomes the basis for the null hypothesis. The null hypothesis H_0 assumes the validity of this model, for example a purely random spatial distribution of all biomolecules. The central idea of significance testing is to quantify the probability for obtaining a certain summary statistics. More precisely, the *p*-value quantifies the probability that drawing from the sampling distribution under the null hypothesis yields a value which is as extreme or more extreme than a given value s_0 (**Figure 3A**). The *p*-value hence is given by the integral $p = \int_{s_0}^{\infty} \rho(s)ds$. Typically, s_0 is the value of the summary statistics obtained from an actual experimental observation.

Per definition, the *p*-value is a random variable in the interval [0, 1]. A *p*-value is valid if it fulfills $\mathbb{P}(p \le a \mid H_0) \le a$ for every $0 \le a \le 1$ under the null hypothesis; if equality holds true for all values of a, the *p*-value is exact. This definition implies that—under the null hypothesis—the *p*-value shows a uniform distribution. In return, if the *p*-value is not distributed uniformly under the null hypothesis, the null hypothesis does not follow the assumed distribution and thus, the *p*-value is not valid. If the employed test statistic is discrete, the distribution of *p*-values will also be discrete. Hence, the *p*-value cannot be uniformly distributed over the whole interval [0, 1], but can take on discrete values only. Nevertheless, the *p*-value will be distributed uniformly in the sense that $\mathbb{P}(p \le a \mid H_0) = a$, if a is a value that can be taken on by the *p*-value, and $\mathbb{P}(p \le a \mid H_0) < a$ otherwise. Hence, the *p*-value is valid.

As the *p*-value is based on the sampling distribution, it not only depends on the population but also the sample size (**Figure 3E**). Hence, the same outcome for a summary statistics may yield different *p*-values dependent on the sample size as the width of the sampling distribution varies.

The *p*-value allows to assess statistical significance, i.e., whether a result for a test statistic is more extreme than what can be expected from random chance. It describes how incompatible the observed data are with the statistical model specified by the null hypothesis. Thus, the *p*-value can be used to conduct a hypothesis test, in which the null hypothesis H_0 is tested against the alternative hypothesis H_1. Of note, the two hypotheses H_0 and H_1 should be mutually exclusive and their union should cover the whole range of possible outcomes. The test decision, i.e., whether the null hypothesis is rejected or kept, is based on the *p*-value and a chosen threshold termed the level of significance α. The null hypothesis is rejected if the obtained *p*-value is lower than or equal to α. If the *p*-value is larger than α, the null hypothesis is kept (**Figure 3**).

Let us consider three different scenarios for the application of significance testing to the analysis of SMLM data. First, a test shall

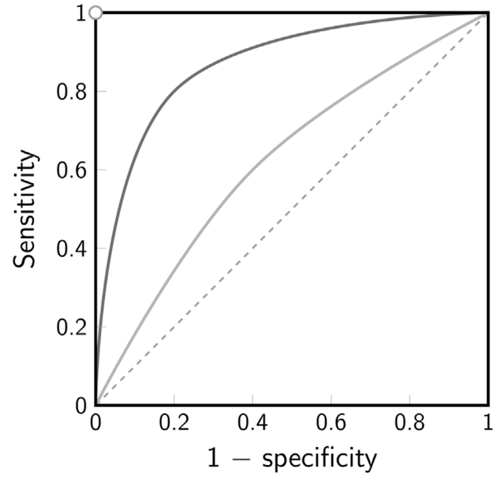

FIGURE 4 | Receiver operating characteristic (ROC). The ROC curve illustrates the trade-off between sensitivity and specificity for a binary classifier. The true positive rate (sensitivity) is plotted against the false positive rate (1-specificity). Note that for a hypothesis test the false positive rate corresponds to the chosen level of significance α. The white dot in the top left corner indicates the point of perfect discrimination, the dashed line indicates the line of no discrimination. The solid lines indicate two scenarios for a binary classifier with low discrimination (light gray) and better discrimination (dark gray).

be performed for the null hypothesis of a random distribution of biomolecules against the alternative hypothesis of (nano-) clustering. As indicated in **Figures 2B,C**, spatial clustering leads to a steeper increase in the empirical CDFs concomitant with a higher value of the determined summary statistics s_0. In this case, it is hence recommendable to use the right-sided p-value (**Figure 3A**) and only reject the null hypothesis in case of extremely high values of s_0. Second, we assume as alternative hypothesis a repulsion of the molecular positions. In this case, molecules would be dispersed across the field of view, concomitant with a smaller value of the determined summary statistics s_0. Consequentially, the left-sided p-value would be used for the test (**Figure 3C**). Third, it may be the case that any deviation from a random distribution is of interest to the experimentalist. In this case, one would opt for choosing the two-sided p-value, and reject the null hypothesis both in case of extremely high and low values of s_0 (**Figure 3D**).

For a valid analysis, the value of the significance level α needs to be specified *a priori*, i.e., before calculating the p-value for a particular experiment (Shine, 1980). Only in this case the level of significance corresponds to the false positive rate of the test. If the level of significance is selected *a posteriori*, the researcher may be biased in the choice of α dependent on the obtained p-value. Thus, the probability for an incorrect rejection of the null hypothesis will be affected.

For the interpretation of results it should be kept in mind that the outcome of a test decision, i.e. the rejection or acceptance of the null hypothesis, may be incorrect. The type I and type II error quantify the probability of a false decision. The *type I error* corresponds to false positives: The null hypothesis is erroneously rejected, i.e. an observed effect is assumed to be real although it is due to random chance alone. Interestingly, the probability of a type I error—i.e. the false positive rate—is directly determined by the chosen level of significance. For a valid p-value it holds that $\mathbb{P}(p \leq \alpha \mid H_0) \leq \alpha$ for all $\alpha \in [0, 1]$. In other words, the probability of falsely rejecting the null hypothesis is smaller than or equal to α. For an exact p-value the false positive rate is exactly α. A type II error occurs in case of false negatives: the null hypothesis is kept, although the alternative hypothesis is true. Of note, the probability of a type II error depends on the sample size; with increasing sample size the sampling variation decreases and even small differences in the summary statistics can be attributed to truly existing effects instead of random noise.

The outcome of the test decision always depends on the chosen level of significance α, which usually affects the probabilities for a type I and type II error. Notably, lowering the chance for one error increases the other. The trade-off between the two errors is best visualized by a ROC (receiver operating characteristic) curve (**Figure 4**). In a ROC curve, the true positive rate (= 1 – false negative rate = sensitivity) of a test is plotted against the false positive rate (= 1 − true negative rate = 1 − specificity). A perfect binary classifier would yield a point in the top left corner (0, 1) of the ROC plot, corresponding to 100% sensitivity and 100% specificity. In general, however, a certain probability for either of the two types of errors in the classification remains. A classifier based on random guesses would yield a ROC curve given by the diagonal (*line of no discrimination*, indicated by the dashed line in **Figure 4**).

3 2-CLASTA

Often, the sampling distribution of the summary statistics under the null hypothesis is not known analytically. In our 2-CLASTA method, we create estimations of the summary statistics under the null hypothesis of a random biomolecular distribution directly from the recorded localization maps. For this, a toroidal shift is applied to one of the color channels (**Figures 5A,B**): All localizations are shifted by a random vector $\vec{v}$ and moved back into the regions of interest according to periodic boundary conditions. The toroidal shift breaks possible correlations between the two color channels while conserving the characteristics of the localization map of each individual channel. By repeating this procedure for randomly chosen shift vectors, a set of random control images can be generated on the computer which allows to calculate the corresponding CDFs of cross-nearest neighbor distances (**Figure 5C**). Each integral of these CDFs gives an estimate of the summary statistics. Typically, we calculated $n = 99$ toroidal shifts, yielding a good approximation of the sampling distribution of our summary statistics (**Figure 5D**).

Finally, the obtained value s_0 of the summary statistics for the original data is compared with the values s_i obtained for the sampling distribution under the null hypothesis. For the calculation of a p-value, all values of the set $\mathcal{S} := \{s_i \mid i = 0, \ldots, n\}$ are sorted in descending order and a rank is assigned to each value according to its position in the ordered sequence: A

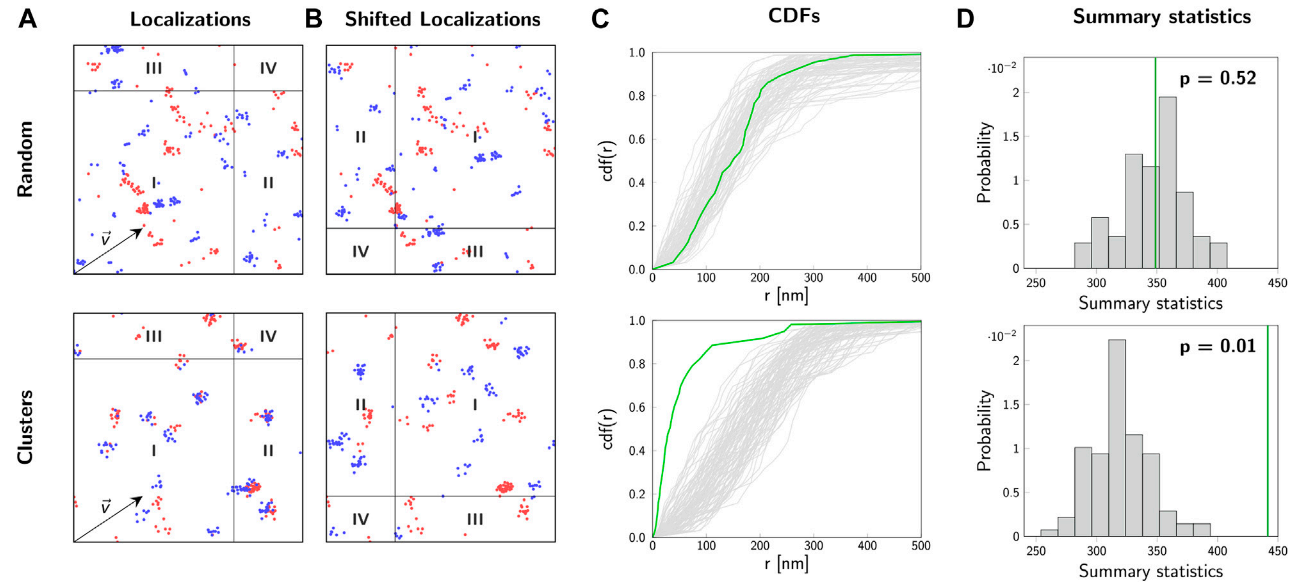

FIGURE 5 | 2-CLASTA method. Analysis of localization maps with 2-CLASTA. **(A)** Simulated two-color localization maps for a random (top) and a clustered (bottom) distribution of biomolecules. Images show a $2 \times 2\ \mu m^2$ region. For the simulation of blinking we used experimental data obtained for SNAP-AF488 (blue channel) and SNAP-AF647 (red channel). **(B)** Shifting all localizations of the blue color channel by the shift vector $\vec{v}$ breaks correlations between the two color channels. **(C)** The CDF of cross-nearest neighbor distances, r, between the two color channels is plotted in green for the localization data shown in panel **(A)**. The functions $\mathrm{cdf}_{\mathrm{rand}}(r)$ of $n = 99$ control curves, generated with randomly chosen toroidal shifts, are depicted in light gray. **(D)** As a summary statistics, the integral of the CDFs was calculated. Based on the rank of the summary statistics s_0 for the original data (green line), we calculated a p-value $p = 0.52$ for the random case, and $p = 0.01$ for the clustered case. Panels **(A–C)** adapted from (Arnold et al., 2020), CC BY 4.0 (https://creativecommons.org/licenses/by/4.0/).

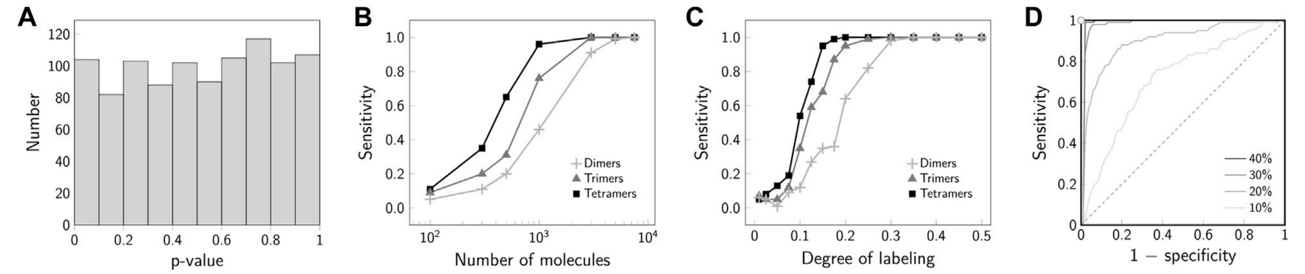

FIGURE 6 | Specificity and sensitivity of 2-CLASTA. **(A)** Specificity. The histogram of p-values shows a uniform distribution under the null hypothesis of a random biomolecular distribution. **(B)** Sensitivity for a varying number of observed molecules. Results are shown for simulations of dimers (**+**), trimers (**▲**) and tetramers (**■**). The sensitivity increases with a increasing number of observed molecules. **(C)** Sensitivity for varying degree of labeling. Results are shown for simulations of dimers (**+**), trimers (**▲**) and tetramers (**■**). For a degree of labeling above 30%, maximum sensitivity can be achieved. **(D)** ROC curves are plotted for simulations of dimers with a degree of labeling varying from 10% (light gray) to 40% (black). With increasing degree of labeling the discrimination power of the test increases, i.e., the ROC curve approaches the point of perfect classification in the top left corner. The gray dashed line indicates the line of no discrimination. The sensitivity for each parameter set was determined based on 100 independent simulations. Panels **(A–C)** adapted from (Arnold et al., 2020), CC BY 4.0 (https://creativecommons.org/licenses/by/4.0/).

value s_i has the rank j if it is the jth largest element; consequently, the largest value of the set has rank 1. Since we want to test the null hypothesis of a random distribution against the alternative hypothesis of nanoclustering, we are interested whether the original data shows a tendency towards shorter nearest neighbor distances. Deviations towards larger distances are not considered of importance here. Hence, we calculate

$$p = \frac{\mathrm{rank}\,(s_0, \mathcal{S})}{n+1}, \qquad (1)$$

where $\mathrm{rank}\,(s_0, \mathcal{S})$ denotes the descending rank of s_0 within the set $\mathcal{S}$. Under the null hypothesis the calculated values p show the expected uniform distribution in the interval [0, 1] (**Figure 6A**) and, hence, can be interpreted as right-sided p-values.

In order to perform the significance testing it is important now to select a significance level α. In the following, we chose $\alpha = 0.05$, equivalent to a 5% false rejection rate of the null hypothesis of a random biomolecular distribution. In our approach, the obtainable p-values are constraint to discrete values in the set $\{\frac{i}{n+1} \mid i = 1, \ldots, n+1\}$. It is hence important to ensure that $\alpha > \frac{1}{n+1}$.

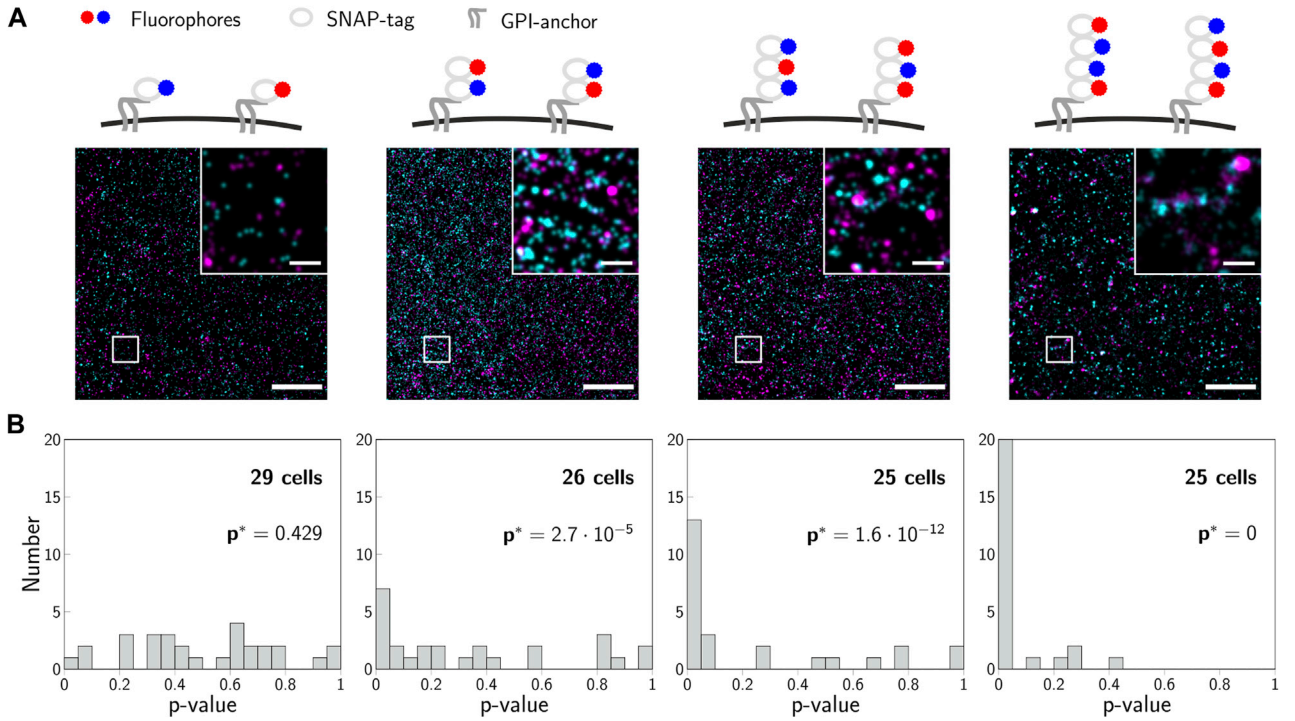

FIGURE 7 | Experimental validation of 2-CLASTA. **(A)** Illustrations and representative localization maps recorded for SNAP-monomers, -dimers, -trimers and -tetramers (left to right). Scale bars: 250 nm (inset) and 2 μm. **(B)** Histograms of *p*-values obtained for multiple recorded cells, which were analyzed individually with the 2-CLASTA method. For each SNAP construct, we also calculated the joint *p*-value p^* according to **Eq. 2**, with the threshold $p_0 = 0.05$. Panels **(B)** and **(C)** adapted from (Arnold et al., 2020), CC BY 4.0 (https://creativecommons.org/licenses/by/4.0/).

In the example shown in **Figure 5**, we obtained a *p*-value of 0.52 for the random biomolecular distribution (top row) and a *p*-value of 0.01 for the clustered scenario (bottom row). Our test hence yielded a correct test decision in both cases.

While the validity of a *p*-value is described by the correct rejection rate of the null hypothesis, its power is linked to the sensitivity for detecting aberrant scenarios. In the following, we give examples of the sensitivity of 2-CLASTA to detect biomolecular oligomers from dimers up to tetramers. As expected, the sensitivity strongly depends on the number of analyzed molecules within the region of interest (**Figure 6B**). This reflects the larger spread of the sampling distribution for small data sets (cf. **Figure 2**). For data sets containing more than 3000 molecules, the identification even of dimers works robustly with a sensitivity above 80%. In a biological experiment, it is difficult to achieve a degree of labeling of 100%. With decreasing degree of labeling, two-color colocalization will be out-diluted by apparent monomeric signals, which arise from underlabeled oligomers. **Figure 6C** shows that a degree of labeling of 30% is sufficient to reliable detect all analyzed cluster scenarios. The improved sensitivity for high degree of labeling is also apparent in the ROC plot (**Figure 6D**). While for 10% degree of labeling we obtained results close to the line of no discrimination, 40% degree of labeling approaches the point of perfect discrimination extremely well. Of note, we showed previously that minor chromatic aberrations hardly affect the analysis, as they do not break correlations between the two color channels [see Supplementary Figure S4 in (Arnold et al., 2020)]. If one desires to use a single dye only (e.g. due to its superior photophysical properties), one can perform an Exchange-PAINT experiment (Jungmann et al., 2014) with two different docking strands, which would then be taken as the two different channels in the 2-CLASTA analysis.

For a validation experiment, we previously generated concatamers of SNAP-tags fused to a GPI-anchor, which are located in the cellular plasma membrane (Arnold et al., 2020). The fusion-constructs were labeled with mixtures of blue and red substrates so that similar degrees of labeling were achieved for both colors (**Figure 7A**). For each construct, we recorded 2-color SMLM experiments on at least 25 cells, analyzed them according to the 2-CLASTA method and determined a *p*-value for each image (**Figure 7B**). The resulting histograms in the case of monomeric constructs yielded a rather uniform distribution, whereas all other constructs showed a substantial deviation from this uniform distribution, with an increased fraction of small *p*-values with increasing oligomer degree. Importantly, the rather small region of interest and suboptimal degree of labeling generally compromise sensitive identification of the presence of oligomers from a single experiment, yielding multiple experiments with an outcome above the significance threshold.

4 ACCOUNTING FOR MULTIPLE EXPERIMENTS

In order to assess the overall outcome of multiple experiments in a single joint statistical analysis, one straightforward option seems to be taking the minimum of all observed p-values as overall p-value and reject the null hypothesis if this minimum p-value is significant. However, this procedure is not valid as it drastically increases type I errors, i.e. the false positive rate. This can be seen from a simple example: For m independent experiments, the probability that none of the obtained p-values is significant under the null hypothesis can be calculated as $(1 - \alpha)^m$. For $m = 10$ experiments and a significance level of $\alpha = 0.05$, the probability to incorrectly obtain a significant result would be $1 - (1 - 0.05)^{10} = 0.4$, which is much higher than the significance level. This is also evident from the probability distribution of the minimum p-value. In case of a continuous p-value, the distribution of the minimum of m uniformly distributed values $p_{\min} = \min(p_1, \ldots, p_m)$ is not uniform but follows the probability density function $m(1 - p_{\min})^{m-1}$.

In order to adjust the overall p-value for m experiments, Wieser et al. (Wieser et al., 2008) suggested to apply the transformation function $p^\star = 1 - (1 - p_{\min})^m$, yielding a uniform distribution of $p^\star$ on the interval [0, 1]. However, in case of bootstrapping and Monte Carlo approaches the p-value is not continuously distributed, but can only take on discrete values $\frac{i}{n+1}$ for $i = 1, \ldots, n + 1$, where n is the number of bootstrapped or simulated control samples. Therefore, the lower bound of $p^\star$ is $1 - (\frac{n}{n+1})^m$, which approaches 1 for m approaching infinity. Hence, for a large number of experiments m the null hypothesis would never be rejected.

In case of discrete p-values we propose here a different method to adjust the p-value for multiple experiments. The p-values for single experiments then show a discrete uniform distribution under the null hypothesis given by $\mathbb{P}(p = \frac{i}{n+1}) = \frac{1}{n+1}$ for $i = 1, \ldots, n + 1$, where n is the number of simulated controls. In order to combine the p-values obtained from multiple experiments, we can determine whether the number of observed p-values below a user-defined threshold p_0 agrees with a discrete uniform distribution. Under the null hypothesis, the probability to obtain a p-value below or equal to the threshold p_0 in exactly k out of m experiments is given by a Binomial distribution $B(k \mid p_0, m)$.

Therefore, we can perform a Binomial test in order to determine whether the p-values obtained from m independent experiments agree with the null hypothesis. In general, one is interested in identifying significant results characterized by a high proportion of low p-values. Hence, a right-sided Binomial test of the null hypothesis is appropriate. The overall p-value $p^\star$ for multiple experiments is calculated as

$$p^\star = \mathbb{P}(X \geq k) = \sum_{i=k}^{m} B(i \mid p_0, m) = \sum_{i=k}^{m} \binom{m}{i} p_0^i (1 - p_0)^{m-i}$$

$$= 1 - \sum_{i=0}^{k-1} \binom{m}{i} p_0^i (1 - p_0)^{m-i}, \tag{2}$$

where k is the number of observed p-values below the chosen threshold p_0, and m the number of performed experiments. If $p^\star$ is smaller than the chosen level of significance $\alpha^\star$ for the joint analysis of experiments, the null hypothesis is rejected.

The increase in sensitivity for the joint analysis of multiple 2-CLASTA analyses compared to a single experiment is shown in **Figure 8A**. For this, dimers were simulated with varying labeling efficiency, assuming a 1 : 1 label ratio between the two colors. A joint analysis of 25 or 50 simulated experiments yielded a drastic increase of the sensitivity compared to the analysis of a single experiment only. Interestingly, the method is very robust with regard to the chosen threshold p_0 (**Figure 8B**). As expected, the higher the number of analyzed experiments, the higher is the sensitivity of the method. Also in the ROC plot we observed a strongly improved performance that approaches the ideal test (**Figure 8C**). The proposed joint analysis of all performed experiments was also applied to the experimental results obtained on the SNAP constructs from our previous paper (Arnold et al., 2020). The calculated overall p-values for multiple experiments are indicated as $p^\star$ in **Figure 7B**. As anticipated, the null hypothesis of a random protein distribution was not rejected for the monomeric 1-SNAP construct. For all the oligomeric constructs representing dimers, trimers and tetramers, the null hypothesis was rejected and the biomolecular distribution was correctly identified as clustered.

5 SINGLE PARTICLE TRAJECTORIES

As a final example, we will discuss here the application of significance tests to the analysis of single particle trajectories. In practice, such trajectories suffer from a limited observation time due to restrictions in the overall imaging experiments, diffusion of the molecule out of the region of interest, or photobleaching of the fluorescence marker molecules. In the following, we present a guideline how to compare sets of single particle trajectories recorded under two different conditions A and B via permutation tests (Good, 2000).

Figure 9 shows the typical workflow of such a test approach. All data points recorded under condition A and B are combined, yielding the average values μ_A for sample A and μ_B for sample B, respectively. We choose here as summary statistics the difference $s_0 = \mu_A - \mu_B$. One may use as a realization of the null hypothesis, i.e., no difference between the sample A and B, a random splitting of the combined data sets in two new subsamples A_i and B_i each containing the same amount of data points as the original samples A and B. For each permutation, a new sample statistics $s_i = \mu_{A_i} - \mu_{B_i}$ is calculated. Finally, s_0 is compared with the sampling distribution of all obtained values of s_i. The p-value is obtained via the rank of s_0 as described in **Section 3**, **Eq. 1**.

To evaluate this approach, we simulated representative single molecule trajectories, consisting of a time series of a recorded parameter $E(t)$. This could be the FRET efficiency in a single molecule FRET experiment, the size of displacement steps in a single particle tracking experiment, the excited state lifetime in a spectroscopic experiment, to name a few. Representative trajectories for this evaluation are shown in **Figure 9A**.

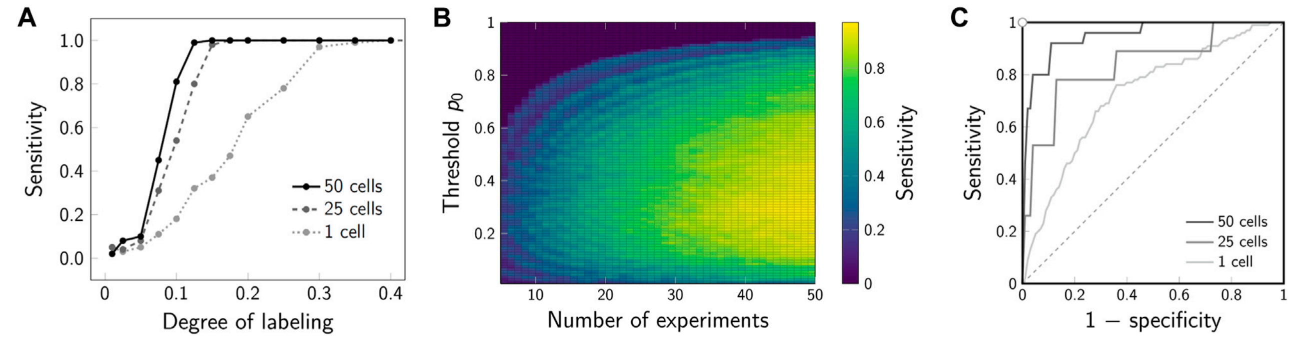

FIGURE 8 | Sensitivity for joint analysis of multiple experiments. **(A)** Sensitivity for varying degree of labeling. Dimers were simulated and analyzed with 2-CLASTA. The sensitivity for analysis of a single experiment is shown by the dotted line. The sensitivity in case of joint analysis of 25 and 50 cells is shown by the dashed and solid lines, respectively; a threshold of $p_0 = 0.05$ was chosen. **(B)** Influence of the threshold p_0 and the number of experiments on the sensitivity. The obtained sensitivity is indicated by color. **(C)** ROC plot for joint analysis of multiple experiments. For the simulations in panels B and D, the degree of labeling was set to 10%. Sensitivity was calculated from 100 simulation runs; the level of significance was set to $\alpha^* = 0.05$.

To verify the validity of this approach for calculating a correct *p*-value, we plotted the distribution of obtained *p*-values under the null hypothesis for thousand repetitions of this hypothetical experiment. As discussed in **Figure 6A**, a valid *p*-value has to show a uniform distribution under the null hypothesis. Interestingly, in our case we observed massive deviations from such a uniform distribution, with a strong peak for small *p*-values (**Figure 10D**). When applied to a significance test, the experimenter would hence incorrectly reject the null hypothesis too often.

To understand the reason for this incorrect judgement, let us have a closer look on the single molecule trajectories. In our case, we did not assign binary values to a time series randomly, but instead we considered states with a specific duration characterized by transition rate constants. In consequence, the data used for the sampling distribution are not independent, thereby violating a basic assumptions of most significance testing approaches.

To solve this problem, we used a block permutation test approach. In this approach, the trajectories recorded in the samples *A* and *B* are not split, but instead kept together for the permutations performed in step *C* in **Figure 9**. This approach correctly accounts for the correlations in the trajectories when generating the permuted samples A_i and B_i. Indeed, application of this approach leads to uniform distribution of the *p*-value under the null hypothesis (**Figure 10E**).

We applied the new method to experimental data recorded previously in our lab, which shows the analysis of single molecule FRET trajectories of a molecular force sensor (Göhring et al., 2021). Briefly, T-cells were seeded on a glass supported lipid bilayer, which was functionalized by specific proteins to activate the T-cells. One of these proteins was a force sensor, carrying a spider silk spring element, which connected a membrane anchoring motive with a specific ligand to the T-cell receptor on the T-cell surface. A donor and an acceptor fluorophore were conjugated to the spider silk region and used for reading out the elongation of this spring element via single molecule FRET, which was eventually used to calculate forces. For each experimental run, two different conditions were recorded: Condition *A* (orange) corresponding to the FRET signal of the force sensor without T-cells, and condition *B* (blue) corresponding to the FRET signal recorded in the synapse between the T-cell and the supported lipid bilayer (**Figure 11**).

When using a gel-phase lipid bilayer, we observed a clear difference between the two conditions corroborated by a highly significant *p*-value. In contrast, fluid-phase bilayers yielded similar results when comparing the two conditions. The block permutation test yielded $p = 0.205$, and hence, no significant deviation from the null hypothesis for a chosen significance level of $\alpha = 0.01$. Of note, the simple permutation test not accounting for correlations would have yielded a *p*-value of $p = 0.004$, and hence, would have indicated a significant difference between the two samples.

6 DISCUSSION

Calculating a *p*-value can be very useful for researchers in order not to be fooled by random chance. Random variations often lead to outcomes that can easily be misinterpreted as interesting patterns. The *p*-value allows to quantitatively assess whether an observed effect likely occurred due to random chance alone or whether it is worth to study the effect in more detail. As an example, SMLM experiments on cellular proteins often revealed notable deviations from a random distribution of localizations (Lillemeier et al., 2010; Rossy et al., 2013). When analyzed via cluster detection methods such as Ripley's K function, DBSCAN or modified versions of it (Ripley, 1977; Ester et al., 1996; Rubin-Delanchy et al., 2015), one would arrive at the conclusion of biomolecular clustering in the sample of interest. More elaborate analysis allowed to include the aspect of overcounting due to the inherent blinking processes in SMLM (Annibale et al., 2011; Sengupta et al., 2011; Baumgart et al., 2016; Rossboth et al., 2018; Bohrer et al., 2021), putting some of these clusters into question.

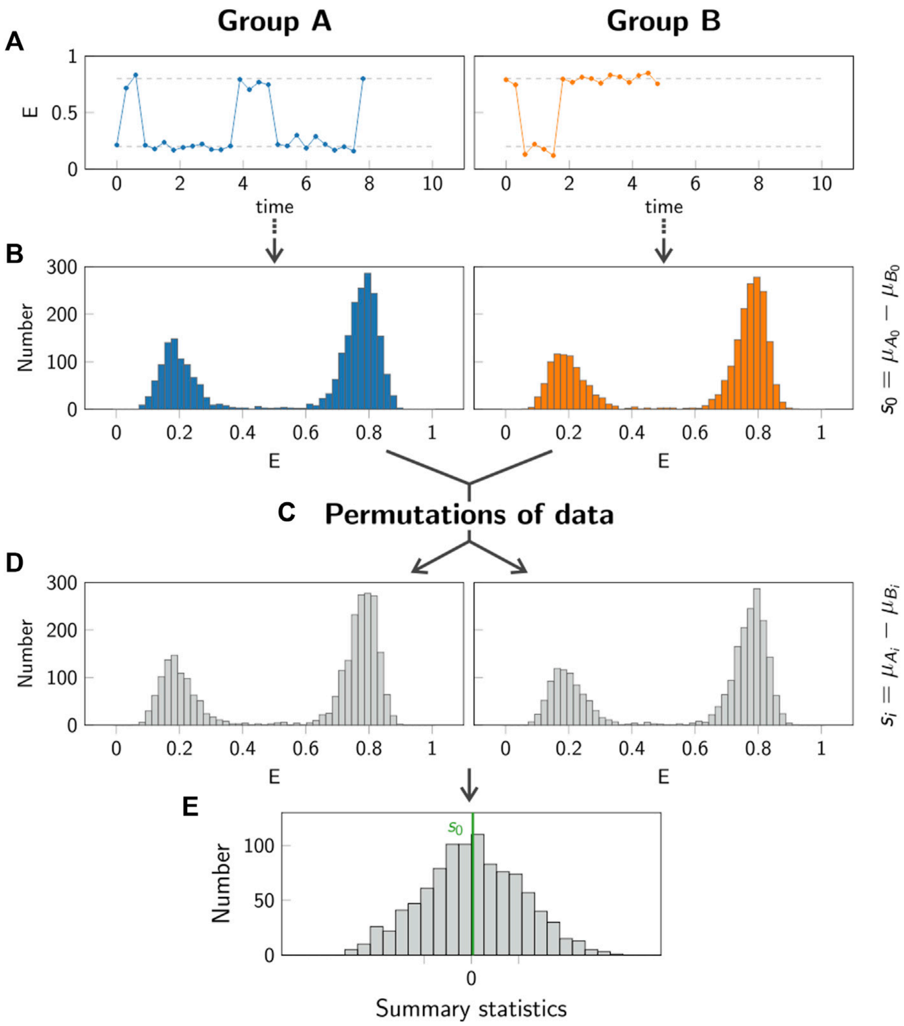

FIGURE 9 | Principle of permutation test. In the permutation test, the group *A* (left column, blue) is compared to the group *B* (right column, orange). Step **(A)**: Individual single molecule trajectories are recorded for both groups *A* and *B*. Step **(B)**: The data obtained from all trajectories in each group is pooled. The summary statistics s_0 is calculated in order to compare the two groups. Step **(C,D)**: Random permutations of the data in the two groups are generated, yielding new samples A_i and B_i. For each permutation, the summary statistics s_i is calculated. Step **(E)**: The *p*-value is obtained by comparing the value s_0 (green line) to the values s_i obtained for 1000 permutations.

But also the application of these refined methods is not straight forward as it requires either the adjustment of user-defined parameters, or the recording of single molecule blinking traces.

In this paper, we proposed a different approach towards such problems. Our idea is not a direct quantitative interpretation of the data, but a statistical assessment of hypotheses (Baddeley and Bewersdorf, 2018). If one opts for such an approach, two issues need to be considered:

(i) Which hypothesis describes the problem most appropriately? In an SMLM experiment a typical example for the null hypothesis would be: *The spatial distribution of detected localizations agrees with a random point pattern.* Due to overcounting this hypothesis will likely be rejected in most data sets. A modified hypothesis may thus be: *The spatial biomolecular distribution agrees with a random point pattern.* We addressed this hypothesis in **Section 3** of this paper. If also this hypothesis is rejected, one may opt for coming up with more precise hypotheses about the lateral extension of the biomolecular clusters and the degree of clustering. The result of such an approach will hence be rather similar to the classical quantitative approaches; its advantage is that it additionally provides a *p*-value. We previously used such a strategy to test experimental results against thousands of quantitatively well-defined hypotheses to analyze single molecule tracking data (Wieser et al., 2008; Axmann et al., 2012) and FRET recordings (Schrangl et al., 2018).

(ii) How can we derive a *p*-value to test the null hypothesis? Here, the major limitation comes from the fact that the underlying sampling distribution of the summary statistics is typically unknown. In principle, one could derive such a sampling distribution analytically or generate it on the computer. The

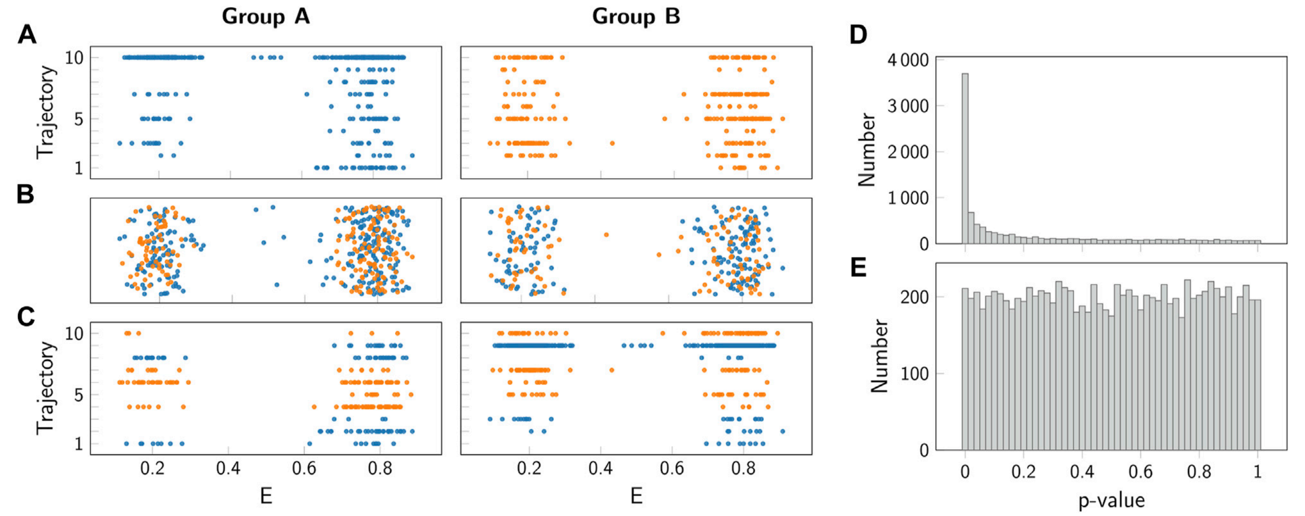

FIGURE 10 | Comparison of permutation test and block permutation test. **(A)** Representative simulated FRET efficiencies for 10 simulated trajectories of group *A* (left, blue) and *B* (right, orange). Both groups were simulated using the same parameters (see **Section 7**). **(B)** Representative random permutation of the data from panel **(A)**. **(C)** Representative block permutation of the data from panel **(A)**. Here, data from individual trajectories is kept together. **(D,E)** Histogram of *p*-values obtained for the standard permutation test panel **(D)** and the block permutation test panel **(E)**. As a test summary statistics the difference between the means of the groups *A* and *B* was taken. As both groups were simulated using the same parameters, the null hypothesis of no difference between the groups was fulfilled. Importantly, only the block permutation test provides a uniform distribution and hence a valid *p*-value.

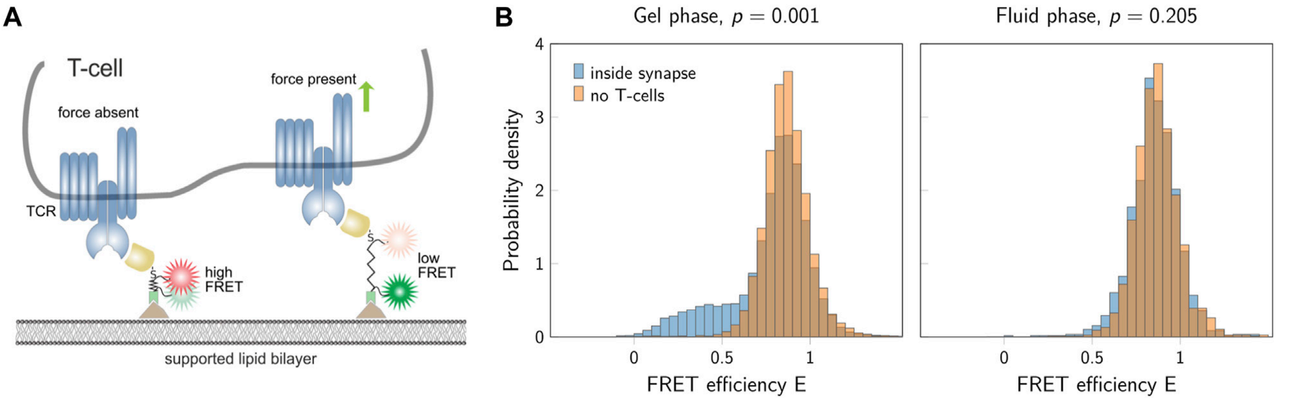

FIGURE 11 | FRET data from T-cell experiments. **(A)** Sketch of a T-cell and the force sensor. If no force is applied, the sensor shows a high FRET signal (left). In the presence of forces, a low FRET signal is detected (right). **(B)** FRET efficiencies for a gel-phase bilayer (left) and a fluid-phase bilayer (right). The two histograms show data inside the T-cell synapse (blue) and in the absence of T-cells (orange). The *p*-values indicated in the figure are the results of the block permutation test. The standard permutation test would yield a *p*-value of 0.001 and 0.004 for the gel- and fluid-phase bilayer, respectively. Figure adapted from (Göhring et al., 2021), CC BY 4.0 (https://creativecommons.org/licenses/by/4.0/).

drawback of it is that additional experiments are required to obtain the molecular parameters describing the behavior of the single fluorophores (Platzer et al., 2020). We opted here for a different approach, which makes use of the experimental data themselves: In case of 2-CLASTA (**Section 3**), a toroidal shift was used for reassigning molecular positions in one of the two color channels, which allowed to calculate a set of computer-generated control samples representing the null hypothesis of the absence of correlations between the two color channels. In case of the single particle tracking experiments (**Section 5**), the problem was different: Now, correlations present in the data had to be correctly accounted for also in the computer-generated control samples. We achieved this using a block permutation strategy.

It should be noted that the *p*-value and significance testing have recently become an issue of dispute. A variety of articles and comments have been published, both arguing for and against the validity of *p*-values (Halsey et al., 2015; Lazzeroni et al., 2016;

Altman and Krzywinski, 2017; Amrhein et al., 2019; Lakens, 2021). This is mainly due to misinterpretations of how to correctly interpret *p*-values. In 2016, the American Statistical Association released a statement addressing several misconceptions about the *p*-value (Wasserstein and Lazar, 2016).

Importantly, the *p*-value is not the probability that the null hypothesis is true, but rather indicates how compatible the observed data are with the null hypothesis. In other words, a rejection of the null hypothesis does not prove that the null hypothesis is false: The null hypothesis could still be true, but instead a very unlikely event occurred. Vice versa, not rejecting the null hypothesis does not prove its truth. Strictly speaking, a non-significant test result has no relevance at all.

The test decision always depends on the chosen level of significance, which usually affects the probabilities for a type I and type II error. Notably, lowering the chance for one error increases the other, and a certain probability for either error always remains. Hence, an outcome of a test should never be taken as a proof for *proving* a hypothesis.

One major issue is known as *fishing for* p*-values*. In case of a true null hypothesis, there is still a certain probability to obtain a significant *p*-value. For one single hypothesis test, this probability corresponds to the level of significance α. If one conducts multiple experiments and performs a hypothesis test for each, the probability to obtain a significant *p*-value is given by $1 - (1 - \alpha)^m$, where m denotes the number of experiments. Evidently, $1 - (1 - \alpha)^m$ approaches 1 for large values of m, i.e. for a large number of experiments, one will obtain by chance a significant *p*-value with high probability.

As *p*-values have been controversial, the use of alternatives such as estimation statistics and confidence intervals have been encouraged (Claridge-Chang and Assam, 2016). A confidence interval is an interval estimate for an unknown parameter. It is always associated with a certain confidence level, which corresponds to the percentage of confidence intervals containing the true parameter. Nevertheless, both *p*-values and confidence intervals are based on the same statistical theories. Inferences about statistical significance based on either are directly linked: If a *p*-value is smaller than the level of significance α, the $1 - \alpha$ confidence interval will not include the null hypothesis value. Vice versa, if the $1 - \alpha$ confidence interval does not include the null hypothesis value, the *p*-value will be smaller than α.

In conclusion, as long as random variability is involved, no effect can be strictly proven merely based on a (small) sample of observations alone. Scientific conclusions must not merely be based on whether a *p*-value passes a user-set threshold without any other supporting evidence or reasoning. Moreover, also a true but possibly small difference might be of no essential practical importance. In general, it is necessary that researchers are aware of what statistical significance testing really means in order not to misuse it. Merely replacing the *p*-value with other methods will not solve the problem, but rather only shift it (Verhulst, 2016; Lakens, 2021). Particularly, completely abolishing any assessment of statistical significance poses the risk of researchers being fooled by random chance.

7 METHODS

7.1 2-CLASTA

7.1.1 Simulations

Simulations were performed as described previously (Arnold et al., 2020). In short, the underlying distribution of biomolecules was simulated on a region of interest of $10 \times 10 \mu m^2$. For the simulation of dimers, two biomolecules were assigned to each dimer position. Subsequently, two different types of labels were assigned randomly and competitively to the simulated molecules according to the specified label ratio. For simulation of blinking, a random number of detections was assigned to each label according to blinking statistics determined previously for SNAP-AF647 and SNAP-AF488 (Arnold et al., 2020). Next, the localization coordinates were displaced by random localization errors, which were distributed normally with mean 0 and standard deviation according to the localization precision of 30 nm. Further, to account for experimental errors we included 5 unspecifically bound labels per μm^2 in each color channel. In addition, we added a background of 1 and 2 signals per μm^2 for the red and blue color channel, respectively. Background signals were simulated with blinking statistics obtained previously from unlabeled cells (Arnold et al., 2020). If not mentioned otherwise, we used the following parameters: 75 molecules per μm^2, 40% degree of labeling and 1:1 label ratio. All simulations were carried out in MATLAB (R2019b, The MathWorks Inc., Natick, MA) on a standard personal computer.

7.1.2 Calculation of *p*-Value for Multiple Experiment

The overall *p*-value p^* for multiple experiments was calculated as $p^* = 1 - \sum_{i=1}^{k-1} \binom{m}{i} p_0^i (1 - p_0)^{m-i}$, where m is the number of performed experiments, k the number of observed *p*-values smaller or equal to the threshold p_0, and $\binom{m}{i}$ denotes the Binomial coefficient. If not stated otherwise, the level of significance for the joint analysis of *p*-values was set to $\alpha^* = 0.05$. As input for the calculation we used the *p*-values derived in (Arnold et al., 2020).

7.2 Single Particle Trajectories

7.2.1 Simulation of FRET Trajectories

Simulations were performed as described previously (Schrangl et al., 2018). In short, we first simulated a ground truth state transition trajectory. Here, a two-state model was simulated, characterized by the FRET efficiencies $E_1 = 0.2$ and $E_2 = 0.8$ for the two states. Stochastic transitions between the two states were simulated based on the lifetimes $\tau_1 = 2$ and $\tau_2 = 4$ for state 1 and 2, respectively. Subsequently, the state transition trajectory was sampled with finite time resolution according to the exposure time $t_{\text{ex}} = 0.1$ and a delay time $t_{\text{del}} = 0.2$. All times are given in arbitrary units. For simulation of the fluorescence signal, the donor brightness $d(t_i)$ and acceptor brightness $a(t_i)$ at each time point t_i were randomly drawn from a lognormal distribution with mean values $m_{\mathrm{don}}(t_i) = n_{\mathrm{phot}}(1 - e(t_i))$ and $m_{\mathrm{acc}}(t_i) = n_{\mathrm{phot}}e(t_i)$, respectively, where $e(t_i) = (\sum_i t_i E_i)/t_{\mathrm{ex}}$ denotes the apparent FRET efficiency and $n_{\mathrm{phot}} = 200$ the average number of emitted photons (sum of donor and acceptor fluorophores). The standard deviation σ of the lognormal distribution was calculated via $\sigma = 0.3\ \mathrm{m} - 13.61$ for the donor, and $\sigma = 0.3\ \mathrm{m} - 1.92$ for the acceptor, following values determined previously for the fluorophores AF555 and AF647 (Schrangl et al., 2018). The final FRET efficiency was calculated as $E = \frac{a}{d+a}$. For each simulation run, we simulated 100 trajectories for each group. The lengths of the trajectories was distributed randomly according to a lognormal distribution with a mean of 27.1 and a standard deviation of 35.5. All simulations were carried out in Python on a standard personal computer.

7.2.2 Permutation Test

We compared two groups A and B and assessed whether they originated from the same distribution, i.e. the null hypothesis. First, the summary statistics s_0 was calculated for the original samples A_0 and B_0 with sample size n_A and n_B, respectively. As a summary statistics, we used the difference between the mean of the two samples, i.e. $s_0 = \mu_{A_0} - \mu_{B_0}$. Second, the data from the two samples was pooled to form the set $M \coloneqq A \cup B$. Next, permutations of the data were created, i.e. the set M was split into new samples A_i and B_i. For the standard permutation test, all data points were assigned randomly to one of the two groups. The size of the new samples was n_A and n_B, respectively. For the block permutation test, data from individual trajectories were kept together, but each trajectory was randomly assigned to one of the new groups A_i or B_i. Both groups contained 100 trajectories. For each random permutation $i = 1, \ldots, 1000$ of the data, the summary statistics $s_i = \mu_{A_i} - \mu_{B_i}$ was calculated. Finally, The two sided p-value was calculated as the proportion of generated permutations for which the absolute difference $|s_i|$ was greater than the value $|s_0|$ observed for the original data.

AUTHOR CONTRIBUTIONS

Both authors conceived and wrote the manuscript, and approved it for publication.

FUNDING

This work was supported by the Austrian Science Fund with project number F 6809-N36 (GS).

REFERENCES

Altman, N., and Krzywinski, M. (2017). Interpreting P Values. *Nat. Methods* 14, 213–214. doi:10.1038/nmeth.4210

Amrhein, V., Greenland, S., and McShane, B. (2019). Scientists Rise up against Statistical Significance. *Nature* 567, 305–307. doi:10.1038/d41586-019-00857-9

Annibale, P., Vanni, S., Scarselli, M., Rothlisberger, U., and Radenovic, A. (2011). Quantitative Photo Activated Localization Microscopy: Unraveling the Effects of Photoblinking. *PLoS One* 6, e22678. doi:10.1371/journal.pone.0022678

Arnold, A. M., Schneider, M. C., Hüsson, C., Sablatnig, R., Brameshuber, M., Baumgart, F., et al. (2020). Verifying Molecular Clusters by 2-color Localization Microscopy and Significance Testing. *Sci. Rep.* 10, 4230. doi:10.1038/s41598-020-60976-6

Axmann, M., Huppa, J. B., Davis, M. M., and Schütz, G. J. (2012). Determination of Interaction Kinetics between the T Cell Receptor and Peptide-Loaded MHC Class II via Single-Molecule Diffusion Measurements. *Biophys. J.* 103, L17–L19. doi:10.1016/j.bpj.2012.06.019

Baddeley, D., and Bewersdorf, J. (2018). Biological Insight from Super-resolution Microscopy: What We Can Learn from Localization-Based Images. *Annu. Rev. Biochem.* 87, 965–989. doi:10.1146/annurev-biochem-060815-014801

Baumgart, F., Arnold, A. M., Leskovar, K., Staszek, K., Fölser, M., Weghuber, J., et al. (2016). Varying Label Density Allows Artifact-free Analysis of Membrane-Protein Nanoclusters. *Nat. Methods* 13, 661–664. doi:10.1038/nmeth.3897

Bohrer, C. H., Yang, X., Thakur, S., Weng, X., Tenner, B., McQuillen, R., et al. (2021). A Pairwise Distance Distribution Correction (DDC) Algorithm to Eliminate Blinking-Caused Artifacts in SMLM. *Nat. Methods* 18, 669–677. doi:10.1038/s41592-021-01154-y

Claridge-Chang, A., and Assam, P. N. (2016). Estimation Statistics Should Replace Significance Testing. *Nat. Methods* 13, 108–109. doi:10.1038/nmeth.3729

Ester, M., Kriegel, H. P., Sander, J., and Xu, X. (1996). A Density-Based Algorithm for Discovering Clusters in Large Spatial Databases with Noise. *Kdd* 96, 226–231.

Garcia-Parajo, M. F., Cambi, A., Torreno-Pina, J. A., Thompson, N., and Jacobson, K. (2014). Nanoclustering as a Dominant Feature of Plasma Membrane Organization. *J. Cel. Sci.* 127, 4995–5005. doi:10.1242/jcs.146340

Göhring, J., Kellner, F., Schrangl, L., Platzer, R., Klotzsch, E., Stockinger, H., et al. (2021). Temporal Analysis of T-Cell Receptor-Imposed Forces via Quantitative Single Molecule FRET Measurements. *Nat. Commun.* 12, 2502. doi:10.1038/s41467-021-22775-z

Good, P. (2000). *Permutation Tests: A Practical Guide to Resampling Methods for Testing Hypotheses*. New York: Springer.

Goyette, J., Nieves, D. J., Ma, Y., and Gaus, K. (2019). How Does T Cell Receptor Clustering Impact on Signal Transduction? *J. Cel. Sci.* 132, jcs226423. doi:10.1242/jcs.226423

Halsey, L. G., Curran-Everett, D., Vowler, S. L., and Drummond, G. B. (2015). The Fickle P Value Generates Irreproducible Results. *Nat. Methods* 12, 179–185. doi:10.1038/nmeth.3288

Jungmann, R., Avendaño, M. S., Woehrstein, J. B., Dai, M., Shih, W. M., and Yin, P. (2014). Multiplexed 3D Cellular Super-resolution Imaging with DNA-PAINT and Exchange-PAINT. *Nat. Methods* 11, 313–318. doi:10.1038/nmeth.2835

Lakens, D. (2021). The Practical Alternative to the P Value Is the Correctly Used P Value. *Perspect. Psychol. Sci.* 16, 639–648. doi:10.1177/1745691620958012

Lazzeroni, L. C., Lu, Y., and Belitskaya-Lévy, I. (2016). Solutions for Quantifying P-Value Uncertainty and Replication Power. *Nat. Methods* 13, 107–108. doi:10.1038/nmeth.3741

Lelek, M., Gyparaki, M. T., Beliu, G., Schueder, F., Griffié, J., Manley, S., et al. (2021). Single-Molecule Localization Microscopy. *Nat. Rev. Methods Primers* 1, 1–27. doi:10.1038/s43586-021-00038-x

Lillemeier, B. F., Mörtelmaier, M. A., Forstner, M. B., Huppa, J. B., Groves, J. T., and Davis, M. M. (2010). TCR and LAT Are Expressed on Separate Protein Islands on T Cell Membranes and Concatenate during Activation. *Nat. Immunol.* 11, 90–96. doi:10.1038/ni.1832

Platzer, R., Rossboth, B. K., Schneider, M. C., Sevcsik, E., Baumgart, F., Stockinger, H., et al. (2020). Unscrambling Fluorophore Blinking for Comprehensive Cluster Detection via Photoactivated Localization Microscopy. *Nat. Commun.* 11, 4993. doi:10.1038/s41467-020-18726-9

Ripley, B. D. (1977). Modelling Spatial Patterns. *J. R. Stat. Soc. Ser. B (Methodol.)* 39, 172–192. doi:10.1111/j.2517-6161.1977.tb01615.x

Rossboth, B., Arnold, A. M., Ta, H., Platzer, R., Kellner, F., Huppa, J. B., et al. (2018). TCRs Are Randomly Distributed on the Plasma Membrane of Resting Antigen-Experienced T Cells. *Nat. Immunol.* 19, 821–827. doi:10.1038/s41590-018-0162-7

Rossy, J., Owen, D. M., Williamson, D. J., Yang, Z., and Gaus, K. (2013). Conformational States of the Kinase Lck Regulate Clustering in Early T Cell Signaling. *Nat. Immunol.* 14, 82–89. doi:10.1038/ni.2488

Roy, R., Hohng, S., and Ha, T. (2008). A Practical Guide to Single-Molecule FRET. *Nat. Methods* 5, 507–516. doi:10.1038/nmeth.1208

Rubin-Delanchy, P., Burn, G. L., Griffié, J., Williamson, D. J., Heard, N. A., Cope, A. P., et al. (2015). Bayesian Cluster Identification in Single-Molecule Localization Microscopy Data. *Nat. Methods* 12, 1072–1076. doi:10.1038/nmeth.3612

Schermelleh, L., Ferrand, A., Huser, T., Eggeling, C., Sauer, M., Biehlmaier, O., et al. (2019). Super-resolution Microscopy Demystified. *Nat. Cel. Biol.* 21, 72–84. doi:10.1038/s41556-018-0251-8

Schrangl, L., Göhring, J., and Schütz, G. J. (2018). Kinetic Analysis of Single Molecule FRET Transitions without Trajectories. *J. Chem. Phys.* 148, 123328. doi:10.1063/1.5006038

Schütz, G. J., and Schneider, M. C. (2021). *Single Molecule Localization Microscopy (SMLM)*. Bristol, UK: IOP Publishing. doi:10.1088/978-0-7503-3059-6ch18

Sengupta, P., Jovanovic-Talisman, T., Skoko, D., Renz, M., Veatch, S. L., and Lippincott-Schwartz, J. (2011). Probing Protein Heterogeneity in the Plasma Membrane Using PALM and Pair Correlation Analysis. *Nat. Methods* 8, 969–975. doi:10.1038/nmeth.1704

Shine, L. C. (1980). The Fallacy of Replacing an A Priori Significance Level with an A Posteriori Significance Level. *Educ. Psychol. Meas.* 40, 331–335. doi:10.1177/001316448004000207

Sigal, Y. M., Zhou, R., and Zhuang, X. (2018). Visualizing and Discovering Cellular Structures with Super-resolution Microscopy. *Science* 361, 880–887. doi:10.1126/science.aau1044

Verhulst, B. (2016). In Defense of P Values. *AANA J.* 84, 305–308.

Wasserstein, R. L., and Lazar, N. A. (2016). The ASA Statement on P-Values: Context, Process, and Purpose. *Am. Stat.* 70, 129–133. doi:10.1080/00031305.2016.1154108

Wieser, S., and Schütz, G. J. (2008). Tracking Single Molecules in the Live Cell Plasma membrane-Do's and Don't's. *Methods* 46, 131–140. doi:10.1016/j.ymeth.2008.06.010

Wieser, S., Axmann, M., and Schütz, G. J. (2008). Versatile Analysis of Single-Molecule Tracking Data by Comprehensive Testing against Monte Carlo Simulations. *Biophys. J.* 95, 5988–6001. doi:10.1529/biophysj.108.141655

Conflict of Interest: The authors declare that the research was conducted in the absence of any commercial or financial relationships that could be construed as a potential conflict of interest.

frontiers in Bioinformatics

METHODS
published: 04 March 2022
doi: 10.3389/fbinf.2022.813494

Multi-Dimensional Spectral Single Molecule Localization Microscopy

Corey Butler[1,2], G Ezequiel Saraceno[1], Adel Kechkar[3], Nathan Bénac[1], Vincent Studer[1], Julien P. Dupuis[1], Laurent Groc[1], Rémi Galland[1]* and Jean-Baptiste Sibarita[1]*

[1]Univ. Bordeaux, CNRS, Interdisciplinary Institute for Neuroscience, IINS, UMR 5297F-33000, F-33000, Bordeaux, France, [2]Imagine Optic, Orsay, France, [3]Ecole Nationale Supérieure de Biotechnologie, Laboratoire de Bioengineering, Constantine, El Khroub, Algeria

Single molecule localization (SML) and tracking (SPT) techniques, such as (spt)PALM, (u/DNA)PAINT and quantum dot tracking, have given unprecedented insight into the nanoscale molecular organization and dynamics in living cells. They allow monitoring individual proteins with millisecond temporal resolution and high spatial resolution (<30 nm) by precisely localizing the point spread function (PSF) of individual emitters and tracking their position over time. While SPT methods have been extended to study the temporal dynamics and co-organization of multiple proteins, conventional experimental setups are restricted in the number of proteins they can probe simultaneously and usually have to tradeoff between the number of colors, the spatio-temporal resolution, and the field of view. Yet, localizing and tracking several proteins simultaneously at high spatial and temporal resolution within large field of views can provide important biological insights. By employing a dual-objective spectral imaging configuration compatible with live cell imaging combined with dedicated computation tools, we demonstrate simultaneous 3D single particle localization and tracking of multiple distinct species over large field of views to be feasible without compromising spatio-temporal resolution. The dispersive element introduced into the second optical path induces a spectrally dependent displacement, which we used to analytically separate up to five different fluorescent species of single emitters based on their emission spectra. We used commercially available microscope bodies aligned one on top of the other, offering biologists with a very ergonomic and flexible instrument covering a broad range of SMLM applications. Finally, we developed a powerful freely available software, called PALMTracer, which allows to quantitatively assess 3D + t + λ SMLM data. We illustrate the capacity of our approach by performing multi-color 3D DNA-PAINT of fixed samples, and demonstrate simultaneous tracking of multiple receptors in live fibroblast and neuron cultures.

Keywords: single molecule localization, single particle tracking, spectral imaging, multi-emitter fitting, live cell imaging

Edited by:
Thomas Pengo,
University of Minnesota Twin Cities,
United States

Reviewed by:
Ke Xu,
University of California, Berkeley,
United States
Hanieh Mazloom-Farsibaf,
University of Texas Southwestern
Medical Center, United States

***Correspondence:**
Rémi Galland
remi.galland@u-bordeaux.fr
Jean-Baptiste Sibarita
jean-baptiste.sibarita@
u-bordeaux.fr

Specialty section:
This article was submitted to
Computational BioImaging,
a section of the journal
Frontiers in Bioinformatics

Received: *11 November 2021*
Accepted: *12 January 2022*
Published: *04 March 2022*

Citation:
Butler C, Saraceno GE, Kechkar A,
Bénac N, Studer V, Dupuis JP, Groc L,
Galland R and Sibarita J-B (2022)
Multi-Dimensional Spectral Single
Molecule Localization Microscopy.
Front. Bioinform. 2:813494.
doi: 10.3389/fbinf.2022.813494

1 INTRODUCTION

Single Molecule Localization Microscopy (SMLM) relies on the optical- (Betzig et al., 2006; Rust et al., 2006; Heilemann et al., 2008) or binding-induced (Jungmann et al., 2014) spatial isolation and computational localization of individual fluorophores attached to a protein of interest. It provides unprecedented biological insight into the nanoscale organization and dynamics of biomolecules, and has allowed major discoveries in cell biology and neuroscience (Choquet et al., 2021; Lelek et al., 2021). The combined analysis of molecular clustering and diffusive properties, known as SPT, allows to identify the organization of a population of a protein of interest with nanometric resolution and single molecule sensitivity (Cognet et al., 2014; Sibarita, 2014), opening up the potential to infer their interactions with other partner proteins. However, SMLM, as any light microscopy technique, suffers from an inherent trade-off between spatial, temporal and spectral resolutions. The localization accuracy, ie. the precision with which the spatial coordinates of a single emitter can be retrieved, scales with $\sqrt{N}$, N being the number of detected photons above the background per single molecule event (Thompson et al., 2002). It determines the ultimate spatial resolution that can be achieved and defines the minimum displacement that can be distinguished between consecutive frames. As a consequence, collecting and analyzing multicolor 3D SMLM data remains a very challenging problem, where the light collected from single molecules must be allocated to specific dimensions, resulting in an inherent need to sacrifice certain dimensions for others. More specifically, imaging several species with single molecule resolution requires either sacrificing time by imaging each species sequentially, or localization precision by optically slitting the wavelengths using dichroic filters (Friedman et al., 2006; Testa et al., 2010). In live SMLM, sequential imaging is not an option since the goal is usually to monitor simultaneous events, but simultaneously imaging more than two colors in 3D with single molecule resolution is challenging. High-density based single molecule localization approaches can be used to improve temporal resolution (Cox et al., 2012; Zhu et al., 2012; Gustafsson et al., 2016), but at the expense of losing access to single molecular coordinates and therefore single molecule tracking capabilities.

To date, multicolor single molecule fluorescence detection has mostly been implemented using band-pass filters to discriminate between fluorophores (Friedman et al., 2006; Testa et al., 2010). This requires the fluorescence emission spectra of each color to be well separated for minimal signal crosstalk, which limits the number of detectable fluorophores and increases the number of laser lines required to excite all fluorophores. Moreover, splitting the collected photons into several different channels lowers the number of photons per localization event, reducing the localization precision and spatial resolution. Finally, separating the wavelengths with filters requires either splitting and reducing the field of view, or using several cameras for each wavelength, which become complex and expensive for more than two colors. Overall, this strategy compromises the spatial resolution and the acquisition throughput. One alternative is spectral demixing, which allows to use a single excitation line and discriminate up to three spectrally close fluorophores (Lampe et al., 2012; Zhang et al., 2020), but has not been applied for single particle tracking up to date.

Alternatively, a particularly powerful class of approaches aims to distinguish different dyes' species by directly measuring their spectral signature instead of using emission filters. This is achieved by measuring simultaneously the position and the emission spectrum for each fluorophore. This can be done by combining confocal (Lundquist et al., 2008) or line-scanning excitation schemes (Cutler et al., 2013) with a spectrometer to record the spectral signature. However, confocal-based detection are slow and lack of sensitivity to achieve resolution at the nanometric scale. Another strategy consists in using a diffractive element, such as a prism (Zhang et al., 2015; Moon et al., 2017; Huang et al., 2018; Yan et al., 2018) or a diffraction grating (Bongiovanni et al., 2016; Dong et al., 2016; Liu et al., 2019; Song et al., 2019), in a standard full-field single molecule localization microscope. In these approaches, each fluorophore generates two images: an image without light dispersion to access to the spatial position of the molecules, and a spectral image using a dispersive optical element. Single objective implementations, which split the collected photons in two different detection paths for localization and spectral information, have been proposed but at the cost of a lower localization precision (Bongiovanni et al., 2016; Dong et al., 2016; Moon et al., 2017; Yan et al., 2018). Other groups proposed a 4Pi configuration, i.e., using two objectives positioned on either side of the samples, to preserve the localization precision while accessing the spectral signature of the detected emitters (Zhang et al., 2015; Liu et al., 2019). While these 4Pi configuration detected up to four colors simultaneously on fixed cells using highly overlapping emission spectra fluorophores, their horizontal implementations were not compatible with live cell imaging, which is typically performed in an inverted geometry, preventing powerful single particle tracking to be performed. Huang et al. proposed a single objective implementation combined with an environmental controlled chamber to track up to three different proteins simultaneously on a living cell (Huang et al., 2018), but with a reduced localization precision. All these implementations aim also to probe the full spectra of the molecules detected, imposing strong limitations on the single molecule density per frames to separate those large spectra onto the camera. They therefore limit the acquisition speed and/or statistics achievable, and reduce the probability of the observation of potential meeting of observed molecules, which could be the signature of an interaction in between them.

We here detail an acquisition and analysis framework for versatile multidimensional (3D + t + λ) SMLM (**Figures 1A,B**), with a focus on its capability to perform 3D multicolor single particle tracking using a spectral detection configuration. Composed of commercially available standard equipment and software, and a freely available analysis solution, we demonstrate that optimal spectral SMLM (up to five colors) can be performed without compromising the 2D and 3D localization and tracking performance. We illustrate 3D multicolor imaging of various fixed and living samples, including the simultaneous nanoscale monitoring of neuronal synaptic receptors' dynamics. We show that using both the spatial and the spectral information we can achieve optimal multidimensional single molecule localization.

2 MATERIALS AND METHODS

2.1 Microscopy Setup

We devised a custom spectral microscope with a 4Pi configuration for versatile ($3D + t + \lambda$) SMLM. It is composed of two commercially inverted microscope bodies (Nikon TiE)

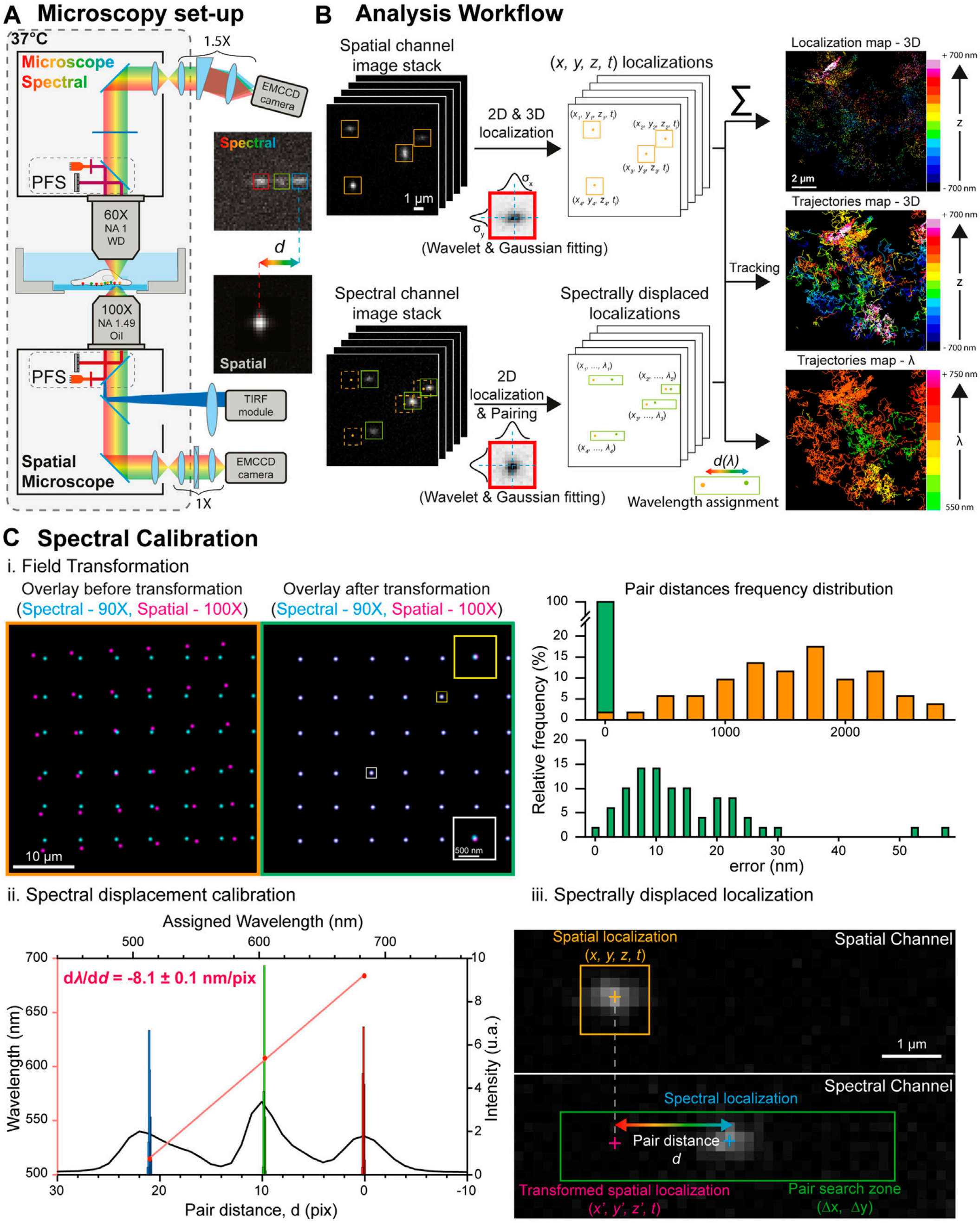

FIGURE 1 | Spectral single molecule microscopy set-up and analysis workflow. **(A)** Microscopy set-up overview: two inverted microscope bodies are positioned one on top of the other to benefit from their stability, automation and active axial feedback through their respective Perfect Focus Systems. The lower (spatial) microscope is equipped with a TIRF/HILO excitation module and a cylindrical lens for astigmatism-based 3D single molecule localization. The upper (spectral) microscope is equipped with a spectral detection arm made of a low dispersive prism (10°) and a ×1.5 magnification relay that converts the spectral information of single molecules into a spatial shift *d*. The insets show 100 nm TetraSpeck beads (excited at 488, 561 and 642 nm) detected by the lower microscope (bottom) and the upper microscope (top) after dispersion, illustrating the spatial shift induced by the prism according to the emission wavelength. **(B)** Spectrally displaced localization workflow. The single molecule localizations in spatial and spectral image stacks are computed using wavelet filtering and bidimensional Gaussian fitting. The localization of the single molecule events in the image stack acquired on the spatial channel enables retrieving their 3D coordinates with nanometric accuracy and reconstruct their trajectories. The spectrally displaced localization, which enables to compute the single molecule's spectral signature, is performed by pairing the localizations of the same single molecule in both channels and computing their relative distance *d* directly related to the emitted wavelength. **(C)** Spectrally displaced localization calibration. **(i.)** Left: superposition of the localizations of a bead displaced throughout the cameras whole field of view obtained through the spatial (magenta, ×100 magnification) and spectral (cyan, ×90 magnification) channels before (left) and after (right) the field transformation. The insets in the right images shows zooms on two beads to illustrate the field transformation. Right: Histograms of the distances between the paired spatial and spectral localizations before (top) and after (bottom) field transformation. After field transformation, the

(*Continued*)

FIGURE 1 | mean shift in between the paired localization is below 12 nm. **(ii.)** Calibration of the prism-induced spectral displacement: The black curve represents a line scan along the three emission peaks of a TetraSpeck bead detected on the spectral channel. Their individual localizations on 1,000 successive frames (histograms) enabled to compute their respective spatial shift depending on their central wavelength (red dots). Linear regression (red curve) leads to the calibration of the prism-induced spatial shift according to the emitted wavelength used for spectrally displaced localization. **(iii.)** Principle of the spectrally displaced localization process: The localization of a single molecule on the spatial channel is reported in the spectral channel after field transformation. A pair search zone (green rectangle) defined according to the prism dispersion axis and an *a-priori* knowledge of the molecule wavelength enables to pair it with its localization on the spectral channel. The pair distance allows the precise determination of the emission wavelength to the localized molecule.

precisely aligned one on top of the other: a first microscope, placed below, to perform state of the art (3D + t) SMLM (called direct or spatial), equipped with an azimuthal TIRF/HiLo illumination device (iLAS2, Gataca Systems); a second microscope, placed on top, for spectral (λ) characterization using photons usually lost in traditional mono objective configurations (**Figure 1A**, **Supplementary Figure S1**). The two microscope bodies are precisely aligned by translating the bottom microscope using a (x, y, θ, φ) stage placed below the bottom microscope (UMS, Scientifica). Such a geometry allows i) to perform state of the art 3D localization using all the photons collected by one high NA TIRF objective (×100 Oil NA1.49, Nikon); ii) to determine the spectral signature of the detected fluorophores using a second high NA objective (×60, Water Dipping NA1, Nikon), without compromising the localization performances (**Figure 1B**). The choice of using commercial microscopes is to benefit from existing hardware (filter cube, objective turret, TIRF illumination module, Perfect Focus System), motorization, software control, and stability for long-term acquisitions. It also provides a user-friendly environment that biologists are familiar with. The whole 4Pi microscope is caged in a custom plexiglass enclosure heated at 37°C for live cell experiments (Life Imaging System) and driven by the MetaMorph software (Molecular Devices). The conventional vertical architecture enables using standard live sample holders, simplifying live sample preparation protocols and imaging. Two synchronized sensitive EMCCDs (Photometrics EVOLVE 512B), one for each detection path, allow the microscope to track bright quantum dots as well as dimmer organic fluorophores and fluorescent proteins across the entire field of view of the EMCCDs, nearly 80 μm × 80 μm @ 30Hz, using conventional filter sets and dichroic mirrors. Axial stability, a crucial parameter for maintaining the desired focal planes for each imaging path, is ensured by their respective integrated Nikon Perfect Focus System (PFS), allowing real-time axial drift compensation based on LED reflection at the coverslip surface. We used special custom filters to ensure the two PFS systems to be used simultaneously without interfering (**Supplementary Figure S2**). Before PFS activation, both spatial and spectral imaging planes are precisely adjusted independently to overlap to each other using fiduciary markers adsorbed at the glass coverslip, and this focal plane overlap is maintained post-PFS activation using the PFS's axial offset.

On the lower detection path, we use an astigmatism-based approach (manual N-STORM kit, Nikon) to achieve state of the art 3D localization (**Figure 2**) and tracking (**Figure 3**). On the upper spectral detection path, we use a low dispersive prism (10° edge prism, PS814-A, Thorlabs) placed in the Fourier plane of a 4f imaging relay to access to the spectral signature of the detected emitters. This 4f system integrates a ~×1.5 zoom to optically match the spatial and spectral FOVs as closely as possible, with a magnification of ×100 and ×90 respectively. Such a relatively low diffracting prism, compared to the highly dispersive element commonly used in other hyperspectral systems so far (Zhang et al., 2015; Bongiovanni et al., 2016; Dong et al., 2016; Moon et al., 2017; Huang et al., 2018; Yan et al., 2018; Song et al., 2019), enables computing the colour of the single emitters without spreading their whole emission spectra onto the upper camera. Hence, it allows higher single molecule density experiments to be performed, which is particularly important to monitor statistically rare events. This dispersive element converts each emitter's wavelength into a spatial displacement, laterally shifting the localization of the single emitter linearly with respect to its spectral mean. We measured a spectral dispersion of −8.1 ± 0.1 nm/pixel using multicolor diffraction limited microbeads (100 nm) with well-defined fluorescence spectra. Once calibrated, the emission wavelength of each localized molecule is precisely determined by computing the dispersion-induced spatial displacement, thanks to the localizations pairing between the upper and the lower detection paths (see below) (**Figure 1C**). Critically, the low dispersion contains the spectrum of common fluorescent dyes to just a few pixels, which allows the use of conventional localization algorithms.

By building on top of commercial microscope bodies, we were able to modify various components to optimize and streamline the usability of the microscope, most notably with the objective configurations. While the original implementation used matching 100X NA 1.49 oil objectives on the spatial and spectral paths, we ran into several difficulties that limited routine use on living samples in this configuration. Since our system supports mismatched objectives, we chose to use a 60X NA1 water dipping objective (90X after 1.5X additional magnification) on the upper optical path, with a 100X NA1.49 oil immersion objective on the lower path, thereby avoiding several optical and mechanical limitations of the matched objective configuration. Mismatching the objectives allowed us: (1) to maintain the collection efficiency of oil immersion objectives for 3D localization and the capacity to perform TIRF illumination, (2) to simplify the sample mounting without the need to mount samples in between two closely spaced coverslips (≈30 μm), (3) to increase the field of view (by 10%) and the depth of field (from ≈0.4 to 0.7 μm) of the spectral channel, and (4) to reduce spherical aberrations induced by imaging 30 μm deep through a coverslip with a high NA oil immersion objective. Altogether, the use of a 60X NA1 water dipping objective on the spectral channel greatly reduces the experimental complexity of using the system by allowing the use of conventional, open-top

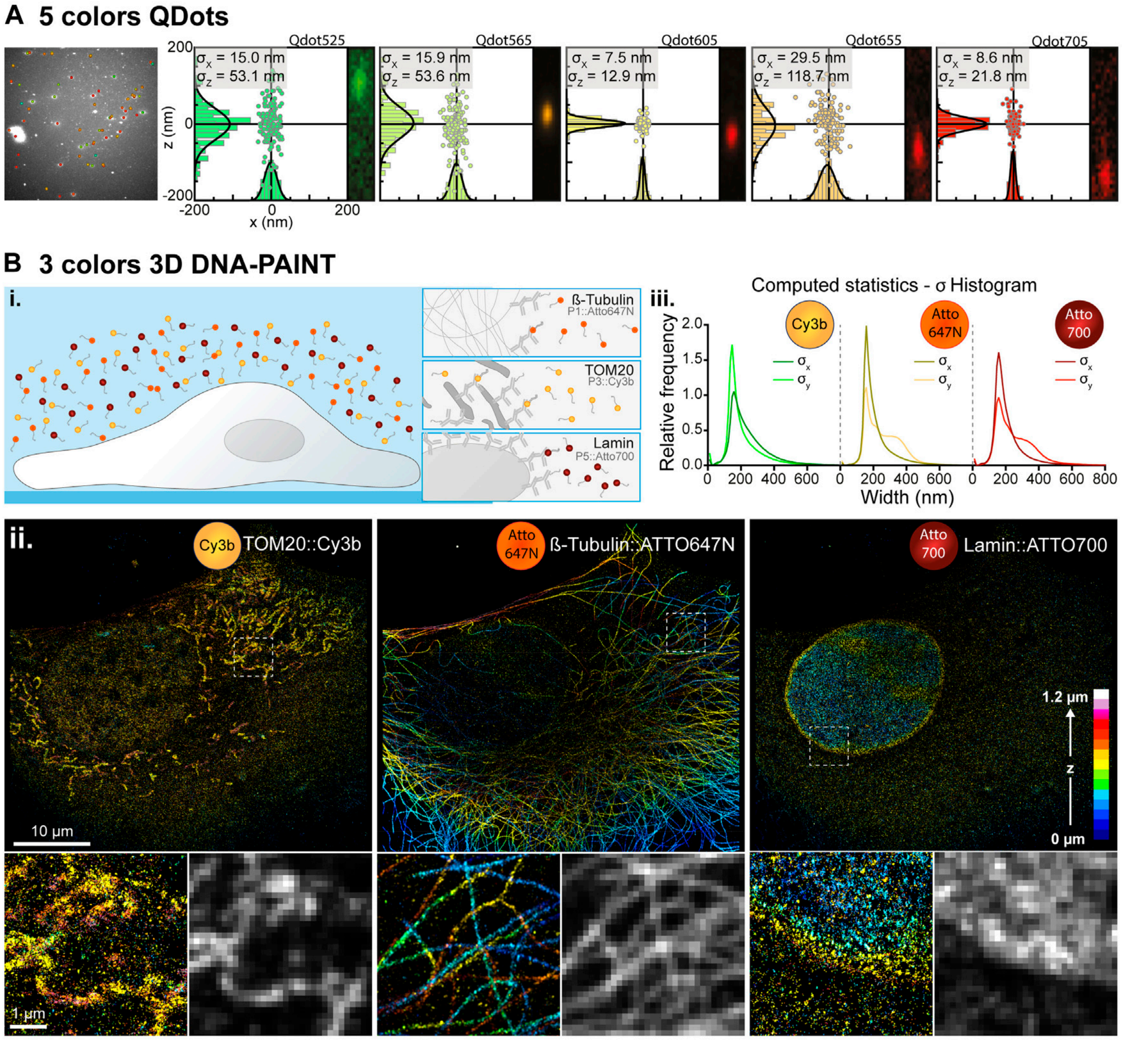

FIGURE 2 | Simultaneous multi-color single molecule detection. **(A)** Simultaneous detection of five spectrally different Qdots. Left: Image of a field of view containing five spectrally different populations of Qdots with their overlaid localization and emission wavelength determined by spectrally displaced localization. Right: Spectral localizations of Qdots computed from 1,000 consecutive frames for each population of QDots with their localization histogram along the x- and z-axis and the associated Gaussian fitting (black curves) for pointing accuracy estimation. The insets represent the images of those Qdots in the spectral (upper) channel inside the pair search zone. **(B)** Simultaneous three colors 3D DNA-PAINT imaging. **(i.)** Experiment principle: Three biological structures of interest (microtubule, TOM20 and LaminB1) are labelled within a COS-7 cell with orthogonal DNA docking strands each associated with an imager strand conjugated to a different fluorescent dye (Atto647N, Cy3b and Atto700 respectively). **(ii.)** Depth color-coded super-resolved 3D reconstructions of the three structures of interest acquired simultaneously and filtered in wavelength to extract each of the three dyes populations. Intensity images have been reconstructed using the ImageJ ThunderSTORM plugin to create a blur effect according to the single molecule localization precision. The lower panels represent zoomed-in images of the dotted white boxes and their comparison with diffraction-limited images of the same areas reconstructed using a fixed Gaussian blur of 100 nm (resp. 250 nm) standard deviation in XY (resp. Z), to simulate diffraction limited spatial resolutions of 230 nm (resp. 575 nm). **(iii.)** Histograms of the astigmatism-based PSF widths along the x- (σ_x) and y-axis (σ_y) for each dyes' population computed by bidimensional Gaussian fitting.

sample holders and maximizing the probability that the upper channel will collect spectral data for each localization on the spatial channel.

2.2 Single Molecules Localization Analysis

We have developed a complete analysis software solution, called PALMTracer, to analyze and represent multi-dimensional (x, y, z, t, λ) SMLM data. It is developed as a plugin of MetaMorph software, to be used either directly on the microscope during the acquisition and provide rapid user-feedback, or in off-line mode to analyze the data post-acquisition. It allows standard 2D and 3D single molecule localization and tracking as well as advanced spectral analysis, integrating quantitative analysis of diffusive properties with various visualizations. It is the result of 10 years of developments with biologist end-users (Rossier et al., 2012; Nair et al., 2013; Garcia et al., 2015; Chamma et al., 2016; Beghin et al., 2017; Floderer et al., 2018; Jullié et al., 2020; Compans et al., 2021), and comes with an intuitive graphical user interface (GUI) (**Supplementary Figure S3**). It integrates a powerful batch engine enabling to systematically and sequentially analyze several files in an entirely automatic fashion, greatly speeding up the analysis of various experiments. Many filtering options are available on the various statistics that can be computed from SMLM localization (Gaussian fit properties) and tracking analysis (diffusion properties) as well as on the spectral characterization.

2.2.1 Single Molecule Localization and Tracking

Single molecule localization is performed using a combination of wavelet decomposition and Gaussian fitting (Izeddin et al., 2012; Kechkar et al., 2013). Wavelet decomposition allows detection of isolated single emitters quickly and robustly to noise and background (Izeddin et al., 2012), while Gaussian fitting enables the precise coordinates determination of the detected emitters, in two and three dimensions (Kechkar et al., 2013). Once localized, molecule trajectories are computed from the molecular coordinates using a simulated annealing algorithm (Racine et al., 2006). Diffusion coefficients are extracted from the trajectories by linear fitting the Mean Square Displacement (MSD) curves, which represent the surface, or volume in 3D, explored by a molecule over time (Sibarita, 2014). Localization coordinates and trajectories, and their related quantitative features (e.g., Gaussian fitting parameters, MSD, diffusion coefficients, etc …) are saved in various CSV files, compatible with popular analysis and visualization software such as VISP (El Beheiry and Dahan, 2013), ThunderSTORM (Ovesný et al., 2014) or SR-TESSELER (Levet et al., 2015) for advanced rendering and point-cloud analysis.

2.2.2 Spectral Analysis by Spectrally Displaced Localization

The spectral determination of each localized molecule is achieved by spectrally displaced localization. It consists in pairing the localizations of single emitters obtained from the two images of the same focal plane collected simultaneously from the direct (lower) and spectral (upper) detection paths, and measuring the spatial shift induced by the prism in the upper detection path (**Figure 1C–iii**). Indeed, this dispersive element converts the emitter wavelength (λ) into a spatial displacement (d), by shifting in a first approximation the localization linearly as a function of the emission wavelength. This spatial shift allows to easily retrieve the emission wavelength of the emitters localized in the lower detection path, allowing their accurate (x, y, z, t, λ) determination.

Spectrally displaced localization is computationally simple and intuitive, as it only relies on standard localization and pairing algorithms. It is a three-step process:

(1) Superposition of the spatial and spectral channels: a calibration step is required to compensate for differences in magnification, rotation, or other field of view distortions between the direct (lower) and spectral (upper) detection paths. The field of view transformation is computed from raster scanning images of a fiducial marker having a single fluorescence emission peak (fluorescent nanodiamonds excited at 647 nm in our case) in a 7 × 7 grid, covering the whole field of view of the two detection paths (**Figure 1C–i**). The corresponding 49 centroids positions are first localized in each channel and paired by nearest neighbor search. Then, a two-dimensional 3rd order polynomial transformation is computed from the paired coordinates by least-squares Levenberg-Marquardt minimization algorithm:

$$x' = a_{x,1}x^3 + a_{x,2}y^3 + a_{x,3}x^2y + a_{x,4}xy^2 + a_{x,5}x^2 + a_{x,6}y^2 + a_{x,7}xy + a_{x,8}x + a_{x,9}y + a_{x,10} \tag{1}$$

$$y' = a_{y,1}x^3 + a_{y,2}y^3 + a_{y,3}x^2y + a_{y,4}xy^2 + a_{y,5}x^2 + a_{y,6}y^2 + a_{y,7}xy + a_{y,8}x + a_{y,9}y + a_{y,10} \tag{2}$$

where x' and y' are the transformed coordinates of x and y, respectively with coefficients $a_{x,n}$ and $a_{y,n}$. This 3rd order polynomial transformation requiring 10 coefficients per spatial dimension is used to render the system as versatile as possible and correct for any non-linear field of view deformations induced by the spectral optics or the cylindrical lens. Once calibrated, this transformation is applied to the lower localizations to match the field of view of the upper camera, resulting in a field-dependent error after transformation typically ranging from 0 to ~60nm, with median values around ε = 12 nm (**Figure 1C–i**). Due to the prism in the spectral detection path, this field of view transformation is wavelength dependent, and this alignment process creates a transformation centered at the spectral mean wavelength λ_0 of the emission of the fiducial marker used.

(2) Pairing of the detected molecules on both channels: Once the direct (lower) coordinates are transformed to match the spectral (upper) coordinates, a linear search around the transformed lower localization is performed to find its paired upper localization (**Figure 1C–iii**). The displacement angle of the prism is aligned with the EMCCD chip to induce a displacement of the localizations in one axis direction as a function of the wavelength (y-axis in our case). It allows minimizing the pair search zone to a reduced linear zone. Minimizing the size of this pair search zone is important as it defines the maximum density of simultaneously fluorescing single molecules per image frame, minimizing missed pairing. The width (Δx) and height (Δy) of the search zone are both user-definable based on *a priori* knowledge of the fluorescent species being imaged. Once the localizations are matched, their pair distance, d, is calculated as $d = y_{upper-}y'_{lower}$ and retained as a proxy for the spectral mean of the emitter.

(3) Wavelength determination: The wavelength (λ) of each paired localization is assigned upon spectral calibration using the following linear function: $\lambda = \lambda_0 + \alpha d$, λ_0 being the reference emission wavelength and α the calibration spectral coefficient. The spectral calibration is performed by imaging isolated tetraspeck multicolor beads (N = 7 beads, 100 planes) adsorbed on a glass coverslip, exciting at λ_{exc} = 488 nm (blue), λ_{exc} = 561 nm (orange), and

λ_{exc} = 640 nm (red). The system was aligned using the red fluorophore as a reference ($\lambda_0 = 683\, nm$) and a distance of 20.90 ± 0.06 pixels (resp. 9.69 ± 0.04) was measured with the blue (resp. orange) fluorophores. Distances were computed from the localization of the three detected peaks of the tetraspeck beads. We considered the mean emission wavelength integrated over the quad-band filter used in detection ($\lambda_{red} = 683\, nm$; $\lambda_{orange} = 607\, nm$; $\lambda_{blue} = 514\, nm$). This calibration allows the precise determination of the spectral dispersion coefficient $\alpha = -8.1 \pm 0.1\, nm/Pix$ of our spectral detection arm (**Figure 1C–ii**).

It is important to note that the spectrally displaced localization process does not alter the accuracy of the spatial localizations from the lower detection path, and merely provides additional spectral information for each localization with no photon cost. In addition, the spatial localization of the emitter's signature in the spectral (upper) channel can also provide additional spatial information allowing overlapping spectrally different emitters to be separated by spectrally-informed multi-Gaussian fitting (**Section 2.2.4**). However, in this specific case of spatially overlapping fluorophores, spectrally displaced localization efficiency is limited by their spectral proximity to several tens of nanometers, depending on the prism-induced spectral dispersion and the spectral width of the fluorophores' emission. This therefore limits the maximum number of fluorophores that can be readily monitored simultaneously.

2.2.3 Lateral Drift Correction

Lateral drifts in either the lower or upper detection path affect the pair distance between matched localizations, deteriorating the spectrally displaced localization quality during the acquisition (**Supplementary Figure S4**). To avoid time-dependence in the spectral assignment, it is necessary to numerically compensate for the drift on each path post-acquisition. We used fiduciary markers to compute and compensate for lateral drifts on each channel separately to correct for drifts incurred during the image acquisition process. Additionally, lateral shifts between the fields of view accumulated between acquisitions on the same coverslip were corrected by simply updating the zero-order coefficients of the field of view transformation ($a_{x,10}$ and $a_{y,10}$ of **Eqs 1, 2**), allowing the use of a previously computed field transformation while compensating for spatial drifts. These automatic corrections of the FOV transformation and independent channel drifts ensure that the two channels remain aligned (pair distance = 0) at a fixed wavelength as long as the same fiducial markers and filter sets are used.

2.2.4 Spectrally-Informed Multi-Gaussian Fitting

In order to distinguish overlapping single molecule signals, occurring when single emitters are separated by less than ~200 nm one from each other, a common solution is to use multi-Gaussian fitting algorithms (Holden et al., 2011; Huang et al., 2011; Babcock et al., 2012). However, in absence of knowledge of the number of single molecule candidates (n), systematic multi-gaussian fitting can lead to artefacts, especially for astigmatism-based 3D localization, which requires more parameters to estimate (Sage et al., 2019). Here, we take advantage of the localization information in the spectral channel to determine the number of molecules to localize, and select either a single or a multiple Gaussian fitting algorithm (**Figure 4A**). Such spectrally-informed multi-Gaussian fitting enables to (1) constrain the number of emitters that have to be retrieved and (2) initialize the spatial positions of those emitters perpendicular to the prism dispersion axis in the fitting process. This is of course only possible if the overlapping emitters have emission wavelengths sufficiently different that they result in two distinct localizations on the spectral channel. The number of single molecule candidates to localize by spectrally-informed multi-Gaussian fitting, either one or two, is determined by the number of localizations in the pairing area (Δx, Δy) of the spectral image (**Section 2.2.2** for definition). We further exploit the information from the spectral channel to improve the accuracy of the multi-Gaussian fitting algorithm by initializing it with the spatial localization in the dimension perpendicular to the spectral displacement, ie. with the x-coordinates if the spectral dispersion is in the y-direction. Such a capacity allows monitoring several proteins simultaneously exploring the same nanoscopic environment smaller than the diffraction limit, opening new venues to monitor potential molecular interactions.

2.2.5 Simulations

The systematic use of a single- or a multi-emitter fitting process may lead to under- or over-counting errors. Indeed, single emitter localization cannot distinguish several emitters within a diffraction limited area, whereas multi-emitter localization sometime detects several emitters in a region where there is only a single emitter (**Figure 4A**). In order to characterize and validate the spectrally-informed multi-Gaussian fitting algorithm, we simulated dual-camera SMLM acquisitions using real-world conditions (**Figure 4B**). We first generated a "ground-truth" localization file containing two spectrally distinct emitters (Qdot655 and Qdot705) on the spatial and spectral images for 320 frames. The intensity and spectral dispersion of the emitters were assigned based on real acquisition data to ensure similar spectrally displaced localization precision. Second, this ground-truth localization file was used to generate image stacks with simulated PSFs. Per-pixel noise statistics were analyzed from real acquisitions and used as background, again to ensure a localization precision similar to real-life conditions. Qdot705 was positioned statically at the center of the frame and Qdot655 displaced horizontally across the field of view at 10 nm/frame, such that the emitters begin separated, then overlap on the spatial image, but never on the spectral image, and then separate again (**Figure 4B–i**). Finally, these simulated image stacks were then analyzed using only the spatial information by single- and multi-fitting algorithms, as well as the spectrally-informed analysis, and compared with the ground-truth localizations. We observed that, when only the spatial information is used, conventional multi-Gaussian fitting resulted in a mean fit error of 229 nm (**Figure 4B–ii**). Such a large mean error stems mainly from pairing errors due to over-localization obtained by systematic multi-Gaussian fitting.

Analyzing the same dataset using the spectrally-informed multi-Gaussian fitting resulted a mean fit error of 56 nm, a 4-times improvement that enables more accurate SPT of two spatially overlapping emitters (**Figure 4B–ii**). This difference is explained by the elongation of the astigmatism-based point-spread function with respect to the axial position of the emitters (**Figure 4B–iii**).

2.3 Imaging Experiments

2.3.1 Simultaneous Detection of Five Qdots

Five different populations of streptavidin conjugated Qdots (Qdot525, Qdot565, Qdot605, Qdot655 and Qdot705, Q10151MP, Invitrogen) were physically adsorbed onto an 18 mm clean coverslips at a very low concentration (**Figure 2A**). The exact concentration for each population was first sequentially adjusted. A solution of a unique diluted streptavidin labelled Qdot population was incubated for 10 min on a clean 18 mm coverslips along with 100 nm fluorescent nanodiamond acting as fiduciaries and reference for spectral calibration (1:1,000 from stock solution, NDNV100 nmMd10ml, Adamas Nanotechnologies INC.) and then rinsed three times with PBS. The coverslips were then imaged on our spectral microscope in order to determine the density of adsorbed streptavidin labelled Qdots and the concentration adjusted accordingly to ensure single molecule detection regime when mixed with four other Qdots populations. Finally, five population of streptavidin Qdots were incubated for 10 min on a coverslip (concentration: Qdot525: 1:1.10^6; Qdot565: 1:2.10^6; Qdot605: 1:5.10^6; Qdot655: 1:2.10^6; Qdot705: 1:2.10^6) along with nanodiamonds, rinsed three times with PBS and mounted onto a Ludin imaging chamber (Life Imaging System). For imaging, all Qdots populations were excited at 488 nm through a Quad-band filter (F66-04TN, AHF) in the lower (spatial) microscope, and a triple laser lines rejection filter (ZET 405/488/561, F67-408, AHF) was added into the upper (spectral) detection path to reject excitation laser light.

2.3.2 Three Color DNA-PAINT Experiments

Cos-7 cells were plated onto 18 mm 1.5H coverslips at 50,000 cells per coverslips for isolated cell experiments. After spreading (around 4 h), cells were prepared using a fixation step with 4% formaldehyde +0.1% Triton X-100 for 10 min, followed by the quenching of the autofluorescence using 150 mM Glycine (Sigma) in PBS for 10 min, and an additional permeabilization step with 0.3% Triton X-100 for 10 min. Unspecific binding sites were then blocked using 3% BSA (Sigma) in PBS for 2 h at room temperature before primary antibodies incubation overnight at 4°C in the same blocking solution. Rat anti-alpha-tubulin (MA1-80017, ThermoFisher) diluted at 1:300, goat anti-Lamin B1 (sc-6217, Santa Cruz) diluted at 1:300 and Rabbit anti-TOM20 (sc-11415, Santa Cruz) diluted at 1:600 were used. After three washing steps with the blocking solution, cells were incubated with the following DNA-PAINT secondary antibodies kindly provided by Ralf Jungmann's lab for 2 h at room temperature: anti-rat conjugated with the P1 DNA handle (1:100), anti-rabbit conjugated with the P3 DNA handle (1:100) and anti-goat conjugated with the P5 DNA handle (1:100). Cells were finally washed three times with the blocking solution and three times with PBS before being stored at 4°C until imaging. Just before imaging, coverslips were incubated with 100 nm nanodiamonds as fiduciaries at 1:1,000 from the stock solution for 10 min and then rinsed three times with PBS. For imaging, a solution containing the following imager strands (Eurofins) were prepared in an imaging solution (PBS +500 mM NaCl): P1*-Atto647N diluted at 30 pM, P3*-Cy3b diluted at 300 pM and P5*-Atto700 diluted at 200 pM and poured onto a coverslip mounted into a Ludin imaging chamber (the star indicates the complementary of the DNA strand). Concentrations of the imager strands were first adjusted individually for each color to ensure adequate single molecule density before being combined for the simultaneous 3-colors experiment. For acquisition, two laser lines at 561 and 642 nm were simultaneously used to excite the fluorophore Cy3b and Atto647N/Atto700 respectively thanks to a quad band filter set in the lower (spatial) microscope. In the upper detection arm (spectral microscope) a quad-band notch filter 400-410/488/561/631-640 (F40-072, AHF) was added to filter out excitation laser light. 120,000 frames were acquired at 5 Hz and then analyzed with PALMTracer (**Figure 2B**).

2.3.3 Multiple 3D QDots Tracking of Membrane Proteins on Living Fibroblasts

Cos-7 cells were electroporated with plasmids coding for the protein NCAM:AP and the enzyme, BirA^{ER} according to the manufacturer's protocol (Lonza), using 2.5 µg (resp. 2 µg) of DNA for 2 million cells. Electroporated cells were immediately seeded on 18 mm 1.5H coverslips at 50,000 cells per coverslips and incubated in high-glucose Dulbecco's modified Eagle's medium (DMEM, Sigma) supplemented with 10% Fetal Bovine Serum (FBS, 16000-044, ThermoFisher), 1% GlutaMAX (35050-061, Gibco) and 1% penicillin-streptomycin (Sigma) and with the addition of 10 µM of biotin according the protocol described in Chamma et al. (Chamma et al., 2017). 48 h post-electroporation, cells were incubated with 100 nm nanodiamonds as fiduciaries at 1:1,000 from the stock solution and streptavidin labelled with Qdot605, Qdot655 and Qdot705 diluted at 1:40,000, 1:40,000 and 1:50,000 from stock solution respectively for 10 min. After washing excess of Qdots' labelled streptavidin with culture media, imaging medium (Fluorobright A1896702, ThermoFisher) supplemented with 10% FBS, 1% Glutamax, and 100 mM Hepes was poured onto the cells for imaging. During imaging a single laser line at 561 nm was used to excite all three Qdot populations through a quad-band filter set in the lower (spatial) microscope, and a triple laser lines rejection filter (ZET 405/488/561) in the upper (spectral) detection path to filter out laser excitation light. Imaging was performed at frame rates ranging from 20 to 100 Hz on field of views ranging from 80 × 80 µm to 20 × 20 µm respectively (**Figure 3A**).

2.3.4 Multiple 3D QDot Tracking of Synaptic Receptors on Living Neurons

Mixed hippocampal cultures containing both neurons and glial cells were prepared from embryonic stage (E18) Sprague-Dawley rats and maintained in Neurobasal Plus medium (Gibco, A3585911) supplemented with GlutaMAX™ (Gibco, #35050-038), B-27™ Plus (Gibco, A3653401), and 10% horse serum for 3–5 days *in vitro* (DIV), at which time the medium was changed to a horse-serum free B27 Plus-containing Neurobasal Plus medium. Neurons were transfected between DIV-7 and DIV-10 with plasmids encoding D1R-cfp and EphrinB2-flag as well as soluble GFP using the calcium-phosphate coprecipitation method. In between DIV-12 and DIV-14, neurons were then prepared for imaging. They were first incubated for 10 min with a mix of rabbit anti-GFP (#A-6455, Thermo Fisher Scientific Inc., 1:10,000) and mouse anti-Flag (#F-1804, Thermo Fisher Scientific Inc., 1:1,000) primary antibodies, then washed and incubated for 10 min with F (ab')2-Goat anti-Rabbit IgG-coupled Qdot655 (#Q11422MP, ThermoFisher Scientific Inc., 1:50000) or Qdot705 (#Q11461MP, ThermoFisher Scientific Inc., 1:50000), F (ab')2-Goat anti-Mouse IgG-coupled Qdot605 (#Q11002MP, ThermoFisher Scientific Inc., 1:50000), and nanodiamonds (1: 1,000) as fiduciaries and wavelength reference. All incubations and imaging were done in conditioned 1% BSA-supplemented Tyrode solution (in mM: 105 NaCl, 5 KCl, 2 MgCl2, 12 D-glucose, 25 HEPES, pH 7.4). Labelled receptors were imaged for 1,000 consecutive frames at 20 Hz frame rate (**Figure 3B**). During imaging, a single laser lines at 561 nm was used to excite all three Qdots populations through a quad-band filter set in the lower (spatial) microscope, and a triple laser lines rejection filter (ZET 405/488/561) was added in the upper (spectral) detection path to filter out laser excitation light.

3 RESULTS

3.1 System Characterization

We first demonstrated the capacity of our method to detect simultaneously five different colors, with single molecule resolution. We imaged five different Qdot populations adsorbed to the surface of a coverslip and excited with a single 488 nm laser (**Section 2.3.1**). 2,000 frames of the two full chip CCD cameras were acquired at 20 Hz and analyzed by spectrally displaced localization. **Figure 2A** shows a single frame with the detected Qdots and their assigned wavelength, demonstrating the homogeneity of the wavelength distributions for each quantum dot population. As the 90X effective zoom (60X objective 1.5X zoom) of the upper detection path images a slightly larger field of view and greater depth of field than the lower 100X objective, it maximizes the probability of matching the detected events on the bottom (spatial) channel to a localization on the upper (spectral) channel for their spatially displaced localization. Localization accuracies were then computed for each Qdot population by localizing the same Qdot for 1,000 consecutive frames and Gaussian fitting each localization distribution. Lateral and axial localization accuracies were estimated to ($\sigma_{xy} = 15.0\,nm$, $\sigma_z = 53.1\,nm$) for QDots525, ($15.9\,nm$, $53.6\,nm$) for QDots565, ($7.5\,nm$, $12.9\,nm$) for QDots605, ($29.5\,nm$, $118.7\,nm$) for QDots655, and ($8.6\,nm$, $21.8\,nm$) for QDots565 depending on the brightness of each Qdot population.

3.2 3D Multicolor DNA-PAINT Imaging

We then demonstrated the possibility to detect simultaneously up to three organic dyes in a DNA-PAINT imaging strategy. Usually, multi-color DNA-PAINT is made using a sequential approach (Jungmann et al., 2014; Klevanski et al., 2020) but at the expense of a very long acquisition time and numerous washing steps. Here we labelled three cellular structures (microtubules, nucleus envelope (lamin B1) and mitochondria (TOM20)) using three orthogonal docking strands. Then we added the three corresponding imager strands conjugated to three spectrally different fluorophores (ATTO700, ATTO647N and Cy3b) into the imaging media. It enabled us to record simultaneously the 3D nanoscale organization of those three different proteins, increasing by two the overall acquisition time as compared to a sequential acquisition (**Figure 2B–i**). Super-resolution images were reconstructed from 688,312 (TOM20), 4,501,791 (microtubule) and 636,483 (Lamin) localizations after wavelength assignment and filtering on the goodness of Gaussian fitting (range [0.6, 1]) representing respectively 3.2, 20.9 and 3% of the total localized single molecules that have been assigned to a wavelength by spectrally displaced localization (**Figure 2B–ii**). **Figure 2B–iii** shows the distributions of σ_x and σ_y single molecule Gaussian fitting parameters for each fluorophore revealing different mean depth of the structure observed.

3.3 Multiple 3D QDot Tracking on COS-7 Cells

Next, we performed three color SPT experiments on the biotinylated NCAM membrane protein, labelled with three spectrally different streptavidin labelled Qdots (Qd705, Qd655 and Qd605). We demonstrated our ability to track simultaneously three Qdot populations in 3D at up to 100Hz frame rate (**Figure 3A**; **Supplementary Figure S5**). The use of Qdots enables using a single laser line excitation (at 561 nm in our case) for the three species, lowering the overall radiation dose on the sample, and minimizing the phototoxicity. All of the Qdot populations showed similar instantaneous diffusion coefficients distributions (**Figure 3A–iii**.), validating our capacity to accurately track three different populations simultaneously, in 3D, at high spatial and temporal resolution.

3.4 Multiple 3D QDot Tracking of Synaptic Receptors on Living Neurons

Finally, we tracked simultaneously several membrane proteins implicated in synaptic transmission and neurodegenerative disorders on live mixed hippocampal neuron cultures. We probed the same protein (D1R) with secondary antibodies tagged with 2 different quantum dots species (Qdot655 and Qdot705), and the Ephrin B2 receptor with Qdot605 (**Figure 3B**). Multicolor data were acquired using our spectral microscope and analyzed using spectrally-informed multi-Gaussian fitting and tracking, from which we could extract Qdots trajectories in 3D for each species. Spectrally-informed multi-Gaussian fitting allowed extracting 1.5 more localizations

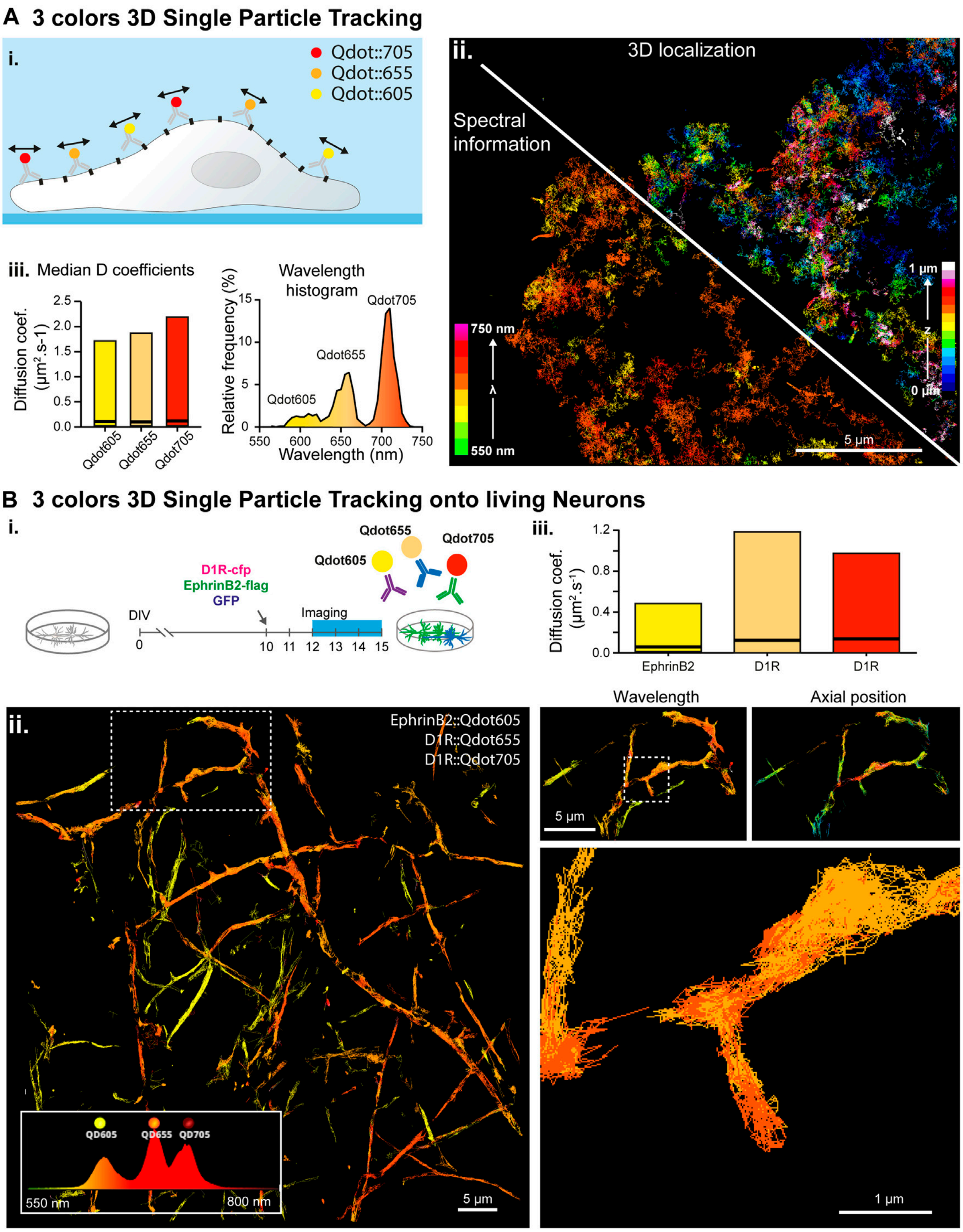

FIGURE 3 | Simultaneous multi-color 3D single molecule tracking. **(A)** Simultaneous three colors 3D single particle tracking on living COS-7 cells. **(i.)** Experiment principle: NCAM membrane receptors in a COS cell are labelled with three populations of spectrally different QDots and tracked in 3D over time. **(ii.)** Reconstructed trajectories of the detected Qdots color-coded for their depth (upper right corner) or for their assigned wavelength (bottom left corner). **(iii.)** Computed median and range of diffusion coefficients for each QDots population (left) and histogram of the wavelengths detected during the acquisition revealing the three Qdot populations (right). **(B)** Simultaneous three colors 3D single particle tracking on living neurons. **(i.)** Experiment principle: Hippocampal dissociated neurons culture are transfected at DIV-10 with the plasmids coding for D1R-cfp, EphrinD2-Flag and soluble GFP. In between DIV12 and DIV15, expressed D1R-cfp proteins are labelled with two populations of spectrally different Qdots (Qdot 655 and Qdots705) and expressed EphrinB2-flag proteins are labelled with Qdots605 before being imaged and analyzed by spectrally informed localization and tracking. **(ii.)** Left: Reconstructed trajectories of the three Qdots populations. Right: Successive zooms of the white dotted regions revealing the main and well distinct zones explored by the two receptors (top) and the trajectory of two spectrally different Qdots (Qd655 and Qd705) within a spine (bottom). **(iii.)** Median and range of diffusion coefficients for each of the three different Qdots population, revealing that the two Qdots conjugated to the same receptors (D1R) behave similarly whereas EphrinB2 receptors diffuse slower.

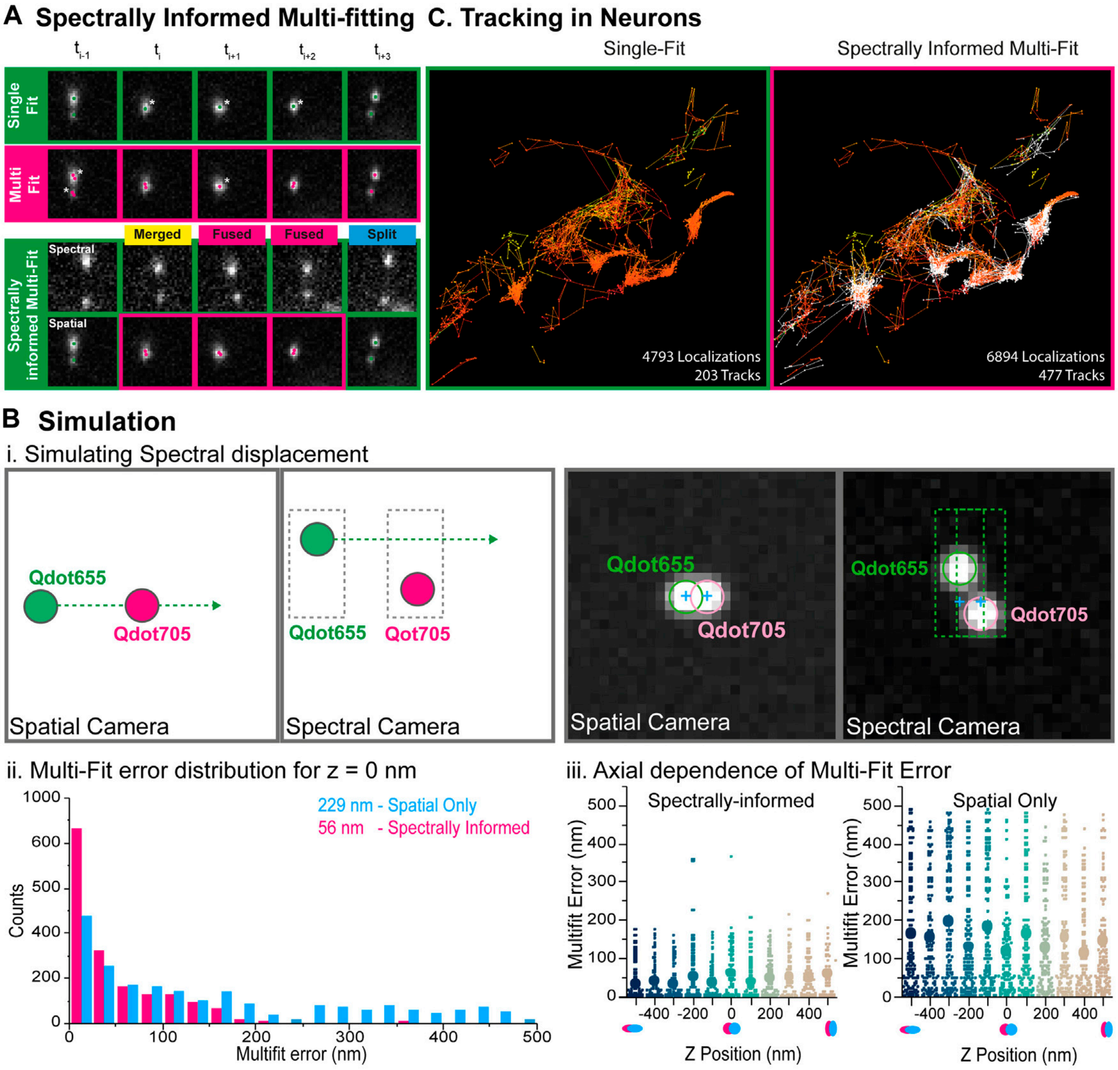

FIGURE 4 | Spectrally-informed multi-fitting principle and benchmarking through simulations. **(A)** Principle of the spectrally-informed multi-Gaussian fitting method. When two fluorescent single particles diffuse together within an area smaller than the diffraction limit of light, it becomes impossible to localize them individually and extract their exact trajectories. A systematic single Gaussian-fitting approach leads to under-counting localization (top) whereas a systematic multi-Gaussian fitting approach sometime leads to over-counting localizations (middle) (Stars indicate over- or under-counting errors in the localization process). If those particles have different spectral signatures, they will be separated in the spectral channel, allowing to precisely determine the number of particles, and to use the multi-Gaussian fitting algorithm when needed to retrieve their coordinates (bottom). The Spectrally-informed multi-Gaussian fitting (magenta) occurs when two emitters overlap on the spatial channel (single localization) and two distinct localizations are detected on the spectral channel. **(B)** Multi-Gaussian fitting simulation for benchmarking. **(i.)** Simulation principle: Two spectrally-distinct emitters (QDot 655 and QDot 705) were simulated for the spectral and spatial cameras for 320 frames. QD655 displaces horizontally across the field of view at 10nm/frame such that the emitters begin separated, then overlapped on the spatial camera but not on the spectral camera, and finally separated again. Right: True camera noise and PSF sizes were used in the simulations. The two emitters overlap on the spatial camera, but not on the spectral camera. **(ii.)** The localization error for each of the multi-Gaussian fitting methods (without and with spectral information) is calculated and compared to the simulated localization for simulated separation distances up to +/- 500 nm. Systematically performing the multi-Gaussian fitting results in a mean square error of 229 nm (magenta), while utilizing the spectrally-informed multi-Gaussian fitting algorithm results in a 4x reduction of localization error to 56 nm (cyan). **(iii.)** The same horizontal-displacement simulation was then performed for various simulated astigmatic z-positions between –500 and 500 nm. Mean error for each of z-position is plotted for each fitting method (without (right) and with (left) spectral information), illustrating that the spectrally-informed multi-fitting significantly improves the localization precision across the range of assignable axial positions. **(C)** Simultaneous three colors Qdots tracking within living neurons. Reconstructed trajectories computed from systematic single-emitter fitting (left) or spectrally informed multi-Gaussian fitting (right). Spectrally-informed Gaussian fitting leads to ≈1.5 times more localizations and ≈2 times more trajectories.

and twice more trajectories, mostly occurring when localized molecules are at a distance below 200 nm (**Figure 4C**). As expected, both populations of D1R receptors were found on the dendrites, while the Ephrin B2 receptors were mostly localized along the axons (**Figure 3B–ii.**), validating the specificity of the antibody labeling cocktail. Furthermore, the two sets of D1R receptors showed similar median diffusion coefficients of 0.12 μm·s^{-1} and 0.14 μm·s^{-1}, while Ephrin receptors displayed lower median diffusion coefficients of 0.06 μm·s^{-1} (**Figure 3B–iii**), in agreement with the literature (Mikasova et al., 2012; Ladepeche et al., 2013).

4 DISCUSSION

We described a powerful and versatile multidimensional single-molecule localization microscopy workflow. It is composed of a mix of commercially available hardware and software with custom freely available analysis software named PALMTracer. It integrates a spectrally-displaced single molecule localization process and a spectrally-informed multi-Gaussian fitting method allowing to precisely determine the emission wavelength of each localized molecule, and separate overlapping single-molecule signals with high reliability. As spectral determination is performed by collecting and analysing the emitted photons through a second microscope objective, it allows state of the art 3D single molecule localization and tracking to be performed, as well as simultaneous spectral analysis without compromising the spatio-temporal resolution and the field of view. Spectral information also permits to precisely determine the number and 3D coordinates of overlapping, yet spectrally distinct single-molecule emitters.

We intentionally chose to use a low dispersive prism in our spectral detection arm in order to spatially limit the spectral extension onto the camera and allow higher single emitter density to be detected while preserving our capacity to separate several spectrally different populations. With the current configuration, we demonstrated the capability of our approach to detect up to five fluorophores simultaneously, which already represents a substantial biological challenge, more especially for live single molecule applications. This capacity could be further enhanced using fluorescent emitters with sharper spectral emission peak, or high-density based localization approaches and especially recent deep learning-based methods (Nehme et al., 2020; Speiser et al., 2021), whose last implementations outperform standard multi-gaussian methods. Trained for spectrally-displaced localization, it could further enhance the localization and spectral identification precision as well as allow higher detection density, opening new possibilities toward the detection of rare events like protein-protein interactions in real-time. On the other side, certain applications might benefit from higher dispersion capacity that can be easily achieved by replacing the current prism with a more dispersive one into the spectral detection path, in order to observe finer spectral signatures. It could enable, for example, to observe FRET events at the single molecules scale, offering new possibilities to characterize interactions in between bio-molecules. It could also provide a solution to characterize the nano-environment using environment sensitive dyes such a pH- or polar-sensitive dyes for instance (Klymchenko and Mely, 2013; Bongiovanni et al., 2016). It would require no fundamental modification of the current analysis software, but simply a finer description of the detected spectrum. Finally, with further developments to the biological assays and the spectral single particle tracking pipeline, we think our method could be extended in the future to quantify live molecular interactions with nanoscale resolution.

DATA AVAILABILITY STATEMENT

The raw data supporting the conclusions of this article will be made available by the authors, without undue reservation.

AUTHOR CONTRIBUTIONS

CB performed experiments and contributed to the development of PALMTracer. GES performed the biological experiments on neurons. AK improved the localization performances of PALMTracer. NB performed some biological experiments and analysis. VS came with the initial idea of the spectral imaging. JPD and LG supervised the experiments on neurons. RG developed the instrument, performed experiments and co-supervised this work. J-BS designed and developed PALMTracer software and supervised this work.

FUNDING

This work was supported by the FranceBioImaging infrastructure ANR-10-INBS-04, ANR NANOPLANSYN and the LabEx BRAIN to J-BS, the ANR soLIVE 16-CE11-0015-01 to RG and Human Frontier Science Program RGP0019/2016 to GS, JD, and LG.

ACKNOWLEDGMENTS

We would like to thank Ralph Jungmann, Maximilian Strauss and Thomas Schlichthärle for providing us the DNA-PAINT labelling kits as well as Olivier Thoumine and Ingrid Chamma for providing us the N-CAM-AP DNA plasmids. We would also like to thank Philippe Rideau from Nikon France for his support, as well as MIFOBIO and the GDR Imabio. We finally would like to thank the Cell Biology Facility, especially Emeline Verdier and L. Groc team's technical staff, for cellular tool productions and general cell biology activity management.

SUPPLEMENTARY MATERIAL

The Supplementary Material for this article can be found online at: https://www.frontiersin.org/articles/10.3389/fbinf.2022.813494/full#supplementary-material

REFERENCES

Babcock, H., Sigal, Y. M., and Zhuang, X. (2012). A High-Density 3D Localization Algorithm for Stochastic Optical Reconstruction Microscopy. *Opt. Nanoscopy* 1, 1–10. doi:10.1186/2192-2853-1-6

Beghin, A., Kechkar, A., Butler, C., Levet, F., Cabillic, M., Rossier, O., et al. (2017). Localization-based Super-resolution Imaging Meets High-Content Screening. *Nat. Methods* 14, 1184–1190. doi:10.1038/nmeth.4486

Betzig, E., Patterson, G. H., Sougrat, R., Lindwasser, O. W., Olenych, S., Bonifacino, J. S., et al. (2006). Imaging Intracellular Fluorescent Proteins at Nanometer Resolution. *Science* 313, 1642–1645. doi:10.1126/science.1127344

Bongiovanni, M. N., Godet, J., Horrocks, M. H., Tosatto, L., Carr, A. R., Wirthensohn, D. C., et al. (2016). Multi-dimensional Super-resolution Imaging Enables Surface Hydrophobicity Mapping. *Nat. Commun.* 7, 13544. doi:10.1038/ncomms13544

Chamma, I., Levet, F., Sibarita, J., Sainlos, M., and Thoumine, O. (2016). Nanoscale Organization of Synaptic Adhesion Proteins Revealed by Single- Molecule Localization Microscopy Proteins Revealed by Single-Molecule Localization. *Neurophotonics* 3, 041810. doi:10.1117/1.NPh.3.4.041810

Chamma, I., Rossier, O., Giannone, G., Thoumine, O., and Sainlos, M. (2017). Optimized Labeling of Membrane Proteins for Applications to Super-resolution Imaging in Confined Cellular Environments Using Monomeric Streptavidin. *Nat. Protoc.* 12, 748–763. doi:10.1038/nprot.2017.010

Choquet, D., Sainlos, M., and Sibarita, J.-B. (2021). Advanced Imaging and Labelling Methods to Decipher Brain Cell Organization and Function. *Nat. Rev. Neurosci.* 22, 237. doi:10.1038/s41583-021-00441-z

Cognet, L., Leduc, C., and Lounis, B. (2014). Advances in Live-Cell Single-Particle Tracking and Dynamic Super-resolution Imaging. *Curr. Opin. Chem. Biol.* 20, 78–85. doi:10.1016/j.cbpa.2014.04.015

Compans, B., Camus, C., Kallergi, E., Sposini, S., Martineau, M., Butler, C., et al. (2021). NMDAR-dependent Long-Term Depression Is Associated with Increased Short Term Plasticity through Autophagy Mediated Loss of PSD-95. *Nat. Commun.* 12, 1–18. doi:10.1038/s41467-021-23133-9

Cox, S., Rosten, E., Monypenny, J., Jovanovic-Talisman, T., Burnette, D. T., Lippincott-Schwartz, J., et al. (2012). Bayesian Localization Microscopy Reveals Nanoscale Podosome Dynamics. *Nat. Methods* 9, 195–200. doi:10.1038/nmeth.1812

Cutler, P. J., Malik, M. D., Liu, S., Byars, J. M., Lidke, D. S., and Lidke, K. A. (2013). Multi-Color Quantum Dot Tracking Using a High-Speed Hyperspectral Line-Scanning Microscope. *PLoS One* 8, e64320. doi:10.1371/journal.pone.0064320

Dong, B., Almassalha, L., Urban, B. E., Nguyen, T. Q., Khuon, S., Chew, T. L., et al. (2016). Super-resolution Spectroscopic Microscopy via Photon Localization. *Nat. Commun.* 7, 12290. doi:10.1038/ncomms12290

El Beheiry, M., and Dahan, M. Vi. S. P. (2013). Representing Single-Particle Localizations in Three Dimensions. *Nat. Methods* 10, 689–690. doi:10.1038/nmeth.2566

Floderer, C., Masson, J. B., Boilley, E., Georgeault, S., Merida, P., El Beheiry, M., et al. (2018). Single Molecule Localisation Microscopy Reveals How HIV-1 Gag Proteins Sense Membrane Virus Assembly Sites in Living Host CD4 T Cells. *Sci. Rep.* 8, 1–15. doi:10.1038/s41598-018-34536-y

Friedman, L. J., Chung, J., and Gelles, J. (2006). Viewing Dynamic Assembly of Molecular Complexes by Multi-Wavelength Single-Molecule Fluorescence. *Biophys. J.* 91, 1023–1031. doi:10.1529/biophysj.106.084004

Garcia, M., Leduc, C., Lagardère, M., Argento, A., Sibarita, J. B., and Thoumine, O. (2015). Two-tiered Coupling between Flowing Actin and Immobilized *N* -cadherin/catenin Complexes in Neuronal Growth Cones. *Proc. Natl. Acad. Sci.* 112, 201423455. doi:10.1073/pnas.1423455112

Gustafsson, N., Culley, S., Ashdown, G., Owen, D. M., Pereira, P. M., and Henriques, R. (2016). Fast Live-Cell Conventional Fluorophore Nanoscopy with ImageJ through Super-resolution Radial Fluctuations. *Nat. Commun.* 7, 1–9. doi:10.1038/ncomms12471

Heilemann, M., van de Linde, S., Schüttpelz, M., Kasper, R., Seefeldt, B., Mukherjee, A., et al. (2008). Subdiffraction-resolution Fluorescence Imaging with Conventional Fluorescent Probes. *Angew. Chem. Int. Ed. Engl.* 47, 6172–6176. doi:10.1002/anie.200802376

Holden, S. J., Uphoff, S., and Kapanidis, A. N. (2011). DAOSTORM: an Algorithm for High- Density Super-resolution Microscopy. *Nat. Methods* 8, 279–280. doi:10.1038/nmeth0411-279

Huang, F., Schwartz, S. L., Byars, J. M., and Lidke, K. A. (2011). Simultaneous Multiple-Emitter Fitting for Single Molecule Super-resolution Imaging. *Biomed. Opt. Express* 2, 1377. doi:10.1364/BOE.2.001377

Huang, T., Phelps, C., Wang, J., Lin, L. J., Bittel, A., Scott, Z., et al. (2018). Simultaneous Multicolor Single-Molecule Tracking with Single-Laser Excitation via Spectral Imaging. *Biophys. J.* 114, 301–310. doi:10.1016/j.bpj.2017.11.013

Izeddin, I., Boulanger, J., Racine, V., Specht, C. G., Kechkar, A., Nair, D., et al. (2012). Wavelet Analysis for Single Molecule Localization Microscopy. *Opt. Express* 20, 2081–2095. doi:10.1364/OE.20.002081

Jullié, D., Stoeber, M., Sibarita, J. B., Zieger, H. L., Bartol, T. M., Arttamangkul, S., et al. (2020). A Discrete Presynaptic Vesicle Cycle for Neuromodulator Receptors. *Neuron* 105, 663–677. doi:10.1016/j.neuron.2019.11.016

Jungmann, R., Avendaño, M. S., Woehrstein, J. B., Dai, M., Shih, W. M., and Yin, P. (2014). Multiplexed 3D Cellular Super-resolution Imaging with DNA-PAINT and Exchange-PAINT. *Nat. Methods* 11, 313–318. doi:10.1038/nmeth.2835

Kechkar, A., Nair, D., Heilemann, M., Choquet, D., and Sibarita, J.-B. (2013). Real-time Analysis and Visualization for Single-Molecule Based Super-resolution Microscopy. *PLoS One* 8, e62918. doi:10.1371/journal.pone.0062918

Klevanski, M., Herrmannsdoerfer, F., Sass, S., Venkataramani, V., Heilemann, M., and Kuner, T. (2020). Automated Highly Multiplexed Super-resolution Imaging of Protein Nano-Architecture in Cells and Tissues. *Nat. Commun.* 11, 1–11. doi:10.1038/s41467-020-15362-1

Klymchenko, A. S., and Mely, Y. (2013). Fluorescent Environment-Sensitive Dyes as Reporters of Biomolecular Interactions. *Prog. Mol. Biol. Translational Sci.* 113, 35. doi:10.1016/b978-0-12-386932-6.00002-8

Ladepeche, L., Dupuis, J. P., Bouchet, D., Doudnikoff, E., Yang, L., Campagne, Y., et al. (2013). Single-molecule Imaging of the Functional Crosstalk between Surface NMDA and Dopamine D1 Receptors. *Proc. Natl. Acad. Sci. U. S. A.* 110, 18005–18010. doi:10.1073/pnas.1310145110

Lampe, A., Haucke, V., Sigrist, S. J., Heilemann, M., and Schmoranzer, J. (2012). Multi-colour Direct STORM with Red Emitting Carbocyanines. *Biol. Cel.* 104, 229–237. doi:10.1111/boc.201100011

Lelek, M., Melina, T. G., Gerti, B., Florian, S., Juliette, G., Suliana, M., et al. (2021). Single Molecule Localization Microscopy. *Nat. Rev. Methods Prim.* 1. doi:10.1038/s43586-021-00038-x

Levet, F., Hosy, E., Kechkar, A., Butler, C., Beghin, A., Choquet, D., et al. (2015). SR-tesseler: a Method to Segment and Quantify Localization-Based Super-resolution Microscopy Data. *Nat. Methods* 12, 1–9. doi:10.1038/nmeth.3579

Liu, X., Longfang, Y., Weidong, Y., Yiyan, F., Lan, M., and Jiong, M. (2019). Spectroscopic Fluorescent Tracking of a Single Molecule in a Live Cell with a Dual-Objective Fluorescent Reflection Microscope. *Appl. Phys. Express* 12, 112007. doi:10.7567/1882-0786/ab4b16

Lundquist, P. M., Zhong, C. F., Zhao, P., Tomaney, A. B., Peluso, P. S., Dixon, J., et al. (2008). Parallel Confocal Detection of Single Molecules in Real Time. *Opt. Lett.* 33, 1026. doi:10.1364/ol.33.001026

Mikasova, L., De Rossi, P., Bouchet, D., Georges, F., Rogemond, V., Didelot, A., et al. (2012). Disrupted Surface Cross-Talk between NMDA and Ephrin-B2 Receptors in Anti-NMDA Encephalitis. *Brain* 135, 1606–1621. doi:10.1093/brain/aws092

Moon, S., Yan, R., Kenny, S. J., Shyu, Y., Xiang, L., Li, W., et al. (2017). Spectrally Resolved, Functional Super-resolution Microscopy Reveals Nanoscale Compositional Heterogeneity in Live-Cell Membranes. *J. Am. Chem. Soc.* 139, 10944–10947. doi:10.1021/jacs.7b03846

Nair, D., Hosy, E., Petersen, J. D., Constals, A., Giannone, G., Choquet, D., et al. (2013). Super-Resolution Imaging Reveals that AMPA Receptors inside Synapses Are Dynamically Organized in Nanodomains Regulated by PSD95. *J. Neurosci.* 33, 13204–13224. doi:10.1523/JNEUROSCI.2381-12.2013

Nehme, E., Freedman, D., Gordon, R., Ferdman, B., Weiss, L. E., Alalouf, O., et al. (2020). DeepSTORM3D: Dense 3D Localization Microscopy and PSF Design by Deep Learning. *Nat. Methods* 17, 734–740. doi:10.1038/s41592-020-0853-5

Ovesný, M., Křížek, P., Borkovec, J., Švindrych, Z., and Hagen, G. M. Thunder. S. T. O. R. M. (2014). A Comprehensive ImageJ Plug-In for PALM and STORM Data Analysis and Super-resolution Imaging. *Bioinformatics* 30, 2389–2390.

Racine, V., Hertzog, A., Jouanneau, J., Salamero, J., Kervrann, C., and Sibarita, J. B. (2006). "Multiple-target Tracking of 3D Fluorescent Objects Based on Simulated Annealing," in 3rd IEEE International Symposium on Biomedical Imaging: Nano to Macro, 2006, Arlington, VA, USA, 6-9 April 2006, 1020–1023. doi:10.1109/isbi.2006.1625094

Rossier, O., Octeau, V., Sibarita, J. B., Leduc, C., Tessier, B., Nair, D., et al. (2012). Integrins β 1 and β 3 Exhibit Distinct Dynamic Nanoscale Organizations inside Focal Adhesions. *Nat. Cel. Biol.* 14, 1057–1067. doi:10.1038/ncb2588

Rust, M. J., Bates, M., and Zhuang, X. (2006). Imaging by Stochastic Optical Reconstruction Microscopy (STORM). *Nat. Methods* 3, 793–795. doi:10.1038/nmeth929

Sage, D., Pham, T. A., Babcock, H., Lukes, T., Pengo, T., Chao, J., et al. (2019). Super-resolution Fight Club: Assessment of 2D and 3D Single-Molecule Localization Microscopy Software. *Nat. Methods* 16, 387–395. doi:10.1038/s41592-019-0364-4

Sibarita, J.-B. (2014). High-density Single-Particle Tracking: Quantifying Molecule Organization and Dynamics at the Nanoscale. *Histochem. Cel. Biol.* 141, 587–595. doi:10.1007/s00418-014-1214-1

Song, K.-H., Zhang, Y., Wang, G., Sun, C., and Zhang, H. F. (2019). Three-dimensional Biplane Spectroscopic Single-Molecule Localization Microscopy. *Optica* 6, 709. doi:10.1364/optica.6.000709

Speiser, A., Müller, L. R., Hoess, P., Matti, U., Obara, C. J., Legant, W. R., et al. (2021). Deep Learning Enables Fast and Dense Single-Molecule Localization with High Accuracy. *Nat. Methods* 18, 1082. doi:10.1038/s41592-021-01236-x

Testa, I., Wurm, C. A., Medda, R., Rothermel, E., von Middendorf, C., Fölling, J., et al. (2010). Multicolor Fluorescence Nanoscopy in Fixed and Living Cells by Exciting Conventional Fluorophores with a Single Wavelength. *Biophys. J.* 99, 2686–2694. doi:10.1016/j.bpj.2010.08.012

Thompson, R. E., Larson, D. R., and Webb, W. W. (2002). Precise Nanometer Localization Analysis for Individual Fluorescent Probes. *Biophys. J.* 82, 2775–2783. doi:10.1016/S0006-3495(02)75618-X

Yan, R., Moon, S., Kenny, S. J., and Xu, K. (2018). Spectrally Resolved and Functional Super-resolution Microscopy via Ultrahigh-Throughput Single-Molecule Spectroscopy. *Acc. Chem. Res.* 51, 697–705. doi:10.1021/acs.accounts.7b00545

Zhang, Y., Schroeder, L. K., Lessard, M. D., Kidd, P., Chung, J., Song, Y., et al. (2020). Nanoscale Subcellular Architecture Revealed by Multicolor Three-Dimensional Salvaged Fluorescence Imaging. *Nat. Methods* 17, 225–231. doi:10.1038/s41592-019-0676-4

Zhang, Z., Kenny, S. J., Hauser, M., Li, W., and Xu, K. (2015). Ultrahigh-throughput Single-Molecule Spectroscopy and Spectrally Resolved Super-resolution Microscopy. *Nat. Methods* 15, 935–938. doi:10.1038/nmeth.3528

Zhu, L., Zhang, W., Elnatan, D., and Huang, B. (2012). Faster STORM Using Compressed Sensing. *Nat. Methods* 9, 721–723. doi:10.1038/nmeth.1978

Conflict of Interest: Author CB was employed by the company Imagine Optic under a PhD Cifre contract.

The remaining authors declare that the research was conducted in the absence of any commercial or financial relationships that could be construed as a potential conflict of interest.

Frontiers in Bioinformatics

Explores innovation in the analysis and interpretation of biological data

An innovative journal that provides a forum for new discoveries in bioinformatics. It focuses on how new tools and applications can bring insights to specific biological problems.

Discover the latest Research Topics

See more →


frontiers

Frontiers in
Bioinformatics

Frontiers
Avenue du Tribunal-Fédéral 34
1005 Lausanne, Switzerland
frontiersin.org

Contact us
+41 (0)21 510 17 00
frontiersin.org/about/contact